

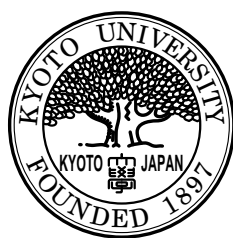
# Indications of Neutrino Oscillation in K2K Experiment

A DISSERTATION

BY

Issei Kato

July 2004



Department of Physics, Graduate School of Science  
Kyoto University



A DISSERTATION SUBMITTED  
TO  
THE GRADUATE SCHOOL OF SCIENCE,  
KYOTO UNIVERSITY  
ON  
28 JULY 2004  
IN  
PARTIAL FULFILLMENT OF THE REQUIREMENTS  
FOR THE DEGREE OF DOCTOR OF PHILOSOPHY  
IN  
PHYSICS

BY

Issei Kato

*Department of Physics, Graduate School of Science, Kyoto University*  
*Kitashirakawa-oiwake-cho, Sakyo-ku, Kyoto 606-8502, JAPAN*  
*issei@scphys.kyoto-u.ac.jp*





## Abstract

This thesis presents the first results of analysis dedicated to neutrino oscillation with the disappearance of muon neutrino in a long baseline neutrino experiment, the K2K experiment. The analysis is based on the data taken June 1999 to July 2001, in correspondence to total number of protons on target of  $4.79 \times 10^{19}$ . In the analysis, the neutrino flux and energy spectrum measurements in the detectors at near site, the beam extrapolation from near to far site validated by a pion monitor measurements, and the observation in far site are all in use with the correlation between energies and interaction cross-sections taken into account. The results indicate the existence of neutrino oscillation  $\nu_\mu \nrightarrow \nu_\mu$ : a reduction of  $\nu_\mu$  flux together with a distortion of the energy spectrum. Fifty-six beam neutrino events are observed in Super-Kamiokande, 250 km from the neutrino production point, with an expectation of  $80.1^{+6.2}_{-5.4}$  in the case of no neutrino oscillation. Twenty-nine one ring  $\mu$ -like events are used to reconstruct the neutrino energy spectrum, which is better matched to the expected spectrum with neutrino oscillation than without. The probability that the observed flux at Super-Kamiokande is explained by statistical fluctuation without neutrino oscillation is less than 1%. The oscillation parameters at the best-fit point are obtained to be  $(\sin^2 2\theta, \Delta m^2) = (1.0, 2.8 \times 10^{-3} \text{ eV}^2)$  for the two flavor oscillation. The 90% C.L. region for the mass squared difference,  $\Delta m^2$ , at  $\sin^2 2\theta = 1$  is estimated to be  $(1.5-3.9) \times 10^{-3} \text{ eV}^2$ . These results are consistent with the results of the atmospheric neutrino observations.



## Acknowledgements

This thesis could not be achieved without any supports. First of all, I would like to express my appreciation to Prof. Koichiro Nishikawa, the supervisor of this thesis and the spokesperson of K2K experiment. He involved me with the most exciting experiments in high energy physics, K2K and Super-Kamiokande, and gave me a great chance to study the most important parts of neutrino physics and high energy physics in the world. It has been an extraordinary time in physics and for me. He has guided me through thick and thin to become a physicist. I would also like to make an appreciation to Prof. Tsuyoshi Nakaya. He has also been one of advisers for this thesis. He has been giving me a number of things interesting about high energy physics. I could learn a lot of things from basic knowledges to technical issues. I thank Prof. Takashi Kobayashi for his many advices all the time since the very beginning of my graduate school life. He has encouraged me to join the HARP experiment at CERN and gave me very precious experiences to enjoy physics abroad and to make discussions with the overseas physicists. I wish to extend my appreciation to Prof. Y. Totsuka, Prof. K. Nakamura, Prof. Y. Suzuki, Prof. C. K. Jung, Prof. R. J. Wilkes, and Prof. M. Sakuda. They have been managed the K2K experiment to accomplish my research.

My study strongly depends on the hard works of many collaborators. For 1KT part, Prof. Y. Ito gave me a lot of instruction about the detector, the analysis software, and the physics issues. I also want to thank Dr. M. Miura, Dr. S. Mine, Dr. S. Nakayama, Ms. J. Zalipska, Dr. A. K. Ichikawa, Dr. C. Mauger, and other 1KT group members for their supports for the stable data taking and analysis. For the beam monitoring, I was supported by Beam Monitor Group, especially Dr. T. Hasegawa, Dr. T. Maruyama, and Dr. J. Hill. I also thank the SciFi and MRD Groups, particularly Prof. M. Sakuda, Dr. T. Ishii, Dr. T. Ishida, Dr. T. Inagaki, Dr. T. Iwashita, and Ms. H. Yokoyama for their instructions on the system and the analysis. The analysis for Super-Kamiokande data is supported by Prof. K. Kaneyuki, Dr. S. Yamada, and all of Super-Kamiokande collaborators. I express my gratitude for their great works on the detector calibrations and data analysis. The complete works for the data taking have been performed by Prof. T. Kobayashi, Dr. Y. Hayato, Dr. M. Yoshida, and many other people, and here I want to thank them. I also give another thank to Dr. Y. Hayato for his supports in the simulation works. I really thank Mr. H. Maesaka, Mr. M. Hasegawa, and Mr. S. Yamamoto for supporting me in my research as collaborating students from Kyoto University. K2K is made possible by the inventiveness and the diligent efforts of the KEK-PS machine and beam channel groups. I would like to give my special thanks to them for their perfect beam operation. Thanks to all of the kind collaborators, I could spend very precious, fruitful, and happy time in the K2K experiment.

For the HARP experiment, which unfortunately could not be included in this thesis, I would like to thank Prof. J. J. Gomez Cadenas who has taken care of me about the data analysis and my stay in CERN as a analysis coordinator and also as a K2K collaborator. I also express my appreciation to Dr. A. Cervera Villanueva who has also co-worked with me on the analysis. I'm very gratitude to Prof. J. Panman and Prof. F. Dydak, spokespersons of HARP experiment, for their kindly inviting us to the experiment. I also want to give thanks to all the other HARP collaborators for their kindness during my stay in HARP. I could have very precious and valuable time and experience there.

I am deeply grateful to all the members of my laboratory in Kyoto University; To Prof. N. Sasao for giving me the first educations on the high energy physics. To Prof. H. Sakamoto, Dr. R. Kikuchi, Dr. T. Nomura, and Dr. M. Yokoyama for encouraging me in my research life and giving me great advices. To Mr. Y. Honda, Mr. A. Shima, and Mr. E. Shin'ya as colleagues at my laboratory. To Mr. M. Suehiro, Dr. Y. Takeuchi, Dr. K. Murakami, Dr.

Y. Ushiroda, Dr. H. R. Sakai, Dr. T. Inagaki, Mr. T. Fujiwara, Mr. and Ms. Nakamura, Dr. S. Nishida, Mr. H. Yokoyama, Mr. H. Yumura, and Mr. S. Mukai for their advices and helps. To Mr. H. Maesaka, Mr. K. Mizouchi, Ms. K. Uchida, Mr. M. Hasegawa, Mr. S. Yamamoto, Mr. T. Sumida, Mr. S. Tsuji, Mr. T. Sasaki, Mr. K. Hayashi, Mr. T. Morita, Mr. S. Ueda, Mr. K. Hiraide, Mr. J. Kubota, Mr. T. Shirai, Ms. N. Taniguchi, Ms. K. Takezawa, and all the other members for making my life in laboratory very interesting, exciting, and happy. I also want to give my thanks to my friends for cheering me up all the time. Here, I would like to make a lot of appreciations to Ms. A. Nakao and Ms. T. Kiyosawa, secretaries of our laboratory, for their appropriate works and kindness, and to Ms. K. Nakagawa, Ms. E. Hirai, Ms. A. Saito, and all the members in the secretariat of the department for their taking care of every official/private businesses.

I thank the KEK and ICRR Directorates for their strong support and encouragement. I gratefully acknowledge the cooperation of the Kamioka Mining and Smelting Company. This work has been supported by the Ministry of Education, Culture, Sports, Science and Technology, Government of Japan and its grants for Scientific Research, by the Japan Society for Promotion of Science (JSPS), by the U.S. Department of Energy, by the Korea Research Foundation, and by the Korea Science and Engineering Foundation. Personally, I have been supported by JSPS Research Fellowship for Young Scientists for the financial support and the promotion of this research. I gratefully acknowledge Prof. Y. Totsuka for his financial support to give me a precious opportunity to attend and give a talk at an authoritative conference of “Recontres de Moriond”. I have also been supported by a Grant-in-Aid for the 21 century COE of “Center for Diversity and Universality in Physics”.

Finally, I would like to express the special appreciation to my parents, to my family, especially to my grandfather, for a number of physical, mental, and financial supports throughout my life, and to Aya Bamba for her loving helps and encouragements, and giving me a happy life.

*Issei Kato  
at Kyoto  
5 July 2004*

## The K2K Collaboration

E. Kearns, S. Likhoded, J. L. Stone, L. R. Sulak, C. Walter, W. Wang  
*Boston University*

R. Helmer, P. Kitching, A. Konaka  
*Canada's National Laboratory for Particle and Nuclear Physics (TRIUMF)*

J. H. Choi, H. I. Jang, J. S. Jang, E. M. Jeong, J. Y. Kim, H. K. Lee, M. J. Lee, I. T. Lim,  
S. H. Lim, K. J. Ma, S. Y. You  
*Chonnam National University*

M. Y. Pac  
*Dongshin University*

I. Endo, M. Inuma, S. Nawang, T. Takahashi  
*Hiroshima University*

R. Ashie, S. Fukuda, Y. Fukuda, J. Hosaka, K. Ishihara, M. Ishitsuka, Y. Itow, T. Kajita,  
K. Kaneyuki, Y. Kobayashi, Y. Koshio, A. Minamino, M. Miura, S. Moriyama, M. Nakahata,  
S. Nakayama, T. Namba, R. Nambu, Y. Obayashi, A. Okada, K. Okumura, T. Ooyabu,  
C. Saji, N. Sakurai, M. Shiozawa, Y. Suzuki, Y. Takenaga, H. Takeuchi, Y. Takeuchi, K. Taki,  
T. Toshito, S. Yamada  
*Institute for Cosmic Ray Research, University of Tokyo*

A. Butkevich, M. Khabibullin, A. Khotjantsev, Y. Kudenko, V. Matveev, S. Mikheyev,  
O. Mineev, N. Yershov  
*Institute for Nuclear Research, Moscow*

T. Chikamatsu, Y. Hayato, A. K. Ichikawa, T. Ichida, T. Ishii, H. Ishino, T. Iwashita,  
J. Kameda, T. Kobayashi, S. B. Lee, T. Maruyama, K. Nakamura, K. Nakayoshi, K. Nitta,  
Y. Oyama, H. S. Park, A. Sakai, M. Sakuda, K. Shiino, M. Tanaka, K. Tauchi, Y. Totsuka  
*Institute of Particle and Nuclear Studies, High Energy Accelerator Research Organization*

S. Aoki, K. Asakura, S. Echigo, K. Fujii, T. Hara, M. Kitamura, M. Kohama, G. Kume,  
Y. Moriguchi, F. Nakata, S. Nishiyama, S. Noda, M. Onchi, T. Otaki, K. Satoh, M. Sekiguchi,  
Y. Suga, A. Suzuki, M. Takatsuki, K. Kakenaka, Y. Tanaka, K. Tashiro  
*Kobe University*

S. H. Ahn, S. An, S. J. Hong, C. O. Kim, T. J. Kim, D. K. Koo, J. W. Lee, J. K. Oh,  
S. H. Park, S. K. Park  
*Korea University*

M. Hasegawa, K. Hayashi, K. Hiraide, T. Inagaki, I. Kato, J. Kubota, H. Maesaka, T. Morita,  
S. Mukai, T. Nakadaira, T. Nakaya, K. Nishikawa, T. Sasaki, N. Sasao, A. Shima, S. Ueda,  
S. Yamamoto, M. Yokoyama  
*Kyoto University*

K. McConnel, K. Scholberg  
*Massachusetts Institute of Technology*

S. Kenmochi, K. Miyano, K. Nakamura, N. Tamura  
*Niigata University*

A. Ikeda, I. Nakano, T. Umeda, T. Yamaguchi  
*Okayama University*

Y. Kuno, Y. Takubo, M. Yoshida  
*Osaka University*

J. Argyriades, J. Bouchez, C. Cavata, M. Fechner, J. Mallet, F. Pierre, S. T’Jampens  
*Saclay (DSM-DAPNIA)*

M. H. Ahn, H. C. Bhang, E. J. Jeon, K. Joo, B. Kang, B. Kim, H. I. Kim, J. H. Kim,  
S. B. Kim, E. Seo, H. So, J. Yoo  
*Seoul National University*

J. Hill, C. K. Jung, D. Kerr, K. Kobayashi, K. Martens, C. Mougier, C. McGrew, A. Sarrat,  
E. Sharkey, C. Yanagisawa  
*SUNY at Stony Brook*

M. Etoh, T. Hasegawa  
*Tohoku University*

T. Inada, T. Kadowaki, S. Kishi, H. Yokoyama  
*Tokyo University of Science*

E. Aliu, X. Espinal, E. Fernandez, F. Sanchez, A. Rodriguez  
*University of Barcelona*

F. Berghaus, T. Kutter, S. Oser, J. Wendland  
*University of British Columbia*

D. Casper, W. Gajewski, W. R. Kropp, S. Mine, M. Smy, H. W. Sobel, V. Tumakov, M. Vagins  
*University of California, Irvine*

A. Blondel, S. Borghi, A. Cervera  
*University of Geneva*

A. Kibayashi, J. G. Learned, S. Matsuno  
*University of Hawaii*

U. Dore, P. F. Loverre, L. Ludovici  
*University of Rome “La Sapienza”*

S. Miyamoto  
*University of Tokyo*

H. G. Berns, S. B. Boyd, R. Gran, K. K. Shiraishi, A. Stachyra, R. J. Wilkes  
*University of Washington*

J. Burguet Castell, J. J. Gomez Cadenas, A. T. Lopez, V. G. Sitjes  
*University of Valencia*

U. Golebiewska, D. Kielczewska, J. Zalipska  
*Warsaw University*

# Contents

<b>1</b>	<b>Introduction</b>	<b>1</b>
1.1	A brief history of neutrinos and their masses . . . . .	1
1.2	Phenomenology of neutrino oscillation . . . . .	2
1.3	Experimental sensitivity to oscillation parameters . . . . .	5
1.4	Summary of neutrino oscillation measurements . . . . .	6
1.5	Outline of this thesis . . . . .	8
<b>2</b>	<b>The K2K Experiment</b>	<b>9</b>
2.1	Conceptual description of the K2K experiment . . . . .	9
2.2	Design of the K2K experiment . . . . .	11
2.2.1	Comparison between the measurements in ND and SK . . . . .	11
2.2.2	Neutrino interaction studies in ND . . . . .	12
2.2.3	Extrapolation of the neutrino flux and spectrum from ND to SK . . . . .	13
2.2.4	Neutrino beam pointing to SK . . . . .	13
2.2.5	Time synchronization between KEK-PS and SK . . . . .	14
2.3	Sensitivity of the K2K experiment . . . . .	15
2.4	History of the experiment . . . . .	15
<b>3</b>	<b>Experimental Components and Their Performances</b>	<b>17</b>
3.1	Accelerator and neutrino beam line . . . . .	17
3.1.1	Proton accelerator and primary beam transportation line . . . . .	17
3.1.2	Production target and focusing horn magnets . . . . .	19
3.1.3	Decay volume and beam dump . . . . .	21
3.2	Primary beam monitors . . . . .	23
3.2.1	Intensity monitors . . . . .	23
3.2.2	Profile and position monitors . . . . .	23
3.3	Secondary beam monitors . . . . .	25
3.3.1	Pion monitor . . . . .	25
3.3.2	Muon monitors . . . . .	29
3.4	Data acquisition system of beam line monitors . . . . .	32
3.5	Near neutrino detectors . . . . .	33
3.5.1	1 kt water Cherenkov detector . . . . .	33
3.5.2	Trigger/veto counters . . . . .	44
3.5.3	Scintillating fiber tracker . . . . .	47
3.5.4	Lead glass Cherenkov calorimeter . . . . .	48
3.5.5	Muon range detector . . . . .	49
3.5.6	Data acquisition system in ND . . . . .	51
3.6	Far neutrino detector . . . . .	52
3.6.1	Detector structure . . . . .	53

3.6.2	Water purification system and water transparency . . . . .	53
3.6.3	Data acquisition system in SK . . . . .	54
3.6.4	ATM, PMT gain, and timing calibrations . . . . .	55
3.6.5	Calibration of the absolute energy scale . . . . .	56
3.7	Global positioning system for the time synchronization . . . . .	57
3.7.1	Overview of GPS . . . . .	57
3.7.2	Time synchronization between KEK and SK . . . . .	57
3.7.3	Stability of GPS system . . . . .	59
<b>4</b>	<b>Monte Carlo Simulations</b>	<b>61</b>
4.1	Neutrino beam simulation: Beam-MC . . . . .	61
4.1.1	Proton injection onto the production target . . . . .	61
4.1.2	Production of secondary particles in the target . . . . .	62
4.1.3	Particle tracking through the horn magnets and decay volume . . . . .	63
4.1.4	Particle decays into neutrino . . . . .	63
4.1.5	Monte Carlo prediction of neutrino properties at ND and SK . . . . .	66
4.2	Neutrino interaction simulation: Neut-MC . . . . .	69
4.2.1	Neutrino interactions in a few GeV region . . . . .	69
4.2.2	CC quasi-elastic and NC elastic scattering . . . . .	70
4.2.3	Single-meson production . . . . .	71
4.2.4	Deep inelastic scattering . . . . .	72
4.2.5	Coherent pion production . . . . .	73
4.2.6	Nuclear effects . . . . .	74
4.2.7	Summary of modifications in Neut-MC . . . . .	75
4.3	Detector simulation: DetSim . . . . .	76
4.3.1	Simulation of water Cherenkov detector, 1KT and SK . . . . .	76
4.3.2	Simulation of fine-grained detector . . . . .	78
<b>5</b>	<b>Analysis Strategy and Data Set for Analysis</b>	<b>79</b>
5.1	Overview of the analysis . . . . .	79
5.2	Data set for analysis . . . . .	80
5.2.1	Good beam condition . . . . .	80
5.2.2	Good GPS status . . . . .	81
5.2.3	Status of data taking in ND and SK . . . . .	81
5.2.4	Total number of POT used in the analysis . . . . .	82
5.3	Beam stability during the data taking . . . . .	83
<b>6</b>	<b>Far-to-near Neutrino Spectrum Ratio</b>	<b>87</b>
6.1	Measurements of pion monitor . . . . .	87
6.2	Extraction of pion momentum and angular distribution . . . . .	88
6.3	Neutrino energy spectra at ND and SK and their ratio . . . . .	89
6.4	Systematic errors on the PIMON measurements . . . . .	90
6.5	Error matrix for the far-to-near ratio . . . . .	92
6.5.1	The form of error matrix . . . . .	92
6.5.2	Error matrix below 1 GeV . . . . .	92
6.5.3	Error matrix above 1 GeV . . . . .	93
6.5.4	Resulting error matrix of far-to-near ratio . . . . .	93



<b>7</b>	<b>Analysis in Near Detector</b>	<b>95</b>
7.1	Analysis flow in 1KT . . . . .	95
7.1.1	Data reduction . . . . .	95
7.1.2	Event reconstruction in 1KT . . . . .	99
7.1.3	Fiducial volume in 1KT analysis . . . . .	103
7.2	Number of neutrino interactions in 1KT . . . . .	104
7.2.1	Outline to obtain the number of neutrino interactions in 1KT . . . . .	104
7.2.2	Event selection for neutrino interaction in the fiducial volume . . . . .	104
7.2.3	Event selection efficiency . . . . .	105
7.2.4	Background rate in the selected events . . . . .	105
7.2.5	Multi-event correction . . . . .	107
7.2.6	Correction from 7 to 9-bunch for data in May and June 2000 . . . . .	107
7.2.7	Total number of interactions in 1KT . . . . .	108
7.2.8	Systematic errors on the number of neutrino interaction in 1KT . . . . .	108
7.3	Expected number of neutrino events in Super-Kamiokande . . . . .	112
7.3.1	Extrapolation of the number of interactions in 1KT to SK . . . . .	112
7.3.2	Systematic errors on the expected number of neutrino events in SK . . . . .	113
7.4	Measurement of neutrino spectrum in near detectors . . . . .	116
7.4.1	Further event selections in 1KT . . . . .	117
7.4.2	Neutrino event selection in FGD . . . . .	119
7.4.3	Basic distributions of FC1R $\mu$ and SciFi-MRD samples . . . . .	123
7.4.4	Choice of neutrino interaction models . . . . .	123
7.4.5	$\chi^2$ -fitting to derive the neutrino spectrum at ND . . . . .	129
7.4.6	Dependence of fitting results on interaction models . . . . .	141
7.5	Summary of ND analysis . . . . .	142
<b>8</b>	<b>Observation in Far Detector</b>	<b>145</b>
8.1	Event selection for beam originated neutrino candidates . . . . .	145
8.2	The number of observed neutrino events in SK . . . . .	151
8.3	Systematic uncertainty in the event selection . . . . .	155
8.4	Error matrix of selection efficiency for 1R $\mu$ events . . . . .	157
<b>9</b>	<b>Analysis for Neutrino Oscillation</b>	<b>159</b>
9.1	Overview . . . . .	159
9.2	Likelihood function for the analysis . . . . .	160
9.2.1	Definition of likelihood function . . . . .	160
9.2.2	Input values for systematic parameters . . . . .	162
9.3	Re-estimation of expected number of neutrino events and spectrum at SK in the case of no oscillation . . . . .	163
9.4	Best-fit point for neutrino oscillation . . . . .	163
9.5	Null oscillation probability . . . . .	166
9.6	Constraint on the neutrino oscillation parameters . . . . .	167
9.7	Dependence of results on neutrino interaction models . . . . .	167
9.8	Comparison with the results from atmospheric neutrino observation . . . . .	170
<b>10</b>	<b>Discussions and Prospects</b>	<b>171</b>
<b>11</b>	<b>Conclusion</b>	<b>173</b>

<b>A</b>	<b>Neutrino oscillation measurements before K2K experiment</b>	<b>175</b>
A.1	Atmospheric neutrino observations . . . . .	175
A.2	Solar neutrino observations . . . . .	179
A.3	Reactor neutrino experiments . . . . .	181
A.4	Accelerator neutrino experiments . . . . .	182
<b>B</b>	<b>Event Reconstruction in Water Cherenkov Detectors</b>	<b>187</b>
B.1	Vertex finding (auto-fit) . . . . .	187
B.1.1	Point-fit . . . . .	187
B.1.2	Ring edge search . . . . .	188
B.1.3	TDC-fit . . . . .	188
B.2	Ring counting . . . . .	190
B.2.1	Ring candidate search . . . . .	190
B.2.2	Ring candidate test . . . . .	191
B.3	Particle identification (PID) . . . . .	192
B.3.1	Expected charge distribution . . . . .	193
B.3.2	Estimation of the particle type . . . . .	194
B.4	Precise vertex finding (MS-fit) . . . . .	195
B.5	Momentum determination . . . . .	196
B.6	Correction to the number of rings (ring correction) . . . . .	197
B.7	Correction to the number of rings for the events in 1KT (ring correction II) . . .	197
<b>C</b>	<b>Systematic Uncertainties in PIMON Analysis</b>	<b>199</b>
	<b>References</b>	<b>205</b>

# List of Figures

1.1	The behavior of experimental sensitivity to oscillation parameters . . . . .	6
1.2	Allowed/excluded regions for $\nu_e \leftrightarrow \nu_\mu$ , $\nu_e \leftrightarrow \nu_\tau$ , and $\nu_\mu \leftrightarrow \nu_\tau$ oscillation parameters	7
2.1	Overview of K2K experiment . . . . .	10
2.2	The expected neutrino energy spectra with and without neutrino oscillation at Super-Kamiokande . . . . .	11
2.3	Correlation between true and reconstructed neutrino energy in Monte Carlo simulation . . . . .	12
2.4	The profile and the energy spectra of neutrino at 250 km distance . . . . .	14
2.5	Sensitivity to the $\nu_\mu \rightarrow \nu_x$ oscillation in K2K experiment . . . . .	15
3.1	Schematic view of K2K experiment . . . . .	18
3.2	Schematic view of KEK-PS and neutrino beam line and location of beam line components. . . . .	18
3.3	Schematic view of the two horn magnets . . . . .	20
3.4	Comparison of the neutrino energy spectrum at SK between with and without horn current . . . . .	21
3.5	Schematic views of the beam dump and the muon-pit . . . . .	22
3.6	An oscilloscope image of a typical CT signal . . . . .	24
3.7	A schematic view of the segmented plate ionization chamber, SPIC, (left) and typical profiles of the proton beam measured by the V39out- and TGT-SPICs (right) . . . . .	24
3.8	A schematic view of the pion monitor (PIMON) . . . . .	26
3.9	Distributions of $\beta$ for protons, pions, muons, and electrons/positrons after the 2nd horn magnet . . . . .	27
3.10	The principle of spherical mirror . . . . .	28
3.11	The momentum distributions of muons, pions, and neutrinos at muon-pit . . . .	29
3.12	A schematic view inside the muon-pit . . . . .	30
3.13	Typical muon profiles measured by ionization chamber (ICH) and silicon pad detector arrays (SPD) . . . . .	31
3.14	A schematic view of near detectors . . . . .	33
3.15	A schematic view of 1KT detector . . . . .	34
3.16	A schematic view of 20-inch photo-multiplier tube used in 1KT and SK . . . .	35
3.17	A schematic diagram of the water purification system in 1KT . . . . .	36
3.18	A schematic diagram of the data acquisition system in 1KT . . . . .	38
3.19	Charge-to-counts and Time-to-count responses of ADC and TDC in ATM module	40
3.20	A schematic view of the laser calibration system in 1KT . . . . .	41
3.21	A typical plot of the detected charge versus timing in a PMT, "T-Q map" . . . .	42
3.22	Position of the pre-calibrated PMTs in 1KT . . . . .	42
3.23	A schematic view of the Xenon calibration system in 1KT . . . . .	43

3.24	Typical event displays of vertical (left) and horizontal (right) cosmic-ray muons .	45
3.25	The comparison between data and Monte Carlo simulation in the charge scale distribution of vertical- $\mu$ and horizontal- $\mu$ events, and the distribution of reconstructed $\pi^0$ invariant mass . . . . .	45
3.26	The summary of various measurements on the energy scale in 1KT . . . . .	46
3.27	The distribution of the total number of photoelectrons for single ring $\mu$ -like events with the particle fully contained in the inner detector of 1KT . . . . .	46
3.28	Stability of the energy scale in 1KT during K2K-I period . . . . .	46
3.29	A schematic view of SciFi detector . . . . .	47
3.30	The track finding efficiency in SciFi as a function of the length of track . . . . .	48
3.31	Schematic views of a cell (upper) and a module (lower) of lead glass Cherenkov calorimeter . . . . .	49
3.32	A schematic view of the muon range detector (MRD) . . . . .	50
3.33	The tracking efficiency as a function of the track length in MRD . . . . .	50
3.34	A schematic diagram of the data acquisition system in ND . . . . .	51
3.35	A schematic view of Super-Kamiokande detector . . . . .	52
3.36	Schematic diagrams of the data acquisition system for the inner (upper) and outer (lower) detectors in SK . . . . .	54
3.37	The results of the measurements of absolute energy scale with several calibration sources in SK . . . . .	56
3.38	A schematic view of GPS system in the K2K experiment . . . . .	58
3.39	The stability of LTC in SK site . . . . .	58
4.1	A schematic view of the measurements of the profile and the divergence of the primary proton beam . . . . .	61
4.2	The differential cross-section of positive pion production in past experiments and fitted curves of Cho-CERN model . . . . .	64
4.3	The energy spectrum for each type of neutrinos at ND (left) and SK (right) estimated by Beam-MC . . . . .	67
4.4	Contributions of each decay mode to each type of neutrino . . . . .	67
4.5	The energy spectra of muon neutrino at ND (most left) and SK (middle), and their ratio (most right) predicted by several hadron production models . . . . .	68
4.6	The difference of the neutrino energy spectra at SK between the configurations in June 1999 (K2K-Ia) and since Nov. 1999 (K2K-Ib) . . . . .	68
4.7	Cross-section of each neutrino interaction channel with water as a function of incident neutrino energy . . . . .	69
4.8	Cross-section of CC-qe interaction on a free neutron in our simulation, together with the results of the measurements by bubble chamber experiments . . . . .	70
4.9	Cross-section of CC- $1\pi$ production calculated by our simulator, together with the experimental results . . . . .	72
4.10	Cross-section of the coherent pion production calculated in our simulation, as a function of incident neutrino energy . . . . .	74
4.11	The cross-section of $\pi^+$ - $^{16}\text{O}$ interactions . . . . .	75
5.1	The number of protons delivered onto the production target in the period of from June 1999 to July 2001 . . . . .	80
5.2	Stability of muon yield measured by the silicon pad detector array (SPD) in MUMON . . . . .	84

5.3	Stability of the center of muon profile measured by the ionization chamber (ICH) in MUMON . . . . .	84
5.4	Profile of the vertex of neutrino events measured in MRD . . . . .	85
5.5	Stability of the center of neutrino beam profile measured in MRD . . . . .	85
5.6	Stability of the neutrino event rate measured in MRD . . . . .	86
5.7	Stability of the energy (left) and angular (right) distribution of muons scattered by the neutrino interaction in MRD . . . . .	86
6.1	A typical Cherenkov light distribution observed by the PMT array in PIMON measurements . . . . .	88
6.2	Cherenkov light distributions for various refractive indices measured in Nov. 1999 . . . . .	89
6.3	The fitting results of pion ( $p_\pi, \theta_\pi$ ) distribution in Nov. 1999 run . . . . .	90
6.4	The neutrino energy spectrum at ND and SK and $F/N$ ratio for June 1999 and Nov. 1999 runs . . . . .	91
7.1	A typical neutrino event observed in 1KT . . . . .	96
7.2	A flow chart of data reduction and event selection in the 1KT analysis . . . . .	97
7.3	A typical event display (left), the distributions of PMT hit timing recorded by ATM (right upper) and its PMTSUM signal recorded by FADC (right lower) for a multiple event in a beam spill . . . . .	98
7.4	The efficiency curve for the FADC peak search as a function of the total number of photoelectrons . . . . .	98
7.5	The number of PMTSUM peaks per spill counted using FADC data (left) and their peak timing distribution (right) . . . . .	99
7.6	A flow chart of data reduction and event selection in the 1KT analysis . . . . .	100
7.7	The distribution of PID estimator for the CC-qe events of muon and electron neutrino in 1KT . . . . .	101
7.8	The resolution of the vertex reconstruction for fully contained (FC) and partially contained (PC) single-ring and multi-ring events in 1KT . . . . .	102
7.9	The resolution of the ring direction reconstruction for fully (FC) and partially (PC) contained single-ring events in 1KT . . . . .	102
7.10	Momentum resolution for single-ring $\mu$ -like FC events in 1KT as a function of muon momentum . . . . .	103
7.11	Definition of the fiducial volumes used in 1KT analysis . . . . .	103
7.12	The distributions of the reconstructed vertex in the radius direction (left) and the beam directions (right) . . . . .	105
7.13	Event selection efficiency for Fiducial-C as a function of $R$ , $z$ , and the incident neutrino energy $E_\nu$ . . . . .	106
7.14	The distribution of FADC peak timing for each event spill observed from May 2000 to June 2000 (left) and the correction factors for 7 to 9 bunches obtained in January to March 2000 . . . . .	108
7.15	Long term stability of the neutrino event rate measured in 1KT . . . . .	109
7.16	Reconstructed vertex profiles in horizontal (leftmost), vertical (middle), and longitudinal (rightmost) directions in 1KT . . . . .	110
7.17	Categories of neutrino events in 1KT . . . . .	118
7.18	The distribution of $p_{\max 20deg}$ in 1KT . . . . .	118
7.19	Distributions of the ring counting likelihood for single and multiple ring separation (left) and the number of ring distribution (right) in 1KT . . . . .	119

7.20	The distribution of the likelihood for particle identification, for FC 1-ring sample in 1KT . . . . .	120
7.21	The distribution of the total number of photoelectron for the FC1R $\mu$ sample in 1KT . . . . .	120
7.22	Event display of a typical SciFi-MRD 2-track events . . . . .	121
7.23	The distribution of cosine of the angular difference between the expected and the observed second track directions, $\cos \Delta\theta_p$ , in SciFi-MRD 2-track events . . . . .	122
7.24	The momentum (upper left) and angular (upper right) distributions of scattered muons in FC1R $\mu$ sample, and the distributions of the reconstructed neutrino energy (lower left) and the reconstructed 4-momentum transfer squared (lower right) for FC1R $\mu$ sample . . . . .	124
7.25	The momentum (upper left) and angular (upper right) distributions of scattered muons in SciFi-MRD 1-track sample, and the distributions of the reconstructed neutrino energy (lower left) and the reconstructed 4-momentum transfer squared (lower right) for SciFi-MRD 1-track sample . . . . .	125
7.26	The momentum (upper left) and angular (upper right) distributions of scattered muons in SciFi-MRD 2-track QE sample, and the distributions of the reconstructed neutrino energy (lower left) and the reconstructed 4-momentum transfer squared (lower right) for SciFi-MRD 2-track QE sample . . . . .	126
7.27	The momentum (upper left) and angular (upper right) distributions of scattered muons in SciFi-MRD 2-track non-QE sample, and the distributions of the reconstructed neutrino energy (lower left) and the reconstructed 4-momentum transfer squared (lower right) for SciFi-MRD 2-track non-QE sample . . . . .	127
7.28	Systematic studies on the effect of the uncertainty in the energy scale on the momentum (left) and reconstructed neutrino energy (right) distributions in FC1R $\mu$ sample . . . . .	128
7.29	Systematic studies on the effect of the angular biases in the reconstruction on the angular (left) and reconstructed 4-momentum transfer squared (right) distributions in FC1R $\mu$ sample . . . . .	128
7.30	Comparison of the muon momentum and angular distributions between NEUT-0000 and NEUT-1211 for FC1R $\mu$ sample . . . . .	129
7.31	Two-dimensional distributions of the muon momentum versus scattering angle for data (red plot) and for the Monte Carlo simulation for each energy bin and each interaction mode (blue plots) . . . . .	131
7.32	Contributions of various uncertainties to the momentum and angular distributions in FC1R $\mu$ sample . . . . .	132
7.33	Distributions of the muon momentum (upper left), the muon angle (upper right), the reconstructed neutrino energy (lower left), and the reconstructed $Q^2$ (lower right) after the fitting for FC1R $\mu$ sample . . . . .	138
7.34	Distributions of the muon momentum (upper left three figures), the muon angle (upper right three figures), the reconstructed neutrino energy (lower left three figures), and the reconstructed $Q^2$ (lower right three figures), after the fitting for SciFi-MRD samples . . . . .	139
7.35	Behavior of $\Delta\chi^2$ around the best fit point as a function of each fitting parameter value . . . . .	140
7.36	Comparison of the fitting results between 1KT only fitting and FGD only fitting, together with the 1KT+FGD merged fitting . . . . .	140
7.37	Error size of the fitting parameters . . . . .	141

7.38	Dependence of fitted $R_{\text{nqe}}$ values on neutrino interaction models (top) and $\chi^2/\text{d.o.f.}$ values at the best-fit points (bottom) . . . . .	142
7.39	The neutrino energy spectrum measured at ND . . . . .	143
8.1	Event display for one of the K2K beam neutrino candidates with FC 1-ring $\mu$ -like Cherenkov ring . . . . .	146
8.2	A flow chart of the data reduction and the event selection in the Super-Kamiokande analysis . . . . .	147
8.3	Distribution of the total number of photoelectrons in 300 nsec time window ( $\text{PE}_{300}$ ) for the events after high energy trigger cut . . . . .	148
8.4	Distributions of $\text{PE}_{\text{max}}/\text{PE}_{300}$ for the events after total photoelectron cut (left) and the goodness of vertex fitter for flasher cut for the events with the number of hit ID-PMTs less than 500 (right) . . . . .	149
8.5	Distributions of the number of hit PMTs in the largest OD hit cluster ( $N_{\text{hitac}}$ ) for the events after flasher cut (left) and the number of hit OD-PMTs within 800 nsec time window ( $N_{\text{hita800}}$ ) for the events after $N_{\text{hitac}}$ cut (right) . . . . .	150
8.6	Distribution of the goodness of vertex fitting (TDC-fit) for the events after OD cut . . . . .	151
8.7	Distribution of the visible energy ( $E_{\text{vis}}$ ) for the events after fitting goodness cut . . . . .	151
8.8	Distribution of the time difference between two UTC time stamps ( $\Delta T$ ) . . . . .	152
8.9	Distribution of the distance from the vertex point to the nearest wall of inner tank ( $D_{\text{wall}}$ ) for the events after visible energy cut for the atmospheric neutrino sample in SK (left) and for the K2K event candidates (right) . . . . .	152
8.10	Selection efficiency in SK as a function of incident neutrino energy, estimated by a Monte Carlo simulation . . . . .	153
8.11	Relation between the accumulated number of protons on target (POT) and the number of observed events in SK . . . . .	153
8.12	Distribution of the reconstructed vertex points (circles) and momentum of each ring in an event (lines) observed in SK . . . . .	154
8.13	The Momentum and angular distributions for FC1R $\mu$ events in SK . . . . .	156
8.14	The distribution of the reconstructed neutrino energy for FC1R $\mu$ events in SK . . . . .	156
9.1	The distribution of expected numbers of neutrino events (left) and the reconstructed neutrino energy (right) in SK for many trial of random number generation without neutrino oscillation . . . . .	164
9.2	Contribution of various uncertainties to the reconstructed neutrino energy spectrum . . . . .	165
9.3	The reconstructed neutrino energy distribution for 1R $\mu$ sample . . . . .	166
9.4	Allowed region of oscillation parameter constrained by K2K experiment . . . . .	168
9.5	Behaviors of the log-likelihood difference $-\Delta \ln \mathcal{L}$ as a function of $\Delta m^2$ along the axis of $\sin^2 2\theta = 1$ (left) and as a function of $\sin^2 2\theta$ along $\Delta m^2 = 2.8 \times 10^{-3} \text{ eV}^2$ (right) . . . . .	168
9.6	The 68% allowed regions of oscillation parameter space in the case of using normalization term only or spectrum shape term only (left) and their behavior of the log-likelihood difference, $-\Delta \ln \mathcal{L}$ , as a function of $\Delta m^2$ along the axis of $\sin^2 2\theta = 1$ (right) . . . . .	169
9.7	Comparison of different neutrino interaction models for the reconstructed neutrino energy and allowed parameter region . . . . .	169
9.8	The allowed region of oscillation parameters constrained by K2K experiment together with that constrained by the atmospheric neutrino observation in SK . . . . .	170

A.1	The zenith angle dependence of the $\mu$ -like and $e$ -like events in Super-Kamiokande	177
A.2	Allowed regions of the oscillation parameters for $\nu_\mu \rightarrow \nu_x$ mode . . . . .	178
A.3	The solar neutrino spectrum predicted by the standard solar model . . . . .	179
A.4	The fluxes of $^8\text{B}$ solar neutrino, $\phi(\nu_e)$ and $\phi(\nu_{\mu,\tau})$ , deduced from SNO experiment.	181
A.5	The allowed/excluded regions for $\nu_e \leftrightarrow \nu_\mu$ , $\nu_e \leftrightarrow \nu_\tau$ , and $\nu_\mu \leftrightarrow \nu_\tau$ oscillation parameters . . . . .	185
B.1	A typical distribution of $\text{PE}(\theta)$ (upper figure) and its second derivative (lower figure) . . . . .	189
B.2	The basic idea of the ring candidate search (left) and a typical charge of Cherenkov rings derived by Hough transformation . . . . .	190
B.3	Typical Cherenkov ring images for an electron event (left) and a muon event (right)	192
B.4	A schematic view of the Cherenkov radiation from a muon . . . . .	194
B.5	The distribution of the PID estimator for fully-contained (FC) single-ring events	195
B.6	A typical event in which the ring correction II is done and the fake ring is removed in 1KT . . . . .	198



# List of Tables

1.1	The summary of current upper limit on each neutrino mass . . . . .	2
2.1	The precise positions of the production target at KEK and the center of SK water tank measured by GPS survey . . . . .	14
2.2	The history of the K2K experiment . . . . .	16
3.1	Specifications of KEK-PS components and its operations for K2K experiment . .	19
3.2	Specifications of 20 inch photo-multiplier tube, R3600 made by Hamamatsu Photonics Corporation, used in 1KT and SK . . . . .	36
4.1	Summary of the beam parameters for the runs in K2K-Ia and K2K-Ib . . . . .	62
4.2	The fitted parameters of the Sanford-Wang formula for the positive pion production in Sanford-Wang, Cho-ANL, and Cho-CERN compilations . . . . .	63
4.3	The kaon decay modes taken into account for the contribution to neutrino beam in Beam-MC . . . . .	65
4.4	The list of the correspondence of abbreviations to models . . . . .	77
4.5	The list of the processes considered in our detector simulation . . . . .	78
5.1	Chart of the definition of beam spills in use . . . . .	82
5.2	Summary of the number of protons on target used in the analysis for each month	82
6.1	Summary of the operation of the PIMON measurements in June 1999 and Nov. 1999 runs . . . . .	87
6.2	Components of error matrices contributing to the error matrix of $F/N$ ratio below 1 GeV, $M_{F/N}^{\text{hadron}}$ . . . . .	94
6.3	Error matrices of each uncertainty in the PIMON measurements . . . . .	94
7.1	Summary of the number of interactions measured in 1KT . . . . .	106
7.2	Summary of systematic errors on the number of interactions measured in 1KT .	109
7.3	Comparison of event rate in various fiducial volume in 1KT . . . . .	111
7.4	Summary of the expected number of neutrino events in SK . . . . .	114
7.5	Summary of the systematic errors on the expected number of neutrino events in SK . . . . .	116
7.6	Summary of the event selections for FC1R $\mu$ sample in data and a Monte Carlo simulation . . . . .	120
7.7	The central values and the uncertainties of systematic parameters incorporated in the $\chi^2$ function of FGD . . . . .	135
7.8	Summary of the numbers used in the constraint term of PIMON in the $\chi^2$ function	136
7.9	Summary of the $\chi^2$ fitting results . . . . .	137
7.10	Error matrix for $f_i^\phi$ and $R_{\text{nqe}}$ obtained in the $\chi^2$ fitting . . . . .	137

7.11	The central values, errors, and error matrix for $f_i^\phi$ and $R_{\text{nqe}}$ used in the oscillation analysis . . . . .	143
8.1	Summary of the number of selected events in each reduction step in SK . . . . .	146
8.2	Summary of observed events in SK . . . . .	153
9.1	Summary of contribution of each systematic uncertainty to the expected number of neutrino events in SK in the case of no oscillation . . . . .	164
9.2	The Best-fit points for several conditions . . . . .	166
9.3	Effect of each systematic uncertainty on the null oscillation probability . . . . .	167
A.1	Summary of the observed $R$ values in atmospheric neutrino experiments . . . . .	176
A.2	Summary of the results from solar neutrino experiments and a comparison with the SSM predictions . . . . .	180
A.3	Summary of the results from reactor neutrino experiments . . . . .	182
A.4	Summary of the results from accelerator neutrino experiments . . . . .	183
C.1	Summary of systematic errors of the PIMON measurements on the spectra at ND and SK in June 1999 . . . . .	202
C.2	Summary of systematic errors of the PIMON measurements on the spectra at ND and SK in Nov. 1999 . . . . .	203
C.3	Summary of systematic errors of the PIMON measurements on the far-to-near spectrum ratio in June 1999 and Nov. 1999 . . . . .	204

# Chapter 1

## Introduction

Neutrinos, which are identified as elementary particles constructing the universe today, are believed that they have been played important roles in the evolution of the Universe since the very beginning of the Universe. However, detailed properties of neutrinos are still in mystery, because of their weakness of interaction with materials. In particular, the existence of their finite masses and their flavor mixing had been unknown until quite recent, and it is one of the hot topics in present high energy physics, elementary particle physics and astrophysics. Neutrino oscillation is one of the phenomena which directly proves non-vanishing neutrino mass and flavor mixing in the lepton sector. In this chapter, a brief history of neutrino physics and phenomenology of neutrino oscillation are described. In addition, current knowledges from experiments on neutrino oscillation and the motivation of K2K experiment are also referred to. Finally, an outline of this thesis is provided in the last section.

### 1.1 A brief history of neutrinos and their masses

The history of neutrino physics began with W. Pauli's letter written in 1930 [1], in which he postulated the existence of a new particle, neutrino, in order to explain the observed continuous electron spectrum accompanying nuclear  $\beta$ -decay. In his hypothesis, neutrino was required to be a neutral particle with spin 1/2 and a very tiny mass. Learning of Pauli's idea, E. Fermi proposed his theory of  $\beta$ -decay in 1934 [2]. The first experimental evidence of a neutrino induced interaction was brought by F. Reines and C. L. Cowan in search for the inverse  $\beta$ -decay,  $\bar{\nu}_e p \rightarrow e^+ n$  [3]. In 1962, muon neutrino was discovered by L. M. Lederman, M. Schwartz, J. Steinberger *et al.* [4], and it was proved that muon neutrino is distinguishable from electron neutrino. In addition to these two neutrinos, the existence of tau neutrino was inferred by M. L. Perl *et al.* in 1975 [5], and finally discovered by DONUT experiment in 2000 [6].

As more and more experimental evidence became available, our understanding of weak interaction and neutrino physics was greatly developed. Along the experimental and theoretical progresses, S. L. Glashow [7], S. Weinberg [8], and A. Salam [9] advocated the modern weak interaction theories which became a part of the framework of the "standard model". This model is capable of describing almost all the known physics of weak and electromagnetic interactions, incorporating almost all the experimental results in energy range available at present accelerators. In the standard model of elementary particles, neutrino is assumed to be a massless lepton, and the number of types of neutrino is believed to be three, which is strongly favored by the results of LEP experiments [10]. These three types of neutrino are distinguished as electron neutrino ( $\nu_e$ ), muon neutrino ( $\nu_\mu$ ), and tau neutrino ( $\nu_\tau$ ) in the correspondence to electron ( $e$ ), muon ( $\mu$ ), and tau ( $\tau$ ) charged leptons, respectively, in the weak interaction. The masslessness of neutrino requires that the neutrinos can be expressed only in the flavor eigenstates of weak

**Table 1.1:** The summary of current upper limit on each neutrino mass. For upper three items, the values are evaluated by Particle Data Group [20]. Several upper limits are derived in the analyses of Supernova SN1987A, typically a few 10 eV. The last item is the result from the WMAP observation.

Flavor of Neutrinos	Experimental Technique	Upper Limit
$\nu_e$	${}^3_1\text{H}$ $\beta$ -decay kinematics	3 eV (95% C.L.)
$\nu_\mu$	$\pi$ decay kinematics	170 keV (90% C.L.)
$\nu_\tau$	$\tau$ decay kinematics	18.2 MeV (95% C.L.)
$\nu_e$	Supernova SN1987A	14 $\sim$ 23 eV [15, 16, 17, 18]
$\sum \nu_l$	Cosmic Microwave Background	0.69 eV (95% C.L.) [19]

interaction like  $\nu_e$ ,  $\nu_\mu$ , and  $\nu_\tau$ .

Although it is assumed that all the neutrinos are massless in the standard model, their masses are not necessarily vanishing theoretically. If the neutrinos indeed have finite masses, they can also be expressed in the eigenstates of masses as well as in the flavor eigenstates, and then a number of questions are coming up: Whether are the neutrino masses of Dirac type or of Majorana type? Whether are the massive neutrinos stable or not? Does the flavor mixing in lepton sector exist? If exists, how does it differ from what observed in quark sector? How about the CP violation in the lepton sector? And so on. Therefore, observation of non-zero neutrino mass and flavor mixing in the lepton sector will make great impact on the current particle physics and will give important keys to explore the physics beyond the standard model.

Up to now, in spite of a number of experimental efforts to measure the masses of neutrinos directly using decay kinematics of parent particles, no experiment has found a finite mass over the experimental errors because of their very tiny masses.

The most sensitive experiment to measure the mass of the electron neutrino was that measures the energy spectrum of electron emitted in the  $\beta$ -decay of tritium:  ${}^3_1\text{H} \rightarrow {}^3_2\text{He} e^- \bar{\nu}_e$ , in which the end-point of spectrum shifts if neutrino is massive. Although various experiments have been analyzed, they give only upper limits of several eV [11, 12].

The best limit on the mass of muon neutrino have been obtained from the measurement of muon momentum in pion decay at PSI to be 170 keV with the confidence level of 90% [13].

The current limit on the tau neutrino mass was derived by ALEPH detector in LEP experiments from the kinematics of the tau decay into three or five pions plus a tau neutrino. It set the upper limit of  $m_{\nu_\tau} < 18.2 \text{ MeV}/c^2$  with the confidence level of 95% [14]. The upper limits on neutrino masses are summarized in Table 1.1.

In addition to these experimental limits, astronomical and cosmological limits on neutrino mass also exist. The observations of the arrival time spread of the neutrinos from Supernova SN1987A provided upper limits on  $m_{\nu_e}$  around a few 10 eV [15, 16, 17, 18]. Recently, WMAP collaboration have derived a most stringent limit on the neutrino mass to be less than 0.23 eV for three degenerate neutrino species by observing the anisotropy cosmic microwave background radiation [19]. However all the observations result in just setting upper limits up to now.

## 1.2 Phenomenology of neutrino oscillation

There exists another experimental method of search for finite masses of neutrinos via a phenomenon known as “neutrino oscillation”. The highlights of the phenomenology of neutrino oscillation are described in this section. With the phenomenon of neutrino oscillation, lep-

ton number conservation is violated in a subtle way, because the neutrino mass terms are not diagonal when expressed in terms of flavor eigenstates.

A flavor eigenstate of neutrino,  $|\nu_\alpha\rangle$  ( $\alpha = e, \mu, \tau$ ), can generally be expressed by superpositions of mass eigenstates,  $|\nu_i\rangle$  ( $i = 1, 2, 3$ ):

$$|\nu_\alpha\rangle = \sum_i U_{\alpha i}^* |\nu_i\rangle \quad , \quad (1.1)$$

where  $U_{\alpha i}$  is a element of a unitary matrix referred as MNS matrix, which was first proposed by Z. Maki, M. Nakagawa, and S. Sakata [21], and is in correspondence to the CKM matrix [22] in quark sector. In the case of that lepton sector consists of 3 flavors, the matrix  $U$  is  $3 \times 3$  with four independent parameters: three mixing angles,  $\theta_{12}$ ,  $\theta_{23}$ , and  $\theta_{13}$ , and one CP phase,  $\delta$ ;

$$\begin{aligned} U &= \begin{pmatrix} 1 & 0 & 0 \\ 0 & c_{23} & s_{23} \\ 0 & -s_{23} & c_{23} \end{pmatrix} \begin{pmatrix} c_{13} & 0 & s_{13}e^{-i\delta} \\ 0 & 1 & 0 \\ -s_{13}e^{i\delta} & 0 & c_{13} \end{pmatrix} \begin{pmatrix} c_{12} & s_{12} & 0 \\ -s_{12} & c_{12} & 0 \\ 0 & 0 & 1 \end{pmatrix} \\ &= \begin{pmatrix} c_{12}c_{13} & s_{12}c_{13} & s_{13}e^{-i\delta} \\ -s_{12}c_{23} - c_{12}s_{23}s_{13}e^{i\delta} & c_{12}c_{23} - s_{12}s_{23}s_{13}e^{i\delta} & s_{23}c_{13} \\ s_{12}s_{23} - c_{12}c_{23}s_{13}e^{i\delta} & -c_{12}s_{23} - s_{12}c_{23}s_{13}e^{i\delta} & c_{23}c_{13} \end{pmatrix} \quad , \quad (1.2) \end{aligned}$$

where  $c_{ij} = \cos \theta_{ij}$  and  $s_{ij} = \sin \theta_{ij}$ .

Neutrino is generated and interacts as a flavor eigenstate in weak interaction, whereas the state of neutrino evolves in time as mass eigenstates following the Schrödinger's equation. Applying Schrödinger's equation to the  $\nu_i$  component of  $\nu_\alpha$  in the rest frame of that component, we obtain

$$|\nu_i(\tau_i)\rangle = e^{-im_i\tau_i} |\nu_i(0)\rangle \quad , \quad (1.3)$$

where  $m_i$  is the mass of  $\nu_i$ , and  $\tau_i$  is time in the  $\nu_i$  frame. The Lorentz-invariant phase factor in Eq. (1.3) is written in terms of the time  $t$  and position  $L$  in the laboratory frame;

$$e^{-im_i\tau_i} = e^{-i(E_i t - p_i L)} \quad . \quad (1.4)$$

Here,  $E_i$  and  $p_i$  are respectively the energy and momentum of  $\nu_i$  in the laboratory frame. In practice, neutrino is extremely relativistic due to the tininess of the mass, so we can make following replacements in Eq. (1.4);

$$t \approx L \quad , \quad (1.5)$$

$$E_i = \sqrt{p_i^2 + m_i^2} \approx p_i + \frac{m_i^2}{2p_i} \quad . \quad (1.6)$$

All of  $\nu_\alpha$ 's mass eigenstates have a common momentum, since  $\nu_\alpha$  should have been produced with a definite momentum  $p$ . Therefore, we can use this  $p$  for all  $\nu_i$  components instead of  $p_i$ . With all the replacements above, the phase factor is approximately

$$e^{-i(m_i^2/2p)L} \quad . \quad (1.7)$$

From this expression and Eq. (1.1), the state of  $\nu_\alpha$  after a neutrino produced as  $\nu_\alpha$  has propagated a distance  $L$  has become

$$|\nu_\alpha(L)\rangle \approx \sum_i U_{\alpha i}^* e^{-i(m_i^2/2E)L} |\nu_i(0)\rangle \quad , \quad (1.8)$$

where  $E \simeq p$  is the average energy of the various mass eigenstate components of the neutrino. Using the unitarity of matrix  $U$  to invert Eq. (1.1), and inserting the result in Eq. (1.8), we find that

$$|\nu_\alpha(L)\rangle \approx \sum_\beta \left[ \sum_i U_{\alpha i}^* e^{-i(m_i^2/2E)L} U_{\beta i} \right] |\nu_\beta\rangle \quad . \quad (1.9)$$

We see that  $\nu_\alpha$  has turned into a superposition of all the flavors in traveling the distance  $L$ . This phenomenon is called “neutrino oscillation”. The probability  $P(\nu_\alpha \rightarrow \nu_\beta)$  that the flavor  $\beta$  is observed after  $\nu_\alpha$  travels the distance  $L$  is

$$\begin{aligned} P(\nu_\alpha \rightarrow \nu_\beta) &= |\langle \nu_\beta | \nu_\alpha(L) \rangle|^2 \\ &= \delta_{\alpha\beta} - 4 \sum_{i>j} \text{Re}(U_{\alpha i}^* U_{\beta i} U_{\alpha j} U_{\beta j}^*) \sin^2 \frac{\Delta m_{ij}^2 L}{4E} \\ &\quad - 2 \sum_{i>j} \text{Im}(U_{\alpha i}^* U_{\beta i} U_{\alpha j} U_{\beta j}^*) \sin \frac{\Delta m_{ij}^2 L}{2E} \quad , \end{aligned} \quad (1.10)$$

where  $\Delta m_{ij}^2 \equiv m_i^2 - m_j^2$ , the mass squared difference between  $\nu_i$  and  $\nu_j$ . The sign of the last term in Eq. (1.10) is + instead of  $-$  in the case of the expression for anti-neutrinos.

From Eq. (1.10), the conditions where neutrino oscillation can take place are found as following:

1. At least one of three  $\Delta m^2$ 's should be non-zero, or neutrino masses should not completely degenerate.
2. At least one of three mixing angles should be non-zero, or flavor eigenstates should not completely identical with mass eigenstates.

When the previously omitted factors,  $\hbar$  and  $c$ , are included in Eq. (1.10), and  $\Delta m_{ij}^2$ ,  $L$ , and  $E$  are expressed in the unit of  $\text{eV}^2$ ,  $\text{km}$ , and  $\text{GeV}$ , respectively, the oscillation phase can be written as

$$\Phi_{ij} \equiv \frac{\Delta m_{ij}^2 L}{4E} \cong 1.2669328 \cdot \Delta m_{ij}^2 [\text{eV}^2] \cdot \frac{L [\text{km}]}{E [\text{GeV}]} \quad , \quad (1.11)$$

which gives the oscillation probability to be dependent on the neutrino flight distance  $L$  and the neutrino energy  $E$ . (We usually use the number 1.2669328 in Eq. (1.11) with a significance of three-digit, i.e. 1.27.)

Because of the condition  $\Delta m_{12} + \Delta m_{23} + \Delta m_{31} = 0$  to be imposed, the independent parameters for neutrino oscillation are in total six in the case of three lepton generations: three mixing angles,  $(\theta_{12}, \theta_{23}, \theta_{13})$ , one CP phase,  $\delta$ , and any two out of three mass squared differences,  $\Delta m^2$ 's.

We usually take two  $\Delta m^2$  values as are suggested by solar and atmospheric neutrino observations;

$$\Delta m_{12}^2 = \Delta m_{\text{sol}}^2 \sim \mathcal{O}(10^{-4} - 10^{-5}) \text{ eV}^2 \quad , \quad (1.12)$$

$$\Delta m_{23}^2 = \Delta m_{\text{atm}}^2 \sim \mathcal{O}(10^{-2} - 10^{-3}) \text{ eV}^2 \quad . \quad (1.13)$$

An overview of these observations is described in Appendix A. For an oscillation with  $E \sim \Delta m_{23}^2 \cdot L$ , which is the case of the K2K experiment, the subject of this thesis, the contribution

of  $\Delta m_{12}^2$  terms are negligibly small, and the oscillation probabilities can be expressed by two mixing angles [23];

$$\begin{aligned} P(\nu_\mu \rightarrow \nu_\mu) &\simeq 1 - \cos^4 \theta_{13} \cdot \sin^2 2\theta_{23} \cdot \sin^2 \Phi_{23} \\ &\equiv 1 - \sin^2 2\theta_{\mu\tau} \cdot \sin^2 \Phi_{23} \quad , \end{aligned} \quad (1.14)$$

$$\begin{aligned} P(\nu_\mu \rightarrow \nu_e) &\simeq \sin^2 \theta_{23} \cdot \sin^2 2\theta_{13} \cdot \sin^2 \Phi_{23} \\ &\equiv \sin^2 2\theta_{\mu e} \cdot \sin^2 \Phi_{23} \quad , \end{aligned} \quad (1.15)$$

$$P(\nu_e \rightarrow \nu_e) \simeq 1 - \sin^2 2\theta_{13} \cdot \sin^2 \Phi_{23} \quad . \quad (1.16)$$

Here,  $\sin^2 2\theta_{\mu\tau} \equiv \cos^4 \theta_{13} \cdot \sin^2 2\theta_{23}$  and  $\sin^2 2\theta_{\mu e} \equiv \sin^2 \theta_{23} \cdot \sin^2 2\theta_{13}$ . These expressions can be regarded as the case of two flavor oscillations with their effective mixing angles of  $\theta_{\mu\tau}$  and  $\theta_{\mu e}$ .

According to the mechanism of neutrino oscillation described above, if neutrino oscillation is actually observed, it proves the both facts that neutrino has non-vanishing mass and that there exists the flavor mixing in the lepton sector, giving the constraint on the parameter space of  $(\sin^2 2\theta, \Delta m^2)$ .

### 1.3 Experimental sensitivity to oscillation parameters

In this section, it is discussed that how experimental sensitivity to oscillation parameters behaves. For simplification, the case of two flavor oscillation is considered. The oscillation probability in two flavor case is

$$P(\nu_\alpha \rightarrow \nu_\beta) = \sin^2 2\theta \cdot \sin^2 \left( 1.27 \Delta m^2 \frac{L}{E} \right) \quad . \quad (1.17)$$

In real experiment,  $E$  and  $L$  have spread due to various effects. However, there is a well-defined  $\langle L/E \rangle$ , average of  $L/E$ , about which events distribute. If a toy model in which  $b \equiv 1.27L/E$  has a Gaussian distribution with standard deviation of  $\sigma_b$  about the central value of  $b_0$ , then the convolution of this Gaussian with  $P$  as given in Eq. (1.17) results in [20]

$$\langle P \rangle = \frac{1}{2} \sin^2 2\theta \left[ 1 - \cos(2b_0 \Delta m^2) \cdot \exp \{ -2\sigma_b^2 (\Delta m^2)^2 \} \right] \quad . \quad (1.18)$$

The value of  $\langle P \rangle$  is set by the experiment, for example, as an upper limit on oscillation probability, and so on. With this fixed  $\langle P \rangle$ ,  $\sin^2 2\theta$  can be found as a function of  $\Delta m^2$ . A schematic drawing of this function is shown in Fig. 1.1. The contour line in the figure, which in some cases is the boundary of allowed/excluded region by a measurement and in other cases is the boundary of the sensitivity region of the experiment, has the following features:

1. For large  $\Delta m^2$ , oscillation is fast and is completely washed out by the experimental resolution. The boundary is  $\sin^2 2\theta = 2\langle P \rangle$ .
2. The maximum sensitivity to  $\sin^2 2\theta$  occurs at  $\Delta m^2 = \frac{\pi}{2b_0}$  with the value of  $\sin^2 2\theta = \langle P \rangle$ , if the resolution is good.
3. For large  $\sin^2 2\theta$ , the nearly straight-line segment at the bottom is described by  $\Delta m^2 \approx \frac{\sqrt{\langle P \rangle}}{b_0 \sqrt{\sin^2 2\theta}}$ , which intercepts the axis of  $\sin^2 2\theta = 1$  at  $\Delta m^2 = \frac{\sqrt{\langle P \rangle}}{1.27 \langle L/E \rangle}$ .

The wiggles depends on the experimental features such as the size of the neutrino source, the neutrino energy distribution, detector resolution, and analysis details.

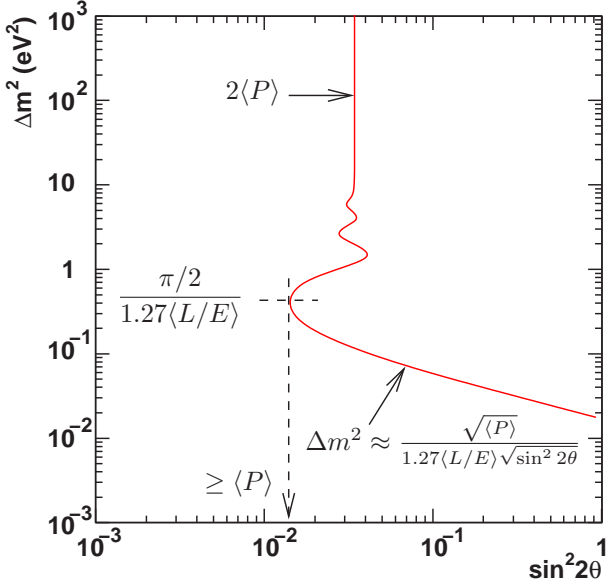


**Figure 1.1:** The behavior of experimental sensitivity to oscillation parameters. The red contour line shows how the experimental limit on oscillation parameters behaves when the observed oscillation probability is  $\langle P \rangle$  with a certain confidence level.

As a summary of the discussion above, aside from the details, the experimental sensitivity to  $\Delta m^2$  is determined by  $\langle L/E \rangle$  of the experiment to be around  $\Delta m^2 = \frac{\pi}{2\langle L/E \rangle}$ , while that to  $\sin^2 2\theta$  by  $\langle P \rangle$ , which mainly depends on the statistics of the experiment in the usual case.

## 1.4 Summary of neutrino oscillation measurements

Up to now, a number of experiments and observations to search for neutrino oscillation have been performed around the world. They are categorized into four types according to their source of neutrinos; atmospheric neutrino observations, solar neutrino observations, reactor neutrino experiments, and accelerator neutrino experiments. Detailed descriptions on them are provided in Appendix A. Allowed/excluded regions from their results are also shown in Fig. 1.2. In summary, there are three possible regions remaining for neutrino oscillation parameters.

1. Atmospheric region:  $\Delta m^2 = (1.5-5) \times 10^{-3} \text{ eV}^2$  ( $\sin^2 2\theta \sim 0.88-1$ )
2. Solar region:  $\Delta m^2 = (3-19) \times 10^{-5} \text{ eV}^2$  ( $\sin^2 2\theta \sim 0.64-0.97$ )
3. LSND region:  $\Delta m^2 = 0.2-1 \text{ eV}^2$  ( $\sin^2 2\theta \sim 0.003-0.04$ )

As mentioned in Sec. 1.2, only two  $\Delta m^2$ 's can independently exist and three  $\Delta m^2$ 's should satisfy the relation  $\Delta m_{12}^2 + \Delta m_{23}^2 + \Delta m_{31}^2 = 0$  in the framework of three neutrino scenario, whereas these results do not. If these results are true, introduction of some new framework, such as the fourth generation, sterile neutrinos, or other exotic reduction scenarios, may be needed to the current Standard Model in order to explain all the experimental results. However, before that, these results should be investigated by systematically different experiments so that they are surely confirmed or rejected.

The KamLAND experiment [24], a reactor neutrino experiment in Japan with long baseline of about 180 km, has been performed since early in 2002 to explore small  $\Delta m^2$  region down to  $\sim 10^{-5}-10^{-6} \text{ eV}^2$  including the “solar region”. In the case of that neutrino oscillation exists, it



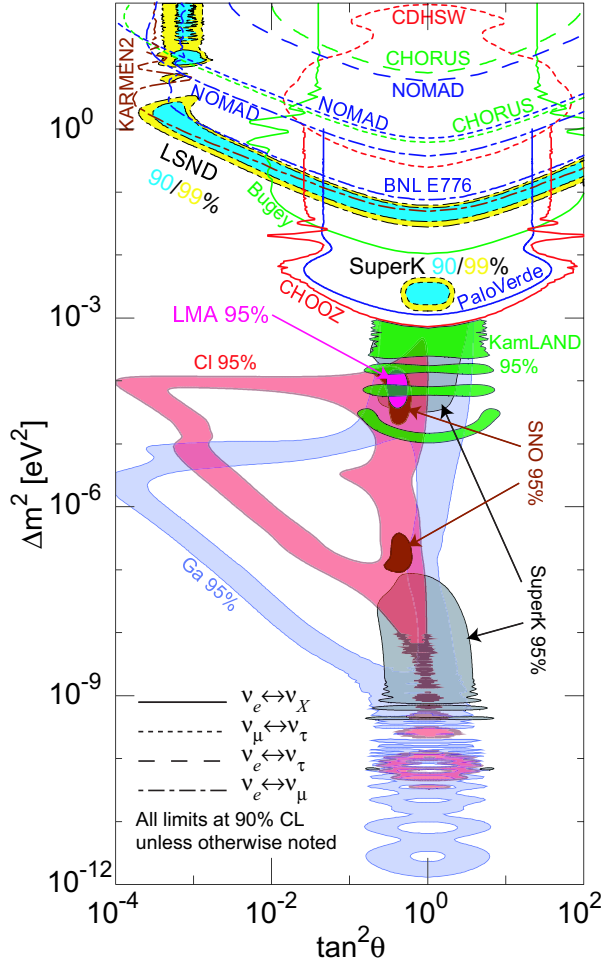


**Figure 1.2:** Allowed/excluded regions for  $\nu_e \leftrightarrow \nu_\mu$ ,  $\nu_e \leftrightarrow \nu_\tau$ , and  $\nu_\mu \leftrightarrow \nu_\tau$  oscillation parameters. Filled regions are the allowed ones derived from positive results, while blank regions are excluded by measurements with negative results. Only the results of experiments which provided the most stringent limits are figured. The CPT invariance is assumed and neutrinos and anti-neutrinos are both shown together. There are three regions remaining to be allowed; atmospheric region:  $\Delta m^2 = (1.5-5) \times 10^{-3} \text{ eV}^2$  ( $\sin^2 2\theta \sim 0.88-1$ ), solar-LMA region:  $\Delta m^2 = (3-19) \times 10^{-5} \text{ eV}^2$  ( $\sin^2 2\theta \sim 0.64-0.97$ ), LSND region:  $\Delta m^2 = 0.2-1 \text{ eV}^2$  ( $\sin^2 2\theta \sim 0.003-0.04$ ). This figure is taken from [28].

can see the reduced number of events with the observed energy spectrum distorted\*.

For the “LSND region”, a short baseline accelerator neutrino experiment, the MiniBooNE experiment [26], at Fermi National Accelerator Laboratory in U.S. has been in operation since the summer in 2002. The energy of muon neutrino beam and the length of baseline are 1–1.5 GeV and  $\sim 500$  m, respectively. MiniBooNE will analyze in the  $\nu_\mu \rightarrow \nu_e$  appearance mode. The sensitivity to  $\Delta m^2$  and  $\sin^2 2\theta$  is down to  $2 \times 10^{-2} \text{ eV}^2$  at  $\sin^2 2\theta = 1$  and  $10^{-3}$  for large  $\Delta m^2$ , respectively, which completely covers the whole allowed region of LSND.

In order to investigate the “atmospheric region”, the K2K experiment [27] have been done since June 1999. The K2K experiment is the first long baseline experiment in the world, and it uses accelerator-produced muon neutrino beam with a baseline of 250 km. K2K can explore down to  $\sim 10^{-3} \text{ eV}^2$  by looking at the reduction in the number of events and the distortion of energy spectrum in comparison of the measurements at near and far sites. Therefore, if the oscillation parameters really exist in the “atmospheric region”, K2K will provide a firm evidence for the neutrino oscillation.

Understanding of the entire picture of neutrino oscillation will play an important role to understand the structure of mass hierarchy of elementary particles and the mixing between generations, which bring us some crucial clues to go beyond the Standard Model.

\*Recently, KamLAND experiment has confirmed the  $\bar{\nu}_e$  disappearance with a set of oscillation parameters to be around the “solar region” [25].

## 1.5 Outline of this thesis

After the first two years of the K2K experiment, we analyzed the data using both flux and spectrum information for the first time, and we obtained strong indications for neutrino oscillation. This thesis details the first analysis and results on neutrino oscillation in the K2K experiment with the use of the data taken in the period from June 1999 to July 2001.

First, an overview of the K2K experiment are briefly described in Chapter 2. Then the description on experimental components and their calibrations and stabilities are detailed in Chapter 3. Some Monte Carlo simulations are used for neutrino beam to be extrapolated from near to far site, and for detector response and interaction models to be compared with data, and so on. Chapter 4 explains these simulations. Following chapters from Chapter 5 to Chapter 9, are dedicated to describe the method and the results of the analysis for neutrino oscillation in detail. Finally, the discussions and the prospects of the future analysis are given in Chapter 10, and the conclusion of this thesis are mentioned in Chapter 11.

# Chapter 2

## The K2K Experiment

A long baseline neutrino oscillation experiment, “K2K experiment” (KEK-PS-E362), using accelerator-produced neutrinos was proposed in 1995 [27]. In K2K experiment, neutrinos are produced by 12 GeV proton synchrotron in High Energy Accelerator Research Organization (KEK) in Tsukuba, Ibaraki, travel the distance of 250 km in the earth, and are detected at Super-Kamiokande detector located in Kamioka, Gifu (Fig. 2.1). The main purpose of the K2K experiment is to investigate in detail the neutrino oscillation indicated by the atmospheric neutrino observations. K2K started its physics data taking in June 1999, and have been in operation about six months per year until July 2001. In this chapter, an overview of the K2K experiment is described.

### 2.1 Conceptual description of the K2K experiment

K2K experiment uses an accelerator-produced neutrino beam to probe the same  $\Delta m^2$  region as that explored with atmospheric neutrinos. The neutrino beam is produced using 12 GeV proton synchrotron (KEK-PS) accelerator in KEK. After protons hit an aluminum target, the produced positively charged particles, mainly pions, are focused by a pair of magnetic horns [29, 30]. Then neutrinos are produced via mainly the decay of pions in flight:

$$\pi^+ \rightarrow \mu^+ \nu_\mu \quad . \quad (2.1)$$

The neutrino beam consists of 98% pure muon neutrinos, and has a mean energy of 1.3 GeV. Generated neutrinos travel in the earth a distance of 250 km to Super-Kamiokande, the far detector of K2K experiment. A set of detectors is located 300 m downstream the proton target as near detectors (ND). Properties of neutrino beam, such as the flux, the energy spectrum, and the purity of muon neutrino, before neutrinos travel the 250 km distance are measured in ND. Simultaneously, they are measured also in Super-Kamiokande (SK). Finally, the measurements at near and far sites are compared with each other in order for neutrino oscillations to be investigated, and in order for the oscillation parameters to be determined in the case of that neutrino oscillation exists.

The main characteristics of K2K experiment are as follows: Accelerator-produced neutrinos are controlled and monitored by measuring the primary protons, secondary pions, and muons so that the uncertainties in the neutrino source become as small as possible. Concerning the sensitive region to the oscillation parameter  $\Delta m^2$ , the neutrino beam with a mean energy of 1.3 GeV and the neutrino flight distance of 250 km make the region of  $\Delta m^2$  around  $10^{-2} - 10^{-3} \text{ eV}^2$  to be accessible, as is calculated using Eq. (1.14). This region is corresponding to the region explored by atmospheric neutrino observations. The simultaneous measurements at near and far sites

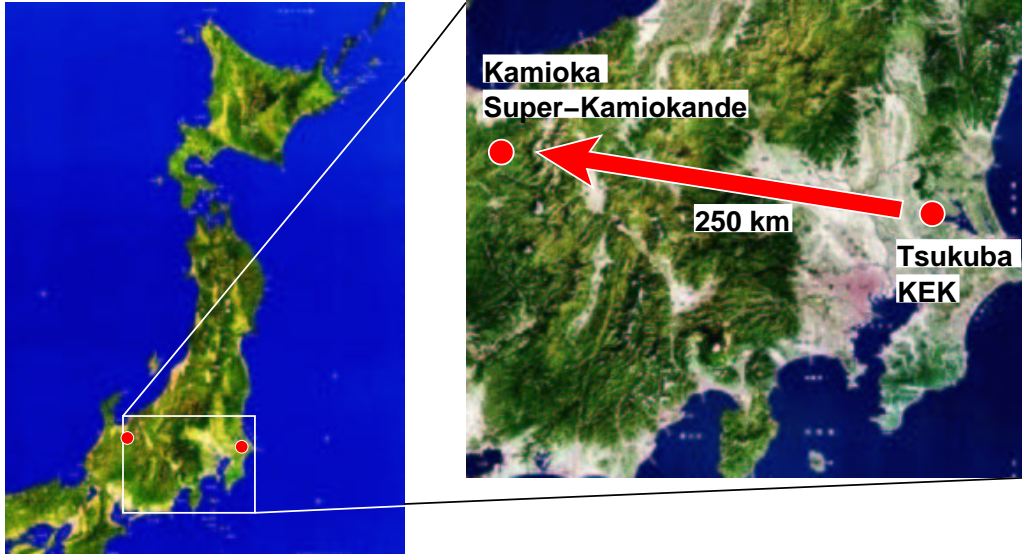


**Figure 2.1:** An overview of K2K experiment. The neutrino beam is produced in KEK at Tsukuba, Ibaraki, and detected in Super-Kamiokande at Kamioka, Gifu, after neutrinos travel a distance of 250 km.

and their comparison enable us to cancel out most of uncertainties of systematics such as the flux and the spectrum shape of the neutrino beam, cross-section of neutrino interactions, and so on. To use Super-Kamiokande, the most massive neutrino detector in the world, is also one of the features of K2K experiment. Since the cross-section of neutrino interactions with matter is very tiny, and since the geometrical acceptance is small due to the distance of 250 km from the neutrino source, the number of neutrino events in far detector becomes small. However, the use of SK gains enough number of events to be analyzed. In K2K experiment, expected event rate at SK in the case of no neutrino oscillation is typically 0.4 events per day.

Taking the advantages mentioned above, detailed studies on neutrino oscillation become possible. The oscillation modes which can be studied in K2K experiment are as follows.

Disappearance of muon neutrino: If the neutrino oscillation indicated by the observation of atmospheric neutrinos takes place, muon neutrinos oscillate into mainly tau neutrinos. In K2K case, the energy of neutrino is mostly below the threshold of tau production, oscillated neutrinos can not react via charged-current interaction. Therefore the reduction of the number of neutrino events, “disappearance of muon neutrino”, is expected in the far detector. Furthermore, because the flight distance of neutrino is fixed to be 250 km, the reduction factor have a dependence on the energy of neutrino as expressed in Eq. (1.14), and hence the neutrino energy spectrum is distorted like Fig. 2.2 in the case of that neutrino oscillation exists. The oscillation parameters ( $\sin^2 2\theta$ ,  $\Delta m^2$ ) are determined by studying these two characteristics. This mode is referred to as  $\nu_\mu \rightarrow \nu_x$  mode, or  $\nu_\mu \nrightarrow \nu_\mu$  mode, and is the main subject of K2K experiment.

Appearance of electron neutrino: If the mixing angle  $\theta_{13}$  in Eq. (1.2) is not vanishing, another oscillation,  $\nu_\mu \rightarrow \nu_e$ , may also take place. In the K2K experiment, the neutrino beam consist of almost pure muon neutrinos and the contamination of electron neutrino is estimated to be as small as about 1%. Therefore, when the  $\nu_\mu \rightarrow \nu_e$  oscillation exists, electron events are observed

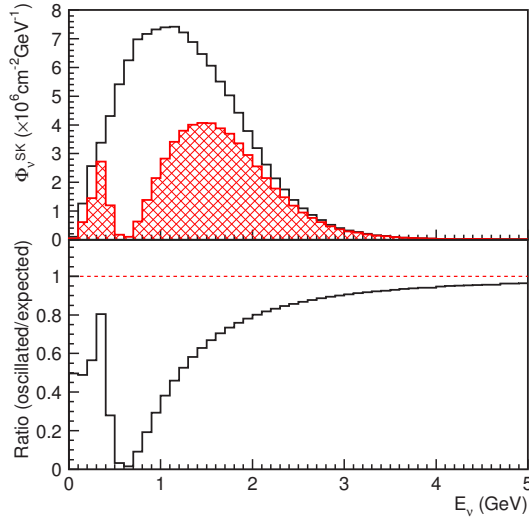


**Figure 2.2:** The expected neutrino energy spectra with and without neutrino oscillation at Super-Kamiokande. The Blank and hatched histograms in the upper figure respectively shows the expected neutrino energy spectrum without and with neutrino oscillation, and their ratio is plotted in the lower figure. In these figures, a set of oscillation parameters of  $(\sin^2 2\theta, \Delta m^2) = (1.0, 3 \times 10^{-3} \text{ eV}^2)$  is assumed in the oscillated case.

in the far detector, while only muon events are expected to be observed in the case of no  $\nu_\mu \rightarrow \nu_e$  oscillation.

Search for sterile neutrino: Even if the disappearance of muon neutrino is observed, there still remains a possibility that the oscillation is induced by sterile mode,  $\nu_\mu \rightarrow \nu_s$ . Sterile neutrino is a neutrino which does not react with matter, therefore when neutrino is detected by muon producing interaction, its oscillation signal may behave as similar to the oscillation into tau neutrino in the energy region of K2K. However the difference of sterile neutrino from normal ones can be seen in the neutral-current interaction; sterile neutrino does not react with matter even via neutral-current interaction, while normal ones do. Therefore the number of neutral-current interaction in SK is also expected to be reduced when the oscillation occurs with  $\nu_\mu \rightarrow \nu_s$  mode, whereas the reduction is not observed in the case of  $\nu_\mu \rightarrow \nu_\tau$  mode.

This thesis is devoted to the studies on the disappearance of muon neutrinos by looking at the reduction in number of neutrino events and the distortion in energy spectrum of neutrino.

## 2.2 Design of the K2K experiment

In order to investigate neutrino oscillation in detail, the knowledge of the neutrino flux and the energy spectrum at both near and far sites is indispensable. In addition, the study of cross-section of neutrino interactions is also important because its ambiguity does not completely cancel out in comparison of measurements in the near and the far detectors, especially in oscillated case. For these purposes, a number of experimental components are equipped in the K2K experiment. The design and the construction of the components have been done so that the following key issues are satisfied. Further detailed descriptions for each components are provided in Chapter 3.

### 2.2.1 Comparison between the measurements in ND and SK

Super-Kamiokande is a water-Cherenkov type detector, in which neutrino interacts with water ( $\text{H}_2\text{O}$ ) and the scattered charged particles are detected as Cherenkov rings when its momentum

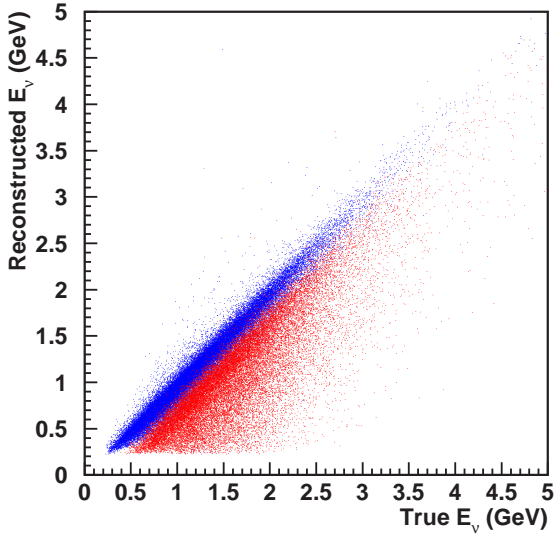


**Figure 2.3:** Correlation between true and reconstructed neutrino energy in Monte Carlo simulation. Blue and red dots are charged-current quasi-elastic (CC-qe) and charged-current non-quasi-elastic (non-qe) events, respectively. Energy of neutrino can be well reconstructed in CC-qe events, while that in non-qe events cannot due to that additional invisible particles are emitted in the interaction.

is greater than its Cherenkov threshold in the water. If measurements were done only in SK, the uncertainties in the neutrino interactions cross-section and the detection efficiency for neutrino events fully come into the systematic errors on the measurements of the number of neutrino events and energy spectrum. In order to avoid these “additional” systematic errors to be quoted, a similar detector to SK, 1 kiloton water-Cherenkov detector (1KT), is installed in the near detector system. The target of neutrino in 1KT is also water, and its detection technique is same as SK. Therefore, by comparing the measurements between in 1KT and in SK, the large part of the uncertainties in the neutrino cross-section and the detection efficiency can be canceled out.

### 2.2.2 Neutrino interaction studies in ND

As mentioned above, the ambiguity of cross section of neutrino interactions can be almost canceled out in comparing the measurements in ND and SK. However, when the spectral distortion is studied, the situation becomes a bit different.

To measure the energy spectrum of neutrino in SK, events which have only one muon-like Cherenkov ring (1R $\mu$ ) are selected in order to enhance the fraction of charged-current quasi-elastic interactions,  $\nu_\mu n \rightarrow \mu^- p$ , where only the muon is visible since the proton is typically below Cherenkov threshold. In 1R $\mu$  events, the energy of the parent neutrino can be calculated by using the observed muon momentum, assuming CC-qe interactions, and neglecting Fermi momentum of nucleons;

$$E_\nu^{\text{rec}} = \frac{1}{2} \cdot \frac{m_p^2 - m_n^2 - m_\mu^2 + 2m_n E_\mu}{m_n - E_\mu + p_\mu \cos \theta_\mu} \quad , \quad (2.2)$$

where  $m_p$ ,  $m_n$ ,  $m_\mu$ ,  $E_\mu$ ,  $p_\mu$ , and  $\theta_\mu$  are the proton mass, the neutron mass, the muon mass, the muon energy, the muon momentum, and the scattering angle of muon relative to the neutrino beam direction, respectively. The neutrino mass is ignored.

Correlation between the true neutrino energy and the reconstructed neutrino energy calculated by Eq. (2.2) for 1R $\mu$  sample in Monte Carlo simulation is shown in Fig. 2.3. For CC-qe events, the reconstructed energy reproduces well the true one as plotted by blue dots. However, in K2K beam, about 50% of 1R $\mu$  events are from interactions other than CC-qe. In these non-qe



events, particles other than muon or proton are also emitted but invisible due to that they have lower momentum than Cherenkov threshold. Therefore non-qe events have missing energy and the energy of parent neutrino is calculated to be lower than true one, as shown in Fig. 2.3 by red dots.

Non-qe events become a source of background in the study of spectral distortion, and hence they should be understood well. In order to study the neutrino interactions as well as the flux and the energy spectrum of neutrino, a fine-grained detector system (FGD) is installed in ND. It is able to track charged particles even with lower momenta. With the use of the measurements in FGD together with those in 1KT, the fraction of non-qe events with respect to CC-qe events is studied in order to feed it back into the study of spectral distortion in SK.

### 2.2.3 Extrapolation of the neutrino flux and spectrum from ND to SK

Since the acceptances of neutrinos entering ND and SK are different, the measurements in ND can not be easily extrapolated only by multiplying a factor of  $L_{\text{ND}}^2/L_{\text{SK}}^2$ , where  $L_{\text{ND}} = 300$  m and  $L_{\text{SK}} = 250$  km. The difference of acceptances for ND and SK is caused by the finite size of decay volume, the dependence of pion decay point on its energy, and the dependence of spacial spread of neutrinos on the angular spread of pion and its Lorentz boost.

Since the neutrino energy is determined only by the kinematics of pion decay, we can know the energy spectrum of neutrinos at any distance from the production target once the momentum and angular distributions of pions and the geometry of decay volume are provided. However since there has been large uncertainty in the hadron production processes in a thick target around the energy region of K2K, the simulation of pion production is not reliable enough to predict the flux and energy spectrum of neutrino beam.

Our simulation of hadron production processes is validated by measurements of a pion monitor (PIMON), which is installed just downstream the focusing horn magnets and occasionally measures the energy and angular distribution of pions. The flux and the spectrum of neutrino in SK is estimated by multiplying the far-to-near ratio ( $F/N$ ) to the measurements in ND, where the  $F/N$  ratio is the ratio of fluxes at SK to that at ND which is estimated by a beam simulation. By using the simulation in the form of  $F/N$ , large part of uncertainties in the hadron production process and its measurements is canceled out.

### 2.2.4 Neutrino beam pointing to SK

The direction of neutrino beam must always aim the SK within a certain accuracy since the flux and the energy spectrum of neutrino at SK changes as the beam direction changes. Fig. 2.4 shows the profile and the energy spectra of neutrino at the distance of 250 km estimated by a Monte Carlo simulation. According to these figures, both the flux and spectrum do not change more than 1% as long as the neutrino beam is pointing to SK within the accuracy of 3 mrad. Hence the neutrino beam at SK is stable enough when the beam direction is controlled with an accuracy of better than 1 mrad.

The direction of neutrino beam is defined by the direction of pions which is determined by the incident position and angle of proton beam onto the target and by the alignment of the two focusing magnets, called “horn magnets”. In order to monitor the incident position and angle of the proton beam, a number of monitors are installed along the proton beam line, and they measure the profile of the beam on spill by spill basis. The direction of the pion is monitored also on spill by spill basis by measuring the profile of muons emitted from the pion decay using muon monitor (MUMON), which is installed just downstream the beam dump. The direction of neutrino beam itself is measured by muon range detector (MRD) which is installed in ND.

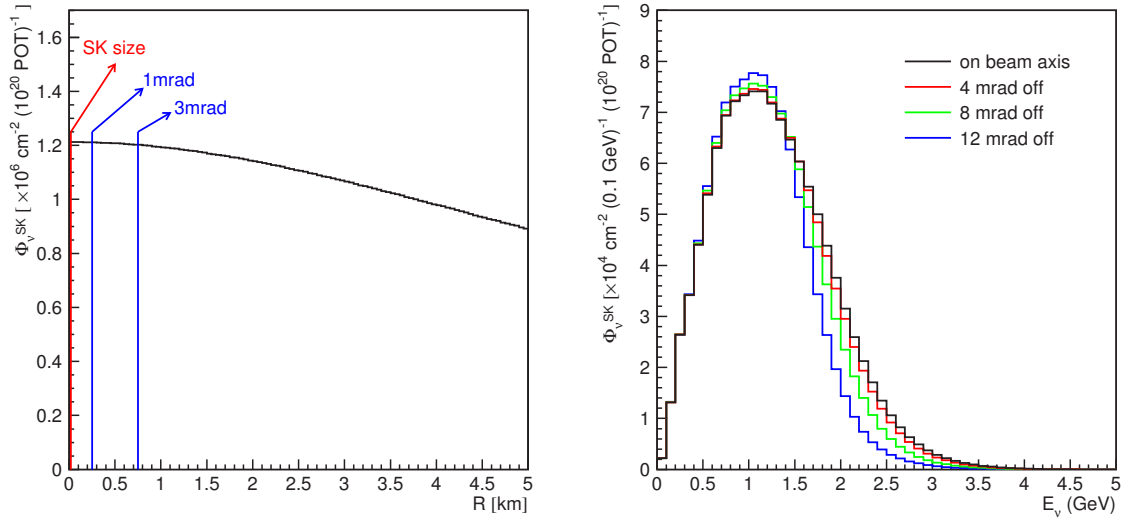


**Figure 2.4:** The profile and the energy spectra of neutrino at 250 km distance. The left figure shows the profile of neutrino, and the right one shows energy spectra of neutrino on beam axis (black), 4 mrad off (red), 8 mrad off (green), and 12 mrad off (blue) the beam axis, which provide that both the flux and energy spectrum does not change over 1% even if the beam direction changes within 3 mrad. These distributions are estimated by a beam Monte Carlo simulation without neutrino oscillation.

**Table 2.1:** The precise positions of the production target at KEK and the center of SK water tank measured by GPS survey. The precise distance from the production target to SK and the downward tilt of the beam are also shown in the table.

Survey point	Latitude	Longitude	Altitude above sea
Production target in KEK	36°09'14.9531" N.	140°04'16.3303" E.	70.218 m
Center of SK water tank	36°25'32.5862" N.	137°18'37.1214" E.	371.839 m
Distance from KEK to SK		249.83 km	
Downward tilt of the beam		1°04'30"	

The MRD has a transverse area of  $7.6 \text{ m} \times 7.6 \text{ m}$ , and hence it can measure the spatial profile over  $\pm 10$  mrad range.

In order to align these components with sufficient accuracy, Global Positioning System (GPS) was utilized. The positions of the production target at KEK and the center of water tank of SK were measured by GPS survey with a precision of within 0.01 mrad [31], which are summarized in Table 2.1. By referring to the GPS survey points, all the experimental components were carefully aligned with the precision of within 0.1 mrad.

### 2.2.5 Time synchronization between KEK-PS and SK

An expected rate of K2K signal in SK is estimated to be about 0.4 event per day in the case of no oscillation, while the event rate of fully-contained atmospheric neutrino events, a main background events in K2K, is about 8 events/day. Therefore, K2K observation in SK might be dominated by background events if no constraint is imposed. The most effective way to identify



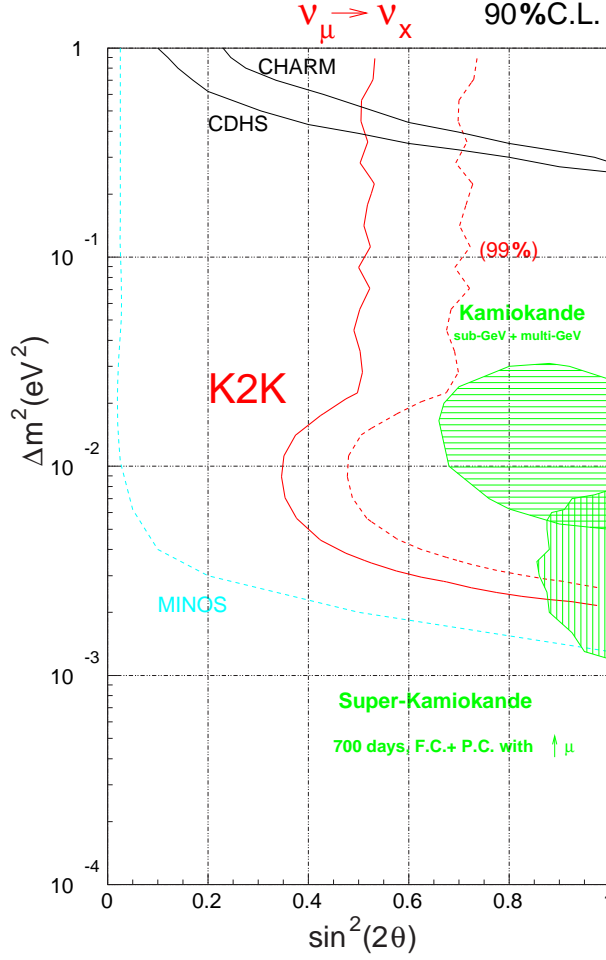


**Figure 2.5:** Sensitivity to the  $\nu_\mu \rightarrow \nu_x$  oscillation in K2K experiment. The vertical and the horizontal axes are  $\Delta m^2$  [ $\text{eV}^2$ ] and  $\sin^2 2\theta$ , respectively. The red lines show the sensitivity contours of K2K experiment with the confidence levels of 90% (solid line) and 99% (dotted line). The results of Kamiokande, Super-Kamiokande, CHARM, and CDHS are also shown in this figure. The hatched results are positive ones, therefore show the allowed regions. These contours are of the confidence level of 90%. In addition, the sensitivity region of the future long baseline neutrino experiment in U.S., MINOS, is also drawn with light blue line.

the neutrino events associated to the K2K beam is to make a time synchronization between KEK-PS beam and SK events.

For this purpose, GPS receivers are set at each site. By receiving the GPS signal at both sites simultaneously, time synchronization with the precision of about 100 nsec is realized. The proton beam is provided every 2.2 sec by fast extraction mode with the extracting duration of 1.1  $\mu\text{sec}$ . A time window of 1.5  $\mu\text{sec}$  is set to select the beam associated neutrino events in the SK analysis. In this way, the background rate is reduced by the order of  $10^{-5}$ .

### 2.3 Sensitivity of the K2K experiment

The K2K experiment is designed to be sensitive to the parameter region constrained by the atmospheric observations. Fig. 2.5 shows the region of sensitivity to the  $\nu_\mu \rightarrow \nu_x$  oscillation in K2K experiment, together with the results from several experiments. As shown in this figure, K2K has the sensitivity to the region of  $\Delta m^2 \gtrsim 10^{-3} \text{ eV}^2$  on the axis of  $\sin^2 2\theta = 1.0$ .

### 2.4 History of the experiment

A brief history of the K2K experiment is summarized in Table 2.2. Civil construction and detector installation had been done by the end of 1998, test operations of the beam extraction and

**Table 2.2:** The history of the K2K experiment. The runs from June 1999 to July 2001 are referred to as K2K-I, and runs after Dec. 2002 are referred to as K2K-II.

Year	Month	Events
1995		Proposal of K2K [27] was approved by KEK.
		Components design was started.
1996		Civil construction was started.
1998		Detector components were installed.
		Civil construction had been finished.
1999	Feb.	Proton beam with the fast-extraction mode was succeeded.
	Mar.	Horn magnets has been operated.
1999	June	Physics run was started. (K2K-I)
		RUN-I with 200 kA horn current (K2K-Ia)
	Oct.–Nov.	RUN-IIa with 250 kA horn current (K2K-Ib, until July 2001)
2000	Jan.–June	RUN-IIb with 250 kA horn current
2001	Jan.–July	RUN-III with 250 kA horn current
2001	Nov.	SK accident.
2002	Mar.–Oct.	SK reconstruction.
	Dec.	Data taking was restarted. (K2K-II)

horn magnets had been done early in 1999. Stable data taking for physics has been performed since June 1999. From June 1999 to July 2001 (K2K-I), we had four periods of data taking; RUN-I, IIa, IIb, and III as shown in Table 2.2. During RUN-I, horn magnets was operated with 200 kA current for safety reason, while the target current is 250 kA and they were operated with 250 kA current after RUN-II. For convenience, we refer to the run in June 1999 as “K2K-Ia”, and the rest of runs in K2K-I as “K2K-Ib”.

In this thesis, whole the data of K2K-I are analyzed, which is corresponding to the accumulated number of protons on target (POT) for physics analysis of  $4.793 \times 10^{19}$ ;  $0.310 \times 10^{19}$  POT in K2K-Ia and  $4.483 \times 10^{19}$  POT in K2K-Ib.

# Chapter 3

## Experimental Components and Their Performances

K2K experiment consists of the accelerator, neutrino beam line, near detector system, Super-Kamiokande, and time synchronization system. The schematic view of arrangement of these components are shown in Fig. 3.1. In this chapter, the description on each component and its performance is provided in the order from the upstream of the beam line. First, the descriptions on the accelerator and the neutrino beam line are given in Sec. 3.1. Second, the monitors for primary proton beam and secondary pions and muons are explained in Sec. 3.2 and Sec. 3.3, respectively. Then, the explanations for the near detector system are provided in Sec. 3.5 and the description on the far detector is given in Sec. 3.6. Finally, the method for time synchronization between KEK and SK is described in Sec. 3.7.

### 3.1 Accelerator and neutrino beam line

The accelerator and the neutrino beam line are consist of KEK 12 GeV proton synchrotron, primary proton transportation line to the production target, the production target, a set of focusing horn magnets for secondary particles, decay volume, and beam dump. They are briefly explained in this section.

#### 3.1.1 Proton accelerator and primary beam transportation line

In order to produce neutrino beam, a 12 GeV proton synchrotron accelerator in KEK (KEK-PS) is used. A schematic view of KEK-PS is shown in Fig. 3.2 and its specifications are summarized in Table 3.1.

First, protons are accelerated step-by-step by 750 keV pre-injector, 40 MeV LINAC, and 500 MeV rapid-cycle booster synchrotron, and then they are injected into the main ring of KEK-PS. In the main ring, more than  $7 \times 10^{12}$  protons are accelerated up to the kinetic energy of 12 GeV in one cycle. The number of bunches in the main ring is 9, which is corresponding to the harmonic number of the main ring. After acceleration finished, all the 9 bunches are extracted just in single turn to the EP1 neutrino beam line by kicker magnet system at EP1-A section (shown in Fig. 3.2). The duration of an extraction, or “a spill”, is  $1.1 \mu\text{sec}$ . This is called “fast extraction mode”.

The extracted beam is collimated and led to EP1 neutrino beam line. Typical beam intensity just after the extraction is about  $6 \times 10^{12}$  protons in a spill. The EP1 neutrino beam line consists of 61 quadrupole and 44 dipole magnets to leads proton beam to the production target through

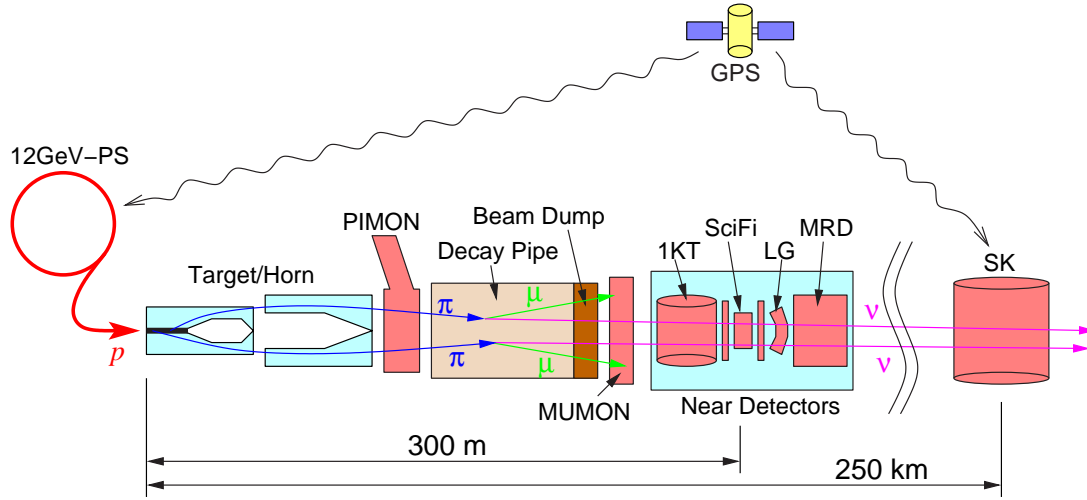
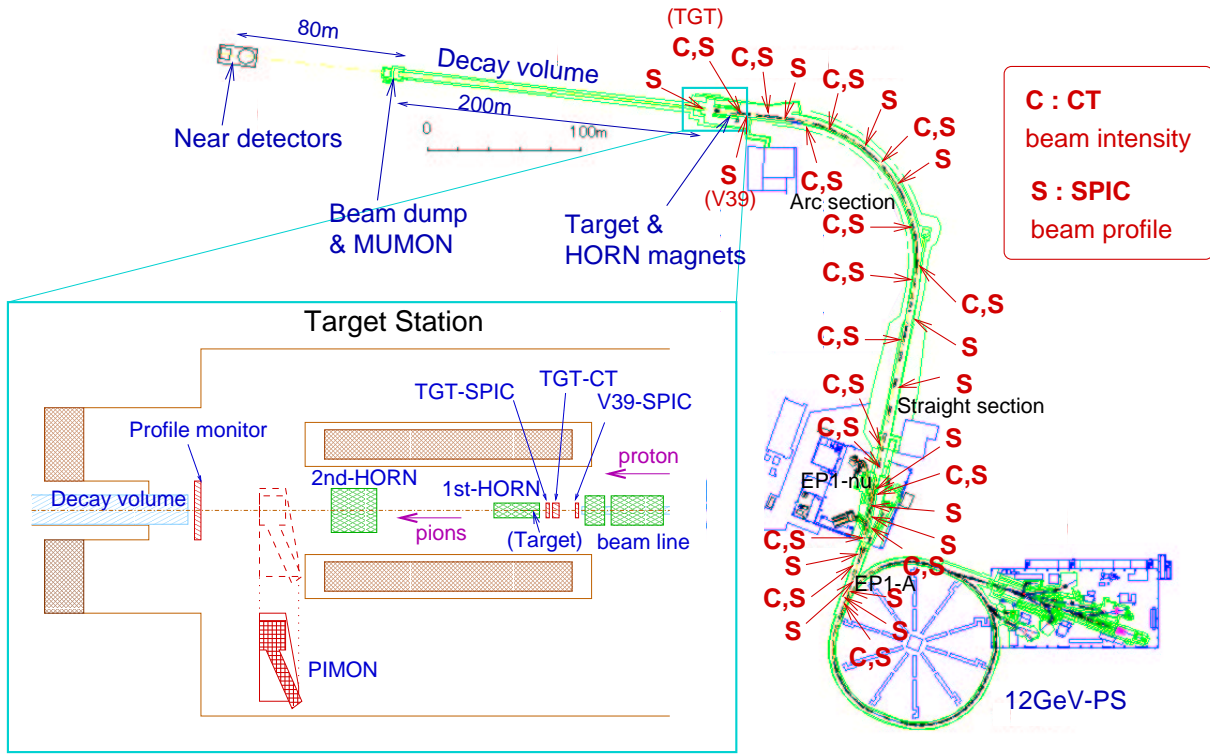


Figure 3.1: Schematic view of K2K experiment.



**Figure 3.2:** A schematic view of KEK-PS and neutrino beam line and the location of beam line components. The EP1 neutrino beam line leads protons through a distance of 400 m from EP1-A extraction point to the target station via the straight and arc sections. The characters “C” and “S” in the figure show the location where CT and SPIC are installed, respectively. The lower-left inset is a magnified view of the target area.

**Table 3.1:** Specifications of KEK-PS components and its operations for K2K experiment.

Components/Parameters	Values
Accelerator components:	
Pre-injector	750 keV (Cockroft-Walton acc.)
LINAC	40 MeV
BOOSTER	500 MeV
Main Ring	12 GeV (in kinetic energy)
Accelerator operations:	
Operation mode for K2K	fast extraction (single turn) to EP1-A
Typical intensity in main ring	$7 \times 10^{12}$ protons/spill
Typical intensity at EP1	$6 \times 10^{12}$ protons/spill
Typical intensity at target	$5 \times 10^{12}$ protons/spill
Number of bunches	9 bunches
Bunch repetition	about 120 nsec
Spill duration	1.1 $\mu$ sec
Repetition cycle	2.2 sec

a distance of 400 m. As shown in Fig. 3.2, the beam extracted toward the north direction is bent by about 90 degrees toward the direction of SK at the arc section.

The target station is built after the arc section. The proton beam is finally focused onto the production target at target station. Just before the target, a steering magnet is placed, which directs the beam to SK by about 1 degree downward from the horizontal level. Then protons are going to hit the target and produce a number of secondaries.

The efficiency to transport the proton beam from EP1-A to the target is about 85%, and the beam intensity just before the target is about  $5 \times 10^{12}$  protons in a spill.

In order to monitor the intensity, 13 current transformers (CTs) are installed in the neutrino beam line. Furthermore, 28 segmented plate ionization chambers (SPICs) are also placed in the beam line to monitor the position and profile of the beam. These properties of the beam are monitored on spill-by-spill basis. More detailed descriptions for the beam monitoring are provided in Sec. 3.2.

### 3.1.2 Production target and focusing horn magnets

Secondary particles, mainly pions, are generated by hadron interactions of 12 GeV protons inside a production target. Two toroidal magnetic horns are used in order to focus pions toward SK. A schematic view of the horn magnets is shown in Fig. 3.3. The dimensions of the 1st horn are 0.70 m in diameter and 2.37 m in length, while those of the 2nd horn are 1.65 m in diameter and 2.76 m in length. Both horns are cylindrically symmetric in shape. The production target, a rod of a length of 66 cm and a diameter of 3 cm which is made of aluminum alloy 6061-T, is embedded inside the 1st horn. This length of aluminum is corresponding to 1.67 interaction length. The target also plays a role of inner conductor of the 1st horn, making a strong magnetic field inside the horn to achieve high focusing efficiency. The 2nd horn is located 10.5 m downstream of the 1st horn, and plays a role of a reflector which re-focuses over-bent low energy pions as well as under-bent high energy pions. Except for the target part, central region of both horns is made to be vacant in order to avoid a loss of pion yield due to its secondary interaction with horn materials. The horn conductors are also made to be as thin as the requirement for strength is

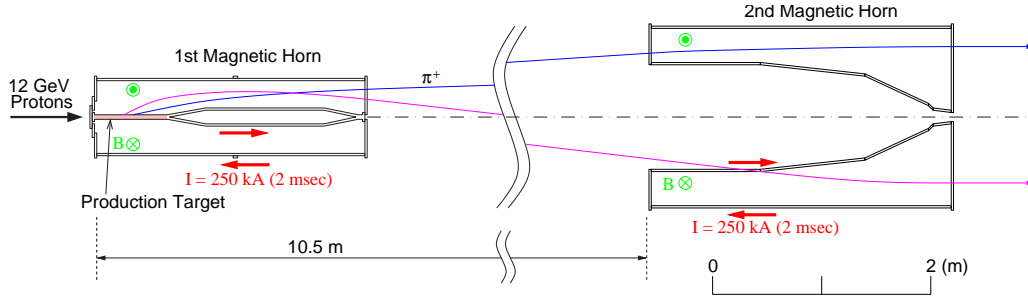


**Figure 3.3:** Schematic view of the two horn magnets. Electrical current of 250 kA is supplied to the both horns, making toroidal magnetic field inside the horns. The production target, an aluminum rod of 66 cm in length and 3 cm in diameter, is embedded inside the 1st horn magnet, which also plays a role of inner conductor of horn. The 2nd horn is located 10.5 m downstream of the 1st horn.

permitted.

Pulsed coaxial electrical current of a duration of 2 msec and an amplitude of 250 kA is supplied to the inner and outer conductors of the horns. This current makes toroidal magnetic field between the inner and outer conductors of the horn. The operation in pulsed mode is needed to avoid the conductors melted down. The repetition cycle is 2.2 sec which is synchronized with the beam cycle. The peaking time of the current is adjusted to match with the beam timing.

When the current of  $I_{\text{horn}}$  [kA] is supplied, the magnetic field  $B$  [kG] at the point of radius of  $r$  [cm] is

$$B = \begin{cases} \frac{I_{\text{horn}}}{5R^2} r & (r \leq R, \text{ inside the target}) \\ \frac{I_{\text{horn}}}{5r} & (r > R, \text{ outside the target}) \end{cases}, \quad (3.1)$$

where  $R$  is the radius of the target rod, i.e. 1.5 cm. The maximum magnetic field of 33 kG is achieved at the surface of rod when  $I_{\text{horn}} = 250$  kA. The direction of the magnetic field is clockwise seen from the upstream of the beam. Therefore, the positively charged particles are focused to the forward direction, while the negatively charged ones are swept out. In this way,  $\pi^+$ 's are selectively collected toward the decay volume. Typical transverse momentum focused by the horn magnets is about 100 MeV/c per m, and pions after the horn magnets distribute mainly around the momentum of 2–3 GeV/c, which corresponds to about 1.0–1.5 GeV in the energy of neutrino decayed in the focused direction. In addition to the focusing effect of horns, since protons twine around the magnetic field inside the target, the targetting efficiency improves. Monte Carlo simulation shows that almost all protons interact inside the target by some interactions including elastic one. The horn magnets with 250 kA current gain 22 times more flux of neutrinos above 0.5 GeV than that without horn current, as shown in Fig. 3.4.

Various measurements had been performed to understand the characteristics of the horn magnets, such as measurements on magnetic field, tests for the performance of the cooling system, and so on. For example, the magnetic field inside the prototype of the 1st horn was measured using pickup coils, resulting that the radial distribution of the field is in agreement with the designed one and the azimuthal symmetry had been confirmed within a measurement error of 15%. Including the descriptions on these measurements, more detailed descriptions on horn magnets can be found in [29, 30, 32, 33].

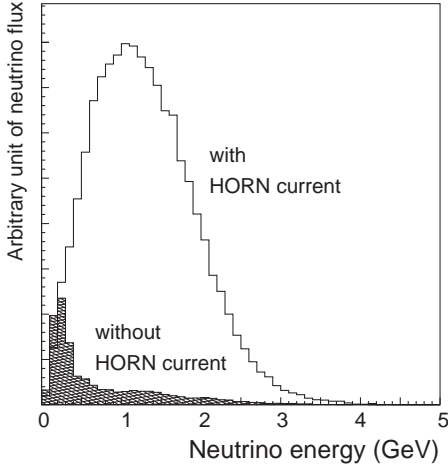


**Figure 3.4:** Comparison of the neutrino energy spectrum at SK between with and without horn current. The blank histogram is in the case of with horn current of 250 kA, and hatched one is in the case of without horn current, which show that the horn magnet system gains 22 times more neutrino flux than that without horn current. These histograms are estimated by Monte Carlo simulation.

The values of the electrical current supplied to the horn magnets are read out by current transformers put in power feeders and recorded by Flash-ADC on spill by spill basis. These data are used to select the beam spills with good condition, which is described in Chapter 5.

Only at the beginning of the experiment, the experiment had been done with a different configuration in the horn system. During the term of K2K-Ia, the diameter of the target was 2 cm and the peak current of horns was 200 kA. Due to mechanical problems, the target of 3 cm in diameter has been used since Oct. 1999 (during the K2K-Ib period), and the horns have been operated with the peak current of 250 kA, as mentioned above.

### 3.1.3 Decay volume and beam dump

The positive pions focused by the horn magnets are sent to a 200 m long decay volume, which starts from 19 m downstream of the production target. The decay volume is cylindrical pipe in shape, and is separated into three sections with respect to their different dimensions. The diameters of the pipe are 1.5 m, 2 m, and 3 m in the first 10 m, the following 90m, and the remaining 100 m sections, respectively. The decay volume is filled with helium gas of 1 atm to avoid a possible loss of pions by absorption and to avoid incontrollable pion production in the gas.

Inside the decay volume,  $\pi^+$  decays into  $\mu^+$  and  $\nu_\mu$ :

$$\pi^+ \rightarrow \mu^+ \nu_\mu \quad . \quad (3.2)$$

Since pions are strongly boosted in the laboratory frame, neutrinos are emitted toward SK within the decay angle of several 10 mrad.

After the decay volume, the beam dump is located to stop all the particles except for neutrinos. Schematic views of the beam dump are given in Fig. 3.5. It consists of 3.5 m thick iron shield, 2 m thick concrete, and about 60 m long soil. There is a pit just downstream of the concrete shield, and two detectors (MUMON) are installed there to measure the profile and intensity of muons penetrating through the shields (see Chapter 3.3.2). All the particle other than neutrino are absorbed by iron, concrete, and soil shields, and only neutrinos can pass through into ND and SK.

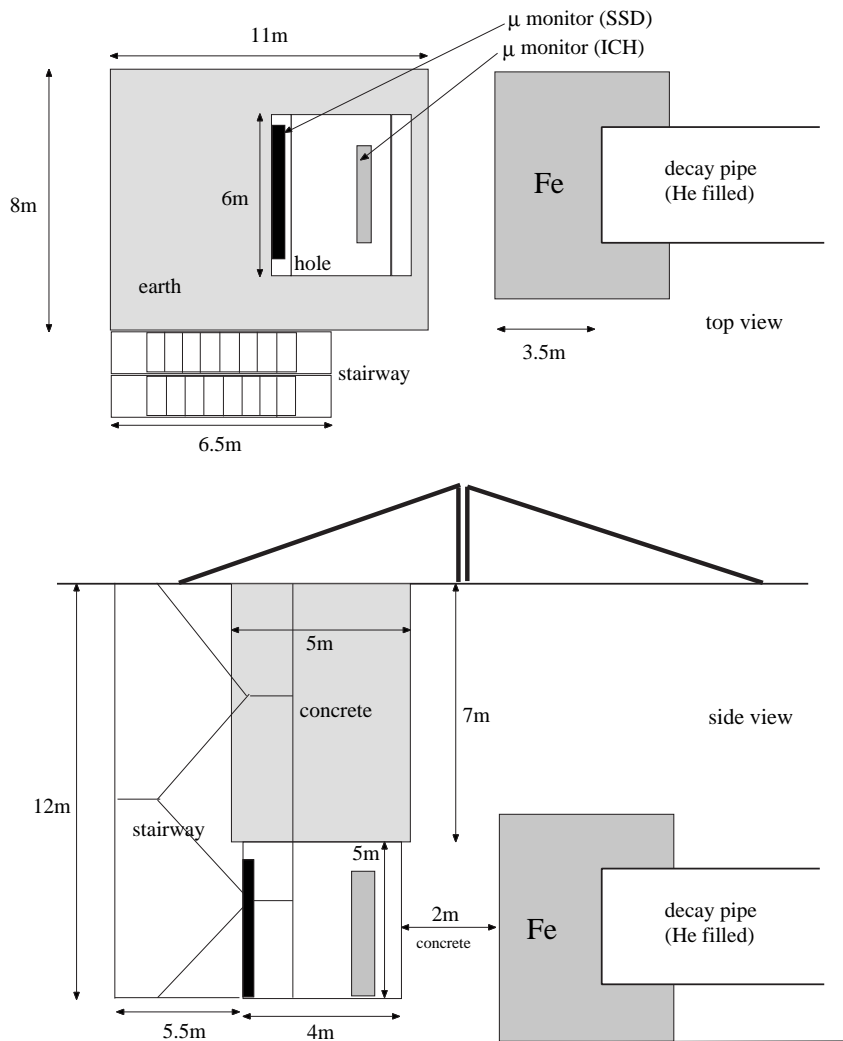


**Figure 3.5:** Schematic views of the beam dump and the muon-pit. The upper and the lower figures show the top and the side views, respectively. The beam dump consists of 3 thick iron shield, 2 m thick concrete shield, and about 60 m long soil. Just after the iron and concrete shield, two types of muon profile monitor (MUMON) installed at 12 m deep underground, called "muon-pit". In this figure, the beam is passing from right to left.



## 3.2 Primary beam monitors

In order to control and monitor the primary proton beam, two types of monitoring system, current transformers (CTs) and segmented plate ionization chambers (SPICs), are installed at a number of points along the neutrino beam line, as shown in Fig. 3.2. CTs monitor the beam intensity, while the SPICs monitor the profile and the position of the beam. The monitoring of both devices is done on spill-by-spill basis. In this section, brief descriptions on them are separately given.

### 3.2.1 Intensity monitors

In order to monitor the intensity of the proton beam, integrated current transformers (CTs) are used, which pick up the induced current made by protons passing through the coil. The inner diameter of CT is about 12 cm, as same size as that of the beam pipe, hence it is large enough to contain the whole beam inside the CT.

Thirteen CTs are installed along the beam line. The locations of CTs are indicated by the characters “C” in Fig. 3.2. Most of the CTs are mainly used to measure the intensity at each CT point and monitor the beam transportation efficiency. One of the CTs, called as “TGT-CT”, placed in front of the production target is used to estimate the total number of protons delivered onto the target.

Fig. 3.6 shows an oscilloscope image of a typical signal from CT, in which clear 9 bunches of the beam can be seen. The signals of CTs are led to the control room outside the radiation area by several 10 m to 100 m long co-axial cables. Then, they are read out by charge integrating ADCs with a gate width of  $1.3 \mu\text{sec}$  which contains the whole beam spill.

The CTs had been calibrated by pulsed current source. Due to the noise induced in 100 m long co-axial cables, the calibration has a systematic uncertainty of  $\pm 10\%$ .

### 3.2.2 Profile and position monitors

Profiles and position of the proton beam are measured by segmented plate ionization chambers (SPICs). Twenty-eight SPICs are installed along the beam line, indicated as “S” in Fig. 3.2. A schematic view of the SPIC is shown in Fig. 3.7 (left). SPIC is an ionization chamber consist of three copper sheet. The sheets with the thickness of  $28 \mu\text{m}$  are used since the proton beam directly hits them. These sheets are arranged with the gaps of 1 cm between each other. The gap is filled with helium gas. The central plane is an anode one to which the negative high voltage of typically  $-1000 \text{ V}$  is supplied. The others are cathode planes for the horizontal and vertical readout.

Twenty-six SPICs out of 28 have the same structure, while two SPICs, one located just in front of the target (TGT-SPIC) and another one located in front of the decay volume (P/PI-SPIC), have different structures from others. The 26 SPICs have a sensitive area of  $16 \text{ cm} \times 16 \text{ cm}$  square, and have 32 channels with 5 mm pitch in both horizontal and vertical readout. The TGT-SPIC is more fine-segmented to measure the profile of well-focused beam. Its pitch and sensitive area is 1.27 mm and  $4.1 \text{ cm} \times 4.1 \text{ cm}$ , respectively. The remaining SPIC, P/PI-SPIC, is to monitor the targetting and focusing by measuring the profile of scattered pions and protons after the target and the horn magnets. It covers a large area of  $2 \text{ m} \times 1.5 \text{ m}$ , and has 192 and 160 channels in the horizontal and vertical projections, respectively, with a pitch of 20 mm.

The electrons ionized by protons (and pions in P/PI-SPIC) are collected to cathode strips by the supplied high voltage, and the signal from each strip is read out by charge sensitive ADC,

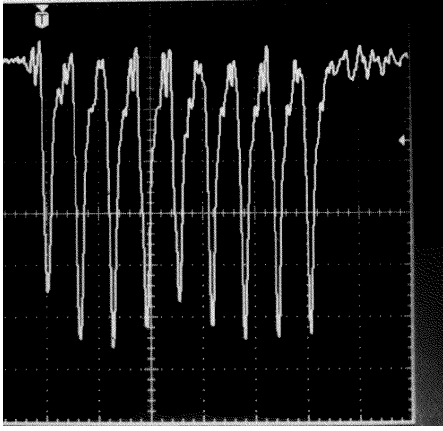


**Figure 3.6:** An oscilloscope image of a typical CT signal. The structure of 9 bunches can be clearly seen. The CT signals are read out by charge integrating ADCs with  $1.3\mu\text{sec}$  wide gate covering the whole beam spill.

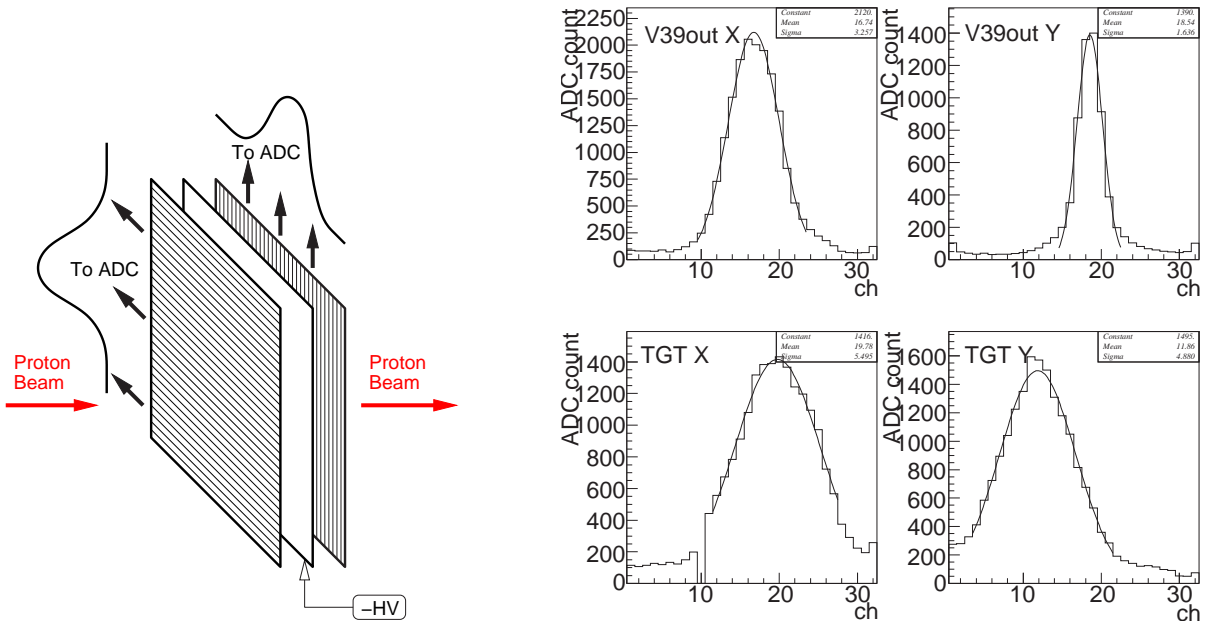


**Figure 3.7:** A schematic view of the segmented plate ionization chamber, SPIC, (left) and typical profiles of the proton beam measured by the V39out- and TGT-SPICs (right). The structure of SPIC is as explained in the text. In the right figures, upper two plots show the profiles in the X (left) and Y (right) directions measured at just after the V39 steering magnet (V39-SPIC), and lower two are corresponding to those at just in front of the production target (TGT-SPIC).

where amount of charge corresponds to the number of particles passing through the each strip region. Fig. 3.7 (right) shows typical profiles of the proton beam at the SPIC just after the steering magnet, “V39out-SPIC”, and at the TGT-SPIC.

The SPICs are used for steering of the beam. The proton targeting is continuously monitored by TGT-SPIC. In addition, V39out- and TGT-SPICs are used to measure the beam emittance (or profile and divergence) just before protons hit on the target.

Further description on the SPIC can be found in [34].

### 3.3 Secondary beam monitors

In the K2K experiment, there are two secondary beam monitors, pion monitor (PIMON) and muon monitor (MUMON). PIMON is a gas Cherenkov imaging detector, and is occasionally installed just after the 2nd horn magnet to measure the momentum and angular distributions of pions entering the decay volume. MUMON is consist of two detectors, an ionization chamber, and an array of silicon pad detectors, and is installed in a pit just downstream of the beam dump, as shown in Fig. 3.5. MUMON is measuring the profile of muons after the beam dump in order to monitor the direction of the beam on spill-by-spill basis. In this section, brief descriptions of these monitors are given.

#### 3.3.1 Pion monitor

Most of neutrinos are produced by the well-known two-body decay of pions, i.e. Eq. (3.2). The energy of neutrino from the decay of pion with the momentum of  $p_\pi$  can be calculated by

$$E_\nu = \frac{1}{2} \cdot \frac{m_\pi^2 - m_\mu^2}{E_\pi - p_\pi \cos \theta} \quad , \quad (3.3)$$

where  $m_\pi$ ,  $m_\mu$ , and  $E_\pi$  are the mass of pion, the mass of muon, and the energy of pion, respectively, and  $\theta$  is the polar angle of neutrino direction with respect to the pion direction in the laboratory frame. Since pion is pseudo-scalar particle, its decay is isotropic in the rest frame of pion. Therefore, if the momentum of pions and the geometry of decay volume are provided, the neutrino fluxes in any position can be predicted.

However, since there have been large uncertainty in the hadron production processes around the energy region of protons in K2K experiment, the momentum distribution of pion is not accurate enough to predict the neutrino fluxes at ND and SK. Pion monitor (PIMON) intends to measure the 2-dimensional distribution of pion momentum ( $p_\pi$ ) versus divergence ( $\theta_\pi$ ) just after the horn magnets. From this  $(p_\pi, \theta_\pi)$  distribution, the neutrino fluxes at both ND and SK are obtained, and we can confirm the validity of our Monte Carlo simulation by comparing the results of PIMON with the estimation of the Monte Carlo simulation.

Fig. 3.8 shows a schematic view of PIMON. PIMON is a gas Cherenkov imaging detector which consists of a gas vessel, a spherical mirror, and an array of 20 photo-multiplier tubes.

#### Gas vessel

The gas vessel of PIMON is a cylinder of 91 cm in diameter and 90 cm in length, with arm of about 3 m attached (see Fig. 3.8). The vessel is made of 5 mm thick stainless steel. There are two aluminum beam windows located at the entrance and exit of the beam. These windows are of 1 mm in thickness in order to reduce interactions in the windows. The radiation length and the interaction length of window are corresponding to  $0.01X_0$  and  $0.0025\lambda_{\text{int}}$ , respectively.

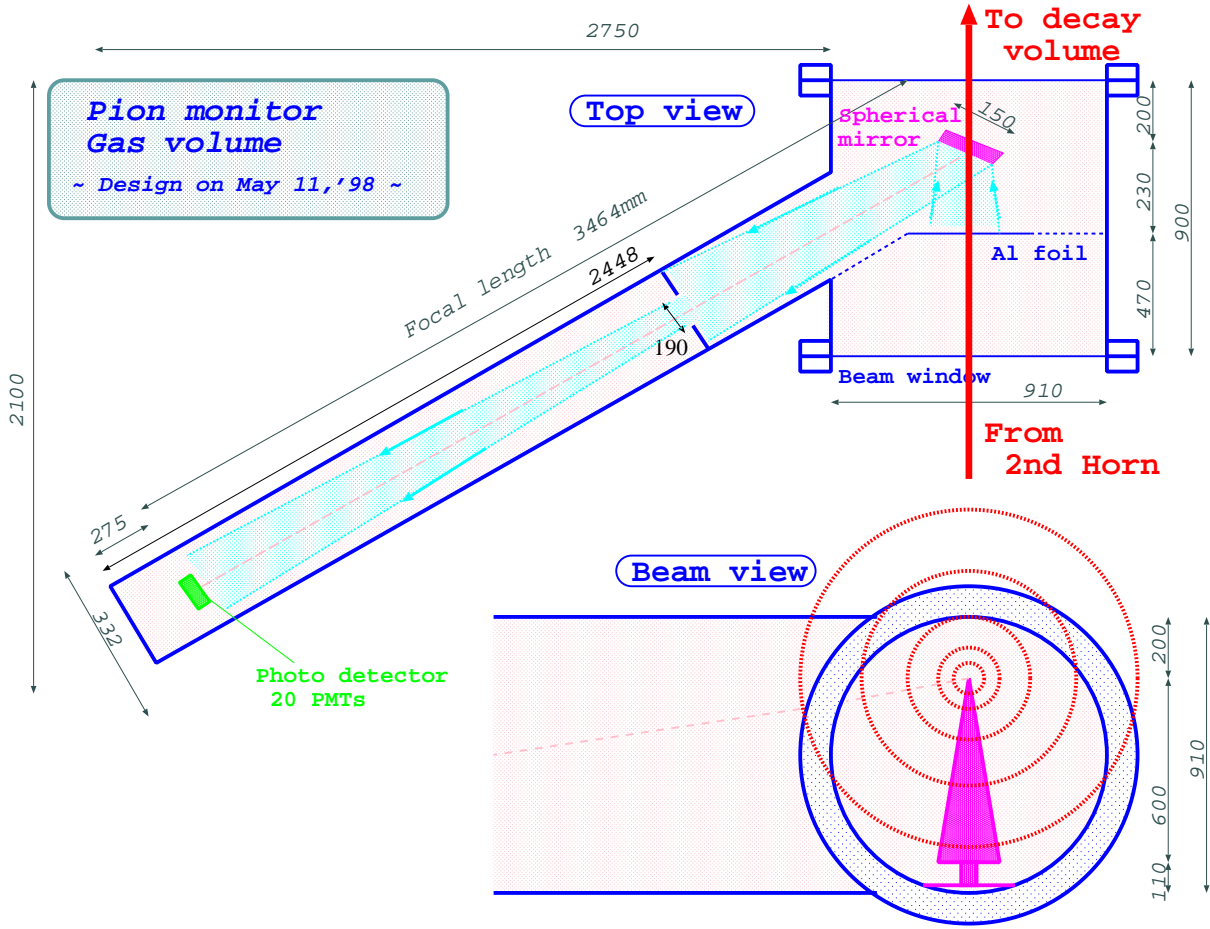


**Figure 3.8:** A schematic view of the pion monitor (PIMON). PIMON consists of a gas vessel, a spherical mirror, and an array of 20 photo-multiplier tubes. The gas vessel is filled with freon gas R-318 ( $C_4F_8$ ). A pie-shaped spherical mirror is set inside the gas vessel and Cherenkov light reflected by the mirror is directed to the array of photo-multiplier tubes which is set on the focal plane of the spherical mirror.

Inside the cylinder, pie-shaped spherical mirror is set to reflect the Cherenkov light toward the photo-detectors located in the arm. An aluminum foil of  $50 \mu\text{m}$  in thickness is set 23 cm in front of the mirror to define the fiducial area of Cherenkov light emission. This area does not change even if the beam windows are deformed by gas pressure.

The gas vessel is filled with freon gas R-318 ( $C_4F_8$ ) to achieve high refractive indices in order to make the momentum threshold of pion as low as possible. However, the refractive index,  $n$ , is controlled not to become above 1.00242 in order to avoid the severe background from the primary protons (see Fig. 3.9). This refractive index corresponds to the Cherenkov threshold of 2 GeV/ $c$  pion.

Gas pressure is controlled by an external gas system. By changing the gas pressure, the PIMON data are taken with the different refractive index between  $n = 1.00024$ – $1.00242$ , which is corresponding to the momentum threshold of pion between 6.4–2.0 GeV/ $c$ . The absolute refractive index is calibrated by Cherenkov photon distribution from 12 GeV primary protons with  $n = 1.00294$ , where 12 GeV protons can emit Cherenkov light [35].

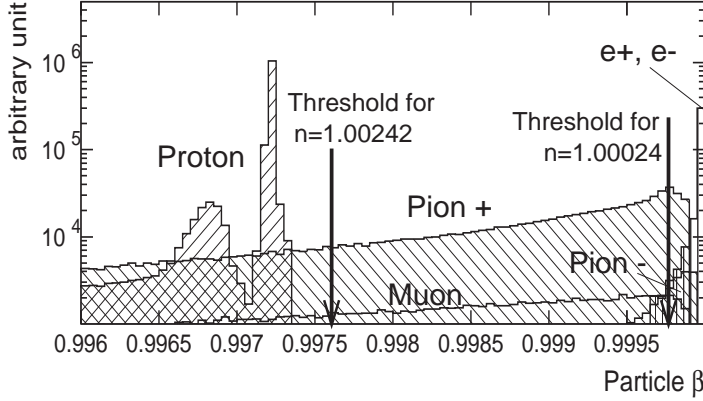


**Figure 3.9:** Distributions of  $\beta$  for protons, pions, muons, and electrons/positrons after the 2nd horn magnet. The refractive index,  $n$ , should be lower than 1.00242 to avoid the primary protons with the kinetic energy of 12 GeV to be above Cherenkov threshold.

### Spherical mirror

A schematic view of the spherical mirror used in PIMON is shown in Fig. 3.8. It focuses the Cherenkov photons onto the same ring when they are emitted by particles with the same  $\beta$  and the same direction, being independent of their emission points, as drawn in Fig. 3.10.  $\beta$  of particle appears as a size of ring image, and the direction of the particle appears as a position of ring image.

The spherical mirror is made of Pyrex glass which is coated with aluminum and frosted by sand to make a pie-shape. The dimensions of the glass are 60 cm  $\times$  15 cm in area and 8 mm in thickness. The radius of curvature of spherical mirror is 6 m. The mirror covers 12° of azimuthal part of the beam. The kick angle, defined as the angle between the beam direction and the normal of mirror, is 30° to reflect the Cherenkov photons to the photo-detectors.

The mechanical hardness for the radiation and heat-up of the mirror is tested using intense proton beam at KEK-Booster. The optics of the mirror was confirmed by LED measurements. The time variation of reflectivity caused by the partial radiation damage is monitored by a laser system. The results of the monitoring shows that the reduction of reflectivity during the one-year run is less than 6%. These tests, measurements, and monitoring are described in detail in [35].

### Photo-detectors

Twenty photo-multiplier tubes (PMTs) are used to detect the photons on the focal plane of the spherical mirror. PMTs are located far away from the beam line, as shown in Fig. 3.8, in order to avoid the radiation damage. They are aligned along the vertical direction with 35 mm interval. Signal of each PMT is led by a 100 m long cable to a charge sensitive ADC placed in the data acquisition room outside the radiation area.

The type of PMT in use is modified-R5600-01Q made by Hamamatsu Photonics Corporation. The size is 15.5 mm in diameter of the outer socket and 8 mm in diameter of the photo-cathode. There are three issues to be noted on this PMT: Quartz window is used against radiation hardness. The tests for the radiation hardness had been done at KEK-PS-K3 beamline [35, 36]. Multi-Alkali (Sb-Na-K-Cs) photo-cathode material is used to enlarge the dynamic range against intense light. This cathode does not saturate up to the photo-cathode current of 10  $\mu$ A, whereas a Bi-alkali photo-cathode saturates around 0.1  $\mu$ A. They are operated with low gain to measure the very intense light of  $\sim 10^9$  photoelectrons in each PMT. Typical gain in our operation is 300 in June 1999 run and 20  $\sim$  50 in Nov. 1999 run.

## Side view

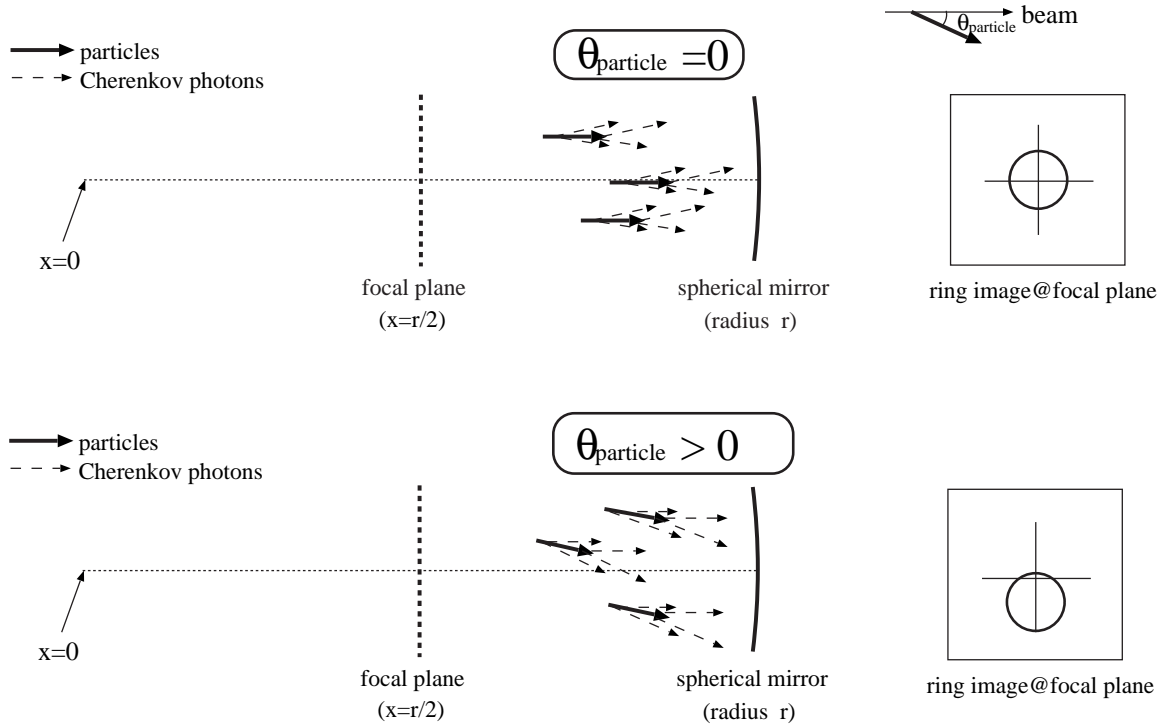


**Figure 3.10:** The principle of spherical mirror. The mirror focuses the Cherenkov photons onto the same ring when they are emitted by particles with the same  $\beta$  and the same direction, being independent of their emission points. The size and the position of ring are corresponding to the  $\beta$  and the direction of particle, respectively.

The relative gain among 20 PMTs was adjusted and calibrated by Xe lamp before the experiment. The gain ratio of neighboring PMTs was also checked using Cherenkov photons during the run. From these measurements, the error on the relative gain calibration is estimated to be 10% for June 1999 run and 5% for Nov. 1999 run [35]. The saturation of PMTs was observed in June 1999 run, while no saturation was observed in Nov. 1999 run. The non-linearity was corrected by a 2nd polynomial function, which was applied only to the data in the June 1999 run. Uncertainty of the correction was estimated to be 4% [35].

Up to now, the data taking of PIMON had been performed twice, one in June 1999 and the other in November 1999, for different experimental configurations. As mentioned before, we operated with a target of 2 cm in diameter and a horn current of 200 kA in June 1999, while with a target of 3 cm in diameter and a horn current of 250 kA in November 1999. PIMON is set on the beam line only during the periods of data taking, and is not on the beam line during the normal neutrino beam runs. The results of the PIMON measurements are described in Chapter 6. Further explanations, the analysis method, and the results of PIMON can be found in [35].



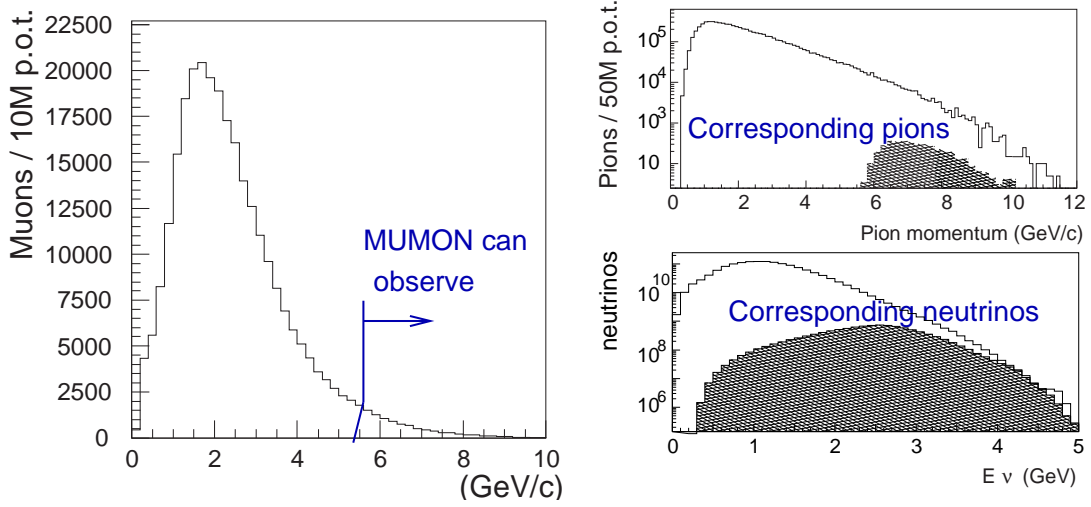


**Figure 3.11:** The momentum distributions of muons, pions, and neutrinos at muon-pit. Left figure shows the muon momentum distribution just before the beam dump. Only the muons above 5.5 GeV/c can reach the MUMON. Right figures show the momentum distributions of generated pions (top) and neutrinos (bottom) in the beam line. The hatched histograms in these figures are corresponding pions and neutrinos to the muons above 5.5 GeV/c. These histograms are estimated by a Monte Carlo simulation.

### 3.3.2 Muon monitors

Muon monitors (MUMONs) measure the profile of secondary muons after the beam dump, which muons come from the decay of pions,  $\pi^+ \rightarrow \mu^+ \nu_\mu$ . Since pion is a pseudo-scalar meson, the profile center of muons is same as that of neutrinos. Using this fact, we can monitor the direction of neutrino beam on spill-by-spill basis.

MUMON is set in a pit, so-called “muon-pit”, located at 220 m downstream of the production target, just downstream of the beam dump. The beam dump consists of 3.5 m thick iron and 2 m thick concrete shields, as shown in Fig. 3.5. Due to the energy loss and the hadron interactions in the beam dump, only muons with the momentum of greater than 5.5 GeV/c can reach the muon-pit. Fig. 3.11 shows the momentum distribution of muons before the beam dump. A fraction of 2.1% of muons are expected to be above 5.5 GeV/c. Their flux is roughly 10<sup>4</sup> muons per 1 cm<sup>2</sup>. Fig. 3.11 also shows the momentum distributions of pions and neutrinos which correspond to the muon above 5.5 GeV/c, indicating that only pions above 5.5 GeV/c can be monitored by measuring the muons above 5.5 GeV/c. However, the direction of high energy pions are more sensitive to the overall beam direction than the low energy ones. For example, when mis-steering of the beam, such as incident proton profile or angle changes, or the horn trouble occurred, then the muon profile always indicates the movement in its center position. Therefore, MUMON works well as a good monitor for the overall beam steering toward the SK. In addition, by monitoring the beam intensity at MUMON, the proton targeting can also be monitored.

MUMON is consist of two types of detectors; one is an ionization chamber (ICH) and the other is an array of silicon pad detectors (SPD). Fig. 3.12 shows a schematic view inside the muon-pit.

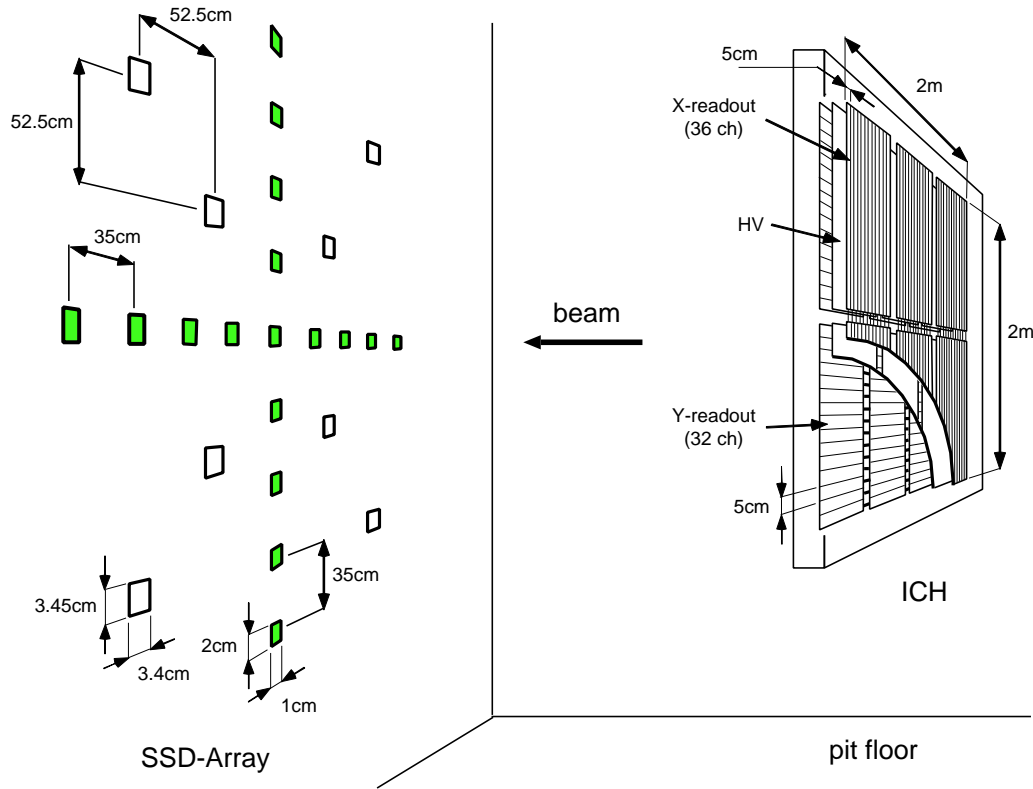


**Figure 3.12:** A schematic view inside the muon-pit. An ionization chamber (ICH) and an array of silicon pad detectors (SPD) are located inside the muon-pit.

### Ionization chamber

An ionization chamber (ICH) in the muon-pit is a segmented plate chamber just like SPIC in the primary beam line. In order to measure the broad muon profile, it is made to be as large as 190 cm (horizontal)  $\times$  175 cm (vertical).

There are three G10 planes, two cathode planes for horizontal and vertical projections, and one anode plane. They are arranged with gaps of 1 cm between these planes. The each cathode is segmented into strip lines of width of 5 cm in each direction. The numbers of readout channels are 36 in horizontal and 32 in vertical direction. Due to the difficulty to make a large G10 plate, the ICH consists of six modules of the size of 60 cm  $\times$  90 cm, 3 modules in horizontal and 2 modules in vertical direction. The corresponding strip lines of adjoining modules are electrically connected to make long strip lines of a length of  $\sim$ 180 cm. There are gaps between modules; 25 cm in horizontal and 15 cm in vertical, and hence they are insensitive regions. Since the electric field is deformed around the edge strips in each module, the numbers of strips available for the measurement are 30 in horizontal and 28 in vertical directions.

Whole modules are installed inside the gas vessel filled with Ar gas. The high voltage of  $-500$  V is supplied to the anode plane. Electrons ionized by the passing muons are collected by the strips and their signals are recorded by charge sensitive ADCs. The quantity of charge read out from each strip corresponds to the number of muons passing through each strip, hence the muon profile is obtained.

The channel-to-channel uniformity is calibrated by moving ICH horizontally and verti-



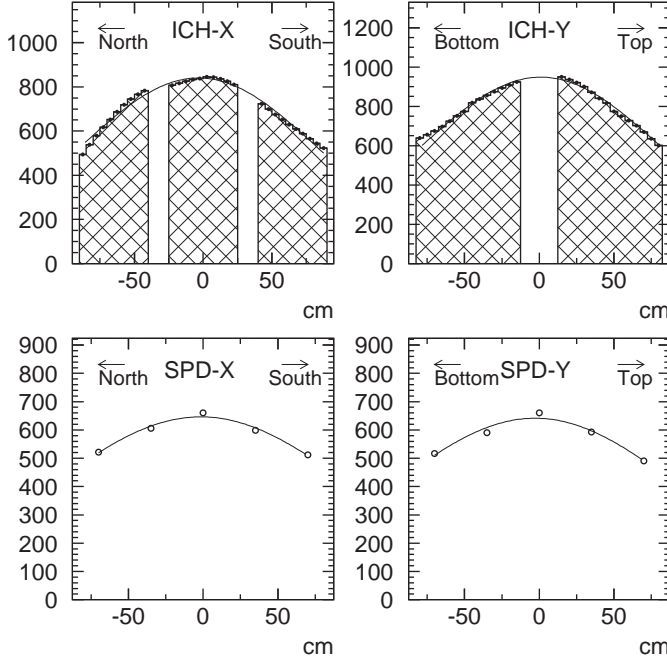


**Figure 3.13:** Typical muon profiles measured by ionization chamber (ICH) and silicon pad detector arrays (SPD). Upper two figures are of ICH in the horizontal (left) and the vertical (right) directions. Gaps shown in these figures are corresponding to the insensitive regions of ICH as described in the text. Lower two are of SPD also in the horizontal (left) and the vertical (right) directions.

cally [35] assuming the stability of muon beam. This measurement had been performed several times during long run periods. The relative gain of channels has been stable within an accuracy of several %. With the use of these correction factors, muon profile is measured on spill-by-spill basis. We can also measure the intensity of the beam by summing the charge of all channels up. The upper two figures in Fig. 3.13 shows a typical muon profile in horizontal and vertical directions measured by ICH. It can measure the profile precisely enough to monitor the beam direction.

### Silicon pad detector array

As is shown in Fig. 3.12, arrays of semi-conducting detectors, silicon pad detectors (SPDs) are also installed on the downstream wall in the muon-pit. There are 17 small-type SPDs arranged along the horizontal and the vertical axis with 35 cm interval, and 9 large-type SPD in diagonal arrays with 74.2 cm interval. The small-SPD has a sensitive area of  $1\text{ cm} \times 2\text{ cm}$  with a depletion layer thickness of  $300\text{ }\mu\text{m}$ , while the large-SPD has a sensitive area of  $3.4\text{ cm} \times 3.05\text{ cm}$  with a depletion layer thickness of  $375\text{ }\mu\text{m}$ .

A muon passing through the SPD,  $2.3 \times 10^4$  and  $2.9 \times 10^4$  electron-hole pairs are created in the depletion layers of small and large SPD, respectively. They are collected by the bias voltage of 100 V for small SPDs and 70–80 V for large SPDs, and the signals are recorded by charge sensitive ADCs.

Uniformity of the sensitivity of small SPDs was measured using LED light source at a test bench. The results show that the sensitivity of each small SPD agrees within 6% [35]. For large SPDs, the uniformity was measured using muon beam at the muon-pit. All the large SPDs were once aligned along the beam axis, and the readout charges from each SPDs were compared, then the relative gain factor for each SPD was obtained although they have an uncertainty of 10% level due to the  $z$ -dependence of the muon beam intensity [35].

By measuring the charge from each SPD, the muon profile can be monitored on spill-by-spill basis. The typical profiles measured by SPD are also shown in Fig. 3.13 (lower 2 figures).

Further information about MUMON can be found in [35],

### 3.4 Data acquisition system of beam line monitors

All the data acquisition (DAQ) systems in the KEK site are triggered by the common signal provided by the accelerator. There are two trigger signals synchronized with the timing of the kicker magnet excitation.

One trigger signal is provided 1.1 msec before the beam extraction. This signal is used only to make the horn magnets fire since it takes about 1 msec to achieve the peak current of horns. The other signal is provided 120  $\mu$ sec before the beam extraction. This signal is used as the beam spill trigger for the data acquisition in all beam line monitors and all detectors at near site. Simultaneously 16-bit spill number is distributed to and recorded at each DAQ site to identify a spill from others.

Signals from beam line detectors, CTs, SPICs, MUMON, and PIMON during the PIMON runs are all digitized and recorded by charge sensitive ADCs on spill-by-spill basis, as described before. There are 4 rooms and 6 front-end computers for DAQ system along the beam line and 1 host PC controls data acquisition processes on other front-end computers.

In addition to the detector information, the beam extraction timing is recorded by the GPS time recording system for the time synchronization with SK. Furthermore, the time interval between previous and current spills is also recorded by VME Trigger Module (TRG). Descriptions about GPS system will be provided in Sec. 3.7.

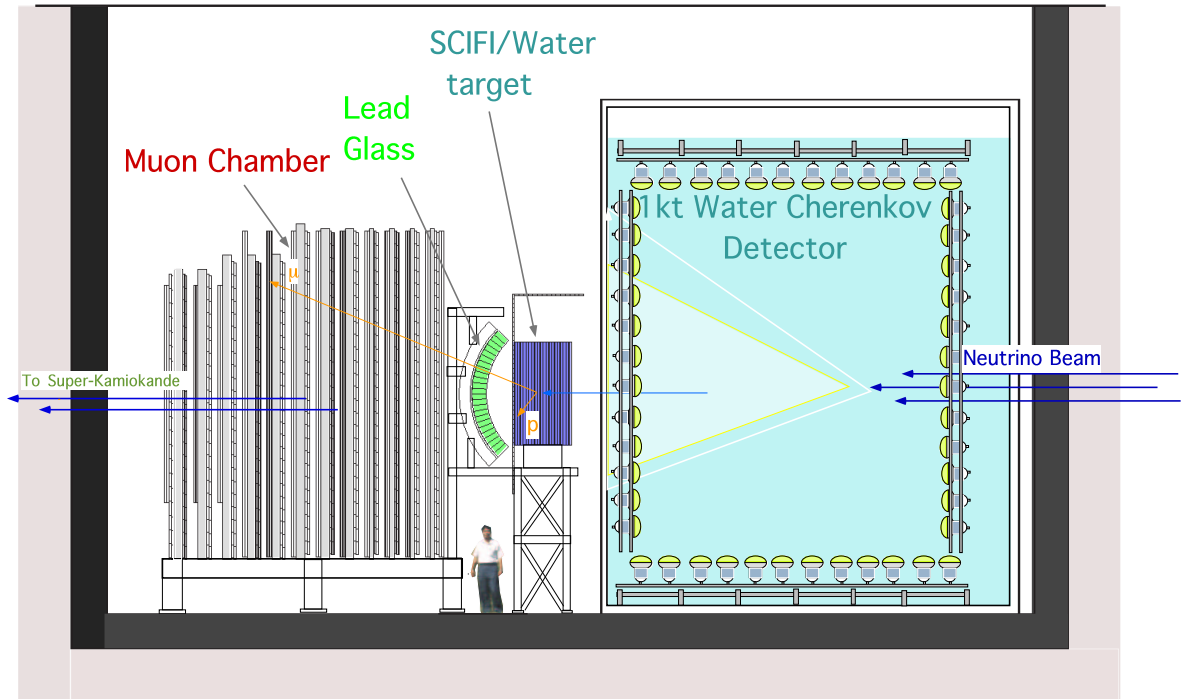


**Figure 3.14:** A schematic view of near detector system. From upstream of the beam, 1 kt water Cherenkov detector (1KT), scintillating fiber tracker (SciFi), lead glass calorimeter (LG), and muon range detector (MRD) are located. Surrounding the upstream and the downstream of SciFi, planes of plastic scintillators (trigger counter, TGC) are installed. In this figure, the neutrino beam is coming from right and going to left side.

## 3.5 Near neutrino detectors

Near neutrino detector system (ND) is located at the distance of 300 m from the production target, 80 m downstream of the beam dump. Since the beam is tilted downward by about  $1^\circ$ , the experimental hall is at 16 m below ground.

ND consists of a 1 kt water Cherenkov detector (1KT), a scintillating fiber tracker (SciFi), a lead glass calorimeter (LG), and a muon range detector (MRD), as shown in Fig. 3.14. Planes of plastic scintillators (trigger/veto counters, TGC) is surrounding the upstream and downstream of SciFi. The detector system of SciFi, LG, MRD, and TGC is called “fine-grained detector system (FGD)”. In this section, a description of each detector, mainly 1KT, and its performance is provided.

### 3.5.1 1 kt water Cherenkov detector

1KT is a water Cherenkov type detector located most upstream of the experimental hall. The center of the water tank is at 294 m downstream of the production target. It measures the neutrino beam properties such as the flux and the energy spectrum. The advantage to use 1KT is to cancel out most of the systematic uncertainties in comparing the measurements in 1KT and SK because of the same detection principle and the same material for neutrino target ( $\text{H}_2\text{O}$ ).

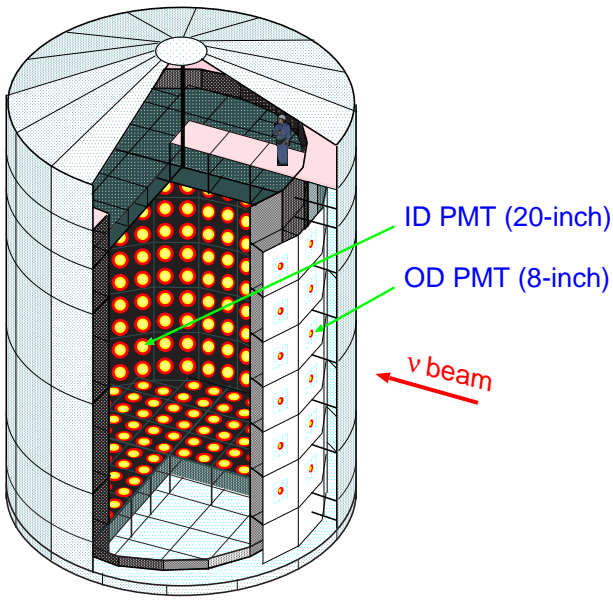


**Figure 3.15:** A schematic view of 1KT detector. The diameter and height of the tank are both 10.8 m, and the tank is filled with about 1,000 tons of water. Inside the tank, the volume is optically separated into two parts; the inner volume and the outer volume. The dimensions of the inner volume are 8.6 m in diameter and 8.6 m in height. There are 680 20-inch PMTs mounted on the wall of the inner volume facing inward with a spacing of 70 cm grid. On the 1/3 part of the upstream wall and the bottom wall of the outer volume, 68 8-inch PMTs are mounted facing outward with a spacing of 140 cm.

### The structure of 1KT

As shown in Fig. 3.15, 1KT consists of a cylindrical tank of 10.8 m in diameter and 10.8 m in height, filled with approximately 1,000 tons of pure water. Inside the tank, it is optically separated into two parts; the inner detector (ID) of the cylindrical volume of 8.6 m in diameter and 8.6 m in height, and the outer detector (OD) surrounding ID. Between ID and OD, there is a stainless steel frame (support frame) on which PMTs are mounted.

There are 680 20-inch PMTs mounted on the support frame facing inward, 456 PMTs are on the barrel wall, 112 PMTs are on the top wall, and the remaining 112 PMTs are on the bottom wall. These PMTs are aligned in a 70 cm grid, which is the same spacing of PMTs in SK. The fraction of photocathode coverage is about 40% of the surface of ID, and the rest of the wall surface is covered by black polyethylene terephthalate sheets which suppress the reflection of Cherenkov light on the wall.

The OD is originally used to veto incoming particles from outside, whereas it is also used to trigger the through-going/stopping cosmic-ray events for the detector calibration. The thickness of water in OD is 1 m for the barrel part and 0.6 m for the bottom part. There are 68 8-inch PMTs mounted on the support frame facing outward, 42 of them are mounted on 1/3 part of the upstream barrel wall, and the remaining 24 PMTs are on the bottom wall. The spacing of PMTs is 140 cm. A 60 cm × 60 cm square plate of wavelength shifter is attached to the surface of each PMT in order to increase the light collection efficiency. Tyvek sheets, which is known as reflective material, cover the OD wall to enlarge the detection efficiency.

PMTs are normally influenced by the magnetic field around them, and their gain and time response may vary even if the magnetic field is as small as the magnitude of the geomagnetic field. The PMTs of 50 cm in diameter are used in 1KT, and hence the effect becomes larger than for small PMTs. In order to prevent PMTs from being affected by the magnetic field, the diameter of the first dynode is made to be as large as possible by adopting a Venetian blind type dynode. Furthermore, Helmholtz type coils are set around the tank in both vertical and horizontal directions in order to compensate the geomagnetic field inside the tank. Thanks to the compensation coils, the magnitude of the magnetic field inside the tank is suppressed to be around 50 mG.

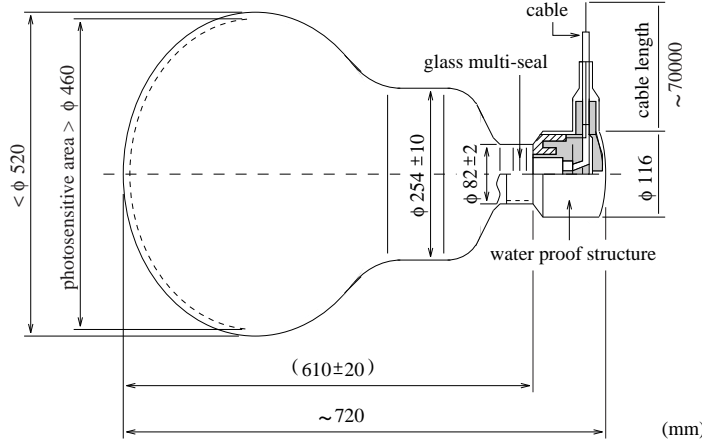


**Figure 3.16:** A schematic view of 20-inch photo-multiplier tube used in 1KT and SK.

### Cherenkov light

Cherenkov photons are emitted by a charged particle traveling in water with the velocity faster than the light velocity in water. These photons are emitted onto a cone around the particle path. The opening angle of the Cherenkov cone,  $\theta$ , is determined by the refractive index of water,  $n$ , and the velocity of particle,  $\beta$ , as

$$\cos \theta = \frac{1}{n\beta} \quad , \quad (3.4)$$

where, for water,  $n = 1.33-1.36$  depending on the wavelength of light. The momentum threshold of Cherenkov radiation for electron, muon, pion, and proton are 0.57, 118, 156, and 1048 MeV/ $c$ , respectively.

The number of Cherenkov photons,  $N$ , emitted by a particle with single charge per unit path length,  $x$ , per unit wavelength,  $\lambda$ , is given by

$$\frac{d^2 N}{dx d\lambda} = \frac{2\pi\alpha}{\lambda^2} \left( 1 - \frac{1}{n^2\beta^2} \right) \quad , \quad (3.5)$$

where  $\alpha$  is the fine structure constant ( $\sim 1/137$ ). A particle with  $\beta = 1$  emits about 340 photons per 1 cm in the wavelength of 300 to 600 nm, to which wavelength our PMT has sensitivity.

### 20-inch photo-multiplier tube

Twenty-inch PMTs, R3600 made by Hamamatsu Photonics Corporation, are used in ID of 1KT, as well as SK, to detect Cherenkov photons. The specifications of the PMT are summarized in Table 3.2. The photo-cathode is made by bi-alkali (Sb-K-Cs) which sensitive region matches the wavelength range of Cherenkov light. The quantum efficiency is about 22% at the wavelength of 390 nm. A Venetian blind type dynode is used in it. The average collection efficiency is about 70%. The gain is as high as  $10^7$  at a supplied high voltage of 2 kV. Thanks to this high gain, single photoelectron can be distinguished. The typical timing resolution is 2 nsec. Further description for the PMT is given in [37, 38].

**Table 3.2:** Specifications of 20 inch photo-multiplier tube, R3600 made by Hamamatsu Photonics Corporation, used in 1KT and SK.

Parameters	Values
Photo-cathode area	50cm in diameter
Shape	Hemispherical
Window material	Pyrex glass, 4 ~ 5 mm
Photo-cathode material	Bialkali (Sb-K-Cs)
Dynodes	11 stages, Venetian blind type
Quantum efficiency	22% at $\lambda = 390$ nm
Sensitive wavelength	300 nm to 600 nm, peak at 390 nm
Typical gain	$10^7$ at $\sim 2000$ V
Dark current	200 nA at gain $10^7$
Dark pulse rate	3 kHz at gain $10^7$
Cathode non-uniformity	less than 10%
Anode non-uniformity	less than 40%
manufactured	Hamamatsu Photonics K.K.

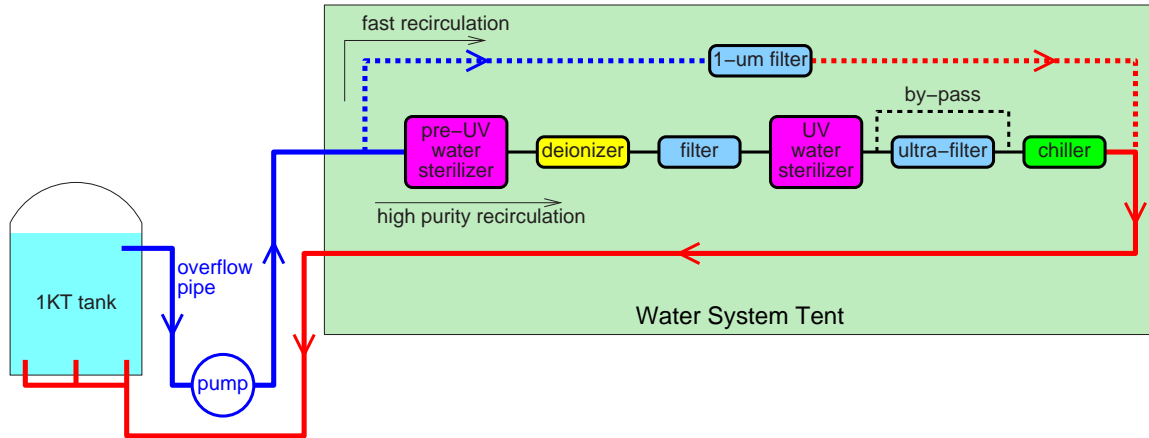


**Figure 3.17:** A schematic diagram of the water purification system in 1KT. Solid lines show main circulation flow, and dotted lines show supplementary one. The equipments inside the green box are located in water system tent on the ground.

### Water purification system and water transparency

Impurities in water, such as small dusts, bacteria, metallic ions, and resolved gases, cause attenuation or scattering of the Cherenkov light, making the event reconstruction performance worse. For this reason, a water purification system is employed in 1KT to remove these impurities.

Fig. 3.17 shows the flow diagram of the water purification system in 1KT. The system is located in the water system tent on the ground, next to the experimental hall. Water which comes from 1KT tank is sent to the system using pump at the underground level in the hall. Pre-UV water sterilizer and UV water sterilizer kill bacteria in the water. Filter removes small dust of the order of  $1\ \mu\text{m}$ . Metallic ions resolved in water is removed by the deionizer. Ultra-filter removes much smaller dust of order of  $10\ \text{nm}$ . The water to be sent to 1KT tank is cooled by chiller down to around  $10^\circ\text{C}$  in order to prevent bacteria to breed in water. This system circulates the water with 20 tons per hour. Purity of the water is monitored by measuring its electrical resistance, which is usually  $10\ \text{M}\Omega/\text{cm}$ . The temperature and the purity of the water have been controlled to be around these values during the whole run periods.

Water transparency is measured by using cosmic-ray muons. By taking the ratio of Cherenkov light inside and outside the Cherenkov cone of cosmic-ray muon's, amount of scattering light can be measured. The attenuation length is over 50 m and is stable through the whole runs.

### Data acquisition system of 1KT

Signals from 748 PMTs (680 PMTs in ID, 68 PMTs in OD) are sent through co-axial cables into the electronics hut on the ground level, and then they are processed by data acquisition system to digitize signals and store the data. Fig. 3.18 shows a schematic view of the data acquisition system in 1KT. Detailed descriptions on the system can be found in [39], and they are briefly described here.

*Front-end electronics:* Front-end electronics digitize and record the charge and the timing information from PMTs, and at the same time, they generate the discriminated pulses for the trigger logics. For these purpose, TKO modules which perform analog-to-digital conversion, named "ATM (Analog Timing Module)" [40, 41], are employed. They had been developed for the use in SK. In one ATM module, 12 PMT signals are precessed, and 66 ATMs are used in total in 1KT. Two sets of TDC and ADC are prepared for each channel inside an ATM to reduce the dead time of the module.

Signal from each channel is, first, divided into four streams; one is led to a discriminator, two are led to two independent ADCs, and the other is used to make an analog sum of 12 PMT signals, called "PMTSUM". The discriminator threshold is set to be equivalent to typically 0.3 photoelectron signal of PMT. The discriminated signal is sent to two independent TDCs, and also used for the timeout signal against the AD conversion of TDCs and ADCs. If GONG (Go/NotGo) module receive a trigger signal before the timeout of ATM, which is about  $1.1\ \mu\text{sec}$ , TDC and ADC start digitizing the signals, 12-bit data is stored in the FIFO memories of ATM, and the data is sent to SCH (Super-Control-Head) module. The conversion factors of TDC and ADC are  $0.4\ \text{nsec/count}$  and  $0.15\ \text{pC/count}$ , respectively. Furthermore, a rectangle pulse with a width of  $200\ \text{nsec}$ , "HITSUM", is generated using the discriminated signal. The pulse height of HITSUM corresponds to the number of hit channels in the ATM, which is about  $10\ \text{mV}$  per one hit channel.

One different usage of ATM from that in SK is to use the accelerator beam timing as enable signal for the module. ATMs are allowed to proceed the above processes only during  $1.3\ \mu\text{sec}$

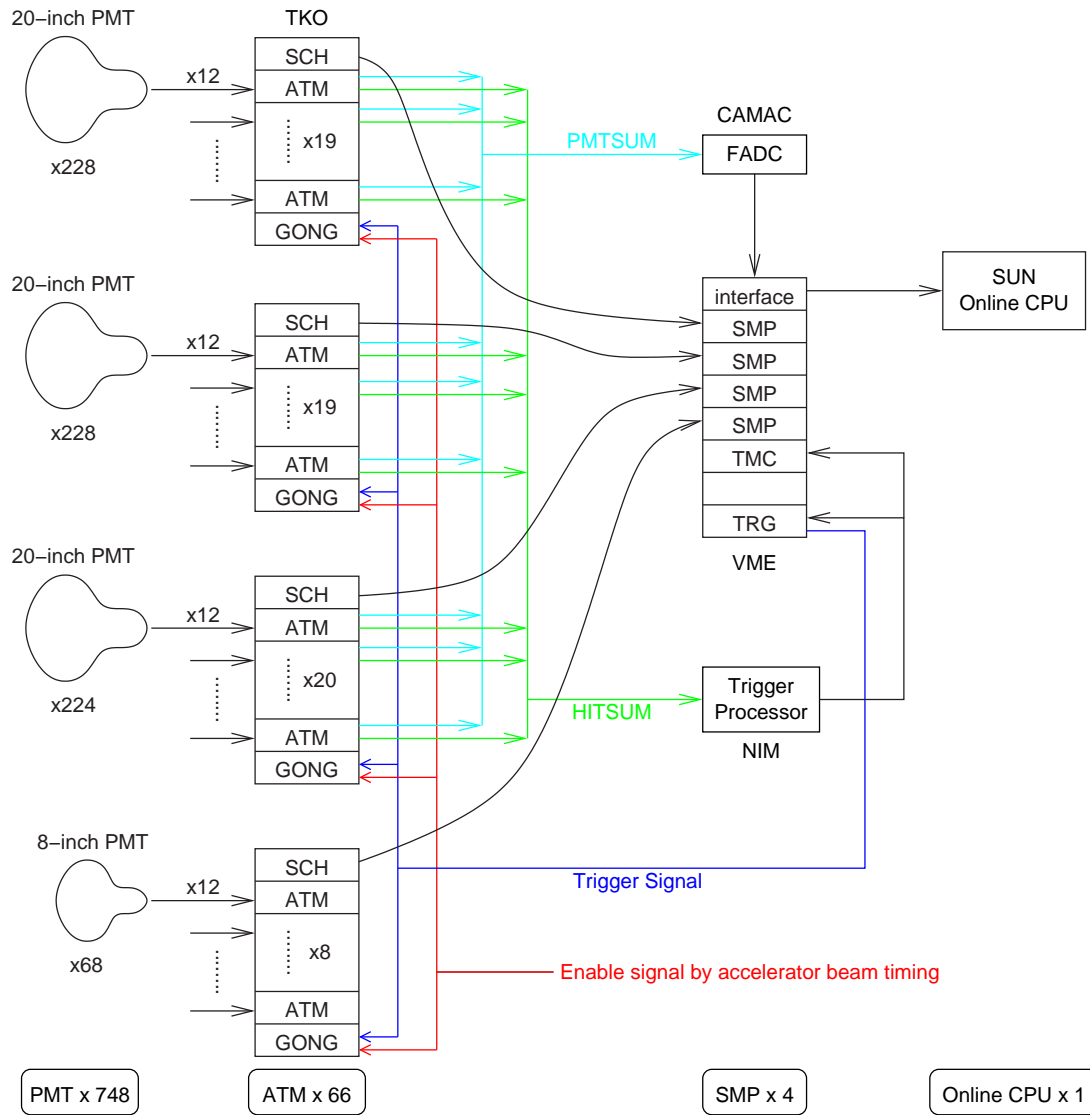


**Figure 3.18:** A schematic diagram of the data acquisition system in 1KT.



synchronized with the beam timing. This enable signal is generated by the accelerator trigger signal which come 120  $\mu$ sec before the beam spill, mentioned in Sec. 3.4.

All PMTSUM signals from ID-PMTs are summed up and sent to CAMAC Flash-ADC (FADC) to record the signal shape. The sampling rate and dynamic range of the FADC is 500 MHz and 8-bit, respectively. This data is used to count the number of events in each beam spill by counting the number of peaks in the PMTSUM signal.

The pulse reflection at the input of ATM had been observed during the run in 1999 due to the impedance mis-matching. In order to avoid the reflection, buffer-amplifiers have been installed on the ATM input since January 2000.

ATM module has its responses dependent on temperature [42], the data acquisition system mentioned above are all in the electronics hut where temperature is controlled to be stable at around 25°C.

Rear-end and other electronics: Four VME-SMPs (Super Memory Partner) are used to collect and temporarily store the data from ATMs. VME-TRG module records the trigger bit of each event and time interval between the previous and the current events. VME input register is used to record the spill number distributed by the beam line DAQ mentioned in Sec. 3.4. VME-TMC (multi-hit TDC) records the event timing in 1KT with respect to the trigger signal sent from accelerator. TMC is also used to record the muon timing which signal comes from MUMON at muon-pit in order to monitor the stability of the time interval between the accelerator trigger signal and the real beam timing. This monitor is very important because all the detectors in KEK is triggered by the accelerator signal.

Trigger electronics: The readout processes are triggered if the 1KT has an event with more than about coincidence of 40 hit PMTs. The coincidence is identified using HITSUM signals from ATMs as following: All HITSUM signals from ID-PMTs are summed up, and then discriminated with the threshold of 450 mV, which corresponds to 40 hit PMTs in 200 nsec time window.

The trigger signal is sent to TRG module, and then distributed to GONGs, VME-SMPs, FADC, and TMC. The signals to GONGs make ATMs start the readout processes. Then, the signals to SMPs force SMPs to collect the data stored in ATMs into SMPs. After all the ATM data are stored in SMPs, it is ready to be read out by online computer. The trigger signal is also sent to TMC to record the trigger timing of the event with respect to the accelerator trigger timing. Delayed trigger signal is sent to FADC to stop its sampling.

Online computer: When all the modules become ready to be read out, an online computer starts collecting the data from SMPs, FADC, TMC, input register, and TRG module. After collected data are sorted on the computer, they are sent to a host computer, or “event builder”, of ND. The event builder makes data from each detector to be of the form of 1-spill data based on the spill number recorded in each detector system.

The event trigger mentioned above is permitted only during four timing gates per one beam spill cycle; “on-spill gate” which is the main gate opened during neutrino beam timing, “delayed gate” which is sequential gate following the on-spill gate to take the succeeding neutrino event such as decay electron from the neutrino-induced muon, “off-spill gate” which is opened 1 msec after neutrino beam spill with the same duration as on-spill gate to estimate the rate of background events such as accidentally incoming cosmic rays, and “cosmic ray gate” which is to collect cosmic ray muons between spills to check the stability of the energy scale of 1KT.

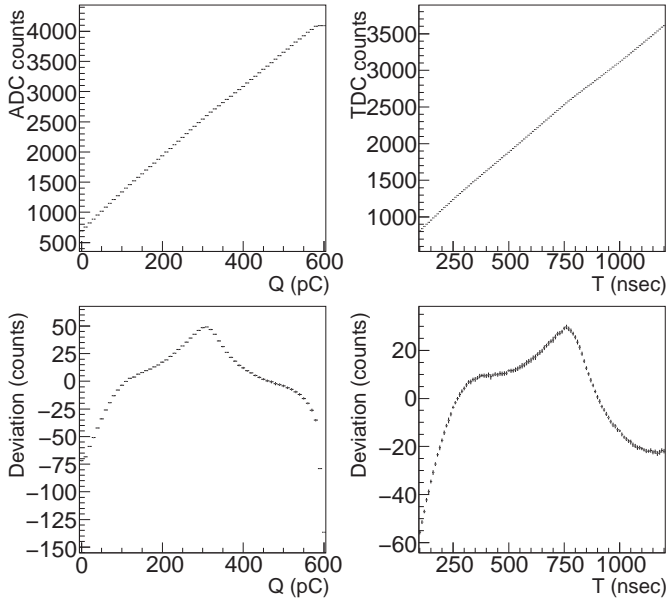


**Figure 3.19:** Charge-to-counts and Time-to-count responses of ADC and TDC in ATM module. Left two figures are for ADC, and right two are for TDC. The upper figures show the charge-to-count and the time-to-count responses of ADC and TDC, and the lower figures show their deviations from linear fitting.

### ATM calibration

The ADC and TDC in ATM module almost linearly response to the input charge and timing, respectively, but they are not perfectly linear responses. In order to correct these non-linear responses, ATM calibration had been performed before the experiment started, and also when the experimental configurations had been changed, such as installation of the buffer-amplifiers.

CAMAC CTG (charge time generator) is used for the ATM calibration. In order to measure the response to the input charge and input timing, pulses with charge of the magnitude of from 0 to 600 pC by 10 pC step and with the timing of from 0 to 1.2  $\mu\text{sec}$  by step of 10 nsec are generated by CTG, and put to each ATM channel. Fig. 3.19 shows the responses of ADC and TDC to the input charge and timing and the deviations of their responses from linear fittings. As is shown in the figure, the responses have some non-linearity. In order to obtain the conversion factors of ADC and TDC counts to charge and timing at any point, intervals between measured points are complemented by linear lines. The deviation of the ADC/TDC count estimated by the complemented lines from actually measured one is known to be within 1 count at any point [42], which is sufficient accuracy.

### Timing calibration

The timing when each PMT receives Cherenkov light is very important for the water Cherenkov detector to reconstruct the vertex of event. However there are several causes which make variation of the timing; PMT-by-PMT different transit time, the cable length, charge-to-timing correlation, and so on. Especially, there is clear correlation between the pulse height of signal and the timing when signal gets over threshold level of the discriminator in the ATM. In order to correct these effects *in situ*, a timing calibration had been performed using laser calibration system.

Fig. 3.20 shows a schematic view of the laser calibration system. A dye/Nitrogen laser is used as a light source since its pulse width is as short as the order of 1 nsec and hence a light emission with a definite timing is available. The wavelength of laser light is 390 nm, which is similar to that of Cherenkov light. The laser light is divided into two paths by a half mirror.

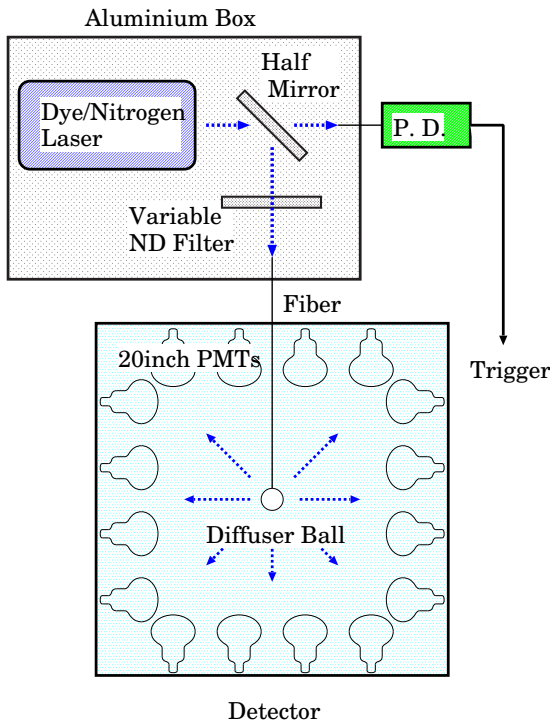


**Figure 3.20:** A schematic view of the laser calibration system in 1KT. Dye/Nitrogen laser light divided into 2 paths by a half mirror, one goes to photo-diode, marked P.D. in the figure, to make a trigger signal, and the other is injected to a optical fiber which another edge light diffusing ball is put on. The light diffuser ball is set at the center inside the 1KT tank, and laser light is almost isotropically emitted from the ball.

One light path goes to photo-diode detector (PD), which has a fast response to the input light. The PD signal is used for the trigger timing. The other light path is attenuated by a variable neutral density filter (ND filter) and injected to a optical fiber which goes into the 1KT tank. Light diffusing ball is put on the other side of the fiber which diffuses the laser light to isotropic direction [43]. The ball is set at the center of the 1KT tank. By changing the magnitude of attenuation at ND filter, light with various intensity is sent to PMTs in 1KT.

The time of flight of light from the diffuser ball to each PMT considered, the light detection timing in each PMT with respect to the trigger timing is obtained at various light intensity, which is in a form of correlation plot of amount of detected charge versus detection timing in each PMT, so-called “T-Q map”. Fig. 3.21 shows a typical T-Q map. The detection timing is corrected according to T-Q map for each PMT,

T-Q maps had been taken before the experiment, and also when the experimental configuration had been changed.

### Equalization of PMT gain

In order to measure the energy of particle precisely, the gain of each PMT should be adjusted so that all the PMTs have almost the same gain. Here, the method to equalize the gain of each PMT is described.

There are 103 PMTs out of 680 ID-PMTs, called “pre-calibrated PMTs”. Before the installation of PMTs into 1KT, the values of high voltage supplied to each of these PMTs had been determined to adjust its gain to be  $6 \times 10^6$  within 1% precision [43]. The location of pre-calibrated PMTs is shown in Fig. 3.22. The pre-calibrated PMTs provide the standard gains to which the gains of all the other PMTs are adjusted. Hamamatsu Photonics Corporation had measure the gain of all PMTs before shipping, and provided the high voltage values which give  $6 \times 10^6$  gain. The high voltage values provided by Hamamatsu Photonics are supplied to PMTs

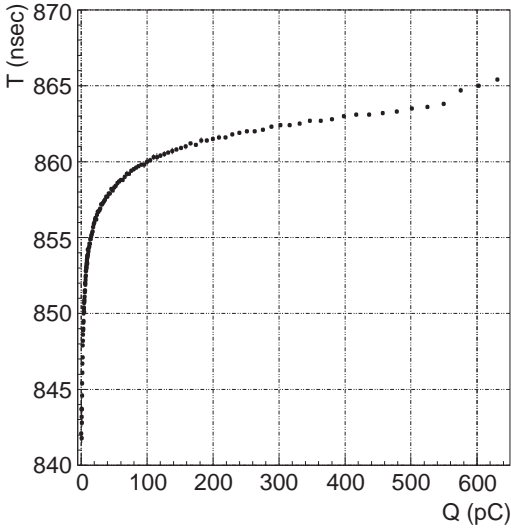


**Figure 3.21:** A typical plot of the detected charge versus timing in a PMT, “T-Q map”. The horizontal axis is amount of charge detected by PMT, and the vertical one is the detection timing with respect to the trigger timing provided by the photo-diode.

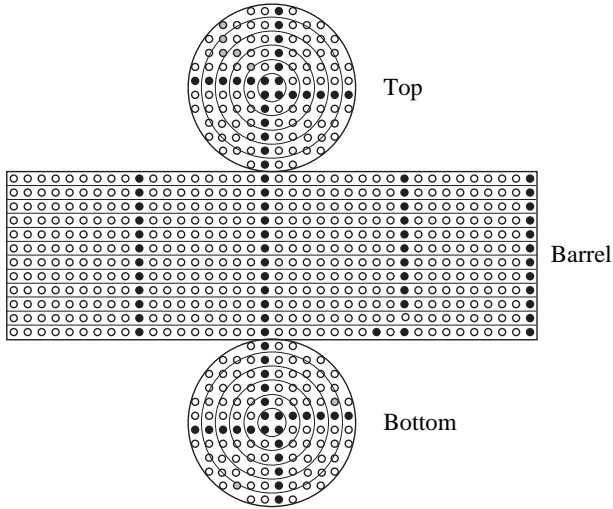


**Figure 3.22:** Position of the pre-calibrated PMTs in 1KT. Circles indicate the position of PMTs, and black closed circles show the “pre-calibrated PMTs” which are used as standard PMTs to equalize the gain of all the other PMTs.

other than pre-calibrated PMTs. By the adjustment of the high voltage for each PMT, the PMT gains are equalized with variation of about 10–20% level.

In order to equalize the PMT gains more precisely, the relative gain to the pre-calibrated ones is measured for each PMT after their installation into the 1KT tank by illuminating uniform light from the center of the tank to all PMTs. This measurement is done using a Xenon calibration system shown in Fig. 3.23. A Xenon lamp is used as a light source of the calibration. The UV filter makes the light with the wavelength of 300–400 nm, the ND filter attenuate the light to be appropriate intensity, and diffuser makes the light uniform. Then the light is injected to four optical fibers; two fibers go to two photo-diodes to monitor the intensity of the light, one fiber goes to 2-inch PMT which makes a trigger signal, and one fiber goes into the 1KT tank. A scintillator ball is put on the other end of the last fiber. Absorbing and re-emitting the Xenon light, the ball almost uniformly illuminates all PMTs inside the tank. The scintillator ball was rotated in the azimuthal direction ( $\phi$ -direction) in order to cancel out the non-uniformity of the light emission in  $\phi$ -direction.

Other sources of non-uniformity to detect the light in each PMT, such as the non-uniformity of the light emission in  $\theta$ -direction, the solid angle of each PMT seen from the scintillator ball,

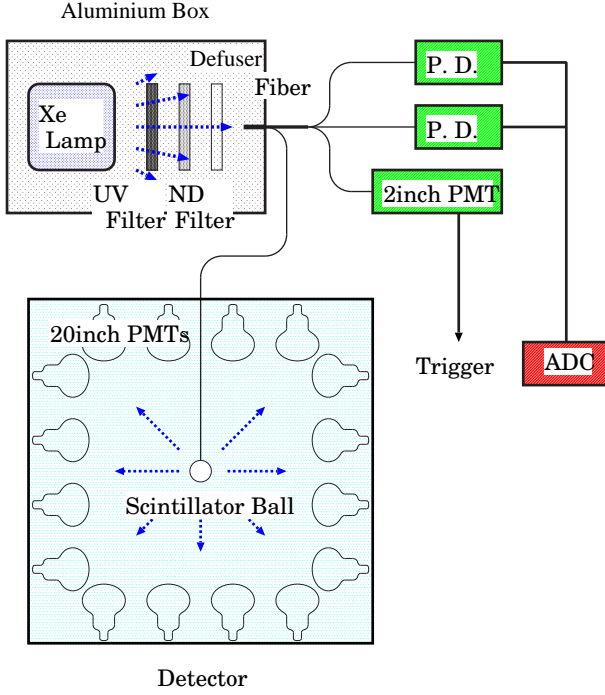


**Figure 3.23:** A schematic view of the Xenon calibration system in 1KT. A Xenon lamp is used as a light source. UV filter makes only the light with the wavelength of 300–400 nm permeate through. ND filter attenuates the intensity of light in order for PMTs to receive  $\sim 100$  photons. Diffuser diffuses the light to be uniform. Then light is injected to 4 optical fibers. Two fibers go to photodiode detectors and is read out by CAMAC ADC to monitor the intensity of light. One of four fibers goes to 2-inch PMT which signal is used for the trigger. The remaining fiber goes into the 1KT tank, on another edge of which fiber, a scintillator ball is put. The ball absorbs the Xenon light and re-emits scintillating photons isotropically. The ball is usually set at the center of the 1KT tank.

and the attenuation of the light in the water, are corrected using correction functions, which were measured in advance [43, 44].

By taking a ratio of detected charge in each PMT to those in pre-calibrated ones located at geometrically same position, most of systematic uncertainties are canceled out, such as water attenuation, solid angle of PMT, non-uniformity of light source in  $\theta$ -direction, the light reflection on the surface of PMTs, and any geometrical effects. Using the relative gain factors to pre-calibrated one, the PMT gains are corrected with the precision of several % level.

However, it is known that the geomagnetic field in 1KT is not uniform, and there exists small difference in PMT gains at lower and upper parts of 1KT. The correction against this effect had been done by using vertically and horizontally through-going cosmic-ray muons, which is described in the next section.

### Energy scale calibration

In order to calibrate the energy scale in 1KT, cosmic-ray muons are in use. As mentioned in the previous section, since the gains of PMTs at lower and upper part of 1KT are different due to the different magnetic field, the gain correction between the bottom part and barrel part of PMTs is also done using cosmic-ray muons. Two different triggers for cosmic-ray muons were made; one is to trigger the vertically through-going muons (vertical- $\mu$ ) and the other is to trigger the horizontally through-going muons (horizontal- $\mu$ ).

The vertical- $\mu$  events are triggered by the coincidence of the scintillation counter set at the top of the tank and the bottom OD-PMTs, while horizontal- $\mu$  events are triggered by the coincidence of the OD-PMT of upstream barrel part and Trigger/veto counter plane (TGC) which located at the downstream of 1KT tank. Typical event displays for the vertical- $\mu$  and the horizontal- $\mu$  event are shown in Fig. 3.24. Major part of Cherenkov light is deposited onto the bottom part of 1KT in vertical- $\mu$  events, while that is deposited onto the barrel part in horizontal- $\mu$  events. Difference of gain in bottom and barrel PMTs, and overall gain factor are

tuned by adjusting the data to agree with a Monte Carlo simulation.

The distribution of the number of total photo-electrons per unit track length of muon, so-called “charge ratio”, is used to compare data with MC. Upper two figures in Fig. 3.25 show the distributions of charge ratio in vertical- $\mu$  and horizontal- $\mu$  events after tuning the gain factors. Data and MC show the reasonable agreement in both distribution. The difference in the mean value of the distribution between data and MC ( $(MC - \text{data})/\text{data}$ ) is  $+2.0 \pm 0.1\%$  in vertical- $\mu$  and  $-2.3 \pm 0.5\%$  in horizontal- $\mu$ .

The energy scale has also been checked using the charge ratio of cosmic-ray muons stopping inside 1KT (stop- $\mu$ ), resulting in the difference of mean value between data and MC of  $+1.2 \pm 0.1\%$ .

The PC events, in which the muon produced by a neutrino interaction in 1KT goes outside the 1KT, are also used to check the energy scale. In PC events, the number of total photoelectrons is directly compared between data and MC. The discrepancy between them is estimated to be  $-2.6 \pm 0.3\%$ .

One more check for the energy scale is done using  $\pi^0$  induced neutrino events. Events with two electron-like Cherenkov rings (2-ring both  $e$ -like events) are selected to enhance  $\pi^0$  candidates. Using the energy and the direction of each ring and assuming both 2 rings are generated from a common vertex, the invariant mass is reconstructed in each event. The lower figure in Fig. 3.25 shows the distribution of the reconstructed invariant mass for 2 rings  $e$ -like events, showing the clear peak around  $\pi^0$  mass. Fitting the peaks in data and MC, the discrepancy between data and MC is found to be  $-2.1 \pm 0.2\%$ .

Fig. 3.26 summarizes the all measurements on the calibration of the energy scale in 1KT. All the measurements settled to be within  $^{+2}_{-3}\%$  differences. Therefore, we quoted this value as the systematic error on the measurement of particle momenta in 1KT. Fig. 3.27 shows the distribution of total number of photoelectrons for the neutrino events which have one muon-like Cherenkov ring with the charged particle track fully contained inside the inner detector of 1KT (FC 1-ring  $\mu$ -like events: 1R $\mu$ ). The distributions in Data and a Monte Carlo simulation is reasonably agrees, showing the energy scale of 1KT is well calibrated.

### Stability of the energy scale

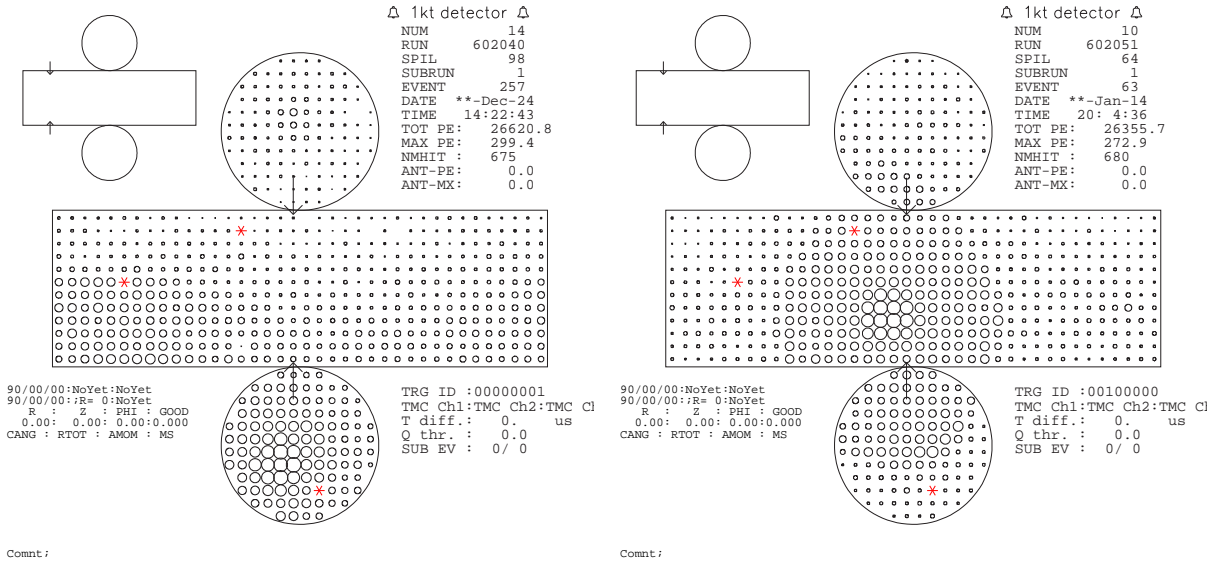
The stability of the energy scale has been monitored using the charge ratio of vertical- $\mu$ . The vertical- $\mu$  events were sometimes taken during the neutrino beam was off. In addition, cosmic-ray events have been also taken between beam spills since Jan. 2001.

Fig. 3.28 shows the stability of the energy scale since Jun. 1999. The energy scale at the very beginning of the experiment was about 3% lower than that of the rest of the periods. It has been stable within 1% since the run in 2000. In the estimation of the expected number of neutrino events in SK, data in 1999 is also used as well as the rest of the data. However the difference of 3% in the energy scale makes only negligible error of less than 1% on the expected number of neutrino events. In the spectral analysis, the data in 1999 is discarded due to the different configuration of horn magnets in June 1999 and a hardware problem in November 1999 (1/4 part of PMTSUM was disconnected from FADC by mistake, mentioned in Sec. 7.1.1).

### 3.5.2 Trigger/veto counters

Two planes of plastic scintillators are located upstream and downstream of the SciFi detector, called trigger/veto counters (TGC). The upstream TGC is used to veto the charged particle coming from upstream of the beam or cosmic-rays. It consists of 20 scintillators of 466 cm in length, 20 cm in width, and 4 cm in thickness, covering an area of 466 cm  $\times$  400 cm in front of





**Figure 3.24:** Typical event displays of vertical (left) and horizontal (right) cosmic-ray muons. The major part of Cherenkov light is deposited onto the bottom part of 1KT in vertical- $\mu$  events, while onto the barrel part in horizontal- $\mu$  events. Asterisk marks “\*” represent dead PMTs.

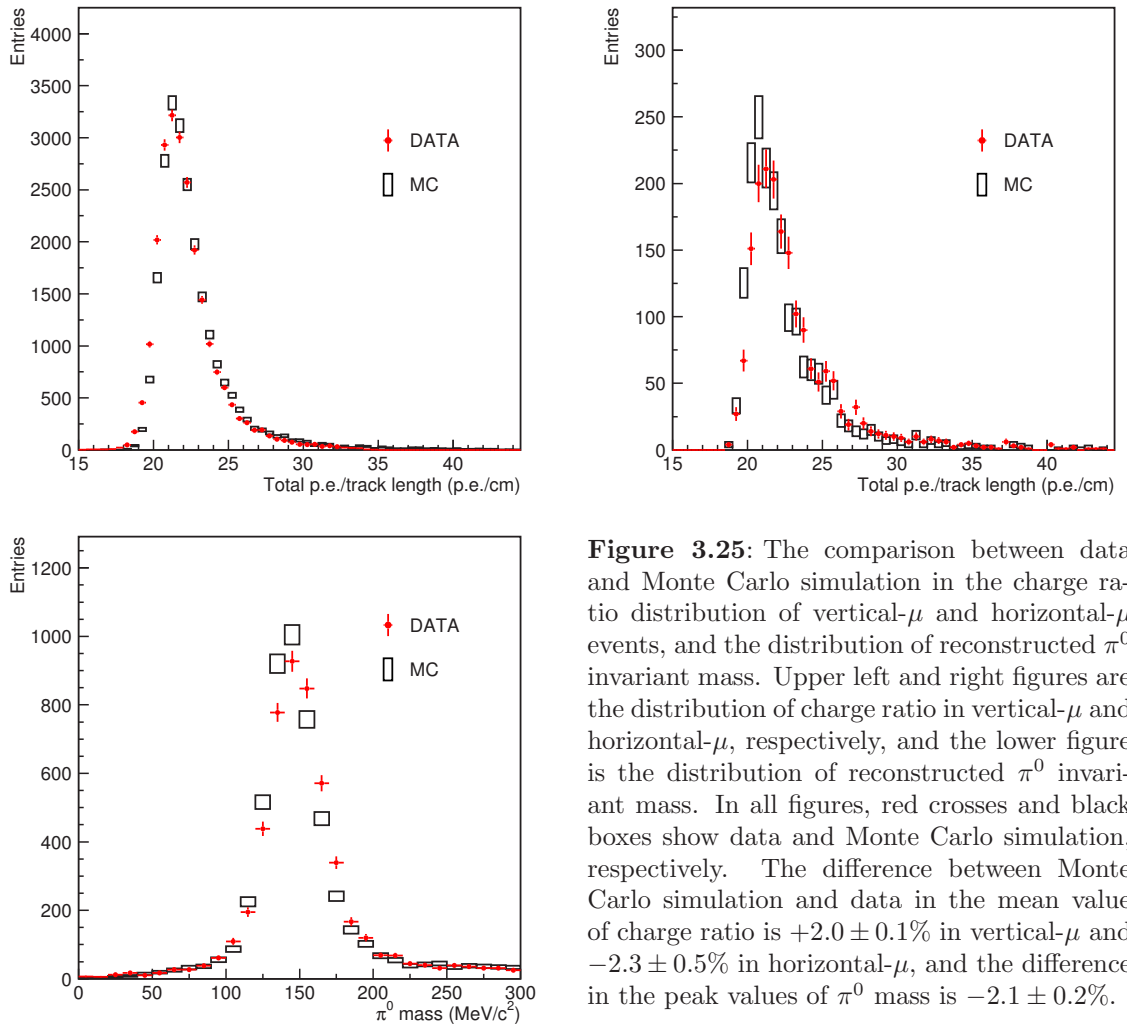


**Figure 3.25:** The comparison between data and Monte Carlo simulation in the charge ratio distribution of vertical- $\mu$  and horizontal- $\mu$  events, and the distribution of reconstructed  $\pi^0$  invariant mass. Upper left and right figures are the distribution of charge ratio in vertical- $\mu$  and horizontal- $\mu$ , respectively, and the lower figure is the distribution of reconstructed  $\pi^0$  invariant mass. In all figures, red crosses and black boxes show data and Monte Carlo simulation, respectively. The difference between Monte Carlo simulation and data in the mean value of charge ratio is  $+2.0 \pm 0.1\%$  in vertical- $\mu$  and  $-2.3 \pm 0.5\%$  in horizontal- $\mu$ , and the difference in the peak values of  $\pi^0$  mass is  $-2.1 \pm 0.2\%$ .

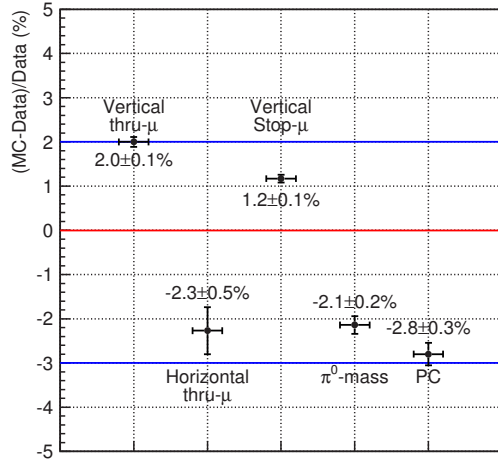


**Figure 3.26:** The summary of various measurements on the energy scale in 1KT. All the results settled to be within  $^{+2}_{-3}\%$  difference. This is quoted as the systematic error on the measurements of particle momentum in 1KT.

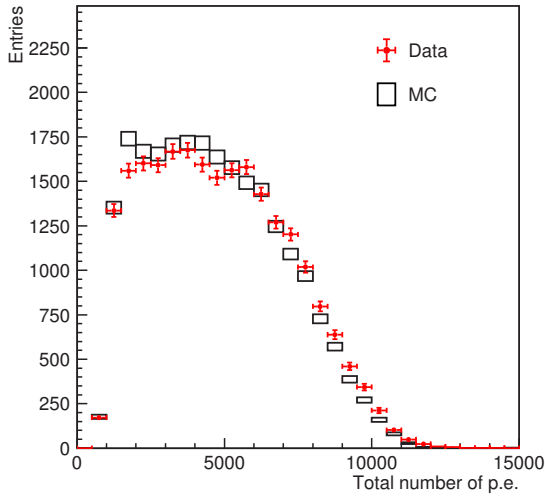


**Figure 3.27:** The distribution of the total number of photoelectrons for single ring  $\mu$ -like events with the particle fully contained in the inner detector of 1KT. Red circles are for data and black boxes are for a Monte Carlo simulation. They reasonably agree, showing the energy scale of 1KT is well calibrated.

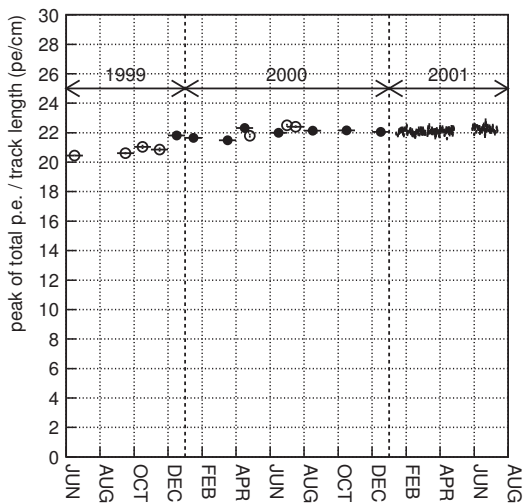


**Figure 3.28:** Stability of the energy scale in 1KT during K2K-I period. The charge ratio for vertical- $\mu$  events is plotted. Closed (open) circles show the data taken with (without) the buffer-amplifiers on the input of ATM. Since Jan. 2001, cosmic ray data have been taken between beam spills during neutrino beam is on, which are drawn by crosses.



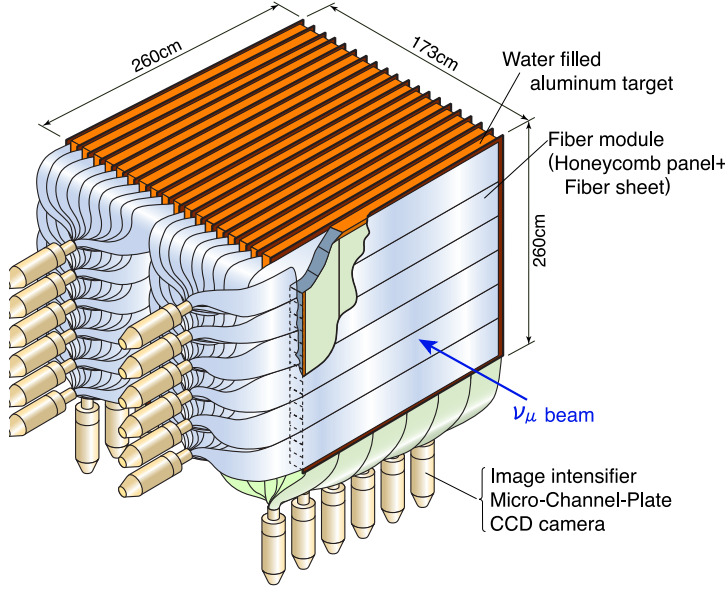


**Figure 3.29:** A schematic view of SciFi detector. It consists of 20 sets of X- and Y- scintillating fiber sheets, 19 water-filled aluminum layers, and 24 image intensifier tubes (IITs).

SciFi. A PMT is attached to each end of a scintillator to read out the scintillation light. The downstream TGC is used as trigger for SciFi and MRD. It consists of 40 scintillators. The dimensions of each scintillator are 466 cm in length, 10 cm in width, and 4 cm in thickness, covering the same area as upstream TGC. PMTs are attached to both ends of a scintillator.

The signals from PMTs are fed to TMCs (Time Mean Cell) and ADCs, where the information on event timing and deposit energy are recorded. Using the relative timing of two PMTs on both ends of a scintillator, the horizontal hit position can be measured with the resolution of better than 5 cm. The energy resolution for minimum ionizing particles (MIP) is measured using cosmic-ray data to be 7.4%.

### 3.5.3 Scintillating fiber tracker

Scintillating fiber tracker [45] with water target tanks (SciFi) is located downstream of the 1KT tank, between the upstream and downstream TGC. The upstream surface of SciFi is at 300 m downstream of the production target.

Fig. 3.29 shows a schematic view of SciFi detector. It consists of 20 tracking layers of 240 cm wide, 19 aluminum tube layers filled with water, and 24 image intensifier tubes (IITs) with CCD cameras (IIT-CCD). Each tracking layer is made of two scintillating fiber sheets, one is in vertical direction (X-layer) and the other is in horizontal direction (Y-layer). The gaps between tracking layers are 9 cm, where water-filled tanks are put. The thickness of the water-fill tanks is 6 cm with aluminum wall of 0.18 cm thick. The water inside the tanks is designed to be the target of neutrino interactions, which is the same as SK and hence the systematic uncertainty on the neutrino cross-section can be reduced. The total target mass is 6.0 tons of water and 1.4 tons of aluminum structures.

When the charged particle passes through the tracking layer, the scintillation light is emitted inside the scintillating fibers, and it is transmitted along the fibers to their edge. Then the light is read out by IIT-CCDs. By analyzing the images detected by CCDs, the hit fibers are identified as pixel clusters, and the tracks of particles are reconstructed by connecting these hits. The resolution of hit position is estimated to be 0.73 mm for muons with the energy of less than

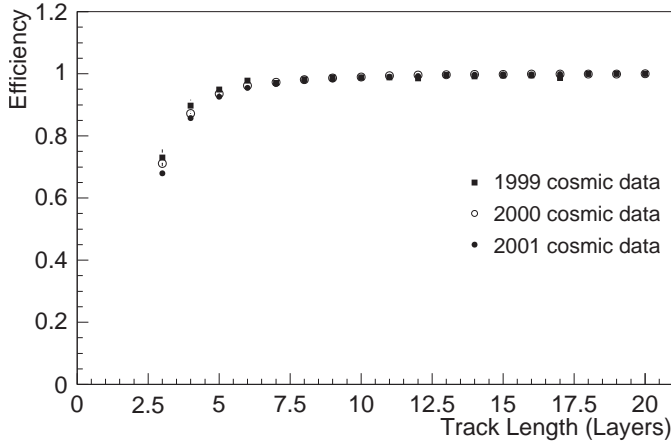


**Figure 3.30:** The track finding efficiency in SciFi as a function of the length of track. The horizontal axis is the number of SciFi layer tracks penetrate. Efficiency is  $\sim 70\%$  ( $\sim 87\%$ ) in the track length of 3 (4) SciFi layers, and approaches 100% in longer tracks. These values are estimated using cosmic-ray data.

1 GeV and 0.61 mm for muons with the energy of greater than 1 GeV [46]. Since SciFi does not have good timing information due to slow light emission of fluorescence sheet in IIT, events in which charged particle penetrates into TGC downstream of SciFi are used in the analysis. Using the timing information of TGC, events in beam spill are selected.

The noise hits in SciFi had been measured using cosmic-ray and random trigger data. These hits are reproduced by Monte Carlo simulation. The average number of noise hits per event due to noise of IIT-CCD is estimated to be 52, and 17 hits per event due to the beam associated backgrounds, which is quite low considering the total number of fibers (274,080) [46].

The hit finding efficiency is estimated to be about 95% for all IIT-CCDs, and it has been stable through the whole run periods within 2% fluctuation [46]. Tracks with more than 3 hit layers are reconstructed in our algorithm. The efficiency to find a track is estimated using cosmic-ray data to be  $\sim 70\%$  in tracks with the length of 3 layers,  $\sim 87\%$  in tracks with the length of 4 layers, and it approaches 100% in longer tracks [46], as shown in Fig. 3.30.

More detailed descriptions on SciFi can be found in [45, 46, 47].

### 3.5.4 Lead glass Cherenkov calorimeter

Lead glass Cherenkov calorimeter (LG) is located downstream of the SciFi detector in order to distinguish electrons from muons for the measurement of the contamination of electron neutrinos in the beam. Fig. 3.31 shows schematic views of a cell and a module of LG. LG consists of 10 modules, and each module consists of 60 LG cells arranged in  $12 \times 6$ . The dimensions of a LG cell are about  $10 \text{ cm} \times 10 \text{ cm} \times 34 \text{ cm}$ . A 5-inch PMT, R1652 made by Hamamatsu Photonics Corporation, is attached to each LG cell to read out the Cherenkov light which is emitted by charged particles passing through the LG cell. LG was once used in the TOPAZ experiment [48], and we re-use it in the K2K experiment.

Information of each cell on hit timing and light yield is recorded by TMC and ADC. ADC information is used to cluster hits and to match the SciFi track with LG cluster.

The energy deposit of MIP in LG is estimated to be 280 MeV when a particle penetrates perpendicular to LG module, i.e. the path length of 34 cm in LG.

Further information on the performance of LG can be found in [49].

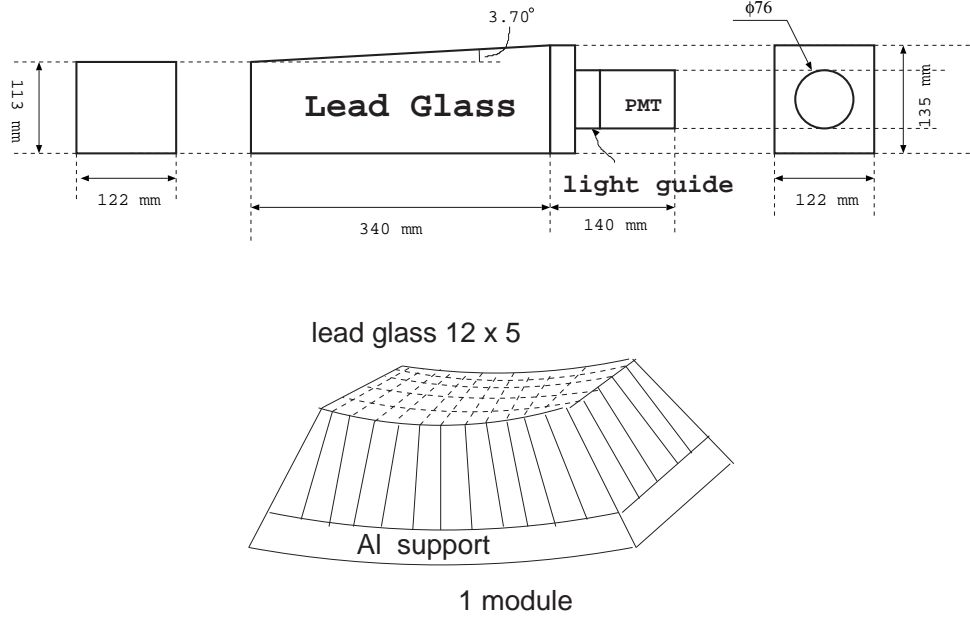


**Figure 3.31:** Schematic views of a cell (upper) and a module (lower) of lead glass Cherenkov calorimeter. One module consists of 60 cell arranged in  $12 \times 5$ .

### 3.5.5 Muon range detector

The muon range detector (MRD) [50] is a range type calorimeter located at the most downstream of ND. The purpose of MRD is to measure periodically the intensity, profile, and energy spectrum of the neutrino beam. It is also used to measure the energy of neutrino induced muons which interactions take place inside SciFi.

Fig. 3.32 shows a schematic view of MRD. It consists of 12 iron absorbers sandwiched with 13 sets of vertically and horizontally aligned drift chambers. The size of each layer is about  $7.6 \text{ m} \times 7.6 \text{ m}$  in area. The most upstream 4 iron plates are of thickness of 10 cm in order to obtained a good energy resolution. The remaining plates are of thickness of 20 cm. The total thickness of iron absorbers is 200 cm which covers the energy of muons up to  $2.8 \text{ GeV}/c$ . Total mass of iron plates is 864 tons which can induce statistically enough neutrino interactions to monitor the stabilities of the intensity and profile of the neutrino beam by each week and the energy spectrum of neutrino beam by each month.

The drift chambers in use are once used in the VENUS detector [51, 52] at TRISTAN. There are 829 modules. Each module has 8 drift tubes of  $5 \text{ cm} \times 7 \text{ cm}$  in cross section and 7.6 m in length. Each drift tube has a tungsten wire of  $70 \mu\text{m}$  in diameter. Twenty-five modules are arranged to make up one layer of drift tubes. The layer covers an area of  $7.6 \text{ m} \times 7.6 \text{ m}$  to be sensitive. There are 6,632 drift tubes in total. Each drift tube is filled with P10 gas which is the mixture of 90% argon and 10% methane. Negative high voltage of 2.7 kV is supplied to each wire in MRD operation.

The timing of each hit wire with respect to the beam spill timing is recorded by 6-bit single-hit TDC with 20 MHz clock. The hit efficiency and the tracking efficiency are estimated using cosmic-ray data. The hit efficiency becomes plateau to be about 97% around 2.5 kV supplied high voltage [50]. The tracking efficiency is about 65% for the tracks with one traversed iron plate and about 95% for the tracks with two traversed plates, and it goes up to 97.5% for much

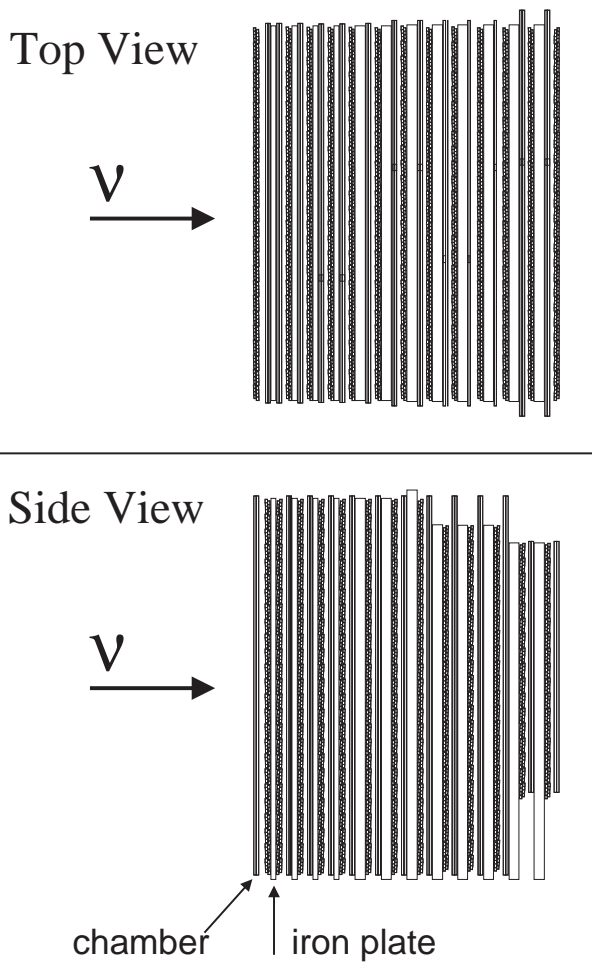


**Figure 3.32:** A schematic view of the muon range detector (MRD). MRD consists of 12 iron absorbers sandwiched with 13 sets of vertical and horizontal drift chambers. The size of each layer is  $7.6 \text{ m} \times 7.6 \text{ m}$  in area. First 4 iron plates are of thickness of 10 cm, and the rests are 20 cm.

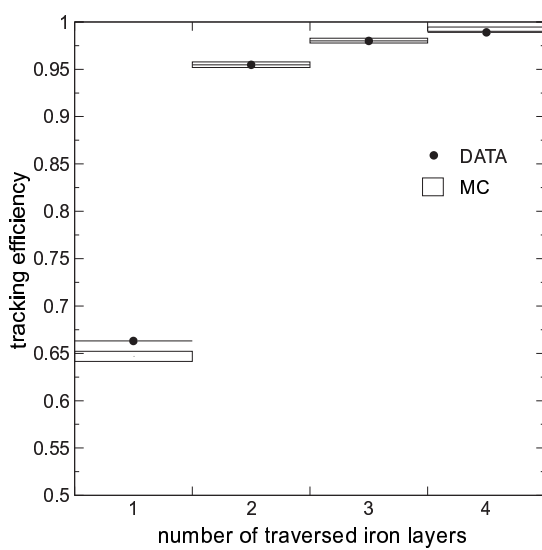


**Figure 3.33:** The tracking efficiency as a function of the track length in MRD. For the tracks with one (two) traversed iron plate, the tracking efficiency is about 65% (95%). It goes up to 97.5% for much longer tracks.

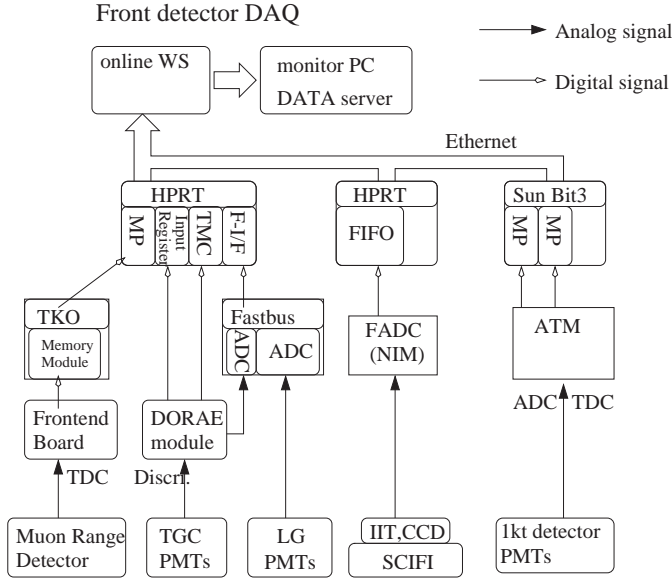


**Figure 3.34:** A schematic diagram of the data acquisition system in ND. Three on-board computers are devoted to collect data in ND. One is SUN Bit3 which is dedicated to 1KT, and the others are to FGD. Another online computer, “event builder”, collect data from each detector, sort it using the beam spill number, and build up a spill data.

longer tracks [50], as shown in Fig. 3.33.

The number of noisy channels in MRD are monitored during the data taking. It is typically about 40–50 channels out of 6,632 channels, which is small enough not to affect the tracking performance.

The more detailed descriptions on MRD can be found in [50, 53].

### 3.5.6 Data acquisition system in ND

The data of each detector in ND is taken spill by spill, which is triggered by the beam timing signal distributed by the accelerator 120  $\mu\text{sec}$  before each beam spill.

Fig. 3.34 shows a schematic diagram of the data acquisition system in ND. The DAQ system in ND has 3 front end computers. A SUN Bit3 computer collects 1KT data from ATM, TRG, FADC, and TMC modules. Two on-board computers, HP-RT, collect FGD data, one is dedicated to the data acquisition in SciFi, and the other is for MRD, LG, and TGC. These computers send the data to another online computer called as “event builder”. The event builder sorts the data from each detector using the beam spill number, and build up “one spill data”. The data size of ND is about 1 MB per spill.

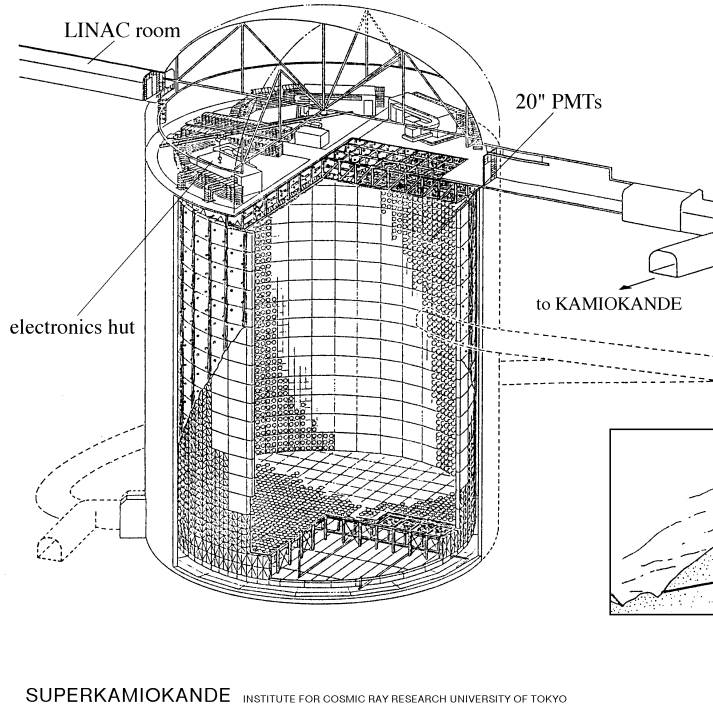


**Figure 3.35:** A schematic view of Super-Kamiokande detector. SK is located 1,000m underground in the Kamioka mine, just below Mt. Ikenoyama. The tank of SK is cylindrical in shape, and its size is 41.4 m in height and 39.3 m in diameter. The tank is optically separated into inner and outer region. The size of inner region is 36.2 m in height and 33.8 m in diameter, and the thickness of outer region is about 2 m. On the wall of inner tank, 11,146 20-inch PMTs are installed, while 1,885 8-inch PMTs are installed on the wall of outer tank.

### 3.6 Far neutrino detector

Super-Kamiokande detector (SK), a cylindrical 50 kt ring image water Cherenkov detector, is employed as the far detector of the K2K experiment. Fig. 3.35 shows a schematic view of SK site. It is located in the Kamioka Observatory of Institute for Cosmic Ray Research, the University of Tokyo, in the Kamioka mine in Gifu. It is 250 km far from KEK, and at 1,000 m underground (2,700 m water-equivalent) just below the peak of Mt. Ikenoyama, which shields cosmic-rays and the intensity of cosmic-ray muons is about  $1/100,000$  of that on the ground. The Super-Kamiokande experiment started its data taking on April 1, 1996 for various physics motivations, such as nucleon decay search, observation of atmospheric neutrinos, solar neutrinos, and Supernova neutrinos.

Since there exist a number of documents on the Super-Kamiokande detector [54, 55, 56, 57], only brief descriptions about the detector, the data acquisition system, and the detector calibrations are provided here.

### 3.6.1 Detector structure

The detector is quite similar to 1KT, except for its size; a cylindrical tank with the dimensions of 41.4 m in height and 39.3 m in diameter. It is filled with 50 kt water. The tank is optically separated into two concentric cylindrical regions by PMT support structure and opaque sheets.

The size of inner region is 36.2 m in height and 33.8 m in diameter containing 32 kt water. This part of detector is referred as the inner detector (ID). On the wall of ID, 11,146 20-inch PMTs, R3600 made by Hamamatsu Photonics Corporation, are attached to the support frame with inward-facing. PMTs are uniformly distributed with 70 cm intervals between PMTs. The photocathode coverage of ID is about 40%. The rest of the surface of the ID wall is covered with black polyethylene telephthalate sheets.

The outer region completely surrounds the ID with the thickness of 2.05 m on the top and bottom and 2.2 m along the barrel wall. This part is referred as outer detector (OD). To the outer side of the support structure, 1,885 8-inch PMTs, R1408, are attached in order to veto the incoming particles. The wall of OD is covered with reflective Tyvec sheets to maximize the detection efficiency.

### 3.6.2 Water purification system and water transparency

The water for SK is provided from the abundant spring water in the Kamioka mine. Dust and radioactive materials in the water make water transparency worse and become sources of background events. In order to reduce them, ultra-pure water is filled in the tank by employing a water purification system. The water system in SK is almost the same as that in 1KT: The bacteria is killed by UV sterilizer, dusts of the size of down to 10 nm are filtered out, and the temperature of the water is kept to be around 13°C to suppress the growth of bacteria. One difference from the system in 1KT is that the vacuum degasifier is employed to remove the dissolved gases in the water, such as oxygen and radon; oxygen makes the water transparency worse, which becomes a problem in a large detector, and radon can become a source of background events in the observation of low energy neutrinos such as solar neutrinos. Furthermore, radon-free air is supplied to the SK site in order to prevent radon dissolving into the water.

The water quality is measured and monitored by two methods; one is a direct measurement of an attenuation length using a light source and photo-detector, and the other is a measurement using cosmic-ray muons.

The dye laser light with several wavelength is led into the tank via a optical fiber and diffused by a diffuser ball which is put on an end of the fiber. The light from the diffuser ball is detected by a CCD camera which is set at the top of the tank. The light intensity is measured with the diffuser ball set at several water depth, and then the attenuation length of the water is directly obtained, which gives an attenuation length of about 98 m [54].

The water transparency is also measured using the Cherenkov light of cosmic-ray muons. The track of muon is reconstructed by connecting the entrance and the exit point, and then the path length of the Cherenkov light from the muon track to each PMT can be calculated. By looking at the dependence of the Cherenkov light intensity on the path length of light, an attenuation length is obtained. This measurement gives the attenuation length of about 95 m [54], which is consistent with the results mentioned above.

The light scattering parameters, such as coefficients of Rayleigh scattering, Mie scattering and absorption, are also measured in SK by injecting well-directional light into the water [54].

All the water parameters are put into our detector simulation.



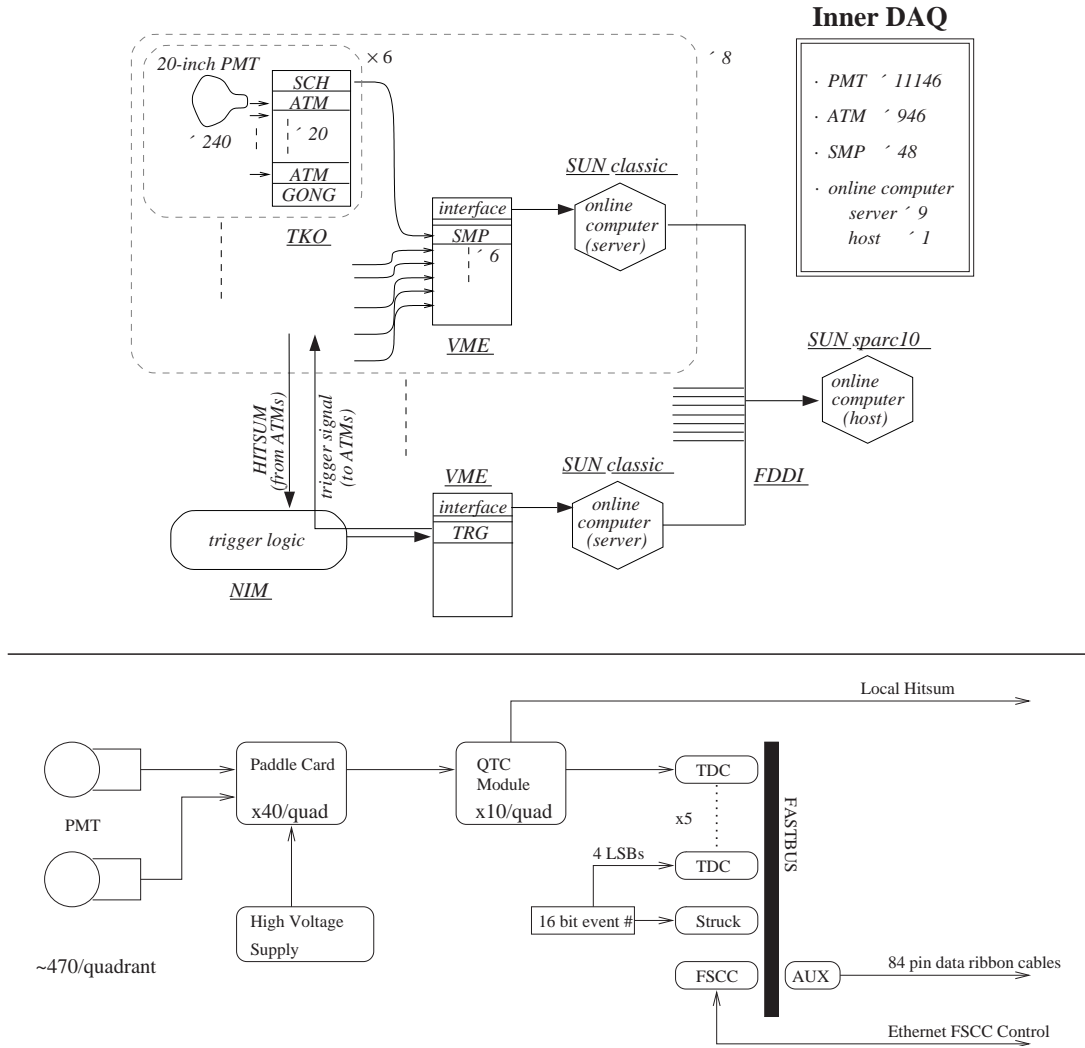


**Figure 3.36:** Schematic diagrams of the data acquisition system for the inner (upper) and outer (lower) detectors in SK.

### 3.6.3 Data acquisition system in SK

#### Electronics for inner detector

The data acquisition system for ID in SK is almost the same as that in 1KT described in Sec. 3.5.1. The upper figure in Fig. 3.36 shows a schematic diagram of the data acquisition system for ID in SK. Four electronics huts are located on the top of the SK tank, each of which collect data of 1/4 part of ID with 2 online computers. In order to receive, digitize, and record charge and timing information from ID-PMTs, 946 ATMs are used in total. The HITSUM signals from ATMs are summed up in each electronics hut and sent to the central hut which is also located on the top of the tank. In the central hut, HITSUM signals from 4 electronics huts are further summed up, and the global trigger decision is made using summed-up HITSUM. If the global trigger is generated, the data in ATMs are read out separately by 8 online computers through 48 SMP modules. Data collected by computers in each huts are transferred to the on-line



host computer via FDDI network and merged to make up a complete event.

### Electronics for outer detector

The lower figure in Fig. 3.36 shows a quadrant of OD electronics. Signals from OD-PMTs are sent via paddle cards to QTCs (charge-to-timing converter). The QTC makes rectangular pulse whose leading edge corresponds to the signal arrival timing and whose width is proportional to the input charge. QTC also makes HITSUM signal which is sent to the central hut to make a trigger decision. The pulses from QTCs are digitized by LeCroy 1877 multi-hit TDC modules in a FASTBUS crate. The dynamic range of TDC is set to be 16  $\mu$ sec with the minimum time unit of 0.5 nsec. The control and read-out of TDC modules are performed by FASTBUS smart crate controller (FSCC) and stored data are sent to the online computers through a VME bus. In addition to the OD-PMT information, GPS timestamps are also taken by a VME module of the OD electronics. The OD data collected by each online computer are also sent to the online host computer to be merged with each other.

### Trigger decision

The global trigger decision is made in the central hut using the pulse height of ID and OD HITSUM signals which are sent from 4 electronics huts. SK has 4 types of trigger; high energy (HE), low energy (LE), super low energy (SLE), and OD trigger, among which first three triggers are of ID.

The HE trigger is used mainly to record atmospheric neutrino events, proton decay candidates, cosmic-ray muons, and K2K-beam neutrino events. The threshold for ID HITSUM is set to be 340 mV which is corresponding to 31 hits in 200 nsec time window. Its trigger rate is about 5 Hz.

The LE trigger is used for solar neutrino events with the energy of greater than 5–6 MeV. The threshold of HITSUM is 320 mV corresponding to 29 hits in 200 nsec time window. The trigger rate for LE events is typically about 11 Hz.

The SLE trigger have been used since May 1997, in order to lower the analysis threshold of solar neutrino to be about 4.6 MeV.

The LE and SLE triggers are not used at all for K2K analysis.

The OD trigger is used to reject cosmic-ray muon events. The threshold is set to be about 19 OD-PMT hits in 200 nsec time window.

If the global trigger is generated, the trigger signal is distributed to all electronics hut to record the data into online computers. The VME-TRG module records the trigger type of each event. The GPS time stamp is also acquired when the trigger type of the event is HE or OD.

### 3.6.4 ATM, PMT gain, and timing calibrations

Several calibrations had been done to obtain better PMT information. The way of each calibration is very similar to that done in 1KT described in Sec. 3.5.1.

The linearity of responses of all ATM channels had been measured in the same method as 1KT described in Sec. 3.5.1. PMT hit timing versus signal pulse height correlation, so-called “T-Q map”, is also measured using laser system. It is also quite the same as 1KT case described in Sec. 3.5.1. These results are used to correct the charge and timing information.

The relative PMT gain is measured by Xenon system. Using its results, the high voltage values supplied to PMTs are determined so that all the PMTs give a common gain. After the

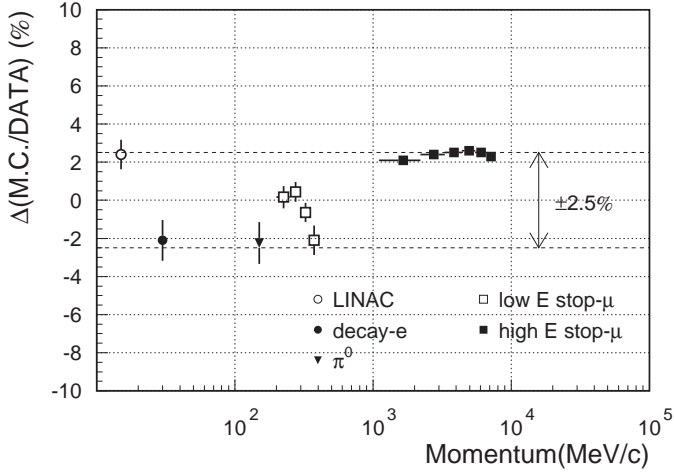


**Figure 3.37:** The results of the measurements of absolute energy scale with several calibration sources in SK. The correspondence of each point to the calibration source is as shown in the figure. Through the entire range of momentum from 16 MeV/ $c$  to 10 GeV/ $c$ , the data and our Monte Carlo simulation are in agreement at 2.5% accuracy.

adjustment of supplied high voltage, the spread of relative gain among PMTs is about 7% [54]. The remaining gain differences are corrected by software.

The absolute gain scale of PMTs had been determined by using the charge distribution of the single photoelectron signal, which is obtained by the low energy gamma emission from the thermal neutron capture on nickel, where  $^{252}\text{Cf}$  is used as a neutron source. A cylindrical polyethylene vessel, which contains Ni wires together with  $^{252}\text{Cf}$  and water, was set at the center of the tank. The neutrons emitted by  $^{252}\text{Cf}$  are thermalized in the water and captured by Ni wires. Then the gamma-rays of the energy of 6–9 MeV are emitted by the nuclear reaction of the capture. The gamma-rays are converted to electron via Compton or photo-electron scattering, and the Cherenkov light is emitted. In these low energy events, the number of photoelectrons detected in a PMT is at most one, and hence a single photoelectron distribution can be obtained by collecting these events. From this calibration, single photoelectron signal is determined to correspond to 2.055 pC [55, 56, 57].

### 3.6.5 Calibration of the absolute energy scale

The determination of absolute energy scale had been done by using four calibration sources; an electron linear accelerator (LINAC), decay electrons from stopping cosmic-ray muons, the invariant mass of  $\pi^0$  induced by neutrino interactions, and cosmic-ray muons stopping inside the tank.

LINAC is used to understand the performance of the detector in the low energy region. Electrons of the energy of 16 MeV accelerated by LINAC are injected into the water, and the reconstructed momentum was compared with a Monte Carlo simulation.

For the energy region of a few tens MeV, electrons emitted by muon decay are in use. The mean value of the energy spectrum of the decay electrons is compared with that of MC.

Neutrino induced  $\pi^0$  invariant mass is also used to understand the absolute energy scale around 100 MeV. It is the same as 1KT case described in Sec. 3.5.1.

The relation between the Cherenkov angle and the momentum of stopping muons with the momentum of  $\lesssim 350$  MeV/ $c$  is used to check the energy scale. For high energy stopping muons, the relation between the track length and the momentum is used. In this sample, muons with the track length of greater than 7 m are selected, corresponding to the energy of greater than about 1.7 GeV. These data are also compared with MC.

Fig. 3.37 shows the summary of the absolute energy scale calibrations. As shown in the

figure, the momentum range from 16 MeV/ $c$  to 10 GeV/ $c$  is examined, and data agree with our Monte Carlo simulation within 2.5% precision throughout the entire momentum range. From these results, we have quoted the uncertainty of the absolute energy scale in SK to be 3%.

### 3.7 Global positioning system for the time synchronization

As previously mentioned, the time synchronization between KEK and SK sites is essential to distinguish the beam neutrino events from atmospheric neutrino background. The global positioning system (GPS) is employed for the time synchronization.

#### 3.7.1 Overview of GPS

GPS is a satellite navigation system founded and controlled by the U.S. Department of Defense (DOD). There are 27 satellites in six orbital planes. Each satellite has an atomic clock, which refers to the master clock at the U.S. Naval Observatory (USNO) and steered to Universal Time Coordinate (UTC). These satellites send their time and position by radio wave. Receiving the information from 4 satellites at the same time, a GPS receiver can calculate its precise position and time.

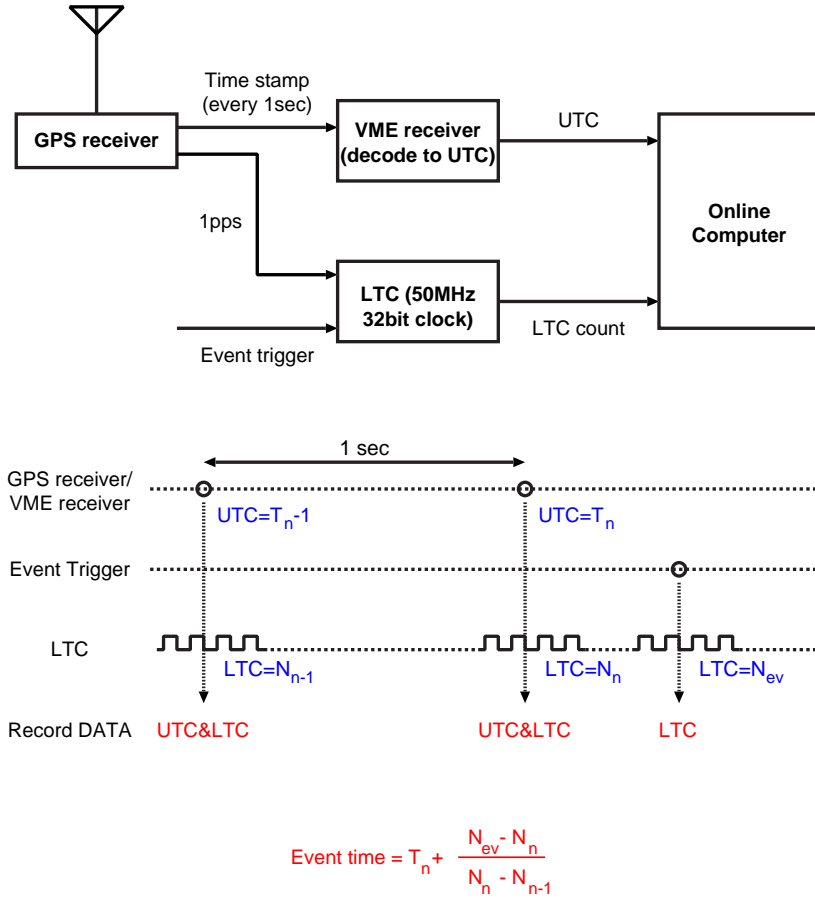
#### 3.7.2 Time synchronization between KEK and SK

Fig. 3.38 shows a schematic view of GPS system used in the K2K experiment. It consists of GPS receivers, a VME receiver, and a 50 MHz 32-bit local time clock (LTC). Two independent GPS receivers (GPS1 and GPS2) are used in parallel in both KEK and SK sites for the hardware backup as well as their quality check with each other. Identical sets of GPS system are set both at KEK and at SK sites. The GPS/VME receivers and LTC are located in the beam line control room and the GPS antennae are mounted on the roof of the room in the KEK site. On the other hand, in SK site, the GPS receivers and their antennae are located at a house outside the Kamioka mine near its entrance, and the VME receiver and LTC are set in the central hut on the top of the SK tank in the mine. The GPS signal is sent to the central hut via a optical fiber through the distance of 1.7 km.

The GPS receiver provides UTC time stamps every 1 sec and 1 Hz square pulses which leading edges are synchronized to UTC. Its accuracy is better than 40 nsec in average and 150 nsec at the worst. UTC time stamp of GPS receiver is sent to and decoded by the VME receiver. LTC is a free-running 50 MHz 32-bit clock counter. It has two input channels. The 1 Hz pulse from the GPS receiver is fed to one of LTC inputs. To another input channel of LTC, beam spill trigger is fed in the KEK site and logical OR of the HE trigger and OD trigger is fed in the SK site. The UTC time stamp and the current count of LTC are recorded when LTC receives the GPS 1 Hz pulse ("GPS-data"), while only the current count of LTC is recorded when it receives an event trigger signal ("event-data"). UTC time stamp and LTC counts are read by online computer.

The principle to determine the event triggered time is also shown in Fig. 3.38. The event triggered time is calculated as followings: When event is triggered, the LTC count at the event trigger  $N_{ev}$  is recorded as an event-data. By looking at the latest two GPS-data, two sets of UTC time stamp and LTC count can be known, i.e.  $(T_{n-1}, N_{n-1})$  and  $(T_n, N_n)$ . The time of the event trigger  $T_{ev}$  is obtained by the linear interpolation;

$$T_{ev} = T_n + \frac{N_{ev} - N_n}{N_n - N_{n-1}} \cdot (T_n - T_{n-1}) \quad (3.6)$$



**Figure 3.38:** A schematic view of GPS system in the K2K experiment. It consists of GPS receiver, VME receiver, and 50 MHz 32-bit LTC clock. The identical systems are set at KEK and SK.

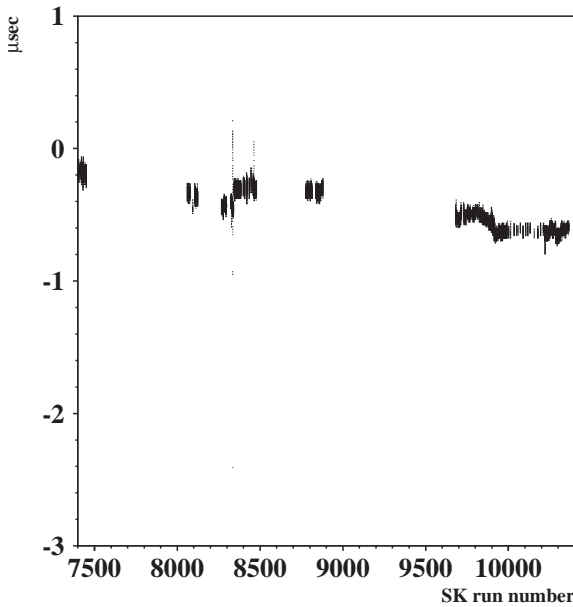


**Figure 3.39:** The stability of LTC in SK site. The vertical axis is the difference of the LTC count for 1 sec interval from the nominal one (50 MHz) expressed in the unit of  $\mu\text{sec}$ . Horizontal axis is the run number of Super-Kamiokande, which range is corresponding to the whole run period, i.e. from June 1999 to July 2001.

The synchronization of GPS receivers at KEK and SK had been taken using an atomic clock before the experiments started. The difference of these two GPS times with respect to the atomic clock was measured to be  $115 \pm 142(\text{syst.})$  nsec [58]. The absolute time synchronization had been done with this accuracy.

### 3.7.3 Stability of GPS system

Two independent GPS were compared as a check of the system, resulting in the agreement with each other within 100 nsec (HWHM) [59]. The stability of the system is continuously monitored in SK site by looking at LTC count in 1 sec,  $N_n - N_{n-1}$ . Fig. 3.39 shows the stability of the LTC frequency during the whole run period, i.e. from June 1999 to July 2001. The vertical axis shows the difference of  $N_n - N_{n-1}$  from the nominal one (50 MHz). In our calculation of the event time, as long as the LTC frequency does not vary abruptly, slow drift of the LTC frequency is not problem since we use LTC count of just 1 sec before. It is stable within 200 nsec throughout the whole run period although there happened jumps several times.



# Chapter 4

## Monte Carlo Simulations

In order to study our detection schemes and various systematics, Monte Carlo simulations are used. Our Monte Carlo simulations consist of three modules; a simulation for the neutrino beam “Beam-MC”, a simulation for neutrino interactions “Neut-MC”, and a simulation for detectors “DetSim”. In this chapter, information on these simulation tools is provided in this order in each section.

### 4.1 Neutrino beam simulation: Beam-MC

A neutrino beam simulation, Beam-MC, simulates properties of our neutrino beam. It starts from the proton injection onto the production target, produces secondaries, then focuses them in the horn magnets, and track them until they decay into neutrinos. The tracks of neutrinos extrapolated to ND and SK, the fluxes and the energy spectrum at ND and SK are provided.

#### 4.1.1 Proton injection onto the production target

Protons with a kinetic energy of 12 GeV are injected onto the aluminum production target. The profile and divergence of the primary proton beam are the input parameters to the Beam-MC, which are measured using V39out- and TGT-SPICs.

Fig. 4.1 shows a schematic view of the measurements for the profile and the divergence of the proton beam. The distance between V39out- and TGT-SPICs ( $L$ ) is 128 cm and that between TGT-SPIC and the surface of the target ( $l$ ) is 37 cm. The  $x$  and  $y$  profiles of the beam at V39out-SPIC and TGT-SPIC are measured and fitted by Gaussian functions with the width of  $\sigma_{1x,1y}$  and  $\sigma_{2x,2y}$ , respectively. Then, they are extrapolated to the surface of the target to obtain the profile at the surface of the target;

$$\sigma_{x,y} = \sigma_{2x,2y} + (\sigma_{2x,2y} - \sigma_{1x,1y}) \cdot \frac{l}{L} \quad . \quad (4.1)$$

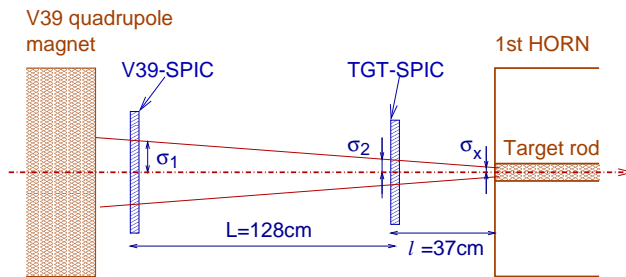


**Figure 4.1:** A schematic view of the measurements of the profile and the divergence of the primary proton beam. The distance between V39out-SPIC and TGT-SPIC is 128 cm and that between TGT-SPIC and the surface of the target is 37 cm.

**Table 4.1:** Summary of the beam parameters for the runs in K2K-Ia and K2K-Ib.

Parameters	K2K-Ia (in June 1999)	K2K-Ib (since Nov. 1999)
Target material	Al 6061-T	Al 6061-T
Rod diameter	2 cm	3 cm
Horn current	200 kA	250 kA
Beam spread in $x$ ( $\sigma_x$ )	1 mm	3.4 mm
Beam spread in $y$ ( $\sigma_y$ )	6 mm	7.2 mm
Beam divergence coefficient in $x$ ( $k_x$ )	-8 mrad/mm	-2.5 mrad/mm
Beam divergence coefficient in $y$ ( $k_y$ )	-0.4 mrad/mm	-0.14 mrad/mm

Assuming the linear correlation in  $(x, \theta_x)$  and  $(y, \theta_y)$  planes, the injection angle (or divergence) of proton  $(\theta_x, \theta_y)$  at the position of  $(x, y)$  is obtained;

$$\theta_x = k_x \cdot x \quad \text{and} \quad \theta_y = k_y \cdot y, \quad (4.2)$$

where  $k_{x,y}$  is the correlation coefficient determined by

$$k_{x,y} = \frac{\sigma_{2x,2y} - \sigma_{1x,1y}}{\sigma_{2x,2y} \cdot L + (\sigma_{2x,2y} - \sigma_{1x,1y}) \cdot l}. \quad (4.3)$$

For our standard Beam-MC, the center of the proton beam is set to be at the center of the target rod. Table 4.1 summarizes the parameters of the beam properties for the runs in June 1999 (K2K-Ia) and in the rest of the periods (K2K-Ib).

#### 4.1.2 Production of secondary particles in the target

There have been various pion production experiments in the energy region of the K2K experiment, whose results are inconsistent with each other. This causes one of the largest ambiguities in the Monte Carlo simulation. There are some models for the pion production, among which three kinds of models are used in our study.

1. *GALOR/FLUKA model;*

GALOR/FLUKA model [60, 61, 62] is a package of hadron simulation prepared for GEANT [63] detector description and simulation tool. This model has larger  $p$ -Al cross-section than other models.

2. *Fit to measurements (I), Sanford-Wang;*

This model is the result of the compilation of the measurements done by Lundy *et al.* at a proton momentum of 13.4 GeV/c [64], Dekkers *et al.* at 11.8, 18.8, and 23.1 GeV/c [65], and Baker *et al.* at 10.9, 20.9, and 30.9 GeV/c [66], fitted to an empirical formula of the differential cross-section for secondary particle production suggested by J. R. Sanford and C. L. Wang [67, 68]: Yamamoto's measurements [69] agrees well with the results of this compilation.

3. *Fit to measurements (II), Cho-ANL and Cho-CERN;*

These are other results of the compilations to fit several measurements to the Sanford-Wang formula. The measurements done by Marmer *et al.* at 12.3 GeV/c [70, 71], Cho *et al.* at 12.4 GeV/c [72], Asbury *et al.* at 12.5 GeV/c [73], and Allaby *et al.* at 19.2 GeV/c [74] are used in the Cho-ANL compilation [72]. There exists another result of compilation called Cho-CERN [75], which uses the data set of mainly from Cho *et al.* at 12.4 GeV/c. These two compilations give almost the same differential cross-sections.



**Table 4.2:** The fitted parameters of the Sanford-Wang formula for the positive pion production in Sanford-Wang [68], Cho-ANL [72], and Cho-CERN [75] compilations.

Compilations	$C_1$	$C_2$	$C_3$	$C_4$	$C_5$	$C_6$	$C_7$	$C_8$
Sanford-Wang	1.09	0.65	4.05	1.63	1.66	5.03	0.17	82.7
Cho-ANL	0.96	1.08	2.15	2.31	1.98	5.73	0.13	24.1
Cho-CERN	1.05	1.01	2.26	2.45	2.12	5.66	0.14	27.3

As mentioned above, the Sanford-Wang formula gives a quantitative description for the secondary particle production. It is an empirical formula based on experimental data as follows;

$$\frac{d^2n}{d\Omega dp} = C_1 p^{C_2} \left(1 - \frac{p}{p_B - 1}\right) \exp\left(-\frac{C_3 p^{C_4}}{p_B^{C_5}} - C_6 \theta (p - C_7 p_B \cos^{C_8} \theta)\right) \quad , \quad (4.4)$$

where  $d^2n/d\Omega dp$  is the differential particle yield per interacting proton,  $\theta$  is the angle between the secondary particle and the beam axis in the laboratory frame,  $p$  and  $p_B$  are the momentum of the secondary particle and the incident proton, respectively, and  $C_i$ 's are the constants to be found by fitting. The fitted results about the positive pion production for Sanford-Wang, Cho-ANL, and Cho-CERN compilations are summarized in Table 4.2. The resulting parameters of the negative pion production for the Sanford-Wang and the Cho-ANL compilations are listed in [72] as well as those of the positive pion production. The comparison of the experimental measurements with the fitting curve of Cho-CERN are shown in Fig. 4.2.

In the case of use of GCALEOR/FLUKA model, the GEANT automatically simulates everything using the GCALEOR/FLUKA package.

In use of other models, the hadron production is simulated according to the formula (4.4) only when enegetic protons with the energy of more than 10 GeV interact with the target aluminum, and other cases of interaction are simulated according to GCALEOR model. In our simulation, the negative pion production is simulated using the parameters of Sanford-Wang model even in the use of Cho-ANL or Cho-CERN models. For the kaon production parts, the formula (4.4) is used with the kaon parameters in reference [69] in all three models.

Since the momentum and anular distribution of the pions measured by PIMON favors the Cho-CERN model better than the others although the PIMON results are consistent with all the models within its errors, we have adopted it as the standard hadron production model in our simulation, while the others are used for comparison and the estimation of systematic uncertainties.

#### 4.1.3 Particle tracking through the horn magnets and decay volume

By using GEANT with GCALEOR hadron simulator, scattered protons and generated secondary particles are traced through 2 horn magnets and decay volume until they decay into neutrinos or absorbed in materials. As described in Sec. 3.1.2, the toroidal magnetic field given by Eq. (3.1) is made inside the horn magnets. The focusing effect of the magnetic field is also simulated by GEANT.

#### 4.1.4 Particle decays into neutrino

In the GEANT simulation, the flavor of neutrinos and their anti-particles are treated as identical particles. However, in our use, they have to be treated differently since we also want to know how

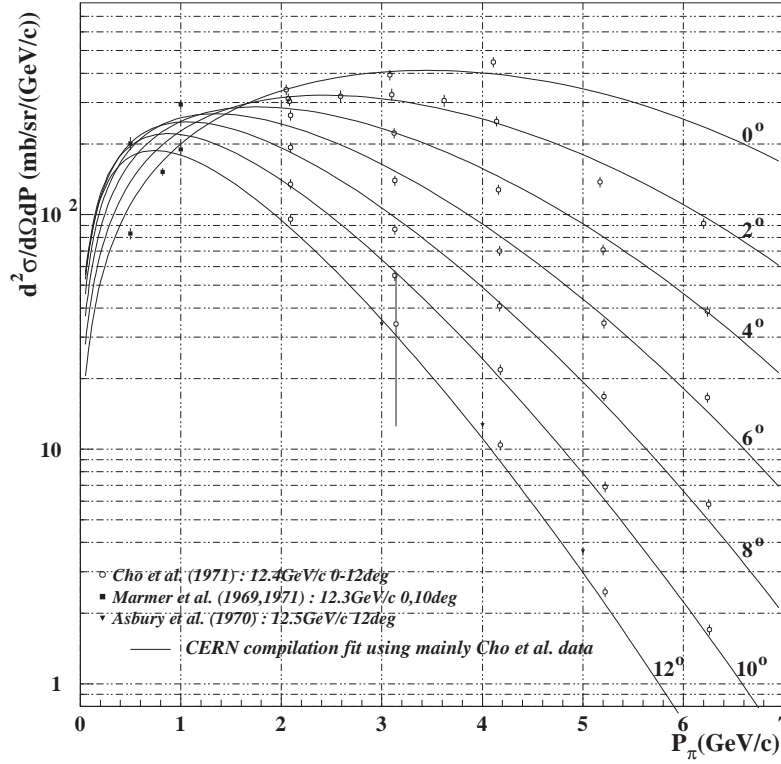


**Figure 4.2:** The differential cross-section of positive pion production in past experiments and fitted curves of Cho-CERN model. The correspondence of data points to measurements are shown in the figure. The solid lines are drawn according to the Sanford-Wang formula with Cho-CERN parameters.

much fraction of the beam is contaminated by neutrinos other than muon neutrino although we want to know the fluxes of muon neutrino at ND and SK. Therefore, the particle decays which emit neutrino, i.e. the decays of charged pions, charged and neutral kaons, and muons in our energy region, and the type of neutrino are treated properly by our self-made simulator.

### Decay of charged pions

Pion decays into muon and neutrino ( $\pi^+ \rightarrow \mu^+ \nu_\mu$ ,  $\pi^- \rightarrow \mu^- \bar{\nu}_\mu$ , called  $\pi_{\mu 2}^\pm$ ) with branching fraction of almost 100%, and hence only this mode is taken into account for the pion decay. Therefore, neutrino from pion decay is always treated as muon neutrino. Since pion is a pseudo-scalar particle, neutrino is emitted isotropically in the pion rest frame, and then it is boosted toward the flight direction of the parent pion to obtain the 4-momentum of neutrino.

### Decay of charged and neutral kaons

Since kaons are also pseudo-scalar particles, their decays are isotropic in the kaon rest frame. The decay modes listed in Table 4.3 are taken into account for the calculation of the neutrino fluxes in our Beam-MC. Other decays are ignored since their branching fractions are quite small. Neutrinos from  $K_S^0$  are also ignored for the same reason.

In  $K_{\mu 2}^\pm$  decays, which is just the two-body decay, the calculation method of neutrino energy

**Table 4.3:** The kaon decay modes taken into account for the contribution to neutrino beam in Beam-MC. In the  $K_L^0$  decays, the charge asymmetry is correctly considered to produce neutrinos or antineutrinos.

Kaon decay modes	Branching fraction	
$K^+ \rightarrow \mu^+ \nu_\mu, K^- \rightarrow \mu^- \bar{\nu}_\mu$	63.43%	(called $K_{\mu 2}^+$ )
$K^+ \rightarrow \pi^0 e^+ \nu_e, K^- \rightarrow \pi^0 e^- \bar{\nu}_e$	4.87%	(called $K_{e 3}^+$ )
$K^+ \rightarrow \pi^0 \mu^+ \nu_\mu, K^- \rightarrow \pi^0 \mu^- \bar{\nu}_\mu$	3.27%	(called $K_{\mu 3}^+$ )
$K_L^0 \rightarrow \pi^- e^+ \nu_e, \pi^+ e^- \bar{\nu}_e$	38.79%	(called $K_{e 3}^0$ )
$K_L^0 \rightarrow \pi^- \mu^+ \nu_\mu, \pi^+ \mu^- \bar{\nu}_\mu$	27.18%	(called $K_{\mu 3}^0$ )

and direction in the laboratory frame is quite the same as that in  $\pi_{\mu 2}^\pm$  decay.

In  $K_{\ell 3}$  decays, the Dalitz plot density  $\rho(E_\pi, E_\ell)$  of  $V-A$  theory [20, 76] is employed in order to obtain the neutrino energy in the kaon rest frame;

$$\rho(E_\pi, E_\ell) \propto f_+^2(t)[A + B\xi(t) + C\xi^2(t)] \quad , \quad (4.5)$$

where

$$\begin{aligned} t &= (P_K - P_\pi)^2, \quad f_\pm(t) = f_\pm(0)[1 + \lambda_\pm(t/m_\pi^2)], \quad \xi(t) = f_-(t)/f_+(t), \\ A &= m_K[2E_\ell(m_K - E_\pi - E_\ell) - m_K E'_\pi], \quad B = m_\ell^2 \left( E_\nu - \frac{1}{2} E'_\pi \right), \quad C = \frac{1}{4} m_\ell^2 E'_\pi, \\ E'_\pi &= E_\pi^{\max} - E_\pi = \frac{m_K^2 + m_\pi^2 - m_\ell^2}{2m_K} - E_\pi. \end{aligned}$$

Assuming time reversal invariance and also  $\lambda_- = 0$ , the  $K_{\ell 3}$  decay distribution is described by the two parameters,  $\lambda_+$  and  $\xi(0)$ . Referring to [20], the set of parameters  $(\lambda_+, \xi(0))$  is taken to be  $(0.028, -0.19)$  for the  $K^\pm$  decays and  $(0.030, -0.01)$  for the  $K_L^0$  decay in our MC.

The charge asymmetry,  $\delta_L(\ell) \equiv [\Gamma(\pi^- \ell^+ \nu_\ell) - \Gamma(\pi^+ \ell^- \bar{\nu}_\ell)] / [\Gamma(\pi^- \ell^+ \nu_\ell) + \Gamma(\pi^+ \ell^- \bar{\nu}_\ell)]$ , is also correctly taken into account in the decays of  $K_{\ell 3}^0$ . We set  $\delta_L(e) = 0.333$  and  $\delta_L(\mu) = 0.304$  for the  $K_{e 3}^0$  and  $K_{\mu 3}^0$  decays, respectively [20].

The neutrino direction is randomly made in the kaon rest frame, and then the 4-momentum of neutrino is boosted by Lorentz boost according to the 4-momentum of the parent kaon.

### Decay of muons

Muon decays via  $\mu^\pm \rightarrow e^\pm \nu_e(\bar{\nu}_e) \bar{\nu}_\mu(\nu_\mu)$ , called  $\mu_{e 3}^\pm$ , with the branching fraction of almost 100%. Polarization of muon is properly taken into account. The energy and angular distributions of the muon antineutrino and the electron neutrino emitted from a positive muon in the muon rest frame are, respectively, calculated by Michel spectra of  $V-A$  theory [76];

$$\frac{d^2 N_{\bar{\nu}_\mu}}{dx d\Omega_{\text{cm}}} \propto \frac{2x^2}{4\pi} [(3 - 2x) + (1 - 2x)P_\mu \cos \theta_{\text{cm}}] \quad , \quad (4.6)$$

$$\frac{d^2 N_{\nu_e}}{dx d\Omega_{\text{cm}}} \propto \frac{12x^2}{4\pi} (1 - x)(1 + P_\mu \cos \theta_{\text{cm}}) \quad , \quad (4.7)$$

where  $x \equiv 2E_\nu/m_\mu$ ,  $\theta_{\text{cm}}$  is the angle between the neutrino momentum vector and the muon spin direction, and  $P_\mu$  is the average muon polarization along the beam direction. Corresponding distributions for muon neutrino and electron antineutrino from negative muon decay are obtained by the replacement of  $P_\mu \rightarrow -P_\mu$ . Then, 4-momentum of each neutrino are boosted toward the muon direction by Lorentz transformation.

#### 4.1.5 Monte Carlo prediction of neutrino properties at ND and SK

Since the horn magnets focus positively charged particles and the hadrons produced in the target are mainly pions, the composition of the neutrino beam is dominated by muon neutrino. Fig. 4.3 shows the energy spectra of each type of neutrino at ND and SK estimated by Beam-MC. About 97.3% (97.9%) of neutrinos at ND (SK) are muon neutrinos decayed from positive pions, and small fraction of the beam is contaminated with neutrinos other than muon neutrino;  $\nu_e/\nu_\mu \sim 0.013$  (0.009),  $\bar{\nu}_\mu/\nu_\mu \sim 0.015$  (0.012), and  $\bar{\nu}_e/\nu_\mu \sim 1.8 \times 10^{-4}$  ( $2.2 \times 10^{-4}$ ) at ND (SK). Contributions of each decay mode to each type of neutrinos are shown in Fig. 4.4. Main contribution to the fluxes of  $\nu_\mu$ ,  $\nu_e$ ,  $\bar{\nu}_\mu$ , and  $\bar{\nu}_e$  are  $\pi_{\mu 2}^+$ ,  $\mu_{e 3}^+$ ,  $\pi_{\mu 2}^-/\mu_{e 3}^+$ , and  $K_{e 3}^0$ , respectively, while the higher energy part of  $\nu_\mu$  is dominated by  $K_{\mu 2}^+$  decay.

The difference of the energy spectra estimated using different hadron production models, GCALOR/FLUKA, Sanford-Wang, and Cho-CERN, are compared in Fig. 4.5. In this figure, the spectra of only muon neutrino are shown. In addition, the far-to-near spectrum ratio ( $F/N$  ratio) predicted by Monte Carlo simulations with these hadron production models is also compared in Fig. 4.5.

The behavior of  $F/N$  ratio as a function of the neutrino energy is qualitatively explained as follows. First, the acceptance of neutrinos for SK does not change so much as a function of neutrino energy because the decay volume seems to be point-like seen from SK. However, in ND, the acceptance of low energy neutrinos below about 1 GeV is smaller than that for high energy neutrinos and it strongly depends on the energy, since the low energy neutrinos, which come from the decay of low energy pions, are emitted mainly at upstream region of decay volume, and the flight length of pions before their decay becomes longer as pion energy becomes higher. This causes a rise of the acceptance for ND as neutrino energy goes up, resulting in the decrease of  $F/N$  ratio as neutrino energy increases in the low energy region. On the other hand, neutrinos with the energy of above 1 GeV come from the pion with the momentum of above 2 GeV/c, which decay point is almost uniformly distributed along the decay volume, and hence the acceptance does not change so much as a function of neutrino energy. However ND have larger solid angle than SK, and ND sees more off-axis neutrinos than SK. This makes the energy spectrum in ND softer than that in SK, making the increase of  $F/N$  ratio above 1 GeV as the neutrino energy goes up.

The difference of the energy spectra for the configurations in June 1999 (K2K-Ia) and after Nov. 1999 (K2K-Ib) are shown in Fig. 4.6. The mean energy of neutrino beam at SK is 1.24 GeV in K2K-Ia, while it is 1.30 GeV in K2K-Ib.

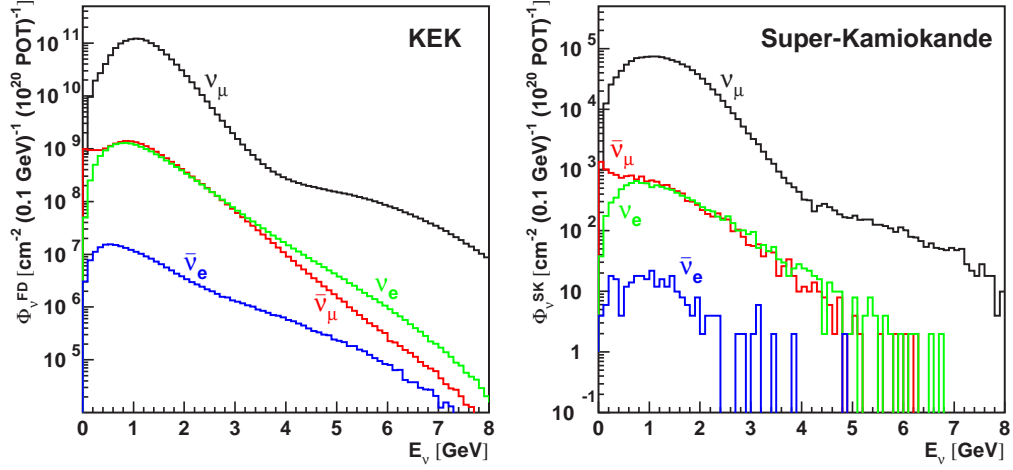


**Figure 4.3:** The energy spectrum for each type of neutrinos at ND (left) and SK (right) estimated by Beam-MC. The neutrino beam is 97.3% (97.9%) pure muon neutrino with the contaminations of  $\nu_e/\nu_\mu \sim 0.013$  (0.009),  $\bar{\nu}_\mu/\nu_\mu \sim 0.015$  (0.012), and  $\bar{\nu}_e/\nu_\mu \sim 1.8 \times 10^{-4}$  ( $2.2 \times 10^{-4}$ ) at ND (SK).

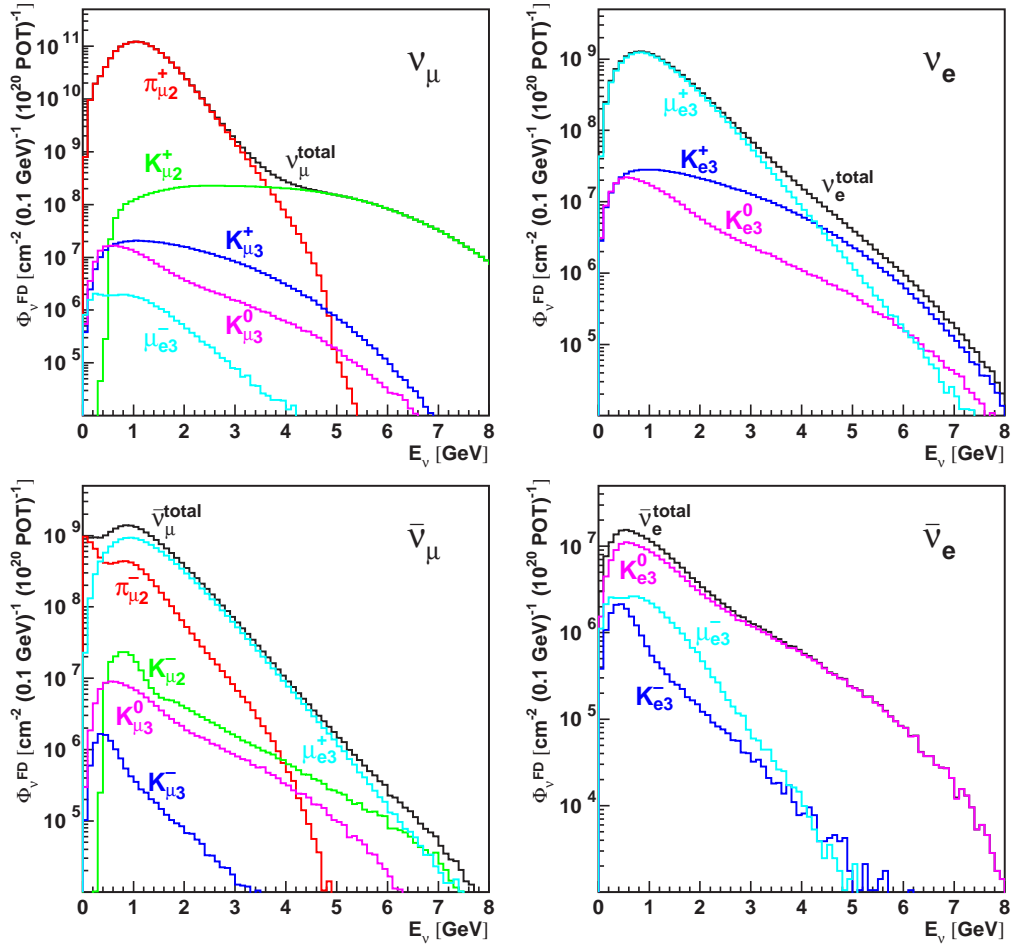


**Figure 4.4:** Contributions of each decay mode to each type of neutrino. Top-left, top-right, bottom-left, and bottom-right figures are for  $\nu_\mu$ ,  $\nu_e$ ,  $\bar{\nu}_\mu$ , and  $\bar{\nu}_e$ , respectively. The fluxes shown here are those estimated by Beam-MC at the position of ND (300 m downstream the production target).

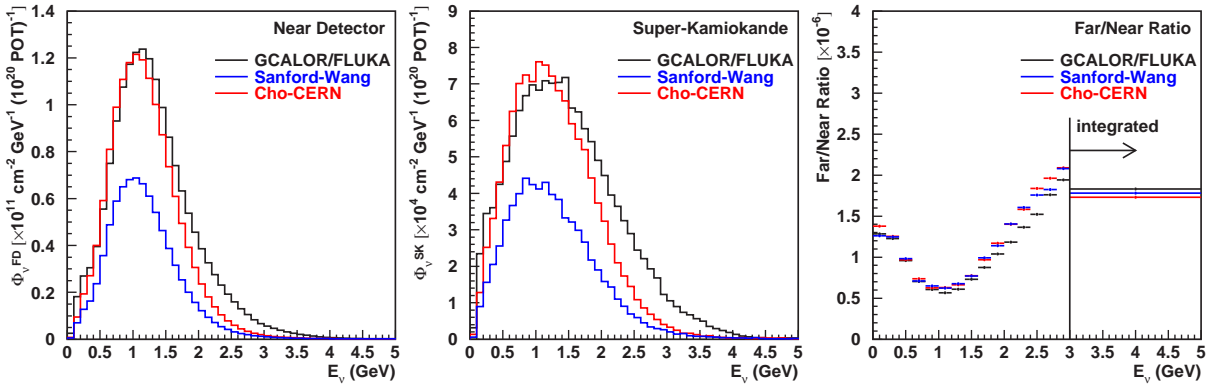


**Figure 4.5:** The energy spectra of muon neutrino at ND (most left) and SK (middle), and their ratio (most right) predicted by several hadron production models. The energy above 3 GeV is integrated in  $F/N$  ratio. In each figure, black, blue, and red histograms are corresponding to GCALOR/FLUKA, Sanford-Wang, and Cho-CERN models, respectively.

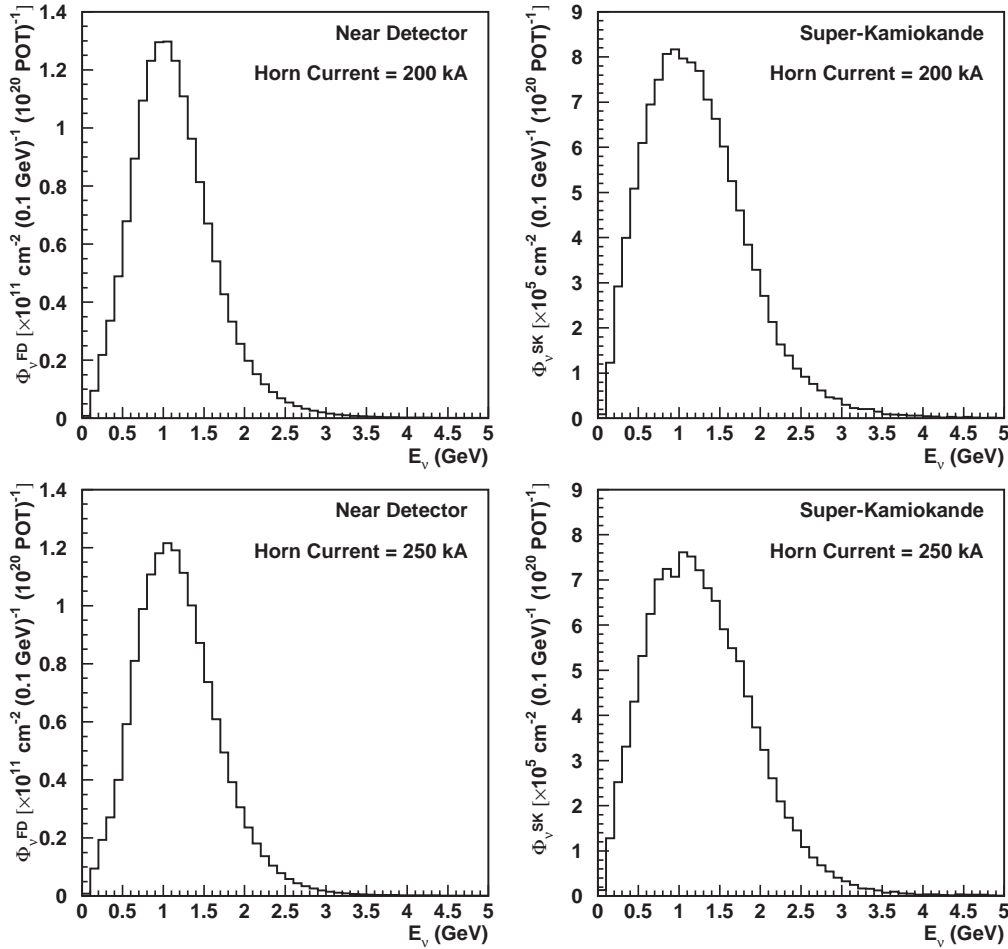


**Figure 4.6:** The difference of the neutrino energy spectra at SK between the configurations in June 1999 (K2K-Ia) and since Nov. 1999 (K2K-Ib). Top two figures show the spectra in K2K-Ia, and bottom two show those in K2K-Ib. In both top and bottom figures, left and right ones are the spectra at ND and SK, respectively.

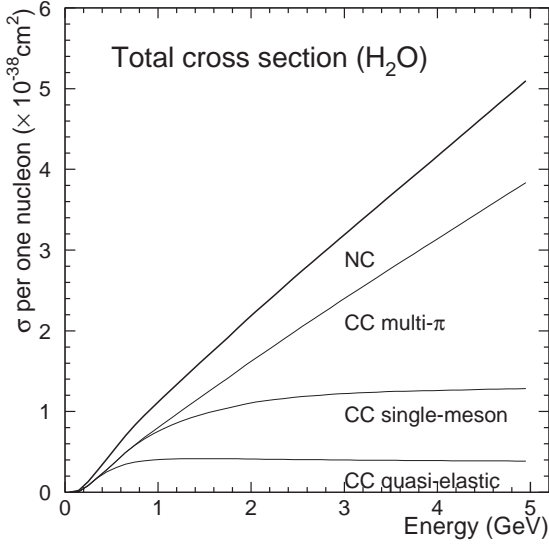


**Figure 4.7:** Cross-section of each neutrino interaction channel with water as a function of incident neutrino energy. The interaction of CC coherent pion production is assorted to that of CC single-meson production. These cross-sections are provided by NEUT simulator.

## 4.2 Neutrino interaction simulation: Neut-MC

The simulated neutrino fluxes described in Sec. 4.1 are passed to a neutrino interaction simulator, “Neut-MC (or NEUT)” [77], which is originally developed and used in the atmospheric neutrino analysis in the Super-Kamiokande experiment [55, 56, 57, 78], although, in our analysis, we have used the cross-section modified from NEUT according to some models in order to reproduce our data well. It simulates neutrino interactions with the target material through the charged current (CC) and the neutral current (NC) weak interactions, providing the 4-momentum of the particles produced in the interaction. The material of neutrino interaction target is  $\text{H}_2\text{O}$  in the water Cherenkov detector. In this section, the calculation method of the cross-section for these interactions in NEUT and the modifications to it for our application are described.

### 4.2.1 Neutrino interactions in a few GeV region

The neutrino interactions in the energy region of our interest, i.e.  $E_\nu \sim 1$  GeV, are as follows:

• CC quasi-elastic scattering (CC-qe)	$\nu N \rightarrow \ell N'$	( $\sim 27\%$ )
• NC elastic scattering (NC-elastic)	$\nu N \rightarrow \nu N$	( $\sim 13\%$ )
• CC single-meson production (CC-1 $\pi$ )	$\nu N \rightarrow \ell N' \pi$	( $\sim 28\%$ )
• NC single-meson production (NC-1 $\pi$ )	$\nu N \rightarrow \nu N' \pi$	( $\sim 10\%$ )
• CC deep inelastic scattering (CC-DIS)	$\nu N \rightarrow \ell N' m\pi$ 's ( $m \geq 2$ )	( $\sim 14\%$ )
• NC deep inelastic scattering (NC-DIS)	$\nu N \rightarrow \nu N' m\pi$ 's ( $m \geq 2$ )	( $\sim 4\%$ )
• CC coherent-pion production (CC-coh. $\pi$ )	$\nu {}^{16}\text{O} \rightarrow \ell^\mp {}^{16}\text{O} \pi^\pm$	( $\sim 2\%$ )
• NC coherent-pion production (NC-coh. $\pi$ )	$\nu {}^{16}\text{O} \rightarrow \nu {}^{16}\text{O} \pi^0$	( $\sim 1\%$ )

where  $N$  and  $N'$  denote nucleons and  $\ell$  is charged lepton. The fraction of each interaction mode is shown at the end of each line, where the cross-section is integrated over the neutrino energy of our beam. In the single-meson productions and deep inelastic scattering, the generated meson and hadrons are pions in the most of the cases. Fig. 4.7 shows the cross-section of each interaction channel with water, calculated by NEUT simulator, as a function of incident neutrino energy.

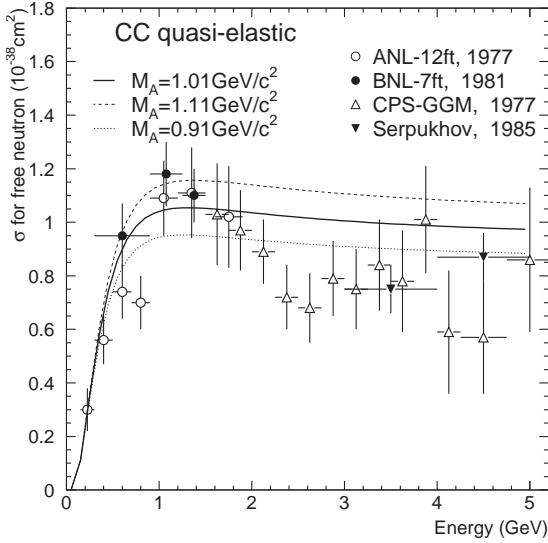


**Figure 4.8:** Cross-section of CC-qe interaction on a free neutron in our simulation, together with the results of the measurements by bubble chamber experiments. Horizontal axis is the incident neutrino energy. Solid, dashed, and dotted lines show the calculation of the cross-section in our simulation with  $M_A = 1.01, 1.11,$  and  $0.91 \text{ GeV}/c^2$ . Data points are from ANL [79], BNL [80], GGM [81], and Serpukhov [82].

#### 4.2.2 CC quasi-elastic and NC elastic scattering

The charged current quasi-elastic (CC-qe) and neutral current elastic (NC-elastic) interactions are the two-body scatterings of neutrino on a nucleon. The differential cross-section for them is described by the 4-momentum transfer squared of the interaction,  $Q^2 \equiv -q^2 = -(p_\nu - p_\ell)^2$ , where  $p_\nu$  and  $p_\ell$  are momenta of incident neutrino and out-going lepton, respectively. Since the target hadron has internal structure, vector and axial vector form factors have to be taken into account. The hadron current is expressed by [83];

$$\langle N' | J_{\text{had}} | N \rangle = \cos \theta_c \bar{u}(N') \left[ \gamma_\lambda F_V^1(Q^2) + \frac{i\sigma_{\lambda\nu} q^\nu \xi F_V^2(Q^2)}{2m_N} + \gamma_\lambda \gamma_5 F_A(Q^2) \right] u(N) \quad , \quad (4.8)$$

where  $\theta_c$  is the Cabbibo angle,  $m_N$  is the nucleon mass. The vector form factors,  $F_V^1, F_V^2$ , are represented as followings;

$$F_V^1(Q^2) = \left( 1 + \frac{Q^2}{4m_N^2} \right)^{-1} \left[ G_E^V(Q^2) + \frac{Q^2}{4m_N^2} G_M^V(Q^2) \right], \quad (4.9)$$

$$\xi F_V^2(Q^2) = \left( 1 + \frac{Q^2}{4m_N^2} \right)^{-1} [G_M^V(Q^2) - G_E^V(Q^2)], \quad (4.10)$$

$$G_E^V(Q^2) = \frac{1}{(1 + Q^2/M_V^2)^2}, \quad G_M^V(Q^2) = \frac{1 + \xi}{(1 + Q^2/M_V^2)^2}, \quad (4.11)$$

where  $\xi \equiv \mu_p - \mu_n = 3.71$  (anomalous magnetic dipole moments), and the vector mass  $M_V$  is set to be  $0.84 \text{ GeV}/c^2$ . The axial vector form factor,  $F_A$ , is given by

$$F_A(Q^2) = \frac{-1.23}{(1 + Q^2/M_A^2)^2}, \quad (4.12)$$

where  $M_A$  is the axial vector mass.  $M_A$  for (quasi-)elastic scattering was set to be  $1.01 \text{ GeV}/c^2$  in NEUT, which is a typical value determined by  $e-p$  and  $\nu-p$  scattering experiments [84] with large errors. However, as described later in the analysis chapters, since the experimental data of K2K favors larger  $M_A$  value than  $1.01 \text{ GeV}/c^2$ , i.e. K2K data have larger scattering angle



than that in NEUT with  $1.01 \text{ GeV}/c^2$ , we set  $M_A$  to be  $1.11 \text{ GeV}/c^2$  for CC-qe and NC-elastic scatterings as a default value for the oscillation analysis, and is varied by  $\pm 10\%$  as its systematic uncertainty in our analysis.

Finally the cross-section is expressed as following;

$$\frac{d\sigma^\nu}{dQ^2} = \frac{m_N^2 G_F^2 \cos^2 \theta_c}{8\pi E_\nu^2} \left[ A(Q^2) \mp B(Q^2) \frac{(s-u)}{m_N^2} + C(Q^2) \frac{(s-u)^2}{m_N^4} \right] , \quad (4.13)$$

where  $G_F$  is the Fermi coupling constant,  $(s-u) \equiv 4m_N E_\nu - Q^2 - m_\ell^2$ ,  $m_\ell$  is the lepton mass, and

$$\begin{aligned} A(Q^2) = & \frac{(m_\ell^2 + Q^2)}{4m_N^2} \left[ \left(4 + \frac{Q^2}{m_N^2}\right) |F_A|^2 - \left(4 - \frac{Q^2}{m_N^2}\right) |F_V^1|^2 + \frac{Q^2}{m_N^2} |\xi F_V^2|^2 \left(1 - \frac{Q^2}{4m_N^2}\right) \right. \\ & \left. + \frac{4Q^2 F_V^1 \xi F_V^2}{m_N^2} - \frac{m_\ell^2}{m_N^2} (|F_V^1 + \xi F_V^2|^2 + |F_A|^2) \right], \end{aligned} \quad (4.14)$$

$$B(Q^2) = -\frac{Q^2}{m_N^2} F_A (F_V^1 + \xi F_V^2) \quad (4.15)$$

$$C(Q^2) = \frac{1}{4} \left( |F_A|^2 + |F_V^1|^2 + \frac{Q^2}{m_N^2} \left| \frac{\xi F_V^2}{2} \right|^2 \right) \quad (4.16)$$

Fig. 4.8 shows the cross-section for the CC-qe interaction used in Neut-MC as a function of incident neutrino energy, giving a consistent result with various bubble chamber measurements around a few GeV region [79, 80, 81, 82].

For the NC elastic scattering, following relations are used [85, 86];

$$\sigma(\nu p \rightarrow \nu p) = 0.153 \times \sigma(\nu n \rightarrow e^- p) \quad \text{and} \quad \sigma(\nu n \rightarrow \nu n) = 1.5 \times \sigma(\nu p \rightarrow \nu p). \quad (4.17)$$

Fermi motion and Pauli blocking effect have to be considered when the target nucleons are bounded in the nuclei. In our simulation, Fermi gas model is adopted to simulate the effect of Pauli blocking by requiring the final nucleon momentum to be larger than the Fermi surface momentum, which is estimated to be  $217 \text{ MeV}/c$  for  $^{16}\text{O}$  nuclei by using the results of  $e\text{-}^{12}\text{C}$  scattering experiment [87].

### 4.2.3 Single-meson production

Single meson production is simulated based on the Rein & Sehgal's model [88, 89]. This model assumes that the interaction occurs via an intermediate baryon resonance state:

$$\begin{aligned} \nu + N &\rightarrow \ell + N^* \\ N^* &\rightarrow N' + \text{meson} \end{aligned} \quad , \quad (4.18)$$

where  $N$  and  $N'$  are initial and final nucleons and  $N^*$  is an intermediate baryon resonance state.

The differential cross-section of single resonance production with its mass of  $M$  and its negligible decay width is written by

$$\frac{d^2\sigma}{dQ^2 dE_\nu} = \frac{1}{32\pi m_N E_\nu^2} \cdot \frac{1}{2} \cdot \sum_{\text{spins}} |T(\nu N \rightarrow \ell N^*)|^2 \cdot \delta(W^2 - M^2) \quad , \quad (4.19)$$

where  $W$  is the invariant mass of the final state hadronic system, and  $T(\nu N \rightarrow \ell N^*)$  is the amplitude of resonance production which is calculated using the FKR (Feynman-Kislinger-Ravndal)

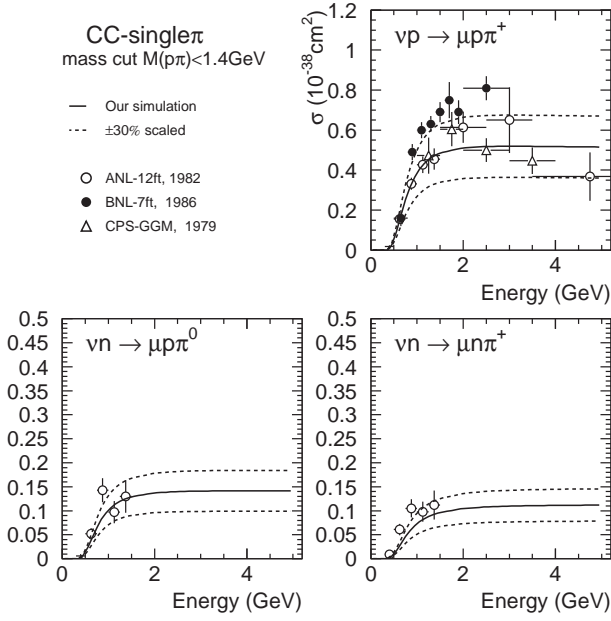


**Figure 4.9:** Cross-section of CC-1 $\pi$  production calculated by our simulator, together with the experimental results. Solid line shows our calculation and dashed lines show the cross-section scaled by  $\pm 30\%$ , where  $M_A = 1.01 \text{ GeV}/c^2$ . The experimental results come from ANL [92], BNL [93], and GGM [94].

baryon model [90]. The value of the axial vector mass  $M_A$  for CC-1 $\pi$  and NC-1 $\pi$  is set to be  $1.01 \text{ GeV}/c^2$  in NEUT, although we have modified it to be  $1.21 \text{ GeV}/c^2$  as our spectrum and oscillation analysis for the same reason as in the case of CC-qe and NC-elastic scatterings.  $M_A$  is varied by 20% as its systematic uncertainty [91]. The differential cross-section for the resonance with a finite decay width  $\Gamma$  can be derived by replacing the  $\delta$ -function in Eq. (4.19) with a Breit-Wigner formula;

$$\delta(W^2 - M^2) \rightarrow \frac{1}{2\pi} \cdot \frac{\Gamma}{(W - M)^2 + \Gamma^2/4} \quad (4.20)$$

The cross-section for the single-meson productions can be calculated as a product of the amplitude of each resonance production and the probability of the resonance decay into a meson and a nucleon. In our simulation,  $\Delta(1232)$  and other 17 resonance states with  $W < 2.0 \text{ GeV}/c^2$  are considered. Fig. 4.9 shows our calculation of the cross-section for single-meson production with  $M_A = 1.01$ , comparing with the experimental measurements [92, 93, 94].

The decay kinematics of  $\Delta(1232)$  is determined by the Rein & Sehgal's model in which the effects of the polarization of the produced resonance are properly considered. For the other resonances, angular distribution of generated meson is set to be isotropic in the rest frame of the resonance state.

#### 4.2.4 Deep inelastic scattering

The charged current deep inelastic scattering, CC-DIS, produces more than one meson with the invariant mass of the hadronic system  $W$  greater than  $1.3 \text{ GeV}/c^2$ . The cross-section of CC-DIS is calculated based on Bjorken scaling, expressed as following;

$$\begin{aligned} \frac{d^2\sigma^\nu}{dx dy} &= \frac{G_F^2 m_N E_\nu}{\pi} \left[ \left(1 - y + \frac{1}{2}y^2 + C_1\right) F_2(x) + y \left(1 - \frac{1}{2}y + C_2\right) [x F_3(x)] \right], \\ C_1 &= \frac{m_\ell^2(y-2)}{4m_N E_\nu x} - \frac{m_N x y}{2E_\nu} - \frac{m_\ell^2}{4E_\nu^2}, \\ C_2 &= -\frac{m_\ell^2}{4m_N E_\nu x}, \end{aligned} \quad (4.21)$$

where  $x \equiv Q^2/(2m_N(E_\nu - E_\ell) + m_N^2)$  and  $y \equiv (E_\nu - E_\ell)/E_\nu$  are the Bjorken scaling variables, and  $m_N$ ,  $m_\ell$ ,  $E_\nu$ , and  $E_\ell$  are the nucleon mass, the lepton mass, the incident neutrino energy, and the final lepton energy, respectively. The nucleon structure functions,  $F_2$  and  $xF_3$ , are taken from GRV94 [95] in NEUT. However, in our oscillation analysis, a modification to the original GRV94 parton distribution functions (PDFs) has been performed, following a model by Bodek and Yang [96] in order to fit the experimental data globally down to low energy region. This modification effectively changes the cross-section by a  $Q^2$ -dependent factor;

$$\frac{d^2\sigma^\nu}{dxdy} \implies \frac{Q^2}{Q^2 + 0.188} \times \frac{d^2\sigma^\nu}{dxdy} . \quad (4.22)$$

Other modifications and corrections done in [96], such as increasing  $d/u$  ratio at high  $x$  and the modification of the scaling variable  $x$  to be  $x_w = x(Q^2 + 0.624)/(Q^2 + 1.735x)$ , are ignored in our simulation since they make only negligible effects in our energy region. With this modification, the cross-section in low  $Q^2$  is suppressed, which behavior is favored by the experimental data of K2K.

The cross-section for NC-DIS is assumed to have following relations;

$$\frac{\sigma(\text{NC-DIS})}{\sigma(\text{CC-DIS})} = \begin{cases} 0.26 & (E_\nu < 3 \text{ GeV}) \\ 0.26 + 0.04(E_\nu/3 - 1) & (3 \text{ GeV} < E_\nu < 6 \text{ GeV}) \\ 0.30 & (6 \text{ GeV} < E_\nu) \end{cases} , \quad (4.23)$$

which are estimated from experimental results [97, 98].

The kinematics of hadronic system is simulated by two different methods depending on the range of its invariant mass  $W$ ; one for  $1.3 < W < 2.0 \text{ GeV}/c^2$  region and the other for  $W > 2.0 \text{ GeV}/c^2$  region.

In the region of  $1.3 < W < 2.0 \text{ GeV}/c^2$ , only pions are considered as outgoing mesons. The mean multiplicity of pions,  $\langle n_\pi \rangle$ , is estimated from the results of 15-foot hydrogen bubble chamber experiment at Fermilab [99] assuming  $\langle n_{\pi^+} \rangle = \langle n_{\pi^-} \rangle = \langle n_{\pi^0} \rangle$  as

$$\langle n_\pi \rangle = 0.09 + 1.83 \ln W^2 . \quad (4.24)$$

The number of pions in each event is determined by using KNO (Koba-Nielsen-Olesen) scaling [100], which describes the pion multiplicity with the mean multiplicity of  $\langle n_\pi \rangle$ . Since the range of  $W$  overlaps with that in single-meson production,  $n_\pi \geq 2$  is required in this  $W$  region in order to keep the consistency between the single-meson production and the deep inelastic scattering channels. The forward-backward asymmetry of pion multiplicity in the hadron center-of-mass system is included according to the results from the BEBC experiment at CERN-SPS [101];

$$\frac{\langle n_\pi^F \rangle}{\langle n_\pi^B \rangle} = \frac{0.35 + 0.41 \ln W^2}{0.5 + 0.09 \ln W^2} . \quad (4.25)$$

In the region of  $W > 2.0 \text{ GeV}/c^2$ , the kinematics of the hadronic system are calculated by using JETSET/PYTHIA package [102].

#### 4.2.5 Coherent pion production

Coherent pion production, CC-coh. $\pi$ /NC-coh. $\pi$ , is a neutrino interaction with a whole nucleus, oxygen for water target, in which the nucleus remains intact without any change in its charge and isospin. One pion with the same charge as the mediating weak boson is produced in the reaction. Since the momentum transfer is small in this interaction, the angular distribution of the outgoing leptons and pions are forward peaking.

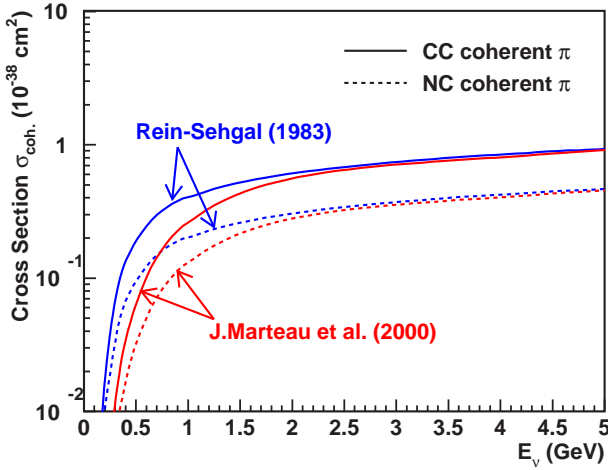


**Figure 4.10:** Cross-section of the coherent pion production calculated in our simulation, as a function of incident neutrino energy. Solid lines show the cross-section of CC-coh. $\pi$  and dashed lines show that of NC-coh. $\pi$ . The cross-section modeled by Rein & Sehgal [103] and Marteau *et al.* [106] are both drawn here with blue and red lines, respectively.

The cross-section and kinematics of coherent pion production in NEUT is calculated based on the Rein & Sehgal's model [103, 104], which is expressed by following formula;

$$\frac{d^3\sigma}{dQ^2 dy dt} = \frac{G_F^2 m_N E_\nu}{2\pi^2} f_\pi^2 A^2 (1-y) \frac{1}{16\pi} (\sigma_{\text{tot}}^{\pi N})^2 (1+r^2) \left( \frac{M_A^2}{M_A^2 + Q^2} \right)^2 e^{-bt} F_{\text{abs}}, \quad (4.26)$$

$$r = \frac{\text{Re}[f_{\pi N}(0)]}{\text{Im}[f_{\pi N}(0)]}, \quad (4.27)$$

where  $f_\pi$  is the pion decay constant taken to be  $0.93 m_\pi$ ,  $A$  is the atomic number which is 16 for oxygen,  $b = (R_0 A^{1/3})^2/3$  is of the order of traverse dimension of the nucleus taken to be  $80 \text{ GeV}^{-2}$ , and  $t$  is the square of the 4-momentum transfer to the nucleus.  $F_{\text{abs}}$  is a factor which takes the pion absorption in the nucleus into account.

Here again, we have made a correction to NEUT in our oscillation analysis according to a neutrino-nucleus interaction model by J. Marteau *et al.* [105, 106], in which the interaction  $\nu \text{ } ^{16}\text{O} \rightarrow \ell^- X$  is considered. In Fig. 4.10, the cross-sections of the CC and NC coherent pion production as a function of incident neutrino energy are shown. The models by Rein & Sehgal and Marteau *et al.* are both included in this figure. In the Model by Marteau *et al.*, the cross-section is slightly reduced in the low energy region compared with that by Rein & Sehgal.

#### 4.2.6 Nuclear effects

Mesons and nucleons generated in the neutrino interactions often cause secondary interactions with nucleons before leaving  $^{16}\text{O}$  nucleus, which is called “nuclear effect”. The inelastic scattering, charge exchange, and absorption of the pions in  $^{16}\text{O}$  nucleus are considered in our simulation. The neutrino interaction point in a nucleus is determined based on the Wood-Saxon type nucleon density distribution,  $\rho(r)$ ,

$$\rho(r) = \frac{Z}{A} \rho_0 \frac{1}{1 + \exp\left(\frac{r-c}{a}\right)}, \quad (4.28)$$

where we choose  $\rho_0 = 0.48 m_\pi^3$ ,  $a = 0.41 \text{ fm}$ , and  $c = 2.69 \text{ fm}$  for  $^{16}\text{O}$  nucleus. The cross-section of each interaction is calculated using the model by L. Salced *et al.* [107]. Fermi motion of nucleons in the nucleus and the Pauli blocking effect are taken into account in the simulation.

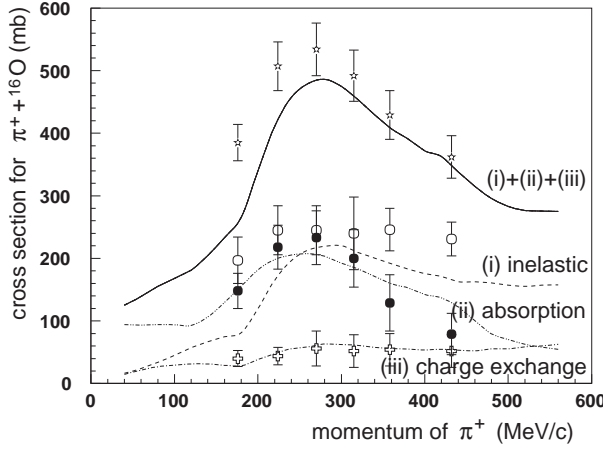


**Figure 4.11:** The cross-section of  $\pi^+ - {}^{16}\text{O}$  interactions. Lines show the results of our calculation based on [107], and the points show the experimental data from [108].

The Fermi surface momentum is defined as

$$p_F(r) = \left( \frac{3}{2} \pi^2 \rho(r) \right)^{\frac{1}{3}}. \quad (4.29)$$

The kinematics in the scattering is determined by using the results of  $\pi$ - $N$  phase shift analysis [109]. Fig. 4.11 shows the calculated  $\pi^+ - {}^{16}\text{O}$  interaction cross-section together with experimental data from C. H. Ingram *et al.* [108], which agrees well with each other.

#### 4.2.7 Summary of modifications in Neut-MC

As mentioned up to now, we have modified the neutrino interaction models for the spectrum analysis in ND and the oscillation analysis which are, respectively, described in Chapter 7 and Chapter 9. Here, the modifications are summarized.

##### Quasi-elastic and elastic scattering

In our oscillation analysis, we set the axial vector mass  $M_A$  in the dipole formula to be  $1.11 \text{ GeV}/c^2$ , while it is  $1.01 \text{ GeV}/c^2$  in NEUT. The uncertainty of  $M_A$  to be  $\pm 10\%$ . Therefore the analysis results with these two values are compared.

##### Single meson production

We set  $M_A$  to be  $1.21 \text{ GeV}/c^2$  in our oscillation analysis, while it is  $1.01 \text{ GeV}/c^2$  in NEUT. We quote the uncertainty of  $M_A$  to be  $\pm 20\%$ . The results with  $M_A = 1.01, 1.11, 1.21, 1.31$ , and  $1.41$  are compared in our analysis.

##### Deep inelastic scattering

We use the model by Bodek *et al.* as a default one in our oscillation analysis, while GRV94 is used in NEUT. Difference of these two models are compared.

##### Coherent pion production

We use the model by Marteau *et al.* as a default one in our oscillation analysis, while the model by Rein & Sehgal is used in NEUT. Difference of these two models are compared.

### Abbreviation for the models

Here, we define the four-digit numbers, “NEUT- $abcd$ ”, to express the models we have compared in our analysis. Among the numbers of four-digit, the first one,  $a$ , is for the model of the quasi-elastic and elastic scattering, the second one,  $b$ , is for the single meson production, the third one,  $c$ , is for the coherent pion production, and the last one,  $d$ , is for the deep inelastic scattering.

For the quasi-elastic and elastic scattering,  $a = 0$  and  $1$  stand for  $M_A = 1.01$  and  $1.11$  GeV/ $c^2$ , respectively. For the single meson production,  $b = 0, 1, 2, 3$ , and  $4$  means  $M_A = 1.01, 1.11, 1.21, 1.31$ , and  $1.41$  GeV/ $c^2$ , respectively. For the coherent pion production,  $c = 0$  expresses the model by Rein & Sehgal, whereas  $c = 1$  expresses the model by Marteau *et al.*. Finally, for the deep inelastic scattering,  $d = 0$  is GRV94, and  $d = 1$  is the model by Bodek *et al.*

According to this notation, the original NEUT is expressed by “NEUT-0000”, or we call it simply “NEUT-std (standard NEUT)”, while the model we employed in our analysis is expressed by “NEUT-1211”. In Table 4.4, the correspondance of abbreviations to models is shown.

## 4.3 Detector simulation: DetSim

The particles generated by Neut-MC are fed to the detector simulators, “DetSim’s”. It simulates the propagation and interaction of particles in the detectors and the responses of the detectors and the readout electronics.

### 4.3.1 Simulation of water Cherenkov detector, 1KT and SK

The DetSim program for the water Cherenkov detectors, 1KT and SK, has been developed based on GEANT package [63]. The materials of the detector are all implemented in the simulation code. The processes listed in Table 4.5 are considered in the DetSim. The CALOR package [60, 61] is employed in order to simulate the hadronic interaction in water. This package is known to reproduce well the pion interactions including low energy region of down to  $\sim 1$  GeV. For still lower energy region ( $p_\pi \leq 0.5$  GeV/ $c$ ), a custom made program [110] is used in DetSim, which program is based on the experimental data from  $\pi$ - $^{16}\text{O}$  scattering [111] and  $\pi$ - $p$  scattering [112]. In this custom made simulator, the elastic scattering, the inelastic scattering, the absorption, and the charge exchange of pions are taken into account.

The Cherenkov photons are generated along the passage of charged particles according to Eq. (3.4) and Eq. (3.5). In the propagation of the Cherenkov photons in the water, Rayleigh scattering, Mie scattering, and absorption are considered: Rayleigh scattering is the interaction of light with small objects like molecule of water, and the Rayleigh scattering coefficient is known to have  $\lambda^{-4}$  dependence, where  $\lambda$  is the wavelength of the light. Mie scattering takes place when the light is scattered by the objects of the same size as or larger than the wavelength. The attenuation coefficients used in our simulation are tuned to reproduce the measurements using the laser system and the cosmic-ray muons described in Sec. 3.5.1 and Sec. 3.6.2. The light reflection and absorption on the surface of detector materials, such as the surface of PMTs and black sheets, are also simulated using probability functions depending on the photon incident angle, which functions are estimated from a direct measurement.

For the simulation of the PMT response, measured quantum efficiency is used. The total amount of photoelectrons detected in each PMT is derived by summing up individual photoelectron signal which is made according to the measured single photoelectron distribution. The hit time of each PMT is smeared according to the time resolution of PMT. The properties of the electronics system, such as the time width of ADC gate and the signal threshold, are taken into account in our simulator.

**Table 4.4:** The list of the correspondence of abbreviations to models. NEUT-0000 is used in the original Neut-MC, while NEUT-1211 is employed in the spectrum analysis in ND and the oscillation analysis.

Abbreviations	CC-qe/NC-elastic ( $M_A$ [GeV/ $c^2$ ])	CC/NC- $1\pi$ ( $M_A$ [GeV/ $c^2$ ])	CC/NCcoh (model in use)	CC/NCDIS (model in use)
NEUT-0000 (std-NEUT)	1.01	1.01	Rein&Sehgal	GRV94
NEUT-0001	1.01	1.01	Rein&Sehgal	Marteanu
NEUT-0010	1.01	1.01	Bodek	GRV94
NEUT-0011	1.01	1.01	Bodek	Marteanu
NEUT-0100	1.01	1.11	Rein&Sehgal	GRV94
NEUT-0101	1.01	1.11	Rein&Sehgal	Marteanu
NEUT-0110	1.01	1.11	Bodek	GRV94
NEUT-0111	1.01	1.11	Bodek	Marteanu
NEUT-0200	1.01	1.21	Rein&Sehgal	GRV94
NEUT-0201	1.01	1.21	Rein&Sehgal	Marteanu
NEUT-0210	1.01	1.21	Bodek	GRV94
NEUT-0211	1.01	1.21	Bodek	Marteanu
NEUT-0300	1.01	1.31	Rein&Sehgal	GRV94
NEUT-0301	1.01	1.31	Rein&Sehgal	Marteanu
NEUT-0310	1.01	1.31	Bodek	GRV94
NEUT-0311	1.01	1.31	Bodek	Marteanu
NEUT-0400	1.01	1.41	Rein&Sehgal	GRV94
NEUT-0401	1.01	1.41	Rein&Sehgal	Marteanu
NEUT-0410	1.01	1.41	Bodek	GRV94
NEUT-0411	1.01	1.41	Bodek	Marteanu
NEUT-1000	1.11	1.01	Rein&Sehgal	GRV94
NEUT-1001	1.11	1.01	Rein&Sehgal	Marteanu
NEUT-1010	1.11	1.01	Bodek	GRV94
NEUT-1011	1.11	1.01	Bodek	Marteanu
NEUT-1100	1.11	1.11	Rein&Sehgal	GRV94
NEUT-1101	1.11	1.11	Rein&Sehgal	Marteanu
NEUT-1110	1.11	1.11	Bodek	GRV94
NEUT-1111	1.11	1.11	Bodek	Marteanu
NEUT-1200	1.11	1.21	Rein&Sehgal	GRV94
NEUT-1201	1.11	1.21	Rein&Sehgal	Marteanu
NEUT-1210	1.11	1.21	Bodek	GRV94
NEUT-1211 (our case)	1.11	1.21	Bodek	Marteanu
NEUT-1300	1.11	1.31	Rein&Sehgal	GRV94
NEUT-1301	1.11	1.31	Rein&Sehgal	Marteanu
NEUT-1310	1.11	1.31	Bodek	GRV94
NEUT-1311	1.11	1.31	Bodek	Marteanu
NEUT-1400	1.11	1.41	Rein&Sehgal	GRV94
NEUT-1401	1.11	1.41	Rein&Sehgal	Marteanu
NEUT-1410	1.11	1.41	Bodek	GRV94
NEUT-1411	1.11	1.41	Bodek	Marteanu

**Table 4.5:** The list of the processes considered in our detector simulation.

Particles	Simulated processes
$\gamma$	$(e^+, e^-)$ pair production, Compton scattering, photoelectric effect
$e^\pm$	multiple scattering, ionization, $\delta$ -rays production, bremsstrahlung, annihilation of $e^+$ , Cherenkov radiation
$\mu^\pm$	multiple scattering, ionization, $\delta$ -rays production, bremsstrahlung, nuclear interaction, decay, Cherenkov radiation, $\mu^-$ capture in $^{16}\text{O}$
hadrons	multiple scattering, nuclear interaction, ionization, $\delta$ -ray production, decay, Cherenkov radiation

### 4.3.2 Simulation of fine-grained detector

In the simulation of the fine-grained detector, GEANT package is also employed. All the materials making up SciFi, TGC, LG, MRD, and their supporting structures are implemented in the code. CALOR hadronic package is also used to propagate hadrons in the detectors.

In the simulation of SciFi, the light yield of the scintilating fibers and the response of IIT-CCD pixels are simulated according to the calibration data using cosmic-ray muons, radioactive source, and LED light [47]. The noise hits are also simulated, which are estimated using cosmic-ray and randomly triggered data.

The responses of the light yield in the TGC and LG simulator are tuned to reproduce the cosmic-ray muon data and results of the beam test [49].

The hit timing information is saved in the MRD simulator. The hit efficiency of about 97.5% and the noise hits are also simulated [53].



# Chapter 5

## Analysis Strategy and Data Set for Analysis

Up to here, the general descriptions on the K2K experiment and the simulations employed in our analysis have been given. From here, we will describe the analysis method and its results in detail. In this chapter, first the overview of our analysis is provided. Then, the data set used in the analysis is summarized. The stabilities of the primary, the secondary, and the neutrino beams are also shown in this chapter.

### 5.1 Overview of the analysis

In order to probe the neutrino oscillation by the reduction in the number of neutrino events and the distortion in energy spectrum, the flux and energy spectrum of the original neutrino beam must be understood. The number of neutrino interactions,  $N_{\text{int}}^{\text{KT}}$ , is measured in 1KT to estimate the absolute flux, while the energy spectrum of neutrino beam at the location of ND,  $\Phi^{\text{ND}}(E_\nu)$ , is measured by whole ND system. These results are extrapolated to those in SK by far-to-near ratio,  $R_{\text{int}}^{\text{SK/ND}}$  and  $R_{\text{flux}}^{\text{SK/ND}}(E_\nu)$ , which are estimated by Beam-MC. Reliability of the Beam-MC is cross-checked by the PIMON measurements. The expected number of neutrino events in SK,  $N_{\text{exp}}^{\text{SK}}$ , is derived by

$$N_{\text{exp}}^{\text{SK}} = N_{\text{int}}^{\text{1KT}} \cdot R_{\text{int}}^{\text{SK/1KT}} \cdot \frac{\text{POT}_{\text{SK}}}{\text{POT}_{\text{1KT}}} \cdot \epsilon_{\text{SK}} \quad , \quad (5.1)$$

where  $\text{POT}_{\text{SK(1KT)}}$  is the number of protons on target used in the SK (1KT) analysis, and  $\epsilon_{\text{SK}}$  is the average detection efficiency for neutrino events in SK. In this formula, the far-to-near ratio,  $R_{\text{int}}^{\text{SK/1KT}}$ , is the ratio of the number of neutrino interactions in SK and 1KT, which is given by

$$R_{\text{int}}^{\text{SK/1KT}} = \frac{\int \Phi^{\text{SK}}(E_\nu) \cdot \sigma_{\text{H}_2\text{O}}(E_\nu) \cdot M_{\text{SK}} dE_\nu}{\int \Phi^{\text{1KT}}(E_\nu) \cdot \sigma_{\text{H}_2\text{O}}(E_\nu) \cdot M_{\text{1KT}} dE_\nu} \quad , \quad (5.2)$$

where  $\Phi^{\text{SK(1KT)}}(E_\nu)$  is the neutrino spectrum at SK (1KT),  $\sigma_{\text{H}_2\text{O}}(E_\nu)$  is the cross-section of neutrino interaction with water, and  $M_{\text{SK(1KT)}}$  is the fiducial mass of SK (1KT).

The neutrino spectrum measured in ND is extrapolated to SK by the far-to-near flux ratio,  $R_{\text{flux}}^{\text{SK/ND}}(E_\nu)$ ,

$$\Phi^{\text{SK}}(E_\nu) = R_{\text{flux}}^{\text{SK/ND}}(E_\nu) \cdot \Phi^{\text{ND}}(E_\nu) \quad (5.3)$$

in the case of no oscillation, where  $R_{\text{flux}}^{\text{SK/ND}}(E_\nu)$  is easily written by

$$R_{\text{flux}}^{\text{SK/ND}}(E_\nu) = \frac{\Phi^{\text{SK}}(E_\nu)}{\Phi^{\text{ND}}(E_\nu)} \quad . \quad (5.4)$$

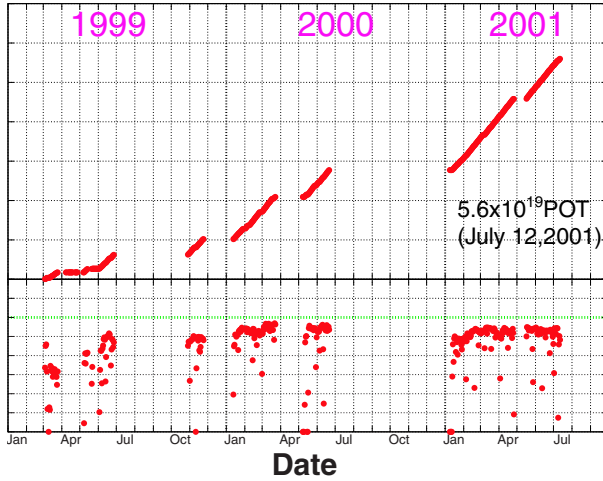


**Figure 5.1:** The number of protons delivered onto the production target in the period of from June 1999 to July 2001. Horizontal axis correspond to the date. Upper figure shows the number of protons on target (POT) accumulated from June 1999, and lower figure shows the POT per spill. Up to July 2001,  $5.6 \times 10^{19}$  POTs are delivered by the KEK-PS accelerator, among which the data corresponding to  $4.7 \times 10^{19}$  POTs are used in the analysis.

In the oscillation analysis described in Chapter 9, these expressions become more complicated and written in more exact forms in order to take the advantage of the systematic uncertainties of measurements canceled out, which is described in detail in Chapter 9.

## 5.2 Data set for analysis

The data taken in the period of from June 1999 to July 2001 (K2K-Ia and K2K-Ib) are used in this analysis. The corresponding runs are RUN-I, IIa, IIb, and III in Table 2.2. During this period,  $5.601 \times 10^{19}$  protons are delivered onto the production target by KEK-PS accelerator to make the neutrino beam, as shown in Fig. 5.1. The corresponding number of beam spills recorded by our data acquisition system is  $1.07 \times 10^7$ . Among these beam spills, those with good beam condition, SK being alive, valid GPS status in both KEK and SK are selected as “good beam spills” and used in the analysis.

### 5.2.1 Good beam condition

Beam spills with good beam condition is defined by the following criteria.

1. Beam spills from June 1999 to July 2001.
2. Beam spills with normal machine status. The beam spills during the periods of the machine study, beam tuning, and the PIMON measurements are discarded.
3. Beam spills with no trouble in the beam line components and data acquisition system.
4. Beam spills with the proton intensity greater than  $1 \times 10^{12}$  protons per spill (or protons per pulse, ppp). Since typical number of protons per spill is  $4\text{--}6 \times 10^{12}$ , as shown in Fig. 5.1, beam spills with too low intensity is discarded.
5. Beam spills with the current of the horn magnets greater than 240 kA (190 kA) in K2K-Ib (K2K-Ia). Instability in the horn current makes different pion focusing effect, and hence makes different neutrino flux and energy spectrum. Beam spills with too low horn current are discarded.

### 5.2.2 Good GPS status

The validity of GPS is very important in our analysis in order to make time synchronization between KEK and SK. GPS system has status bits to record if the current GPS status is good or not. The GPS status bits include the information whether signals from more than four GPS satellites are received or not, there happens an increment by one pulse per second or not, and LTC time stamp is accurate or not. As mentioned in Sec. 3.7, there are 2 GPS receivers equipped in both KEK and SK site. Using their information, beam spills with good GPS status are selected as followings.

In KEK site,

1. If the time difference of GPS1 and GPS2 of a spill,  $|T_{\text{GPS1}} - T_{\text{GPS2}}|$ , is less than 200 nsec, the spill is used for analysis.
2. If criterion 1 is not satisfied, require the status bit of GPS1 to be good. Then, take the time differences of consecutive two spills of GPS1 and TRG,

$$\Delta T_{\text{GPS1}} = T_{\text{GPS1}}^n - T_{\text{GPS1}}^{n-1}, \quad (5.5)$$

$$\Delta T_{\text{TRG}} = T_{\text{TRG}}^n - T_{\text{TRG}}^{n-1}, \quad (5.6)$$

where  $\Delta T_{\text{TRG}}$  for each spill is recorded by VME-TRG module, as mentioned in Sec. 3.4. If  $|\Delta T_{\text{GPS1}} - \Delta T_{\text{TRG}}| < 200$  nsec, the spill is used for analysis with GPS1 giving the beam spill time.

3. If criterion 2 is not satisfied, the same check as criterion 2 is done for GPS2, and if GPS2 status bit is good and  $|\Delta T_{\text{GPS2}} - \Delta T_{\text{TRG}}| < 200$  nsec, the spill is used for analysis with GPS2 giving the beam spill time.
4. If all the criteria above are not satisfied, the spill is discarded.

Beam spills of about 0.1% are discarded by invalid GPS status in KEK site.

The selection criteria in SK site are,

1. Check GPS status bit for each events. If good, use the spill.
2. If one subrun of SK contains more than 10% of events with bad GPS status bit, the whole subrun is discarded.
3. If GPS status bit of a events is bad, the time difference between GPS1 and GPS2,  $|T_{\text{GPS1}} - T_{\text{GPS2}}|$ , and the time difference between GPS1 and LTC,  $|T_{\text{GPS1}} - T_{\text{LTC}}|$  are taken. If both time differences are greater than 200 nsec, then the event is discarded.

So far, there was no event which satisfies the criterion 3, and the number of subruns which were discarded by invalid GPS status is 6 subruns during K2K-I period, where one subrun in SK is corresponding to the data taken in about 90 seconds.

### 5.2.3 Status of data taking in ND and SK

Beam spills during SK being alive are selected. In order to use as much neutrino beam as possible, all the beam spills are used for the analysis as far as SK is alive, even if ND system, especially 1KT, is dead. A chart of the definition of beam spills in use is shown in Table 5.1. In extrapolation of the number of neutrino interactions in 1KT to that expected in SK, the dead

**Table 5.1:** Chart of the definition of beam spills in use. The values in parentheses is corresponding POT accumulated from June 1999 to July 2001. When SK is alive, all the beam spills are used whenever 1KT is alive or dead.

	1KT alive	1KT dead
SK alive	used ( $4.29 \times 10^{19}$ POT)	used, need correction ( $0.50 \times 10^{19}$ POT)
SK dead	not used	not used

**Table 5.2:** Summary of the number of protons on target used in the analysis for each month.

period	Jun.'99	Nov.'99	Jan.'00	Feb.'00	Mar.'00	May.'00	Jun.'00
Target diameter	2 cm $\phi$	3 cm $\phi$					
Horn current	200 kA	250 kA					
From	04-Jun.	29-Oct.	14-Jan.	02-Feb.	01-Mar.	11-May	31-May
To	26-Jun.	24-Nov.	29-Jan.	26-Feb.	23-Mar.	28-May	21-Jun.
POT <sub>SK</sub> ( $\times 10^{18}$ )	3.10	3.57	2.22	4.04	3.70	2.56	3.76
POT <sub>1KT</sub> ( $\times 10^{18}$ )	2.60	2.62	1.81	3.74	3.35	2.42	3.17

period	Jan.'01	Feb.'01	Mar.'01	Apr.'01	May.'01	Jun.'01	Jul.'01
Target diameter	3 cm $\phi$						
Horn current	250 kA						
From	14-Jan.	05-Feb.	08-Mar.	11-Apr.	17-May	27-May.	01-Jul.
To	05-Feb.	08-Mar.	03-Apr.	26-Apr.	27-May	01-Jul.	11-Jul.
POT <sub>SK</sub> ( $\times 10^{18}$ )	3.20	5.04	4.60	2.76	1.75	6.12	1.54
POT <sub>1KT</sub> ( $\times 10^{18}$ )	2.92	4.75	4.27	2.47	1.60	5.79	1.43

$$\begin{aligned} \text{In total : POT}_{\text{SK}} &= 4.79 \times 10^{19} \text{ POT} \\ \text{POT}_{\text{1KT}} &= 4.29 \times 10^{19} \text{ POT} \end{aligned}$$

time of 1KT is corrected by a factor of  $\text{POT}_{\text{SK}}/\text{POT}_{\text{1KT}}$ . The error on this correction,  $\delta_{\text{POT}}$ , is estimated as following;

$$\frac{\text{POT}_{\text{SK}}}{\text{POT}_{\text{1KT}}} = 1 + \frac{\text{POT}_{\text{SK}} - \text{POT}_{\text{1KT}}}{\text{POT}_{\text{1KT}}} \quad , \quad (5.7)$$

$$\delta_{\text{POT}} = \frac{\text{POT}_{\text{SK}} - \text{POT}_{\text{1KT}}}{\text{POT}_{\text{1KT}}} \times \delta S_{\text{1KT}} \quad , \quad (5.8)$$

where  $\delta S_{\text{1KT}}$  is a fluctuation of the neutrino event rate measured in 1KT, which is estimated to be 6%.

#### 5.2.4 Total number of POT used in the analysis

After all the criteria for good beam spill selection are imposed, the total number of protons on target for the analysis is  $4.79 \times 10^{19}$  POT ( $4.29 \times 10^{19}$  POT) in SK (1KT). The number of POT accumulated in each month is summarized in Table 5.2

### 5.3 Beam stability during the data taking

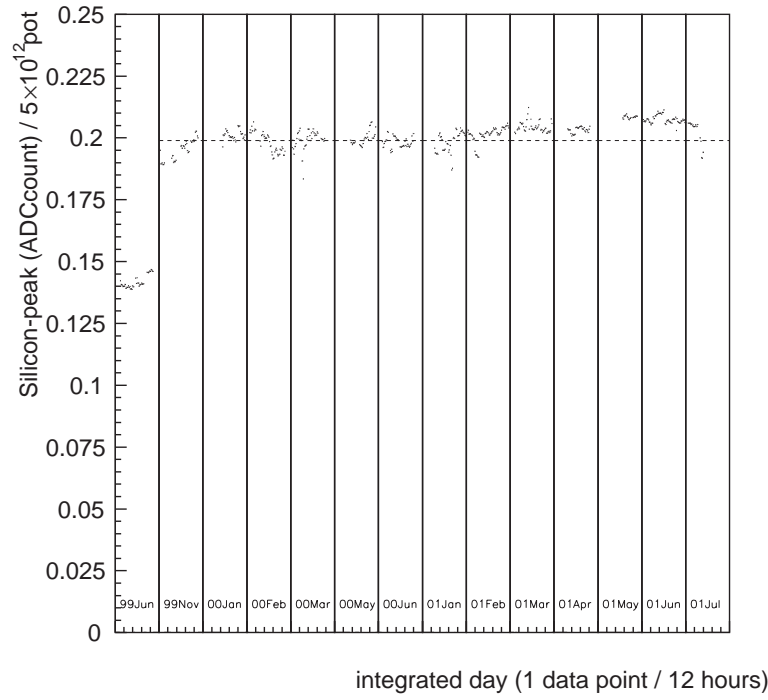
The stabilities of the neutrino beam intensity and direction have been monitored by MUMON on spill-by-spill basis by measuring the yield and profile of muon from pion decay. In addition, stabilities of the profile and intensity of neutrino beam itself have been measured by MRD every a few days.

Fig. 5.2 shows the stability of the muon yield normalized to  $5 \times 10^{12}$  POT measured by the silicon pad detector array (SPD) in MUMON, which indicates that the targetting efficiency of the proton beam have been stable within a few %. Fig. 5.3 shows the stability of the center of the muon profile measured by the ionization chamber (ICH) in MUMON. The beam have been pointed to the direction of SK within  $\pm 1$  mrad during whole run period.

By looking at the distribution of the neutrino interaction vertex in ND, the profile of neutrino beam itself is also monitored, although 3 or 4 days data for each point is needed to accumulate enough statistics. Fig. 5.4 shows the  $x$ - (horizontal) and  $y$ - (vertical) vertex profile measured in MRD, and the stabilities of their center are shown in Fig. 5.5. It provides that the direction of the neutrino beam itself is also stable within  $\pm 1$  mrad except for the statistical fluctuation.

The stability of the neutrino event rate measured in MRD is shown in Fig. 5.6, in which the event rate is normalized to  $5 \times 10^{12}$  POT. The event rate is also stable within statistical fluctuation.

Finally, Fig. 5.7 shows the stabilities of the energy and the angular distributions of muons produced in the neutrino interactions in MRD. Each point is corresponding to one-month accumulated data. Both distributions are stable during whole run period, showing that the energy spectrum of the neutrino beam itself is also stable.



**Figure 5.2:** Stability of muon yield measured by the silicon pad detector array (SPD) in MUMON. The vertical axis is in arbitrary unit, but each data point is normalized to  $5 \times 10^{12}$  POT.

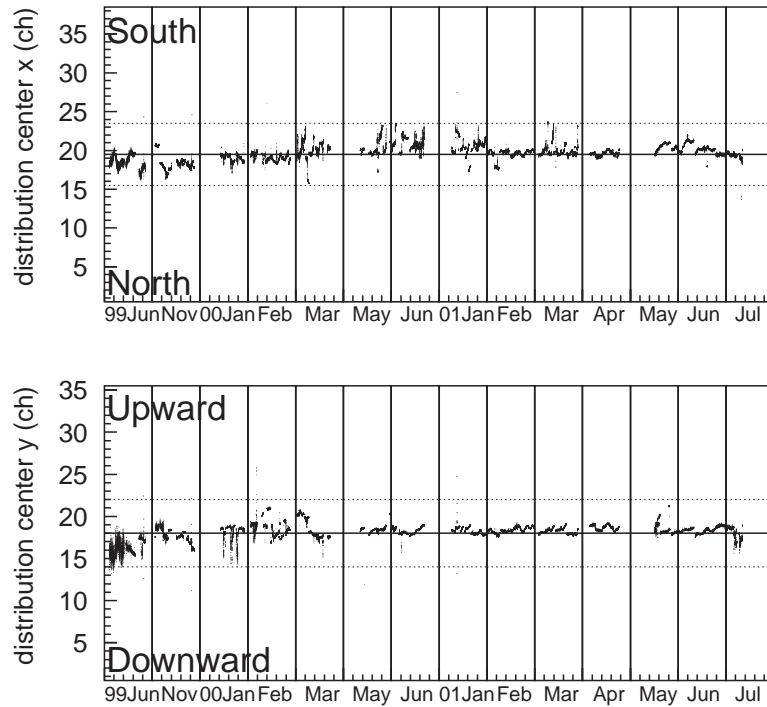


**Figure 5.3:** Stability of the center of muon profile measured by the ionization chamber (ICH) in MUMON. Upper figure shows the profile center of horizontal direction and lower figure shows that of vertical direction. Horizontal solid lines show the nominal beam direction to SK measured by GPS, while dotted lines show the direction of  $\pm 1$  mrad off the center.

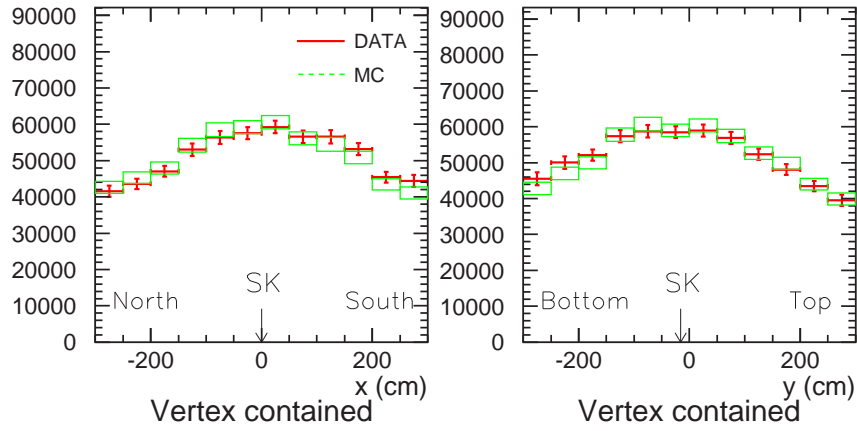


**Figure 5.4:** Profile of the vertex of neutrino events measured in MRD. Left figure shows the  $x$ -vertex (horizontal) distribution, and right figure shows the  $y$ -vertex (vertical) distribution. This is corresponding to the profile of the neutrino beam.

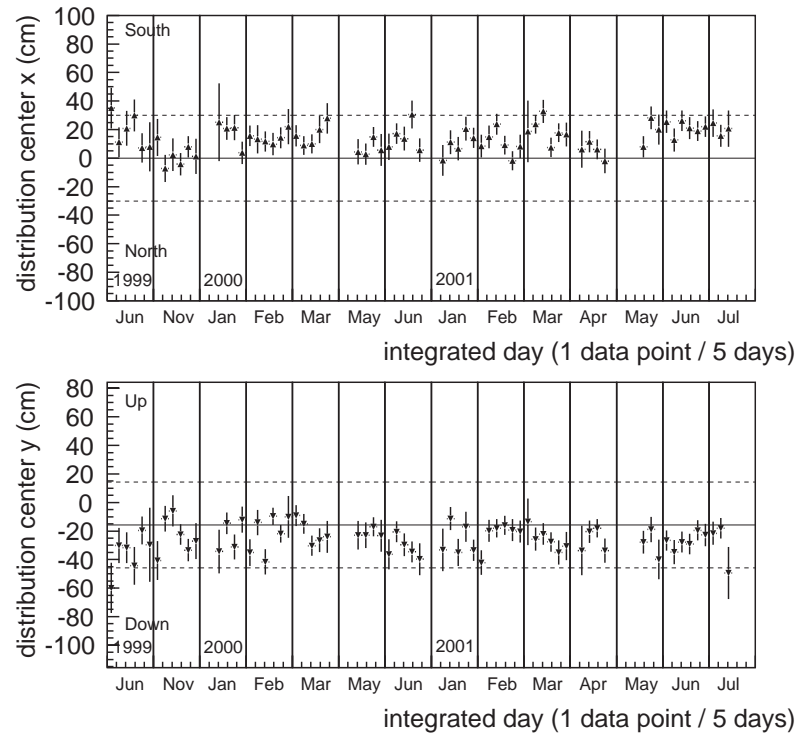


**Figure 5.5:** Stability of the center of neutrino beam profile measured in MRD. Upper and lower figures show the profile center of horizontal and vertical directions.

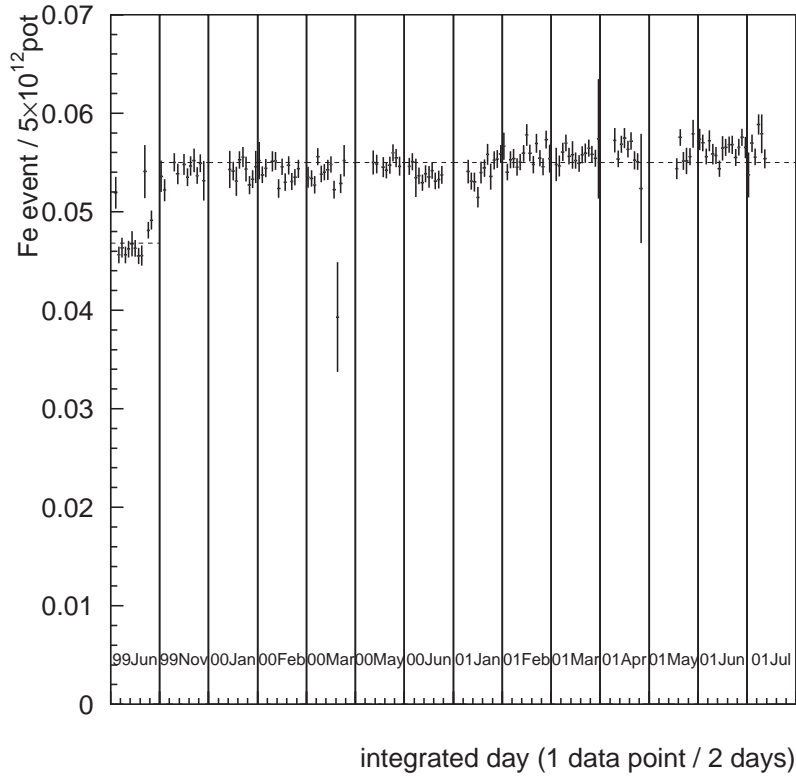


**Figure 5.6:** Stability of the neutrino event rate measured in MRD. Each point corresponds to about two days data, which is normalized to  $5 \times 10^{12}$  POT.

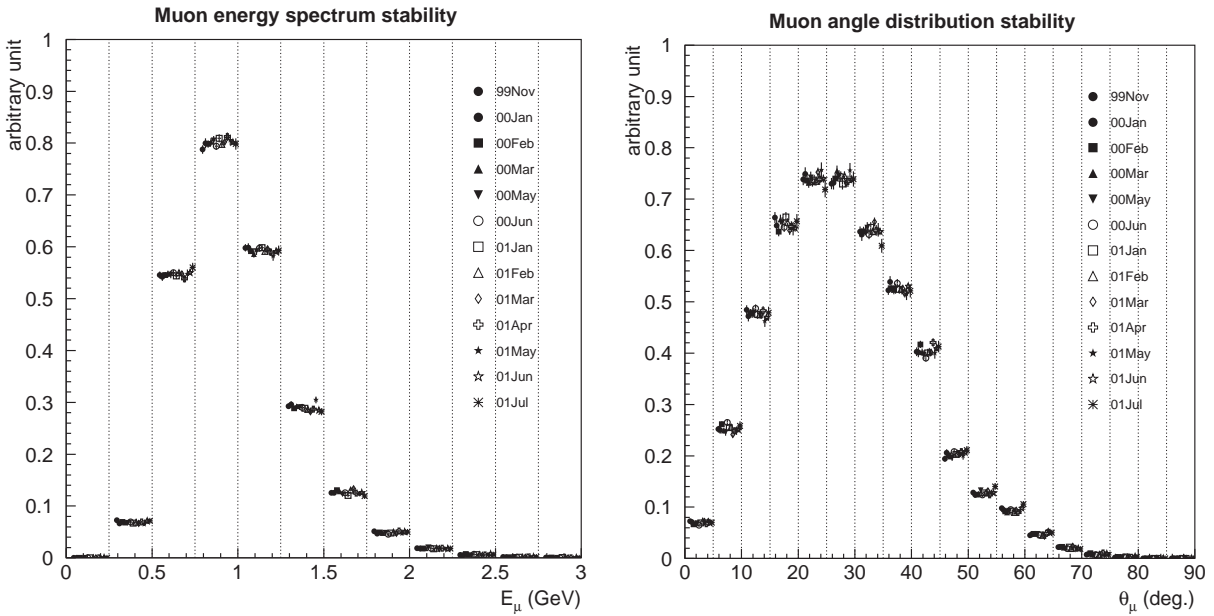


**Figure 5.7:** Stability of the energy (left) and angular (right) distribution of muons scattered by the neutrino interaction in MRD.



# Chapter 6

## Far-to-near Neutrino Spectrum Ratio

As mentioned in Sec. 2.2.3, since the fluxes does not simply obey the  $L^{-2}$  law, a factor, so called “far-to-near ratio ( $F/N$ )”, is needed.  $F/N$  ratio extrapolates the flux and energy spectrum of the neutrino beam measured in ND to those expected in SK. If we know the momentum and angular distribution of parent pions, we can predict the spectrum at any distance because it is determined only by the decay kinematics of pion and the geometry of the beam line. For this purpose, PIMON measurements had been done in the K2K experiment. Since there are some documents in which the PIMON measurements are described in detail [35], only the brief description and the results from the measurements are provided in this chapter. Here, the estimated error matrix for  $F/N$  is also given, which is used in the oscillation analysis in Chapter 9.

### 6.1 Measurements of pion monitor

The PIMON measurements had been done in June 1999 with the horn current of 200 kA and in November 1999 with the horn current of 250 kA using special beam time for the measurements. The PIMON data were taken with the beam intensity of  $7 \times 10^{10}$  ppp of 1 bunch operation in June 1999 run, and with  $7 \times 10^{11}$  ppp of 9 bunch operation in Nov. 1999 run. This low intensity operation was needed to avoid PMT saturation. Large saturation was observed in June 1999 run, and it had been improved in the Nov. 1999 run thanks to the studies on PMT gain adjustment. The operation parameters are summarized in Table 6.1.

In each runs, the refractive index of the freon gas ( $n$ ) was set to be 9 points which makes pions with different momentum above 2 GeV/ $c$  to be sensitive. For each point, the spacial distribution of Cherenkov light was taken by the PMT array placed on the focal plane. A

**Table 6.1:** Summary of the operation of the PIMON measurements in June 1999 and Nov. 1999 runs.

Parameters	June 1999	Nov. 1999
Target diameter	2 cm $\phi$	3 cm $\phi$
Horn current	200 kA	250 kA
Beam intensity	$7 \times 10^{10}$ ppp	$7 \times 10^{11}$ ppp
Number of bunches	1	9
Refractive index	9 points	9 points
PMT gain	300	20 or 50
PMT saturation	exist	no

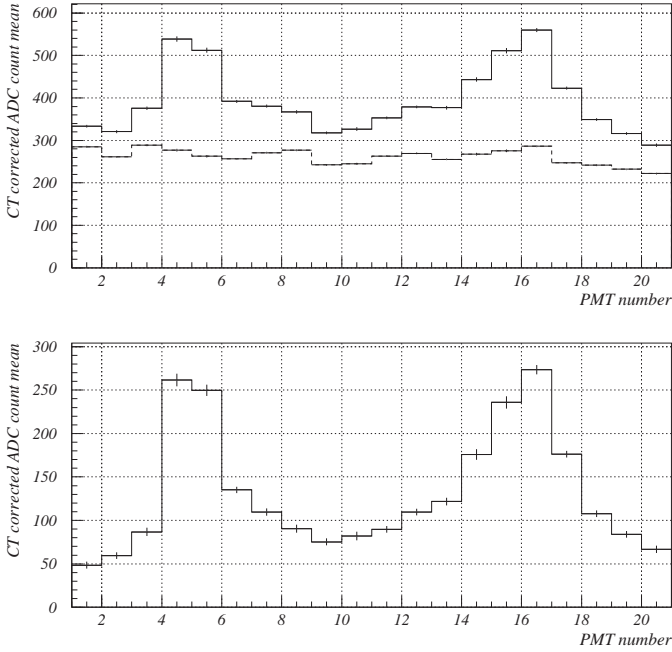


**Figure 6.1:** A typical Cherenkov light distribution observed by the PMT array in PI-MON measurements. Horizontal axis stands for the PMT numbers corresponding to the vertical position on the focal plane. PMT-1 is at the top and PMT-20 is at the bottom. One step of PMT number corresponds to 3.5 cm. Upper figure shows the light distribution with mirror-on and -off, and lower figure shows that with the mirror-off distribution subtracted.

typical Cherenkov light distribution observed by the PMT array is shown in the upper figure of Fig. 6.1. In order to subtract the background contained in the raw distribution, a measurement with the mirror directed off from the direction of PMT array (“mirror-off data”) are taken, and then it is subtracted from “mirror-on” data. The lower figure of Fig. 6.1 shows the background subtracted light distribution. The PMT array was shifted by a half PMT interval to obtain finer distributions, and hence 40 data points (one point for every 1.75 cm) are taken for a light distribution with each refractive index.

There is still non-negligible background from electro-magnetic showers which mainly come from the decay of neutral pions,  $\pi^0 \rightarrow 2\gamma$ . The light distribution of this background is estimated using Beam-MC. The normalization of the subtraction is done by the distribution measured with the lowest refractive index, where the contribution from the electro-magnetic components is dominant.

After all the backgrounds are subtracted, the distribution of the Cherenkov light emitted from pions is obtained for each refractive index, as shown in Fig. 6.2, where the prediction of Beam-MC is also superimposed.

## 6.2 Extraction of pion momentum and angular distribution

In order to extract  $(p_\pi, \theta_\pi)$  2-dimensional distribution from the Cherenkov light distributions with various refractive indices,  $\chi^2$ -fitting is employed. The method is as following:

1.  $(p_\pi, \theta_\pi)$ -plane is binned into  $5 \times 10$  bins; 5 bins in  $p_\pi$  above 2 GeV/ $c$  with 1 GeV/ $c$  step ( $p_\pi > 6$  GeV/ $c$  is integrated) and 10 bins in  $\theta_\pi$  from  $-50$  mrad to  $50$  mrad with 10 mrad step.
2. Using a Monte Carlo simulation, a template of the Cherenkov light distribution emitted by pions in each  $(p_\pi^i, \theta_\pi^j)$ -bin ( $i = 1-5, j = 1-10$ ) is produced for each refractive index, separately. Here, the template distribution for the  $(p_\pi^i, \theta_\pi^j)$ -bin with the  $k$ -th refractive

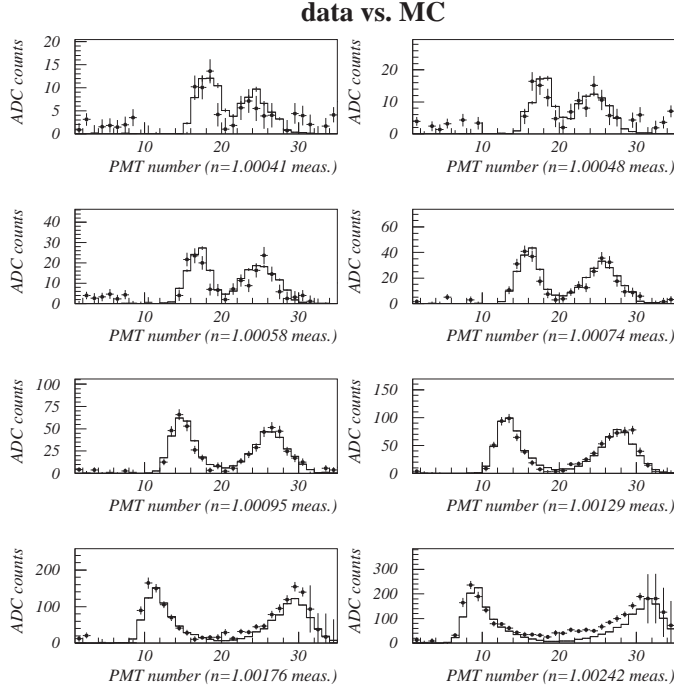


**Figure 6.2:** Cherenkov light distributions for various refractive indices measured in Nov. 1999. Dots show data and the histograms show the Beam-MC. The refractive index for each plot are as written in the figure.

index is expressed by  $dist_{(i,j),k}^{MC}(l)$ , where  $l$  is the light intensity on the  $l$ -th PMT position ( $l = 1-40$ ).

3. We measured Cherenkov light distribution with the  $k$ -th refractive index,  $dist_k^{data}(l)$ . This distribution should be expressed by a superposition of  $dist_{(i,j),k}^{MC}(l)$  using the weighting factors  $W_{(i,j)}$ . Therefore,  $\chi^2$  function is defined as

$$\chi^2 = \sum_k^{\text{ref.index}} \left( \sum_{l=1}^{\text{PMTmax}} \frac{dist_k^{data}(l) - W_{(i,j)} \cdot dist_{(i,j),k}^{MC}(l)}{[\sigma_k(l)]^2} \right), \quad (6.1)$$

where  $\sigma_k(l)$  is the error on the measurement of  $l$ -th PMT with the  $k$ -th refractive index. Fifty  $W_{(i,j)}$ 's being weighted as fitting parameters, this  $\chi^2$ -function is minimized to obtain the fitted  $W_{(i,j)}$  values, which give the relative population of pion in  $(p_\pi^i, \theta_\pi^j)$ -bin.

In this way, the relative pion population in each  $(p_\pi^i, \theta_\pi^j)$ -bin,  $W_{(i,j)}$ , is obtained.

This fitting had been done for the data in June 1999 and in Nov. 1999, separately. The resulting values of fitting parameters and errors on them in Nov. 1999 run are shown in Fig. 6.3.

### 6.3 Neutrino energy spectra at ND and SK and their ratio

In order to extract the neutrino spectrum at ND and SK, the contribution of  $(p_\pi^i, \theta_\pi^j)$ -bin to the  $n$ -th bin of neutrino spectrum at ND (SK),  $\phi_{n,(i,j)}^{ND(SK)}$ , is calculated using MC simulation, which calculation depends almost only on the decay kinematics of pion and the geometry of the beam line. The neutrino energy is binned into 0.5 GeV bins upto 2.5 GeV, and integrated above 2.5 GeV. Therefore, we have 6 bins in neutrino energy. Then the flux of the  $n$ -th bin of the

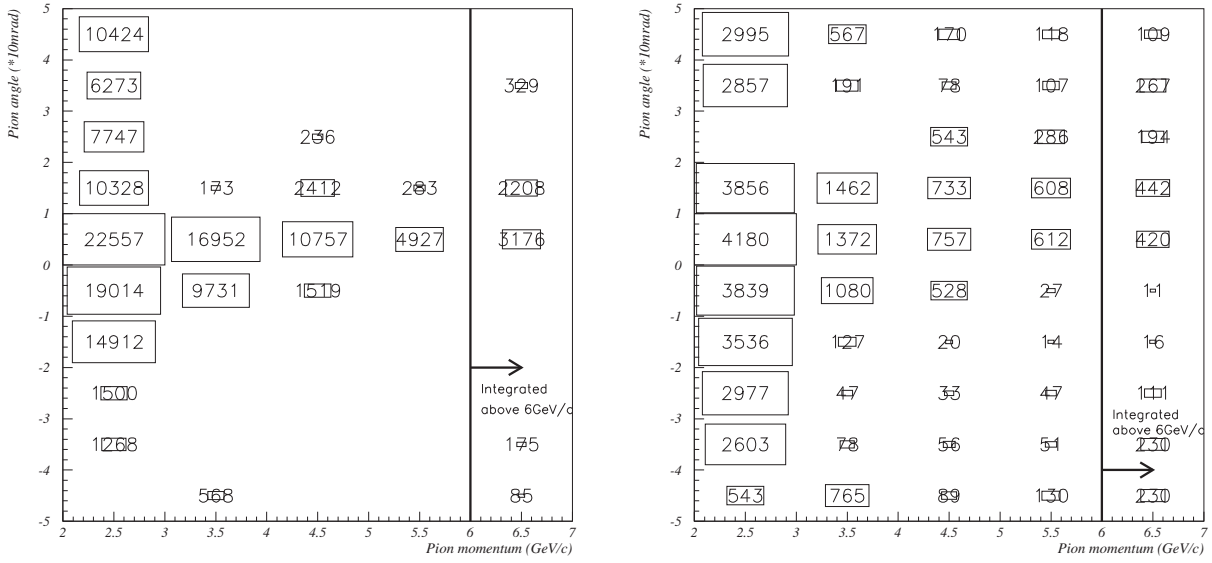


**Figure 6.3:** The fitting results of pion ( $p_\pi, \theta_\pi$ ) distribution in Nov. 1999 run. The left figure shows the resulting central value of the weighting parameters  $W_{(i,j)}$ , and the right figure shows the estimated fitting errors on them.

neutrino energy at ND (SK),  $\Phi_n^{\text{ND(SK)}}(W)$ , is derived by a superposition of  $\phi_{n,(i,j)}^{\text{ND(SK)}}$ ;

$$\Phi_n^{\text{ND(SK)}}(W) = \sum_{(i,j)=1}^{50} W_{(i,j)} \cdot \phi_{n,(i,j)}^{\text{ND(SK)}} \quad (6.2)$$

The  $n$ -th bin of  $F/N$  ratio,  $R_n(W)$ , is obtained by

$$R_n(W) = \frac{\Phi_n^{\text{SK}}(W)}{\Phi_n^{\text{ND}}(W)} \quad (6.3)$$

Since the PIMON data are available only above 2 GeV/c, the neutrino fluxes and the  $F/N$  ratio above the neutrino energy of 1 GeV can be obtained from the PIMON data.

Fig. 6.4 shows the results of the extraction of the neutrino spectra and the  $F/N$  ratio from the PIMON data for June 1999 and Nov. 1999 runs. The predictions of the Beam-MC are also shown in this figure. The errors on the measurements quoted in the plots include all the estimated systematic uncertainties in the PIMON measurements, which are described in Appendix C. The Beam-MC predictions are consistent with the results of the PIMON measurements. Therefore, the Beam-MC is used to calculate the central values of the neutrino spectrum and  $F/N$  ratio for whole energy region, while their errors estimated by PIMON is used for the region above 1 GeV. The errors on the region below 1 GeV are estimated using the Beam-MC by varying the value of parameters in Eq. (4.4) within 90% C.L.

## 6.4 Systematic errors on the PIMON measurements

Systematic errors on the neutrino spectra at ND and SK and  $F/N$  ratio due to various sources are estimated in the PIMON analysis. The methods to estimate them are described in detail in [35], and also briefly explained in Appendix C. The errors on the spectra at ND and SK in

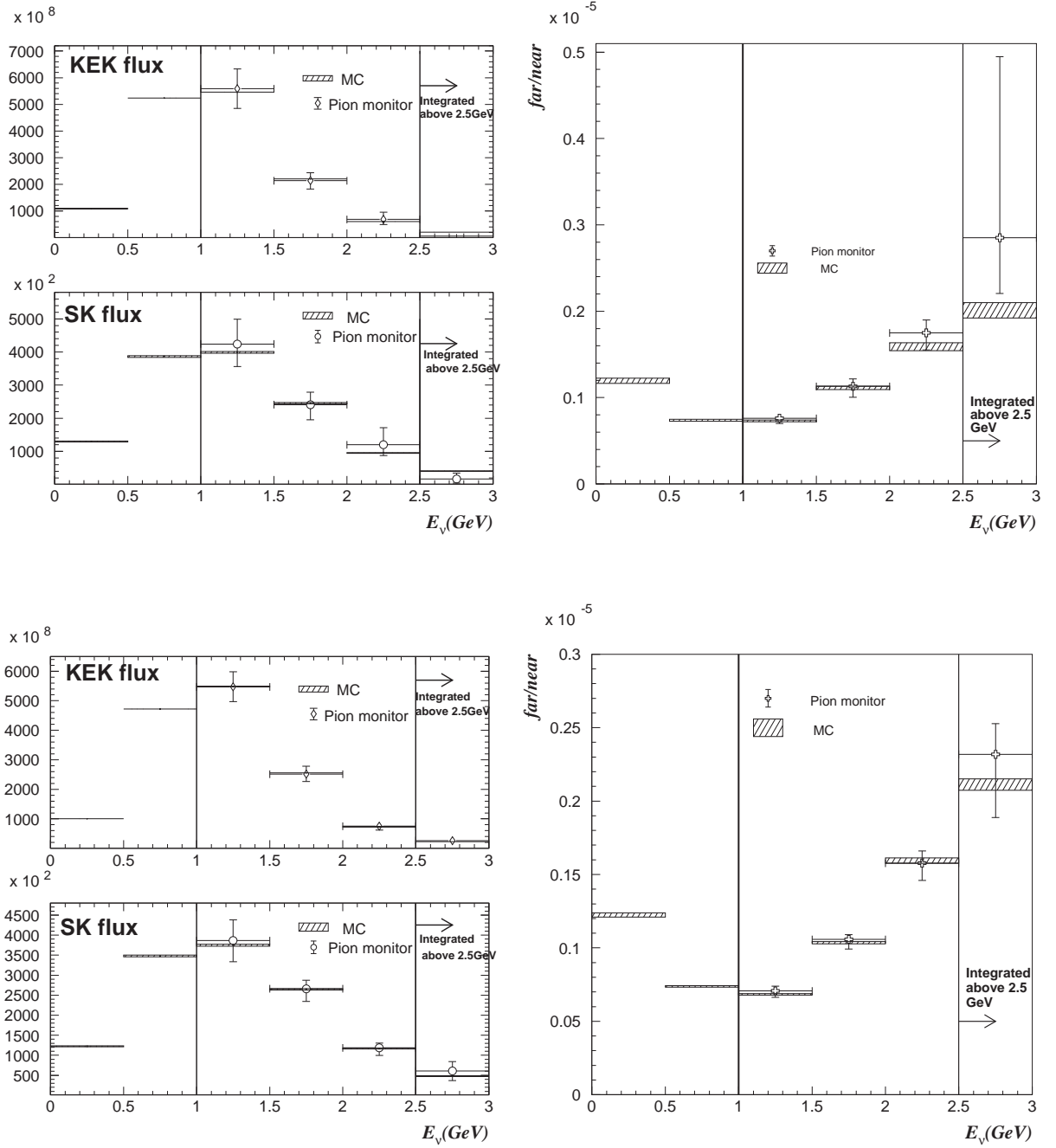


**Figure 6.4:** The neutrino energy spectrum at ND and SK and  $F/N$  ratio for June 1999 and Nov. 1999 runs. Upper two figures are for June 1999 run and lower two figures are for Nov. 1999 run. In both runs, the left upper figure is the neutrino energy spectrum at KEK (300 m downstream the target), the left lower one is that at SK (250 km downstream the target), and the right figure is the  $F/N$  ratio as a function of the neutrino energy. In all figures, cross points with error bars show the results of PIMON measurements and hatched boxes show the prediction of the Beam-MC. The normalization of the neutrino energy spectra between data and MC is done by their entries above 1 GeV at KEK.

June 1999 and in Nov. 1999 are separately summarized in Table C.1, and Table C.2, and the errors on  $F/N$  ratio are summarized in Table C.3. These errors are used in the ND analysis to estimate the errors on the expected number of neutrino events in SK, which is described in Chapter 7, and also used in the oscillation analysis described in Chapter 9. Furthermore, for the spectral studies in the oscillation analysis, the errors on  $F/N$  ratio in Nov. 1999 are re-estimated and expressed in the form of error matrix, which is described in the next section.

## 6.5 Error matrix for the far-to-near ratio

In order to implement the  $F/N$  ratio into the oscillation analysis and take the correlation between energy bins into account, the errors on  $F/N$  ratio must be expressed in the form of an error matrix. Since only the data taken during K2K-Ib period are used in the spectrum shape analysis, we evaluated the error matrix for K2K-Ib configuration. The description on the derivation of the error matrix of  $F/N$  ratio is given in this section.

### 6.5.1 The form of error matrix

As mentioned before, neutrino energy is divided into two regions in  $F/N$  ratio: One is below 1 GeV where PIMON is insensitive and the errors on  $F/N$  are quoted from hadron production model. The other is above 1 GeV where PIMON is sensitive and the errors are quoted from the uncertainties of PIMON measurements. Since the methods of derivation of errors on  $F/N$  below and above 1 GeV are quite different, uncorrelated errors on these two parts are assumed. Therefore, the error matrix of  $F/N$ ,  $M_{F/N}$ , is assumed to have following form:

$$M_{F/N} = \begin{pmatrix} M_{F/N}^{\text{hadron}} & 0 \\ 0 & M_{F/N}^{\text{PIMON}} \end{pmatrix}, \quad (6.4)$$

where  $M_{F/N}^{\text{hadron}}$  is a  $2 \times 2$  matrix corresponding to 2 bins below 1 GeV (0.0–0.5 and 0.5–1.0 GeV bins), and  $M_{F/N}^{\text{PIMON}}$  is a  $4 \times 4$  matrix corresponding to 4 bins above 1 GeV (1.0–1.5, 1.5–2.0, 2.0–2.5, and >2.5 GeV bins).

### 6.5.2 Error matrix below 1 GeV

In order to evaluate the error matrix below 1 GeV,  $M_{F/N}^{\text{hadron}}$ , several sets of Beam-MC with several sets of Sanford-Wang parameter values are employed [113, 114]. It is derived by adding 4 error matrices; uncertainty in Sanford-Wang fitting, uncertainty in extrapolation of nuclear difference, uncertainty in kaon contribution, and uncertainty in beam properties.

Dominant contribution to neutrinos below 1 GeV come from pions below 2 GeV/c, and hence pion production data of below 2 GeV/c is re-fitted to Sanford-Wang formula given by Eq. (4.4). Then Beam-MCs with several sets of Sanford-Wang parameters were generated, where the parameters were randomly generated so that each parameter has a value within its fitting error with the correlations with other parameters. Using the set of Beam-MC, the covariance matrix for  $F/N$  ratio is calculated.

The data of Cho *et al.* [72] was acquired using Beryllium target, while our production target is made of aluminum. Therefore, we need to extrapolate their data to aluminum one. It makes only small effects.

Contribution of kaons to neutrinos is small, but exists. The errors from this part is estimated by considering the results of [69].

Finally, the effect of the injection point and profile of the proton beam is studied by changing these parameters based on the measurements of the beam monitors.

The error matrices due to these uncertainties are summarized in Table 6.2. By adding these 4 matrices, the total error matrix for the energy below 1 GeV,  $M_{F/N}^{\text{hadron}}$ , is obtained to be

$$M_{F/N}^{\text{hadron}} = \left( \begin{array}{c|cc} & 0.0-0.5 & 0.5-1.0 \\ \hline 0.0-0.5 & 6.603 & -2.7 \\ 0.5-1.0 & -2.7 & 18.14 \end{array} \right) \times 10^{-4} . \quad (6.5)$$

### 6.5.3 Error matrix above 1 GeV

The error matrix for the neutrino energy above 1 GeV,  $M_{F/N}^{\text{PIMON}}$ , is derived from the uncertainties of the PIMON measurements. The errors listed in Table C.3 are included in the matrix. Among the errors, *fitting error*, *mirror reflectivity*, *proton injection point*, *pion decay before PIMON*, *radial distribution of pions*, and *binning of pion kinematics* are relatively small compared to the others, and hence these are treated as non-correlated errors, i.e. non-diagonal elements are set to be zero, and the squared values are added to the diagonal elements. The other errors are re-evaluated by randomly changing the systematic parameters within their errors and generating several sets of Beam-MC with these systematic parameters, and then covariance of  $F/N$  ratio is calculated. The resulting error matrices for the uncertainties treated as correlated ones are summarized in Table 6.3.

In total, the error matrix for the energy above 1 GeV is obtained by summing up all the matrices in Table 6.3 and adding uncorrelated errors to the diagonal elements:

$$M_{F/N}^{\text{PIMON}} = \left( \begin{array}{c|cccc} & 1.0-1.5 & 1.5-2.0 & 2.0-2.5 & > 2.5 \\ \hline 1.0-1.5 & 42.67 & 5.747 & -3.19 & -16.15 \\ 1.5-2.0 & 5.747 & 108.8 & 90.85 & 24.53 \\ 2.0-2.5 & -3.19 & 90.85 & 122.84 & 52.17 \\ > 2.5 & -16.15 & 24.53 & 52.17 & 147.75 \end{array} \right) \times 10^{-4} . \quad (6.6)$$

### 6.5.4 Resulting error matrix of far-to-near ratio

In summary, by referring to Eq. (6.4), (6.5), and (6.6), the error matrix of  $F/N$  ratio becomes following:

$$\text{sign}(M_{F/N})\sqrt{|M_{F/N}|} = \left( \begin{array}{cc|cccc} 2.6 & -1.6 & 0 & 0 & 0 & 0 \\ -1.6 & 4.3 & 0 & 0 & 0 & 0 \\ \hline 0 & 0 & 6.5 & 2.4 & -1.8 & -4.0 \\ 0 & 0 & 2.4 & 10.4 & 9.5 & 5.0 \\ 0 & 0 & -1.8 & 9.5 & 11.1 & 7.2 \\ 0 & 0 & -4.0 & 5.0 & 7.2 & 12.2 \end{array} \right) , \quad (6.7)$$

where 6 columns/rows correspond to 6 bins in the neutrino energy, and the values are expressed in the unit of %. This matrix is used in the oscillation analysis described in Chapter 9.

**Table 6.2:** Components of error matrices contributing to the error matrix of  $F/N$  ratio below 1 GeV,  $M_{F/N}^{\text{hadron}}$ . All values are written in the unit of  $10^{-4}$ .

	Sanford-Wang fitting error		Extrapolation Be $\rightarrow$ Al	
	0.0–0.5 GeV	0.5–1.0 GeV	0.0–0.5 GeV	0.5–1.0 GeV
0.0–0.5 GeV	4.65	–0.92	0.63	–2.58
0.5–1.0 GeV	–0.92	4.07	–2.58	10.60
	Kaon contribution		Beam steering	
	0.0–0.5 GeV	0.5–1.0 GeV	0.0–0.5 GeV	0.5–1.0 GeV
0.0–0.5 GeV	0.07	–0.17	1.25	0.97
0.5–1.0 GeV	–0.17	0.62	0.97	2.85

**Table 6.3:** Error matrices of each uncertainty in the PIMON measurements. Only errors which correlation between bins are taken into account are listed, here. All values are written in the unit of  $10^{-4}$ .

Low and high beam intensity				
	1.0–1.5 GeV	1.5–2.0 GeV	2.0–2.5 GeV	> 2.5 GeV
1.0–1.5 GeV	3.70	4.38	3.35	–4.35
1.5–2.0 GeV	4.38	16.3	7.48	–11.4
2.0–2.5 GeV	3.35	7.48	7.25	–6.60
> 2.5 GeV	–4.35	–11.4	–6.60	12.2
Wavelength dependence of the refractive index				
	1.0–1.5 GeV	1.5–2.0 GeV	2.0–2.5 GeV	> 2.5 GeV
1.0–1.5 GeV	8.13	0.21	1.15	2.65
1.5–2.0 GeV	0.21	9.93	15.1	7.60
2.0–2.5 GeV	1.15	15.1	24.7	12.7
> 2.5 GeV	2.65	7.60	12.7	7.02
Beam stability				
	1.0–1.5 GeV	1.5–2.0 GeV	2.0–2.5 GeV	> 2.5 GeV
1.0–1.5 GeV	5.03	–3.06	–3.41	–5.53
1.5–2.0 GeV	–3.06	14.3	16.4	9.02
2.0–2.5 GeV	–3.41	16.4	20.1	15.3
> 2.5 GeV	–5.53	9.02	10.7	17.2
$\phi$ asymmetry of the horn magnetic field				
	1.0–1.5 GeV	1.5–2.0 GeV	2.0–2.5 GeV	> 2.5 GeV
1.0–1.5 GeV	7.19	10.6	2.26	1.13
1.5–2.0 GeV	10.6	43.5	33.4	19.3
2.0–2.5 GeV	2.26	33.4	35.1	20.2
> 2.5 GeV	1.13	19.3	20.2	11.6
Fitting method				
	1.0–1.5 GeV	1.5–2.0 GeV	2.0–2.5 GeV	> 2.5 GeV
1.0–1.5 GeV	7.65	–6.37	–6.53	–10.0
1.5–2.0 GeV	–6.37	17.2	18.5	14.6
2.0–2.5 GeV	–6.53	18.5	20.7	15.3
> 2.5 GeV	–10.0	14.6	15.3	25.9



# Chapter 7

## Analysis in Near Detector

In the near detector system (ND), the properties of the neutrino beam such as its flux and energy spectrum are measured, which are extrapolated to their expectation in SK by  $F/N$  ratio. The number of neutrino events is measured in 1KT, while the energy spectrum of neutrino beam is measured in whole ND system by combining 1KT and FGD data. In this chapter, first, the method to reconstruct neutrino events in 1KT is given in Sec. 7.1. Then the analysis to obtain the number of neutrino events in 1KT and its extrapolation to the expected number of neutrino events in SK is described in Sec. 7.2 and Sec. 7.3. At last, spectral analysis using both 1KT and FGD is given in Sec. 7.4. to obtain the neutrino energy spectrum at the near site.

### 7.1 Analysis flow in 1KT

First, we describe the analysis flow in 1KT. Fig. 7.1 shows a typical neutrino event observed in 1KT. In order to estimate the number of neutrino interactions occurred in the fiducial volume of 1KT, the data reduction, the event reconstruction process, and event selections are applied to the data taken in 1KT. Furthermore, for the study of neutrino energy spectrum, the neutrino events with only one muon-like Cherenkov ring and with the particle fully contained in the 1KT inner detector is used in order to enhance the charged-current quasi-elastic scattering and to make the energy of the produced muon measurable. In this section, the procedures of the data reduction, the event reconstruction, and event selections for the analysis are provided step by step in the order. The flow chart for the data reduction and event selection in 1KT is shown in Fig. 7.2, while the that for the event reconstruction is shown in Fig. 7.6.

#### 7.1.1 Data reduction

##### (1) On-spill data selection

Among four trigger types taken in 1KT, only on-spill data is used for the analysis, which corresponds to the data synchronized to the neutrino beam timing as described in Sec. 3.5.1.

##### (2) Spills with no pre-activity

If any event, such as cosmic ray, accidentally happens before a beam spill, it occupies the electronics buffer and the real beam event may not be recorded in the electronics. In order to avoid such events, spills which have any activity within  $1.2 \mu\text{sec}$  (duration before the electronics timeout) before the spill are rejected. The fraction of the spills with pre-activity event is about 1.9%. These spills are not counted in the accumulated number of spills and POT.

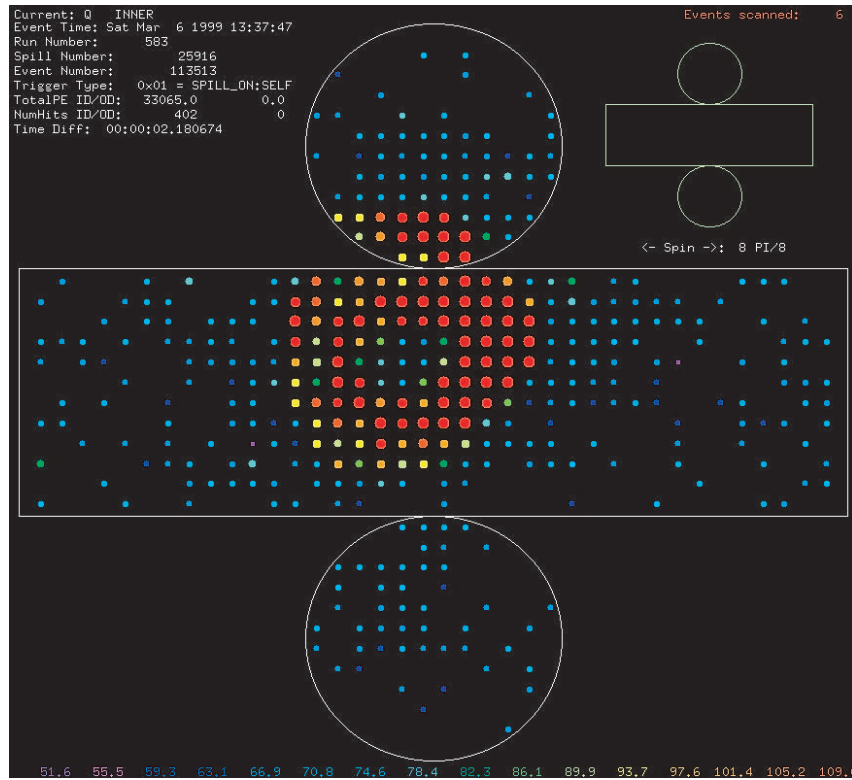


**Figure 7.1:** A typical neutrino event observed in 1KT. This is the expanded view of the cylindrical volume of 1KT. The neutrino beam is directed to the center of this display. Colored circles show the hit PMTs, and the color of each circle correspond to the charge measured in each PMT; violet (red) indicates small (large) charge. The Cherenkov ring pattern is clearly seen around the center of the display.

### (3) Low energy event rejection

Events with low visible energy are not reconstructed in our reconstruction method. The events with the total number of photoelectrons less than 200 photoelectrons are rejected.

The events which satisfy the criteria up to here will be reconstructed using our reconstruction method described later. However, after the event reconstruction, further selection criteria independent from the reconstruction results are imposed to select the events for the analysis, as following.

### (4) Good spill selection

Spills with good beam condition is selected. The criteria for good beam are described in Sec. 5.2.

### (5) Total photoelectrons threshold

Using the pulse shape of PMTSUM signal recorded by FADC (ref. right lower figure in Fig. 7.3), peaks in FADC are searched. The threshold of pulse height to search for a peak is set to be at 1,000 photoelectrons, which is equivalent to a visible energy of about 100 MeV. With this criteria, the background events with lower energy such as an electron from muon decay (which

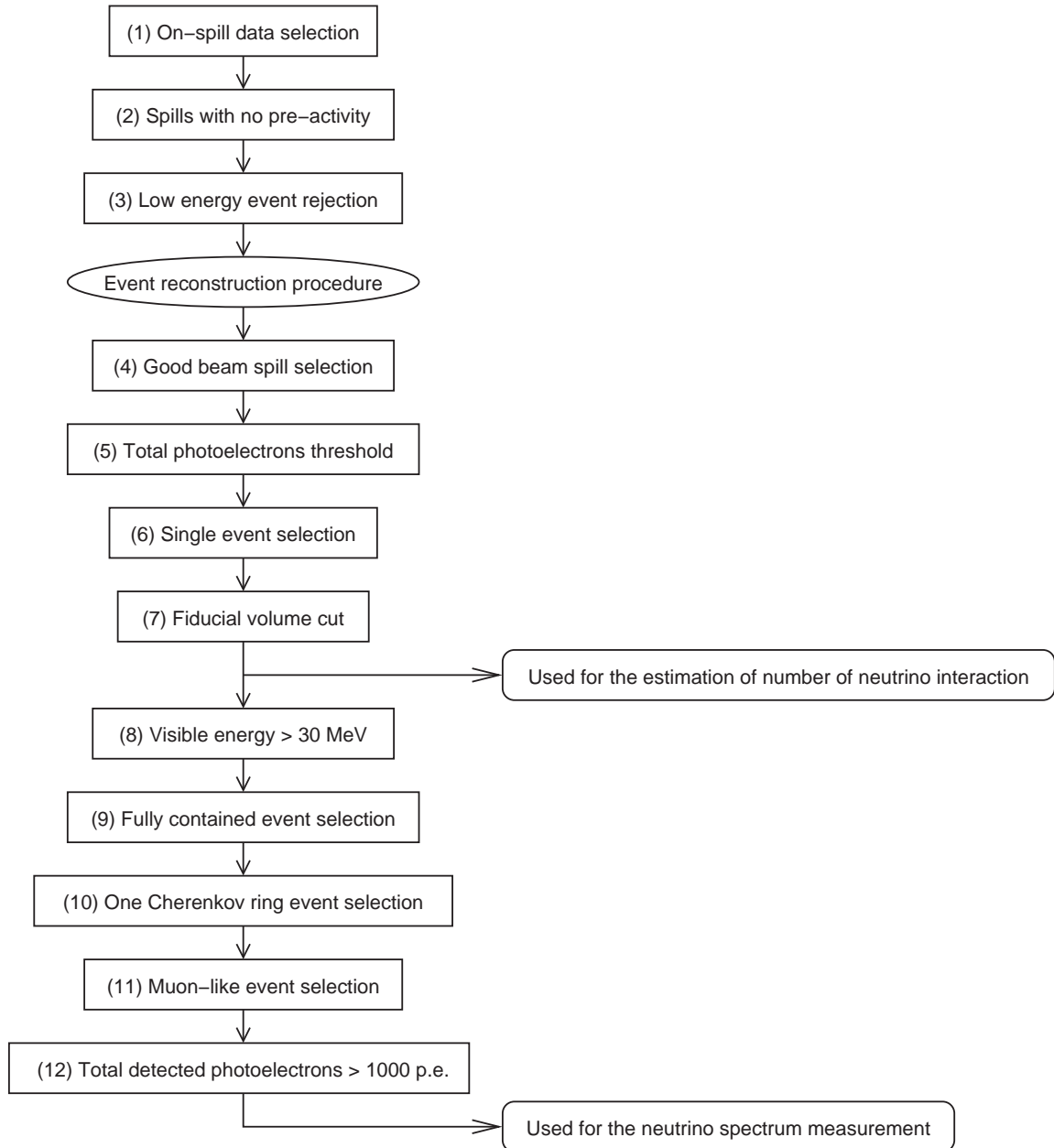


**Figure 7.2:** A flow chart of data reduction and event selection in the 1KT analysis. The event sample remaining after the selection (7) is used to estimate the number of neutrino interactions in 1KT fiducial volume, while that remaining after all the selection is used to estimate the neutrino energy spectrum at the near site.

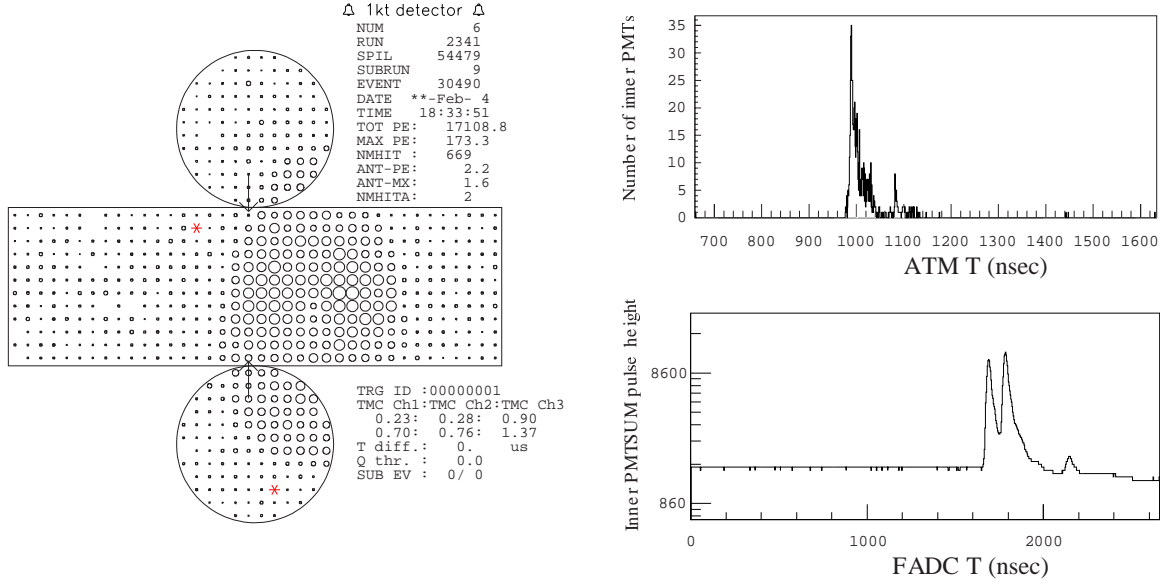


**Figure 7.3:** A typical event display (left), the distributions of PMT hit timing recorded by ATM (right upper) and its PMTSUM signal recorded by FADC (right lower) for multiple event in a beam spill. In the event display, there are two rings which originated from two neutrino interactions in a spill. Their corresponding peaks in PMTSUM can be seen in the FADC data, whereas separation between these events are not clear in the ATM timing distribution.

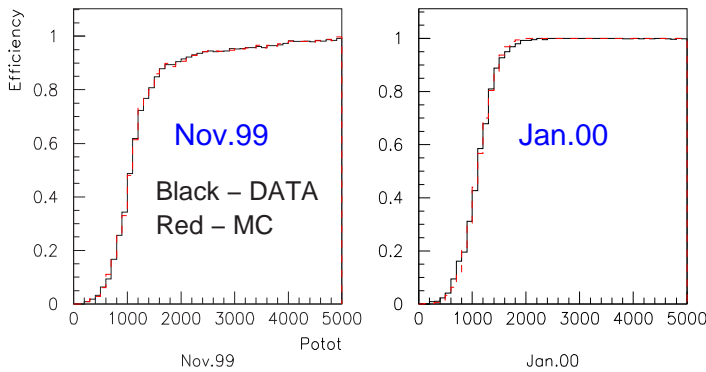


**Figure 7.4:** The efficiency curve for the FADC peak search as a function of the total number of photoelectrons. Horizontal axis shows the total number of photoelectrons observed by ID-PMTs. Left figure is the efficiency curve for data in Nov. 1999 in which 1/4 of PMTSUM signal was not connected to FADC by mistake. Right figure is a typical efficiency curve for data taken by normal situation.

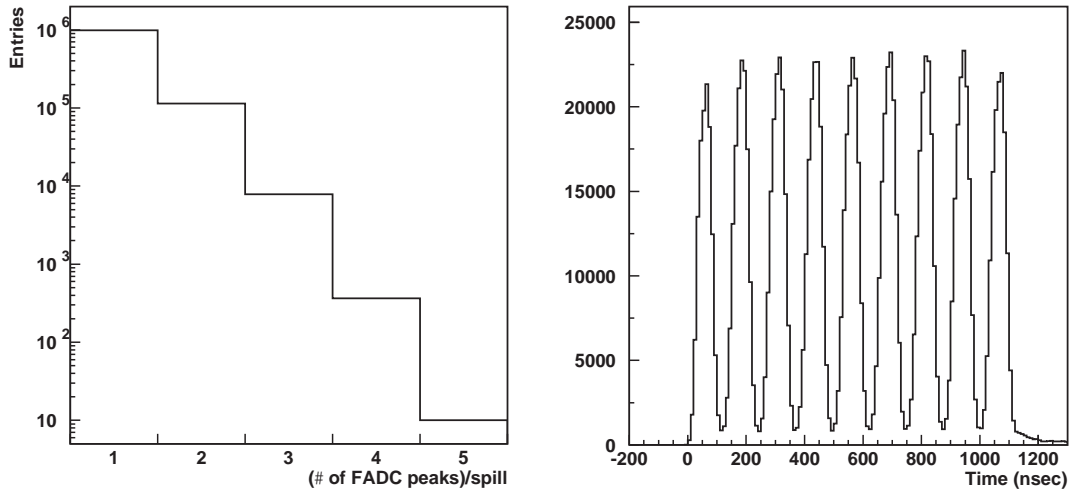


**Figure 7.5:** The number of PMTSUM peaks per spill counted using FADC data (left) and the peak timing distribution (right). The 9-bunch micro structure of spill can be clearly seen in the right figure.

have energy typically less than 52 MeV) are eliminated. Fig. 7.4 shows the efficiency curve for the FADC peak search. The efficiency is rising up around 1,000 photoelectrons and become flat to be unity in larger photoelectron region. In Nov. 1999, the 1/4 of PMTSUM signal was not connected to FADC by a mistake, and hence the behavior of the efficiency curve is different from that in the rest of the periods, as shown in the figure. For this reason, the selection efficiency was decreased by 3.5% for the data in Nov. 1999.

#### (6) Single event selection

The spills which contain only one event are selected since it is hard to reconstruct the vertices of multiple events separately. Fig. 7.3 shows a typical event display for multiple events in a spill, where clear two peaks can be seen in the FADC data. The number of events in a spill is measured by counting the peak of PMTSUM signal in FADC. Fig. 7.5 shows the distribution of the number of PMTSUM peaks per spill counted by the FADC peak search and the peak timing distribution, where the 9-bunch micro structure of spill can be clearly seen. The spills which have only single peak in PMTSUM are selected as spills with single neutrino event. The fraction of spills with multiple events is about 10%, and it is taken into account for the estimation of total number of neutrino interactions in 1KT.

#### 7.1.2 Event reconstruction in 1KT

The vertex point of interaction, the number of Cherenkov rings, and the direction and momentum of each Cherenkov ring are reconstructed for the spill data which satisfy the selection criteria up to (3) mentioned above. Following procedures are applied to reconstruct an event. The detailed description for each reconstruction procedure is provided in Appendix B, and hence the brief explanation of the reconstruction method is given here. A flow chart of the event reconstruction is shown in Fig. 7.6.

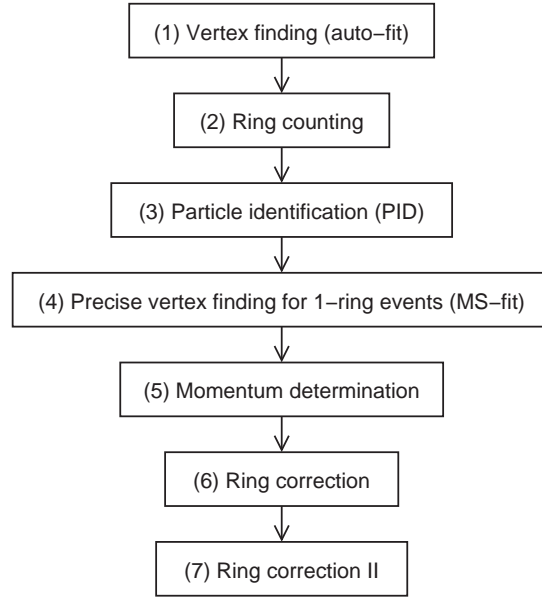


**Figure 7.6:** A flow chart of the event reconstruction in 1KT.

### (1) Vertex finding (auto-fit)

First, the interaction vertex point in each event is determined as a point at which the timing residual (detected time minus time of flight of Cherenkov light) distribution of hit PMTs has the sharpest peak by assuming a point-like source of Cherenkov light (point-fit). Next, the direction and the outer edge of the dominant ring is estimated using the detected photoelectron distribution as a function of polar angle with respect to the vertex point (ring edge search). Then the vertex point and the direction of the dominant ring is more precisely fitted by taking into account the track length of the charged particle (TDC-fit). These three steps are together called “auto-fit”.

### (2) Ring counting

With the knowledge of the vertex point and the direction of the dominant ring, the other possible rings are searched using the Hough transformation. Each ring candidate is tested whether the ring is really ring-like or not by a likelihood method, and the number of rings in each event is determined. Events which have only one reconstructed Cherenkov ring are called “single-ring” events, and those which have reconstructed rings greater than one are called “multi-ring” events.

### (3) Particle identification (PID)

Each ring in a event is classified into two types, showering type ( $e$ -like) or non-showering type ( $\mu$ -like) using the pattern and the opening angle of the ring image. The showering type ring is a candidate for  $e^\pm$  or  $\gamma$ , and the non-showering type ring is a candidate for  $\mu^\pm$  or  $\pi^\pm$ . Fig. 7.7 shows the distribution of PID estimator  $\mathcal{P}_1$  in Eq. (B.20) for the CC-qe single-ring events of muon and electron neutrinos estimated by a Monte Carlo simulation. The muon events and the electron events are clearly separated by the PID algorithm. According to our Monte Carlo simulation, 0.7% of muon neutrino events with single-ring is mis-identified as  $e$ -like events, and

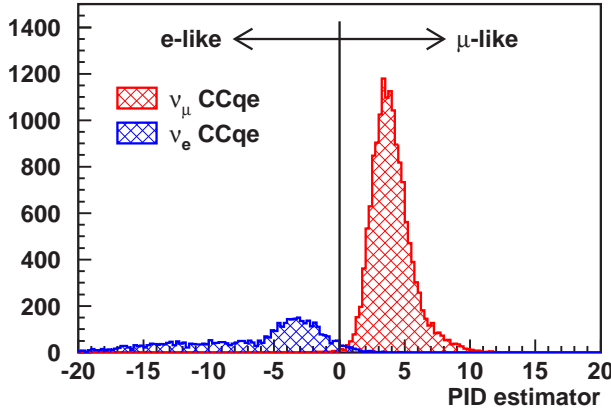


**Figure 7.7:** The distribution of PID estimator for the CC-qe single-ring events of muon and electron neutrino in 1KT. Red (blue) histogram is for muon (electron) neutrino events. Events with the PID estimator  $\mathcal{P}_1$  greater (less) than zero are defined as  $\mu$ -like ( $e$ -like) events. As shown in the figure, the type of particles is almost correctly identified by our algorithm. These distributions are estimated by our Monte Carlo simulation.

3.7% of electron neutrino events with single-ring are mis-identified as  $\mu$ -like ones.

#### (4) Precise vertex finding for single-ring events (MS-fit)

For single-ring events, the precision of vertex point determination in auto-fit is worse in the longitudinal direction, since the sharpness of the time residual distribution is not sensitive to the vertex point shift in the longitudinal direction. Assuming the PID of the Cherenkov ring determined in the previous step, the vertex point is more precisely fitted using the pattern information of the ring image. This algorithm is called “MS-fit”.

The resolution of the vertex reconstruction of MS-fit estimated by a Monte Carlo simulation is shown in Fig. 7.8. The resolutions for the single-ring FC events (in which all the secondary particles generated in neutrino interaction are fully contained in the inner detector of 1KT. See Sec. 7.4.1.), the single-ring PC events (in which some of the secondary particles generated in neutrino interaction are going outside the inner detector of 1KT), the multi-ring FC events, and the multi-ring PC events are separately shown. For single-ring FC/PC events, to which MS-fit is applied, the vertex resolution is 17.3 cm, while it is 33.1 cm and 35.3 cm for FC and PC multi-ring events, respectively, for which events auto-fit result is used as the reconstructed vertex point. Fig. 7.9 shows the resolution of the ring direction also estimated by our Monte Carlo simulation. The distributions of angle between the true muon direction and the reconstructed ring direction for CC-qe single-ring FC and PC events are separately plotted. The directional resolution is  $1.80^\circ$  for FC events and  $1.47^\circ$  for PC events.

Hereafter, we use MS-fit vertex point for single-ring events and auto-fit vertex point for multi-ring events as the reconstructed vertex point of each event.

#### (5) Momentum determination

The momentum of each ring is determined by the number of photoelectrons inside the Cherenkov ring. The conversion factor from the number of photoelectrons to the momentum is estimated based on a Monte Carlo simulation, which is validated by cosmic ray calibration (as described in Sec. 3.5.1). Fig. 7.10 shows the momentum resolution of single-ring  $\mu$ -like events as a function of muon momentum. The resolution is about 2.0–2.5% in the whole momentum range of 1KT.

#### (6) First correction to the number of rings (ring correction)

A mis-fitted ring tends to have low momentum. Rings which have low momentum and overlapped with the other energetic rings are discarded since they are possibly caused by mis-fit and are

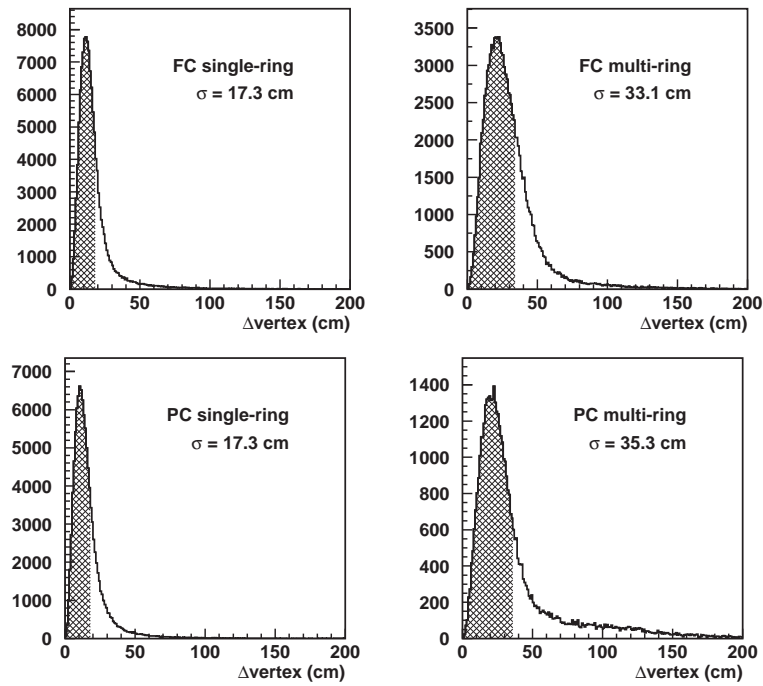


**Figure 7.8:** The resolution of the vertex reconstruction for fully contained (FC) and partially contained (PC) single-ring and multi-ring events in 1KT. Horizontal axis is the distance between the true vertex point and the reconstructed vertex point. The hatched area shows the region in which the 68% of events are contained, defining the  $1\sigma$  of the resolution. These figures are estimated by our Monte Carlo simulation.

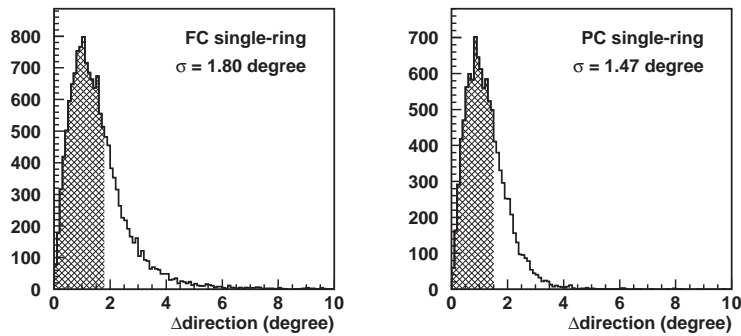


**Figure 7.9:** The resolution of the ring direction reconstruction for fully (FC) and partially (PC) contained single-ring events in 1KT. Horizontal Axis is the angle between the true muon direction and the reconstructed ring direction for CC-qe events. The hatched area shows the region in which the 68% of events are contained, defining the  $1\sigma$  of the resolution. These figures are estimated by our Monte Carlo simulation.



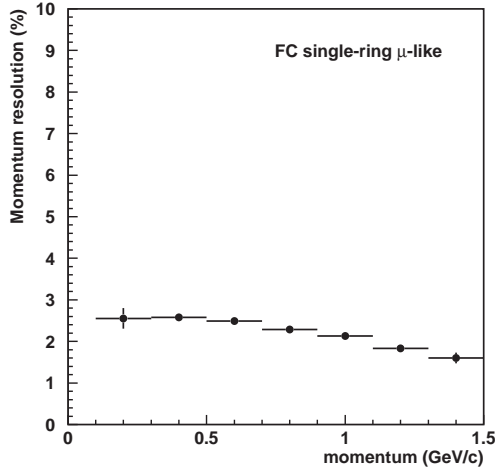


**Figure 7.10:** Momentum resolution for single-ring  $\mu$ -like FC events in 1KT as a function of muon momentum. Single-ring  $\mu$ -like FC events of CC-qe interaction in our Monte Carlo simulation are used to estimate the resolution.

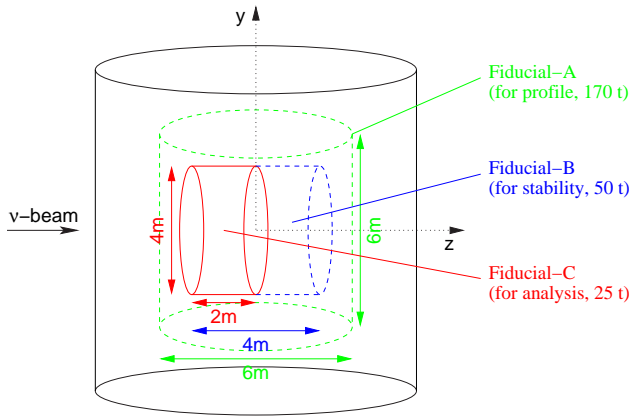


**Figure 7.11:** Definition of the fiducial volumes used in 1KT analysis. Fiducial-A and B are used to measure the neutrino beam profile and event rate stability, respectively. Fiducial-C is used in main analyses to measure the number of neutrino interactions and the energy spectrum of the neutrino beam.

not real rings.

### (7) Second correction to the number of rings (ring correction II)

In 1KT, we have sometimes very large hits which seem to be caused by electric noise and seem not to be associated to any Cherenkov rings. These hits makes a fake (mis-fitted) ring. In the two ring events, a ring candidate which contains hits with large charge and isolated from the other Cherenkov ring is removed as a fake ring.

#### 7.1.3 Fiducial volume in 1KT analysis

After all the data reduction and the event reconstruction procedures are applied, events which vertex point is reconstructed to be inside the fiducial volume are selected for analysis in order to select neutrino interactions inside 1KT.

Three different fiducial volumes are defined and used for different purposes. The definition of each fiducial volume is as follows, as well as shown in Fig. 7.11.

- (a) Fiducial-A, for the measurements of the neutrino beam profile. Cylindrical volume with the radius of 3 m and the height of 6 m, oriented perpendicular to the beam direction and centered at the center of 1KT ID tank. The fiducial mass is 170 t.

- (b) Fiducial-B, for the measurements of the stability of neutrino event rate. Cylindrical volume with the radius of 2 m and the length of 4 m, oriented along the beam direction and centered at the center of ID tank. The fiducial mass is 50 t.
- (c) Fiducial-C, for the measurements of the number of neutrino interactions and the energy spectrum of the neutrino beam. Cylindrical volume with the radius of 2 m and the length of 2 m, oriented along the beam direction, an upper stream half of Fiducial-B. The fiducial mass is 25 t.

## 7.2 Number of neutrino interactions in 1KT

In order to make a prediction for the number of neutrino events in SK, neutrino flux is measured by counting the number of neutrino interactions in 1KT. A merit to use 1KT for this purpose is that most of systematic uncertainties are canceled out because of the same interaction target (water) and the same detection techniques. The description on the measurements of the number of neutrino interactions in 1KT is provided in this section.

### 7.2.1 Outline to obtain the number of neutrino interactions in 1KT

At first, the number of neutrino events which are reconstructed in the fiducial volume Fiducial-C is counted using data which passed all the reduction steps mentioned in Sec. 7.1.1. This number is referred as the number of observed events in 1KT,  $N_{\text{obs}}^{1\text{KT}}$ .

Next, using pulse shape information measured by FADC, the number of spills which have only one peak in FADC ( $N_{\text{peak}}^1$ ) and the total number of peaks ( $N_{\text{peak}}^{\text{total}}$ ) observed in FADC are counted, which is shown in Fig. 7.5.

Then, the total number of neutrino interaction in Fiducial-C,  $N_{\text{int}}^{1\text{KT}}$ , is calculated by

$$N_{\text{int}}^{1\text{KT}} = N_{\text{obs}}^{1\text{KT}} \cdot \frac{N_{\text{peak}}^{\text{total}}}{N_{\text{peak}}^1} \cdot \frac{1}{\epsilon_{\nu_\mu}^{1\text{KT}}} \cdot \frac{1}{1 + R_{\text{B.G.}}} \cdot C_{\text{multi}} (\cdot C_{7 \rightarrow 9}) \quad , \quad (7.1)$$

where

$\epsilon_{\nu_\mu}^{1\text{KT}}$  : detection and selection efficiency for muon neutrino interactions in 1KT.

$R_{\text{B.G.}}$  : fraction of background contamination into the selected events.

$C_{\text{multi}}$  : correction factor for multiple events in a spill which could not be identified as multiple events in the FADC peak search.

$C_{7 \rightarrow 9}$  : correction factor for 7-bunch analysis for the data taken during May and June 2000, as described in Sec. 7.2.6.

The number  $N_{\text{int}}^{1\text{KT}}$  is used to predict the number of neutrino events expected to be observed in SK, as described in Sec. 7.3.

### 7.2.2 Event selection for neutrino interaction in the fiducial volume

Using the reconstructed information, further selections are imposed upon the data remaining in the data reduction described in Sec. 7.1.1 in order to obtain the number of neutrino events in Fiducial-C,  $N_{\text{obs}}^{1\text{KT}}$ .

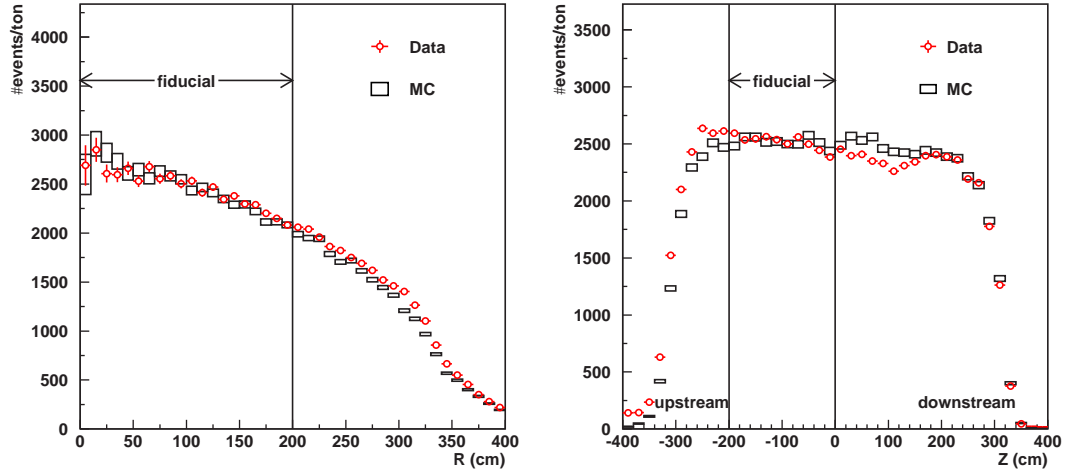


**Figure 7.12:** The distributions of the reconstructed vertex in the radius direction (left) and the beam directions (right). Red circles with error bars show data and black boxes show a Monte Carlo simulation. The events which vertex satisfies that  $R = \sqrt{x^2 + y^2} < 200$  cm and  $-200$  cm  $< z < 0$  cm are selected as the events taking place inside the fiducial volume.

First, in order to ensure that events are correctly reconstructed, the events which have rings equal to or greater than one are selected. Furthermore, since event tends to be misreconstructed if its point-fit vertex is near the wall of the ID tank, the events which point-fit vertex is settled more than 30 cm away from the wall are selected. Then fiducial volume cut to select the events in Fiducial-C is imposed onto the remaining events. Fig. 7.12 shows the reconstructed vertex distributions in the radius direction and the beam direction. As shown in the figure, the criteria on the fiducial volume is that the reconstructed vertex is inside Fiducial-C;  $R = \sqrt{x^2 + y^2} < 200$  cm and  $-200$  cm  $< z < 0$  cm, where  $x$  and  $y$  are the coordinates transverse to the beam direction, and  $z$  is that along the beam direction as shown in Fig. 7.11. Small discrepancy seen in the  $z$  distribution is taken into account for the systematic uncertainty in the fiducial volume cut, which is described in Sec. 7.2.8.

By counting the number of events remaining after these cuts, the number of observed neutrino interactions,  $N_{\text{obs}}^{1\text{KT}}$ , is obtained. In total, 80,024 events are observed in Fiducial-C during the whole run period from June 1999 to July 2001. Table 7.1 summarizes month-by-month observed number of neutrino events, separately.

### 7.2.3 Event selection efficiency

Fig. 7.13 shows the event selection efficiency for Fiducial-C as a function of  $R$ ,  $z$ , and the incident neutrino energy  $E_\nu$ . The averaged efficiency for all interaction modes is about 71% for runs in 1999 and about 75% for runs in 2000 and 2001. The efficiency for each month is also summarized in Table 7.1.

### 7.2.4 Background rate in the selected events

Expected source of backgrounds are cosmic ray muons and beam neutrino induced incoming muons. In addition to them, we had reflection pulse in the signal cables in 1999 runs, which made fake events. These background contaminations are estimated as follows.

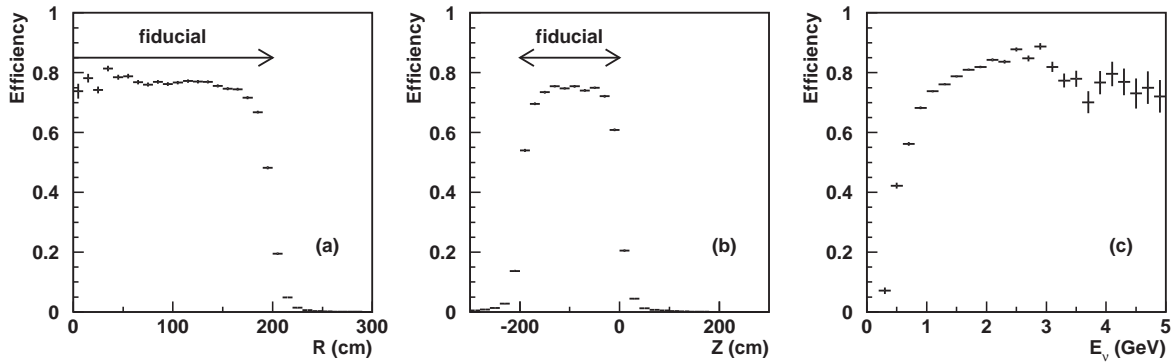
**Table 7.1:** Summary of the number of interactions measured in 1KT.

period	Jun.'99	Nov.'99	Jan.'00	Feb.'00	Mar.'00	May.'00	Jun.'00
Target diameter	2 cm $\phi$	3 cm $\phi$					
Horn current	200 kA	250 kA					
POT <sub>1KT</sub> ( $\times 10^{18}$ )	2.60	2.62	1.81	3.74	3.35	2.42	3.17
# total peaks ( $N_{\text{peak}}^{\text{total}}$ )	109,119	118,321	85,155	174,224	155,643	88,445	114,688
Single event ( $N_{\text{peak}}^1$ )	89,782	96,304	67,678	139,241	122,700	74,227	95,888
Efficiency ( $\epsilon_{\nu_\mu}^{\text{1KT}}$ )	0.706	0.708	0.743	0.748	0.743	0.742	0.742
Background rate ( $R_{B.G.}$ )	0.031	0.031	0.015	0.015	0.015	0.015	0.015
Multi-event corr. ( $C_{\text{multi}}$ )	1.008	1.008	1.008	1.008	1.008	1.008	1.008
7 to 9-bunch corr. ( $C_{7 \rightarrow 9}$ )	—	—	—	—	—	1.282	1.283
# observed events ( $N_{\text{obs}}^{\text{1KT}}$ )	4,282	4,923	3,576	7,139	6,234	3,705	4,933
# interaction ( $N_{\text{int}}^{\text{1KT}}$ )	7,206	8,351	6,013	11,857	10,567	7,573	10,130
Event rate ( $/10^{15}$ POT)	2.77	3.19	3.32	3.17	3.16	3.13	3.20

period	Jan.'01	Feb.'01	Mar.'01	Apr.'01	May.'01	Jun.'01	Jul.'01
Target diameter	3 cm $\phi$						
Horn current	250 kA						
POT <sub>1KT</sub> ( $\times 10^{18}$ )	2.92	4.75	4.27	2.47	1.60	5.79	1.43
# total peaks ( $N_{\text{peak}}^{\text{total}}$ )	136,372	229,826	207,066	120,324	75,864	27,597	67,719
Single event ( $N_{\text{peak}}^1$ )	11,0867	182,166	163,502	95,032	60,113	220,087	53,606
Efficiency ( $\epsilon_{\nu_\mu}^{\text{1KT}}$ )	0.745	0.745	0.745	0.745	0.745	0.745	0.745
Background rate ( $R_{B.G.}$ )	0.015	0.015	0.015	0.015	0.015	0.015	0.015
Multi-event corr. ( $C_{\text{multi}}$ )	1.008	1.008	1.008	1.008	1.008	1.008	1.008
7 to 9-bunch corr. ( $C_{7 \rightarrow 9}$ )	—	—	—	—	—	—	—
# observed events ( $N_{\text{obs}}^{\text{1KT}}$ )	5,746	9,213	8,228	4,743	3,113	11,430	2,759
# interaction ( $N_{\text{int}}^{\text{1KT}}$ )	9,420	15,491	13,888	8,004	5,236	19,102	4,645
Event rate ( $/10^{15}$ POT)	3.23	3.26	3.26	3.24	3.27	3.30	3.26

$$\text{In total : } N_{\text{obs}}^{\text{1KT}} = 80,024$$

$$N_{\text{int}}^{\text{1KT}} = 137,483 \pm 486(\text{stat.}) \pm 5,971(\text{syst.})$$

**Figure 7.13:** Event selection efficiency for Fiducial-C as a function of  $R$ ,  $z$ , and the incident neutrino energy  $E_\nu$ . These are estimated by the Monte Carlo simulation with the configuration since Jan. 2000.

### Cosmic ray muons

The rate of cosmic ray muon contamination is estimated by using randomly triggered data (off-spill trigger). The data was analyzed by the same selection procedures as is done for on-spill data. The contamination of cosmic ray muons into the beam neutrino candidates in Fiducial-C is estimated to be 1.0%.

### Beam neutrino induced incoming muons

On-spill data contains neutrino induced incoming muons, which are generated by neutrino interaction in materials surrounding 1KT tank such as upstream concrete wall of the experimental hall. Most of such muons are coming from upstream of 1KT and penetrate the front side outer detector with making hits in OD-PMTs. Some of the selected neutrino candidates in Fiducial-C were investigated by visually looking at OD hits with the event display (or “eye scanning”). The contamination of beam induced incoming muons is estimated to be 0.5%.

### Reflection pulse in 1999 runs

The reflection pulses in signal cables existed in June and Nov. 1999 runs, making fake events. This problem was fixed by installing buffer amplifiers on ATM input in Jan. 2000 as mentioned in Sec. 3.5.1. The fraction of fake events by reflection pulses during the period before installation of buffer amplifiers is estimated to be 2.6%

In total, background contamination  $R_{B.G.}$  is estimated to be 3.1% and 1.5% for 1999 runs and 2000–2001 runs, respectively, as is also summarized in Table 7.1.

#### 7.2.5 Multi-event correction

In order to extrapolate  $N_{obs}^{1KT}$  by using single peak events in FADC to the total number of interactions in 1KT  $N_{int}^{1KT}$ , the correction factor  $N_{peak}^{total}/N_{peak}^1$  is multiplied to the observed number of events in Fiducial-C. However, since there are a small fraction of multiple events which are not identified as multiple events by the FADC peak search, further correction is needed. In a Monte Carlo simulation, multiple events are generated and the pulse shape of PMTSUM recorded in FADC is also simulated. Then, by employing the same analysis method as data, total number of neutrino interactions in Fiducial-C is estimated, and it is compared with the number of neutrino interaction generated in the Fiducial-C; a fraction of 97.7% events are correctly counted. Among the total number of interactions, the fraction of multiple interactions is estimated to be 0.34, and hence a fraction of mis-counted events is  $(1 - 0.977) \times 0.34 = 0.0078$ . Therefore the correction factor  $C_{multi}$  is estimated to be  $1/(1 - 0.0078) = 1.008$ .

#### 7.2.6 Correction from 7 to 9-bunch for data in May and June 2000

Left figure in Fig. 7.14 shows the FADC peak timing distribution of each event spill observed in May and June 2000 runs. As shown in the figure, the 8th and 9th bunches were sometimes lost. This is due to that the stop-timing signal of FADC was unstable and drifted over a few 100 nsec in this period. Neutrino events in the first 7 bunches are used to obtain the total number of neutrino interactions during this period to avoid uncertainty of the gate window. This effect is corrected by a correction factor,  $C_{7-9}$ . This factor is the ratio of the number of events in the 1–9th bunches to that in the 1–7th bunches, and is obtained using only the data taken during the period when the stop-timing signal was not drifted. The stability of the correction factor

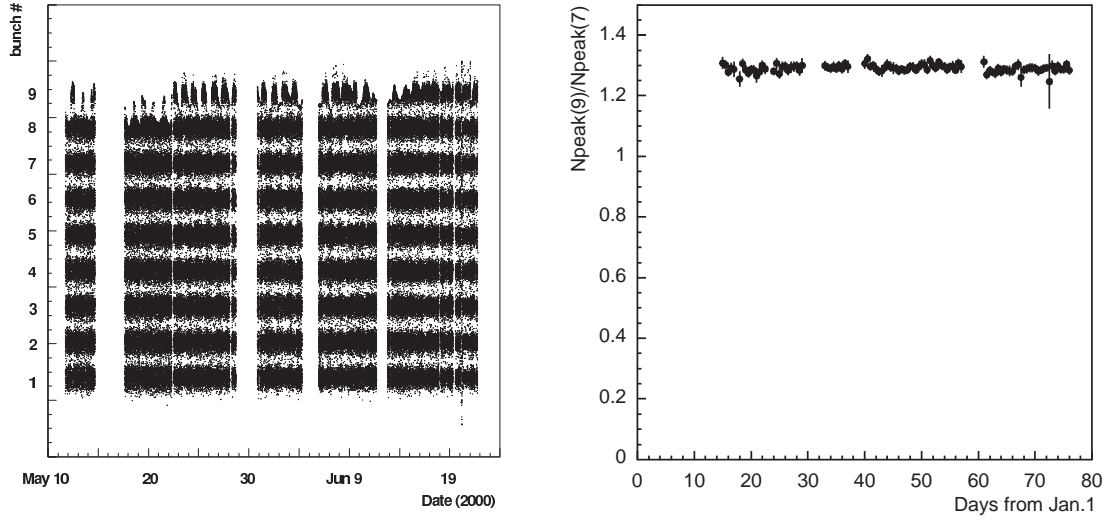


**Figure 7.14:** The distribution of FADC peak timing for each event spill observed from May 2000 to June 2000 (left) and the correction factors for 7 to 9 bunches obtained in January to March 2000 (right). In the left figure, Vertical axis is the peak time of FADC (or bunch number) and horizontal axis is the date from 10 May to 24 June, 2000. The 8th and 9th bunches were sometimes lost due to the drift of the stop-timing signal of FADC. In the right figure, the correction factors  $C_{7 \rightarrow 9}$  during Jan. to Mar. 2000 are stable within 0.4%.

had been confirmed to be within 0.4% during the run period as shown in the right figure of Fig. 7.14.

### 7.2.7 Total number of interactions in 1KT

After all the correction factors and detection efficiency are substituted into Eq. (7.1), the total number of interactions in Fiducial-C,  $N_{\text{int}}^{\text{total}}$ , is estimated to be  $137,483 \pm 486(\text{stat.})$ . Month-by-month total number of interactions is summarized in Table 7.1 together with the number of protons on target for the analysis POT<sub>1KT</sub>, total number of peaks in FADC, number of spills with single peak, number of observed events, event rate, and so on.

Fig. 7.15 shows the stability of neutrino event rate measured in 1KT. The intensity of neutrino beam was also lower in June 1999 than other period due to lower horn magnet current in June 1999. The event rate had been stable within 6%, which is used to estimate the error on the correction of the number of POT used in 1KT to that used in SK as expressed in Eq. (5.8) in Sec. 5.2.3.

### 7.2.8 Systematic errors on the number of neutrino interaction in 1KT

Systematic errors on the total number of neutrino interaction in Fiducial-C in 1KT are explained in this section, which are summarized in Table 7.2.

#### Uncertainty of fiducial volume cut

The performance of the vertex fitter in 1KT had been experimentally studied using cosmic ray muons [44]. In this study, a pipe was installed into the 1KT tank which optically separates

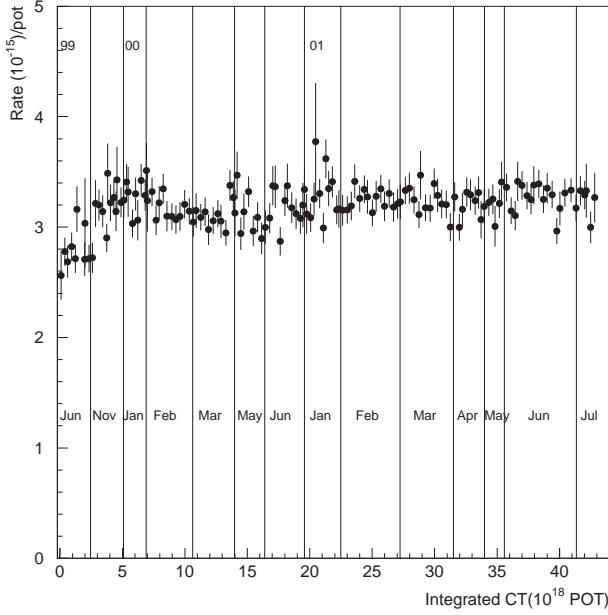


**Figure 7.15:** Long term stability of the neutrino event rate measured in 1KT. In June 1999, the event rate was lower than other period due to lower horn magnet current, and hence lower neutrino beam intensity. The stability is estimated to be within 6% during the whole run period.

**Table 7.2:** Summary of systematic errors on the number of interactions measured in 1KT.

period	Jun.'99	Nov.'99	Jan.'00	Feb.'00	Mar.'00	May.'00	Jun.'00
# interaction ( $N_{\text{int}}^{\text{IKT}}$ )	7,206	8,351	6,013	11,857	10,567	7,573	10,130
Fraction	5.24%	6.07%	4.37%	8.62%	7.69%	5.51%	7.67%
Fiducial volume	4.0%						
FADC threshold	1.0%	1.4%	1.0%				
Energy scale	1.0%						
Background rate	1.0%		0.5%				
Multiple-events corr.	0.7%						
7 to 9-bunch corr.	0.0%					1.2%	
Total	4.4%	4.5%	4.3%	4.3%	4.3%	4.5%	4.5%
period	Jan.'01	Feb.'01	Mar.'01	Apr.'01	May.'01	Jun.'01	Jul.'01
# interaction ( $N_{\text{int}}^{\text{IKT}}$ )	9,420	15,491	13,888	8,004	5,236	19,102	4,645
Fraction	6.85%	11.27%	10.10%	5.82%	3.81%	13.89%	3.38%
Fiducial volume	4.0%						
FADC threshold	1.0%						
Energy scale	1.0%						
Background rate	0.5%						
Multi-events correction	0.7%						
7 to 9-bunch correction	0.0%						
Total	4.3%	4.3%	4.3%	4.3%	4.3%	4.3%	4.3%

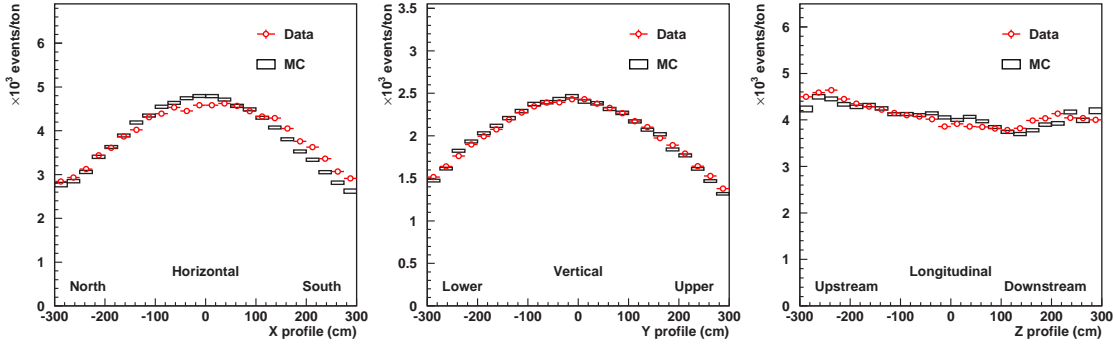


**Figure 7.16:** Reconstructed vertex profile in horizontal (leftmost), vertical (middle), and longitudinal (rightmost) directions in 1KT. The events which vertex is inside Fiducial-A are used, and the difference of target mass in each bin is corrected. In all figures, red crosses are data and black boxes are estimated by a Monte Carlo simulation.

inside and outside the pipe. Cosmic ray muons going through inside the pipe were triggered. The vertex of Cherenkov ring seems to be at the end of the pipe. Using this data, the reconstructed vertex was compared with the true one (end position of the pipe). It is also compared with that in Monte Carlo simulation. The results show that the reconstructed vertex in the transverse direction to the particle track is in good agreement with the true position within a few cm. However the reconstructed vertex point along the particle track direction is shifted from the true position by a few 10 cm in both data and the Monte Carlo simulation, and the size of the shift disagrees between data and the simulation by  $\sim 10$  cm.

In order to quote the error on the number of neutrino interaction due to the known uncertainty in the reconstructed vertex point mentioned above, following method was employed. The profile of reconstructed vertex is analyzed using the selected events in Fiducial-A. Fig. 7.16 shows horizontal ( $x$ ), vertical ( $y$ ), and longitudinal ( $z$ ) vertex profiles, in which the number of events in each bin is corrected by the target mass due to the cylindrical shape of the fiducial volume. Systematic difference between data and the Monte Carlo simulation is clearly seen in horizontal and longitudinal direction, while there is small difference in vertical direction.

For longitudinal direction, by counting the number of events reconstructed in several cylindrical volumes with different lengths in  $z$ , the difference between data and MC is studied as listed in Table 7.3.

For horizontal and vertical direction, there is difference in the center and the width of profiles. The center of the profile in the horizontal direction is  $+9.8$  cm in data and  $-3.7$  cm in MC, and hence there is 13 cm difference between them, while that in the vertical direction is  $-12.3$  cm in data and  $-16.5$  cm in MC, and hence there is 4 cm difference between them. By changing the center of fiducial volume in MC by  $\pm 13$  cm in the horizontal direction and  $\pm 4$  cm in the vertical direction, the difference of the number of events from the default fiducial volume is studied as listed in Table 7.3. The width of profile also have discrepancy by about 13% between data and MC in  $x$ -direction. The same method as the case of the profile center is employed by changing the radius of fiducial volume in MC.

The difference of event rate have settled within 4% in the all studies mentioned above, and hence 4% is taken as the systematic uncertainty of the fiducial volume.



**Table 7.3:** Comparison of event rate in various fiducial volume in 1KT. First column is the definition of fiducial volume, second and third columns are the number of events in each fiducial volume normalized to the target mass of Fiducial-C for data and a Monte Carlo simulation, respectively, and the last column is the ratio of the number of events for data and for the simulation relative to that of Fiducial-C. In the table,  $z$  is the coordinate along the beam direction,  $x_0^{\text{MC}}$  is the center of defined fiducial volume in horizontal direction in MC,  $y_0^{\text{MC}}$  is that in vertical direction in MC, and  $R^{\text{MC}}$  is the radius of defined fiducial volume in MC.

Fiducial volume	Data	MC	Relative Data/MC
Fiducial-C	62,774	74,000	—
$-300 < z < 0$ cm	62,193	70,650	1.037
$-200 < z < 100$ cm	61,284	73,589	0.982
$-200 < z < 200$ cm	60,028	72,747	0.973
$-200 < z < 300$ cm	58,612	70,379	0.982
$x_0^{\text{MC}} = 0 \pm 13$ cm	—	73,819(+13cm) 73,915(−13cm)	0.998(+13cm) 0.999(−13cm)
$y_0^{\text{MC}} = 0 \pm 4$ cm	—	73,972(+4cm) 74,096(−4cm)	0.999(+4cm) 1.001(−4cm)
$R^{\text{MC}} = 200 \pm 25$ cm	—	71,710(+25cm) 76,022(−25cm)	0.969(+25cm) 1.027(−25cm)

### Uncertainty of FADC threshold

The threshold of FADC peak search is set at around 1000 photoelectrons, as shown in Fig. 7.4. The fluctuation of the threshold is estimated to be about 10% for the whole run period. The change in FADC threshold by 10% yield the change in the event rate by 1%, therefore  $\pm 1\%$  is quoted as the systematic uncertainty due to FADC threshold.

In addition, the selection efficiency decreased by 3.5% due to the disconnection of 1/4 part of PMTSUM signal in November 1999 run, as mentioned in Sec. 7.1.1. The uncertainty in the efficiency during this period yields an additional 1% error on  $N_{\text{int}}^{1\text{KT}}$ .

### Uncertainty of energy scale

The uncertainty of absolute energy scale is estimated to be  $^{+2}_{-3}\%$  as described in Sec. 3.5.1. The change in the scale of the total number of photoelectrons detected in 1KT by  $^{+2}_{-3}\%$  yields the change in the event rate by less than 1%, and hence error of  $\pm 1\%$  on the number of the neutrino interactions is assigned as the error due to the uncertainty of the absolute energy scale.

### Uncertainty of background rate

The estimation of the background rate is described in Sec. 7.2.4. The statistical error on the estimation of the background rate is assigned as its systematic uncertainty, which is  $\pm 1.0\%$  in 1999 runs and  $\pm 0.5\%$  in the other runs.

### Uncertainty of multi-event correction

The treatment of multiple events in a spill is described in Sec. 7.2.5. The statistical error in the Monte Carlo study,  $\pm 0.7\%$ , is assigned as the error on the multi-event correction  $C_{\text{multi}}$ .

### Uncertainty of 7 to 9-bunch correction

As mentioned in Sec. 7.2.6, only the events in the first 7 bunches are used for the data taken in May and June 2000 to estimate the number of interactions in 1KT. The statistical error in the calculation of the correction factor  $C_{7 \rightarrow 9}$  is 1%.

In order to validate the 7-bunch analysis method, the same method is applied to the data taken from January to March 2000. The stability of the correction factor  $C_{7 \rightarrow 9}$  during this period is shown in Fig. 7.14. The difference between the event rate estimated by 7-bunch analysis and the standard method is found to be at most 0.4%.

Furthermore, the mis-fitting of vertex point caused by signals which belong to the masked bunches is also considered. When FADC signals in the 8th and 9th bunches are masked, a multi-event may be mis-identified as a single event. Even in these events, the data of each PMT is recorded as usual since ATM gate is about 300 nsec which corresponds to 3 bunches. In such case, the vertex fitter failed to find the vertex point at correct position. Approximately 0.6% of events selected by the 7-bunch analysis is estimated to be in this case, and this value is assigned as the error on the event rate due to 7-bunch analysis.

In total, a systematic error of  $\pm 1.2\%$  is quoted as the uncertainty of the 7-bunch analysis.

All the systematic errors above quadratically summed up, the total systematic error on the number of neutrino interaction in 1KT Fiducial-C during whole period is estimated to be 4.34%.

## 7.3 Expected number of neutrino events in Super-Kamiokande

The total number of interactions estimated in 1KT is extrapolated to the expected number of events in SK. In this section, the method and the results of the extrapolation and the systematic errors on the expected number of events in SK are described.

### 7.3.1 Extrapolation of the number of interactions in 1KT to SK

The expected number of neutrino events in SK ( $N_{\text{exp}}^{\text{SK}}$ ) is derived using the number of neutrino interactions in 1KT ( $N_{\text{int}}^{\text{1KT}}$ ) by following formula,

$$N_{\text{exp}}^{\text{SK}} = N_{\text{int}}^{\text{1KT}} \cdot R_{\text{int}}^{\text{SK/1KT}} \cdot \frac{\text{POT}_{\text{SK}}}{\text{POT}_{\text{1KT}}} \cdot \epsilon_{\text{SK}} \cdot C_{\nu_e} \quad , \quad (7.2)$$

where  $\text{POT}_{\text{SK(1KT)}}$  is the number of protons on target used in the analysis in SK (1KT),  $\epsilon_{\text{SK}}$  is the neutrino detection efficiency in SK averaged over the whole energy of the neutrino beam,  $C_{\nu_e}$  is a factor to correct the effect of the electron neutrino component in the beam, and  $R_{\text{int}}^{\text{SK/1KT}}$  is the ratio of number of neutrino interactions expected in SK to those in 1KT.

### Far-to-near number of neutrino interaction ratio

The  $F/N$  ratio  $R_{\text{int}}^{\text{SK/1KT}}$  is expressed as

$$R_{\text{int}}^{\text{SK/1KT}} = \frac{\int \Phi^{\text{SK}}(E_\nu) \cdot \sigma_{\text{H}_2\text{O}}(E_\nu) \cdot M_{\text{SK}} dE_\nu}{\int \Phi^{\text{1KT}}(E_\nu) \cdot \sigma_{\text{H}_2\text{O}}(E_\nu) \cdot M_{\text{1KT}} dE_\nu} \quad , \quad (7.3)$$

where  $\Phi^{\text{SK(1KT)}}(E_\nu)$  is the neutrino energy spectrum at SK (1KT),  $\sigma_{\text{H}_2\text{O}}(E_\nu)$  is the cross-section of neutrino interaction with water, and  $M_{\text{SK(1KT)}}$  is the fiducial mass of SK (1KT). The neutrino

spectrum at SK and 1KT and the cross-section of neutrino interaction are numerically estimated by using Beam-MC and Neut-MC, while the fiducial masses of SK and 1KT are 22.5 kt and 25 t, respectively.  $R_{\text{int}}^{\text{SK}/1\text{KT}}$  for the run in K2K-Ia and K2K-Ib are estimated to be  $6.81 \times 10^{-4}$  and  $6.71 \times 10^{-4}$ , respectively.

#### Correction for number of protons on target used in analysis

A factor to correct the difference of total number of protons on target used in 1KT and SK analyses is multiplied to  $N_{\text{int}}^{\text{1KT}}$ ;

$$\frac{\text{POT}_{\text{SK}}}{\text{POT}_{\text{1KT}}} = 1 + \frac{\text{POT}_{\text{SK}} - \text{POT}_{\text{1KT}}}{\text{POT}_{\text{1KT}}} \quad , \quad (7.4)$$

which is already described in Sec. 5.2.4.

#### Correction for electron neutrino component

Since the effect of the electron neutrino component in the beam is not taken into account in the calculation of the  $F/N$  ratio  $R_{\text{int}}^{\text{SK}/1\text{KT}}$  and the selection efficiencies in 1KT (SK)  $\epsilon_{\text{1KT(SK)}}$ , a factor to correct this effect is multiplied to the expected number of neutrino events in SK. Using a Monte Carlo simulation, the correction factor ( $C_{\nu_e}$ ) due to these effects is estimated to be 0.996. Since this correction makes only tiny effect on  $N_{\text{exp}}^{\text{SK}}$ , its uncertainty is ignored in the estimation of the systematic errors on  $N_{\text{exp}}^{\text{SK}}$ .

#### Expected number of neutrino events in SK

After all the corrections described above are taken into account, the expected number of neutrino events in SK during the runs from June 1999 to July 2001 is estimated to be

$$N_{\text{exp}}^{\text{SK}} = 80.6 \pm 0.3(\text{stat.})_{-8.0}^{+7.3}(\text{syst.}) \quad \text{for } 4.79 \times 10^{19} \text{ POT} \quad , \quad (7.5)$$

in the case of no neutrino oscillation. It is summarized on a month by month basis in Table 7.4 together with the number of neutrino interactions in 1KT,  $F/N$  neutrino interaction ratio, the correction factors, and so on. The statistical error on the expected number of neutrino events in SK comes from the statistics of number of neutrino events observed in 1KT ( $N_{\text{obs}}^{\text{1KT}}$ ). The sources of the systematic error are described in Sec. 7.3.2.

As references to the above number, it is also estimated using SciFi and MRD. The results are

$$\begin{aligned} N_{\text{exp}}^{\text{SK}}(\text{SciFi}) &= 85.9 \pm 1.0(\text{stat.})_{-8.5}^{+7.8}(\text{syst.}) \quad , \\ N_{\text{exp}}^{\text{SK}}(\text{MRD}) &= 87.4 \pm 0.2(\text{stat.})_{-13.9}^{+12.7}(\text{syst.}) \quad , \end{aligned}$$

which are consistent with the estimation in 1KT.

### 7.3.2 Systematic errors on the expected number of neutrino events in SK

Systematic errors on the expected number of events in SK are described in this section, which are summarized in Table 7.5.

#### Error on the measurements of the number of interactions in 1KT

The uncertainties of the measurements of the number of neutrino interactions in 1KT is as described in Sec. 7.2.8.

**Table 7.4:** Summary of the expected number of neutrino events in SK.

period	Jun.'99	Nov.'99	Jan.'00	Feb.'00	Mar.'00	May.'00	Jun.'00
Target diameter	20 mm $\phi$	30 mm $\phi$					
Horn current	200 kA	250 kA					
POT <sub>SK</sub> ( $\times 10^{18}$ )	3.10	3.57	2.22	4.04	3.70	2.56	3.76
POT <sub>1KT</sub> ( $\times 10^{18}$ )	2.60	2.62	1.81	3.74	3.35	2.42	3.17
$N_{\text{int}}^{\text{1KT}}$	7,206	8,351	6,013	11,857	10,567	7,573	10,130
$R_{\text{int}}^{\text{SK/1KT}}$ ( $\times 10^{-4}$ )	6.81	6.71					
$\epsilon_{\text{SK}}$	0.781	0.785					
$C_{\nu_e}$	0.996						
$N_{\text{exp}}^{\text{SK}}$	4.55	5.97	3.87	6.73	6.14	4.19	6.31
period	Jan.'01	Feb.'01	Mar.'01	Apr.'01	May.'01	Jun.'01	Jul.'01
Target diameter	30 mm $\phi$						
Horn current	250 kA						
POT <sub>SK</sub> ( $\times 10^{18}$ )	3.20	5.04	4.60	2.76	1.75	6.12	1.54
POT <sub>1KT</sub> ( $\times 10^{18}$ )	2.92	4.75	4.27	2.47	1.60	5.79	1.43
$N_{\text{int}}^{\text{1KT}}$	9,420	15,491	13,888	8,004	5,236	19,102	4,645
$R_{\text{int}}^{\text{SK/1KT}}$ ( $\times 10^{-4}$ )	6.71						
$\epsilon_{\text{SK}}$	0.785						
$C_{\nu_e}$	0.996						
$N_{\text{exp}}^{\text{SK}}$	5.42	8.63	7.87	4.70	3.00	10.59	2.63
In total : $N_{\text{exp}}^{\text{SK}} = 80.6 \pm 0.3(\text{stat.})_{-8.0}^{+7.3}(\text{syst.})$							

### Error on the correction of the number of protons on target

Error due to the difference of the number of protons on target used in 1KT and SK analyses is as described in Sec. 5.2.3. Uncertainty of POT comes from only un-overlapped spills between 1KT and SK. Therefore, the error on the correction of POT is as follows;

$$\delta_{\text{POT}} = \frac{\text{POT}_{\text{SK}} - \text{POT}_{\text{1KT}}}{\text{POT}_{\text{1KT}}} \cdot \delta S_{\text{1KT}} \quad , \quad (7.6)$$

where the uncertainty of beam intensity is quoted from the instability of neutrino event rate in 1KT ( $\delta S_{\text{1KT}}$ ), which is estimated to be 6% as mentioned in Sec. 7.2.2.

### Uncertainty of neutrino energy spectrum at near and far sites

Here, systematic errors on  $N_{\text{exp}}^{\text{SK}}$  due to the uncertainties in neutrino energy spectrum and  $F/N$  ratio are considered. The extrapolation of the number of neutrino interactions in 1KT to the expected number of neutrino events in SK is done by Eq. (7.2), where the selection efficiency of neutrino events in SK ( $\epsilon_{\text{SK}}$ ) is factorized out by using the efficiency averaged over the neutrino energy. When Eq. (7.2) is expressed in more strict form, it becomes

$$N_{\text{exp}}^{\text{SK}} = N_{\text{int}}^{\text{1KT}} \cdot \frac{\int R_{\text{flux}}^{\text{SK/1KT}}(E_\nu) \cdot \Phi^{\text{1KT}}(E_\nu) \cdot \sigma_{\text{H}_2\text{O}}(E_\nu) \cdot \epsilon_{\text{SK}}(E_\nu) \cdot M_{\text{SK}} dE_\nu}{\int \Phi^{\text{1KT}}(E_\nu) \cdot \sigma_{\text{H}_2\text{O}}(E_\nu) \cdot \epsilon_{\text{1KT}}(E_\nu) \cdot M_{\text{1KT}} dE_\nu} \quad , \quad (7.7)$$

where  $\epsilon_{1\text{KT}(\text{SK})}(E_\nu)$  is efficiency to detect neutrino interaction of the neutrino energy of  $E_\nu$  in 1KT (SK), and  $R_{\text{flux}}^{\text{SK}/1\text{KT}}(E_\nu)$  is the ratio of the neutrino energy spectra at SK and 1KT as explained in Sec. 5.1 (Eq. (5.4)). In this expression, other corrections such as POT and electron neutrino component are ignored since they make no effect (or very small effect even if they do) on the discussion. For simplicity, we denote some quantities appeared in Eq. (7.7) as following;

$$[n_{\text{obs}}^{\text{SK}}(E_\nu)]_{\text{MC}} = R_{\text{flux}}^{\text{SK}/1\text{KT}}(E_\nu) \cdot \Phi^{1\text{KT}}(E_\nu) \cdot \sigma_{\text{H}_2\text{O}}(E_\nu) \cdot \epsilon_{\text{SK}}(E_\nu) \cdot M_{\text{SK}} \quad , \quad (7.8)$$

$$[n_{\text{obs}}^{1\text{KT}}(E_\nu)]_{\text{MC}} = \Phi^{1\text{KT}}(E_\nu) \cdot \sigma_{\text{H}_2\text{O}}(E_\nu) \cdot \epsilon_{1\text{KT}}(E_\nu) \cdot M_{1\text{KT}} \quad , \quad (7.9)$$

$$[N_{\text{obs}}^{1\text{KT}(\text{SK})}]_{\text{MC}} = \int [n_{\text{obs}}^{1\text{KT}(\text{SK})}(E_\nu)]_{\text{MC}} dE_\nu \quad , \quad (7.10)$$

where  $[n_{\text{obs}}^{1\text{KT}(\text{SK})}(E_\nu)]_{\text{MC}}$  stands for the number of neutrino events with an energy of  $E_\nu$  in 1KT (SK) and  $[N_{\text{obs}}^{1\text{KT}(\text{SK})}]_{\text{MC}}$  stands for the total number of neutrino events in 1KT (SK) estimated by a Monte Carlo simulation.

If  $R_{\text{flux}}^{\text{SK}/1\text{KT}}(E_\nu)$  is changed by  $\Delta R_{\text{flux}}^{\text{SK}/1\text{KT}}(E_\nu)$  and  $\Phi^{1\text{KT}}(E_\nu)$  is changed by  $\Delta\Phi^{1\text{KT}}(E_\nu)$ , then the change in  $N_{\text{exp}}^{\text{SK}}$ ,  $\Delta N_{\text{exp}}^{\text{SK}}$ , is expressed by following two different terms;

$$\begin{aligned} \Delta N_{\text{exp}}^{\text{SK}} \approx & N_{\text{exp}}^{\text{SK}} \cdot \left[ \int \left( \Delta\phi^{1\text{KT}}(E_\nu) \cdot \left[ \frac{n_{\text{obs}}^{\text{SK}}(E_\nu)}{N_{\text{obs}}^{\text{SK}}} - \frac{n_{\text{obs}}^{1\text{KT}}(E_\nu)}{N_{\text{obs}}^{1\text{KT}}} \right]_{\text{MC}} \right) dE_\nu \right. \\ & \left. + \int \left( \Delta r^{\text{SK}/1\text{KT}}(E_\nu) \cdot \left[ \frac{n_{\text{obs}}^{\text{SK}}(E_\nu)}{N_{\text{obs}}^{\text{SK}}} \right]_{\text{MC}} \right) dE_\nu \right] \quad , \quad (7.11) \end{aligned}$$

where

$$\Delta\phi^{1\text{KT}}(E_\nu) = \frac{\Delta\Phi^{1\text{KT}}(E_\nu)}{\Phi^{1\text{KT}}(E_\nu)} \quad \text{and} \quad \Delta r^{\text{SK}/1\text{KT}}(E_\nu) = \frac{\Delta R_{\text{flux}}^{\text{SK}/1\text{KT}}(E_\nu)}{R_{\text{flux}}^{\text{SK}/1\text{KT}}(E_\nu)} \quad , \quad (7.12)$$

and only the first order corrections are considered. In Eq. (7.11), the first term corresponds to correlated error between 1KT and SK which comes from the uncertainty of energy spectrum shape in 1KT, and the second term corresponds to uncorrelated error which comes from the extrapolation of 1KT measurements to SK by  $F/N$  ratio. The systematic errors on  $N_{\text{exp}}^{\text{SK}}$  due to the uncertainties in neutrino energy spectrum and  $F/N$  ratio are estimated by using Eq. (7.11).

In actual case, the neutrino energy is divided into the same bins as the binning of PIMON described in Sec. 6.3, and the integration is replaced by the summation over 6 bins. Using the errors estimated by PIMON measurements listed in Table C.1, C.2, and C.3 as  $\Delta\phi^{1\text{KT}}(E_\nu)$  and  $\Delta r^{\text{SK}/1\text{KT}}(E_\nu)$ , the systematic errors on  $N_{\text{exp}}^{\text{SK}}$  for K2K-Ib (K2K-Ia) are  $^{+3.8\%}_{-3.5\%}$  ( $^{+5.8\%}_{-7.0\%}$ ) from the uncertainties of the neutrino energy spectrum and  $^{+5.6\%}_{-7.3\%}$  ( $^{+13.6\%}_{-9.9\%}$ ) from the  $F/N$  ratio.

### Uncertainty of neutrino interaction cross-section

Since there is small difference of detection efficiency between 1KT and SK for each neutrino interaction mode, the uncertainties of the neutrino interaction cross-section causes some ambiguity in  $N_{\text{exp}}^{\text{SK}}$ . In order to estimate this systematic effect, the ratio of neutral current to charged current interaction cross-section ( $\sigma_{\text{NC}}/\sigma_{\text{CC}}$ ) is changed by  $\pm 30\%$ , yielding a change in  $N_{\text{exp}}^{\text{SK}}$  by  $^{+0.2\%}_{-0.3\%}$ , and the ratio of inelastic to (quasi-)elastic interaction cross-section ( $\sigma_{\text{nonQE}}/\sigma_{\text{QE}}$ ) is changed by  $\pm 30\%$ , yielding a change in  $N_{\text{exp}}^{\text{SK}}$  by  $^{+0.5\%}_{-0.8\%}$ .

**Table 7.5:** Summary of the systematic errors on the expected number of neutrino events in SK.

period	Jun.'99	Nov.'99	Jan.'00	Feb.'00	Mar.'00	May.'00	Jun.'00
$N_{\text{exp}}^{\text{SK}}$	4.55	5.97	3.87	6.73	6.14	4.19	6.31
Errors from 1KT	4.4%	4.5%	4.3%	4.3%	4.3%	4.5%	4.5%
POT correction	1.0%	1.6%	1.1%	0.5%	0.6%	0.3%	1.0%
Neutrino Spectrum	$+5.8\%$ $-7.0\%$	$+3.8\%$ $-3.5\%$					
$F/N$ ratio	$+13.6\%$ $-9.9\%$	$+5.6\%$ $-7.3\%$					
$\sigma_{\text{NC}}/\sigma_{\text{CC}}$	$+0.2\%$ $-0.3\%$						
$\sigma_{\text{nonQE}}/\sigma_{\text{QE}}$	$+0.5\%$ $-0.8\%$						
SK efficiency	$\pm 3\%$						
Total	$+15.8\%$ $-13.3\%$	$+8.8\%$ $-9.9\%$	$+8.6\%$ $-9.7\%$	$+8.6\%$ $-9.7\%$	$+8.6\%$ $-9.7\%$	$+8.7\%$ $-9.8\%$	$+8.7\%$ $-9.8\%$

period	Jan.'01	Feb.'01	Mar.'01	Apr.'01	May.'01	Jun.'01	Jul.'01
$N_{\text{exp}}^{\text{SK}}$	5.42	8.63	7.87	4.70	3.00	10.59	2.63
Errors from 1KT	4.3%	4.3%	4.3%	4.3%	4.3%	4.3%	4.3%
POT correction	0.5%	0.3%	0.4%	0.6%	0.5%	0.4%	0.3%
$E_\nu$ Spectrum	$+3.8\%$ $-3.5\%$						
$F/N$ ratio	$+5.6\%$ $-7.3\%$						
$\sigma_{\text{NC}}/\sigma_{\text{CC}}$	$+0.2\%$ $-0.3\%$						
$\sigma_{\text{nonQE}}/\sigma_{\text{QE}}$	$+0.5\%$ $-0.8\%$						
SK efficiency	$\pm 3\%$						
Total	$+8.6\%$ $-9.7\%$	$+8.6\%$ $-9.7\%$	$+8.6\%$ $-9.7\%$	$+8.6\%$ $-9.7\%$	$+8.6\%$ $-9.7\%$	$+8.6\%$ $-9.7\%$	$+8.6\%$ $-9.7\%$

### Uncertainty of event selection in SK

The event selection in SK, which is described in Chapter 8, have some uncertainties, causing the errors on the expected number of neutrino events in SK. Dominant uncertainty is in the selection of the events with vertex contained in the fiducial volume of SK. By applying two different vertex fitters, TDC-fit and MS-fit, to the atmospheric neutrino data sample and Monte Carlo simulation and comparing the results, the systematic errors  $N_{\text{exp}}^{\text{SK}}$  due to the uncertainty of fiducial cut is estimated to be  $\pm 2\%$ .

Other systematic uncertainties of  $N_{\text{exp}}^{\text{SK}}$  come from the event selection for the neutrinos of K2K beam (1%) and statistics of Monte Carlo simulation (1%). In total, 3% is quoted as the error on  $N_{\text{exp}}^{\text{SK}}$  due to the uncertainties of event selection in SK.

By estimating the errors on the expected number of neutrino events in SK month-by-month,  $+9.1\%$  ( $+7.3$  events)  $-9.9\%$  ( $-8.0$  events) is quoted as the systematic error on  $N_{\text{exp}}^{\text{SK}}$  in total.

## 7.4 Measurement of neutrino spectrum in near detectors

The neutrino energy spectrum at near site is measured using data taken by both 1KT and the fine grained detector (FGD). A momentum and angle with respect to the beam direction of charged lepton produced in the interaction is used to estimate the energy of neutrino.

Events which have only one  $\mu$ -like Cherenkov ring with the particle fully contained inside the inner tank of 1KT (FC1R $\mu$ ) are used as a data sample from 1KT, while events with a vertex contained in SciFi and an end point of scattered charged lepton contained inside MRD are used

as a data sample from FGD. FC1R $\mu$  sample covers the muon momentum range below 1 GeV/ $c$  with high efficiency and with  $4\pi$  coverage in solid angle although 1KT has little efficiency to reconstruct muons with momentum above 1.5 GeV/ $c$  since they exit the detector. FGD, on the other hand, has high efficiency for measuring muons above 1 GeV/ $c$ , and hence 1KT and FGD can complementarily cover the relevant energy range.

In addition, since ND, especially FGD, has sensitivity to separate the non-qe events from CC-qe ones, a fraction of non-qe interactions (or cross-section ratio  $\sigma_{\text{nonQE}}/\sigma_{\text{QE}}$ ) is also measured in ND, which can become a background in the measurements of the neutrino energy.

In this section, first, further event selections for the spectral analysis in 1KT are described. Then event samples from FGD are briefly mentioned. Finally, the analysis to estimate the neutrino energy spectrum at ND as well as non-qe/qe ratio is described.

The spectrum in June 1999 (K2K-Ia) differs from that in the rest of the period (K2K-Ib) since the horn current and target radius in K2K-Ia were different from the rest of the period. In the oscillation analysis described in this thesis, we do not use the spectral information for the data taken in K2K-Ia, and hence only the spectrum for K2K-Ib is estimated here.

#### 7.4.1 Further event selections in 1KT

In order to reconstruct the neutrino energy in 1KT, events which have only one  $\mu$ -like Cherenkov ring with the charged particle fully contained inside the 1KT inner tank (FC1R $\mu$ ) are selected. The criteria to select FC1R $\mu$  are described in this section, which are corresponding to the selections (8)–(12) in the flow chart in Fig. 7.2. The data taken during the period from January 2000 to July 2001 are used in the spectral analysis in 1KT, since we had problem in the threshold of FADC in October and November 1999, as described before (1/4 of PMTSUM was disconnected).

##### Events with a visible energy greater than 30 MeV

In order to eliminate the low energy background events, events are required to have a visible energy greater than 30 MeV. Since the threshold of FADC peak search is set around 1,000 p.e., corresponding to 100 MeV visible energy, this cut does not reduce so many events; only 0.01% of events in Fiducial-C are discarded.

##### Events with all the particles fully contained inside the inner tank of 1KT

In 1KT analysis, we classify the neutrino events into two categories; “fully contained (FC)” and “partially contained (PC)” events. Fig. 7.17 shows a schematic view of each event category. The events in which all secondary charged particles are contained in the inner detector (ID) of 1KT are referred as FC events, and those in which some of secondary charged particles are going out of ID are referred as PC events.

In practice, the numbers of photoelectrons detected by individual PMTs are used to classify each event into FC or PC category. The PMT which have the largest number of photoelectrons among the PMTs inside a cone of  $20^\circ$  opening angle along the direction of the most energetic ring (referred as “*pomax20deg*”) is selected in each event. Fig. 7.18 shows the distribution of *pomax20deg*. When a charged particle exits the inner tank, the ID PMTs near the exit point receive intense Cherenkov light, and ATM channels of these PMTs tends to saturate. By selecting the events with *pomax20deg* less than 200 p.e., PC events are effectively eliminated, and contamination of PC events into FC events is negligible. Among the events used in the estimation of the expected number of neutrino events in SK (events with vertex inside Fiducial-C), 74.8% are selected as FC events.



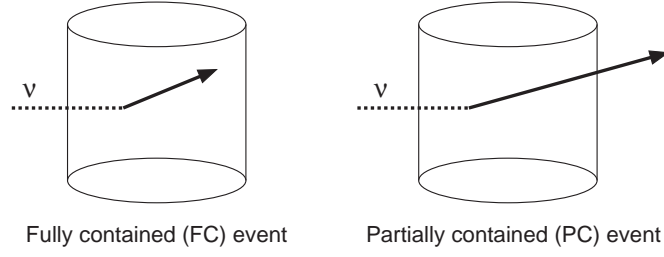


**Figure 7.17:** Categories of neutrino events in 1KT. Dashed lines show the trajectories of primary neutrinos, and solid arrows show those of secondary charged particles. The events in which the secondary charged particles are fully contained in the inner detector of 1KT are referred as “fully contained (FC)” events, and those in which some of secondary charged particles are going outside the inner detector of 1KT are referred as “partially contained (PC)” events.

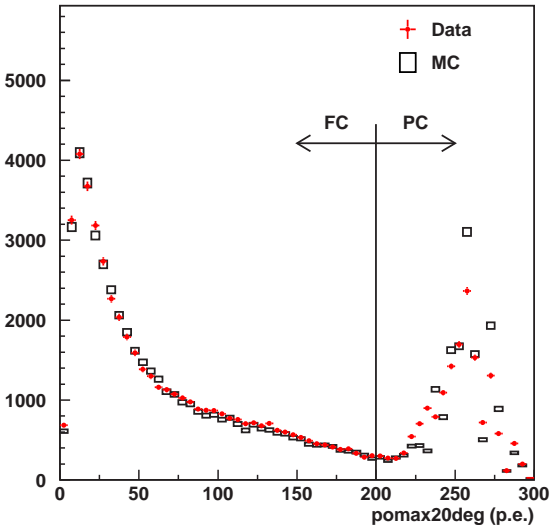


**Figure 7.18:** The distribution of  $pomax20deg$  in 1KT. Red points show data and black boxes show a Monte Carlo simulation. A peak around 250 p.e. corresponds to the saturated point of readout electronics (ATM), which is caused by intense Cherenkov light of exiting particle. Events with  $pomax20deg$  less than 200 p.e. are classified as fully contained (FC) events, and events with  $pomax20deg$  equal to or greater than 200 p.e. are classified as partially contained (PC) events.

### Events with one Cherenkov ring

In order to enhance CC-qe events for which the energy of incident neutrino can be reconstructed, events which have only one Cherenkov ring are selected, since the Cherenkov threshold for proton in water is  $1.07 \text{ GeV}/c$  and recoil protons in CC-qe interaction typically have a momentum below the threshold in the energy range of the K2K neutrino beam. A likelihood function  $\mathcal{F}$  (or *DLFCT*) for the separation between one and more than one ring is used to select one ring events, which is described in Sec. B.2.2. Fig. 7.19 shows the distribution of the likelihood function  $\mathcal{F}$  and the number of ring distribution. Events with  $\mathcal{F} < 0$  are selected as one ring events ( $\#ring = 1$ ). By requiring the number of ring to be one, 55.3% of FC events with vertex in Fiducial-C are remaining.

### Events with a muon-like ring

In order to select the events with a muon type ( $\mu$ -like) ring, the likelihood for particle identification for the single ring events,  $\mathcal{P}_1$ , is used. The definition of  $\mathcal{P}_1$  is described in Sec. B.3.2. Fig. 7.20 shows the distribution of the likelihood  $\mathcal{P}_1$  for FC 1-ring events. The events with  $\mathcal{P}_1$  greater than 0 are selected as the events with a  $\mu$ -like Cherenkov ring. By this selection, 9.8%



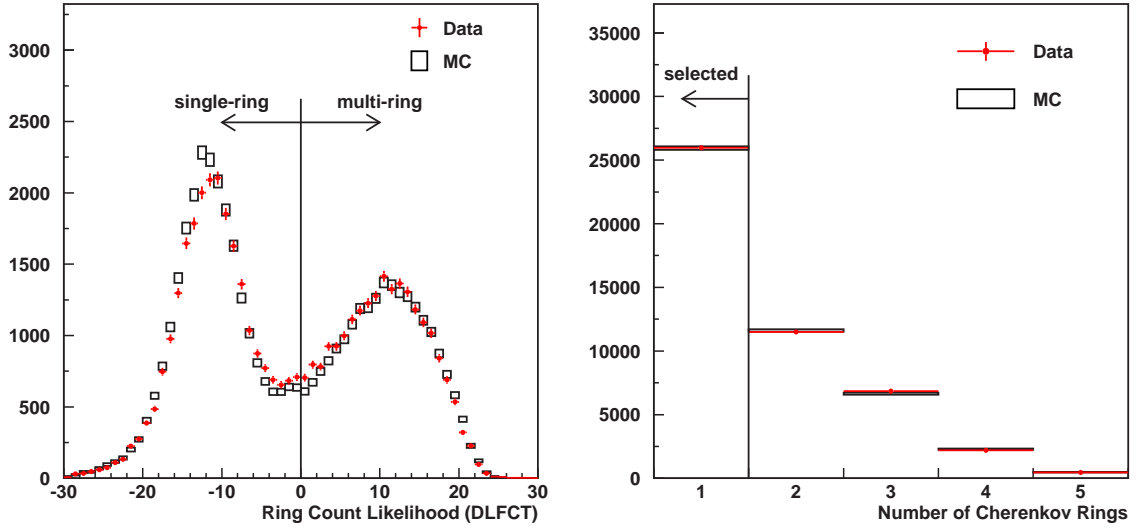


**Figure 7.19:** Distributions of the ring counting likelihood for single and multiple ring separation (left) and the number of ring distribution (right) in 1KT. Red points show data and black boxes show a Monte Carlo simulation. In left figure, the ring counting likelihood  $\mathcal{F}$  (DLFCT) less than 0 is corresponding to event with only one Cherenkov ring.

of FC 1-ring events are rejected as  $e$ -like events.

#### Events with total photoelectrons greater than 1000 p.e.

Up to here, FC1R $\mu$  events with the vertex in Fiducial-C are selected. In addition, a criterion to select events with a total number of photoelectrons greater than 1000 p.e. is imposed onto the sample in order to define a clear threshold of the detected charge and to make systematic studies on the behavior of the threshold easier. Fig. 7.21 shows the distribution of total number of photoelectrons for FC1R $\mu$  sample. This cut reduces 0.7% of FC1R $\mu$  events, and the remaining events are used in the spectral analysis as a final data sample from 1KT.

The reduction rate in each selection step is summarized in Table 7.6. After all the selection criteria are imposed, 23,254 FC1R $\mu$  events with a vertex in Fiducial-C and a total photoelectrons greater than 1000 are remaining. According to a Monte Carlo simulation, a fraction of about 53% events in FC1R $\mu$  sample is induced by CC-qe interaction.

#### 7.4.2 Neutrino event selection in FGD

Events which have one or two tracks with a reconstructed vertex point in the fiducial volume of SciFi, at least one track penetrating into MRD and its end point contained inside MRD (SciFi-MRD sample) are used in the spectral analysis. Fig. 7.22 shows a typical event of MRD sample. Methods to reconstruct tracks in SciFi and MRD are described in [47] and [53], respectively. Here, only criteria for event selection are briefly described, which are also described in [46, 47, 115]. FGD data taken from November 1999 to July 2001 are used in the spectral analysis.

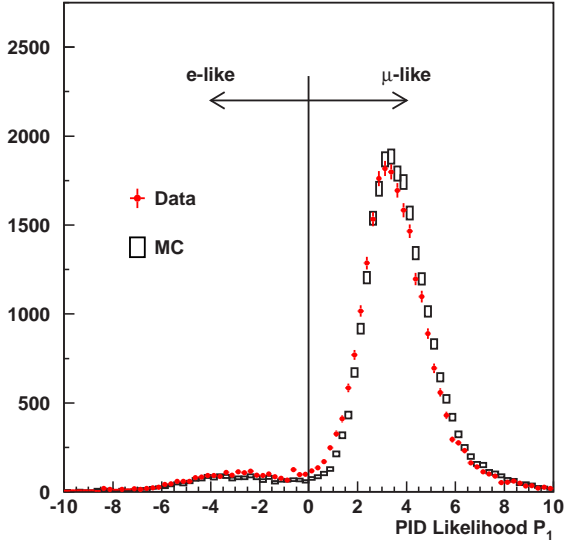


**Figure 7.20:** The distribution of the likelihood for particle identification for FC 1-ring sample in 1KT. Red points show data and black boxes show a Monte Carlo simulation. The likelihood  $\mathcal{P}_1$  greater than 0 is corresponding to  $\mu$ -like Cherenkov ring, while  $\mathcal{P}_1$  less than 0 is corresponding to  $e$ -like ring.

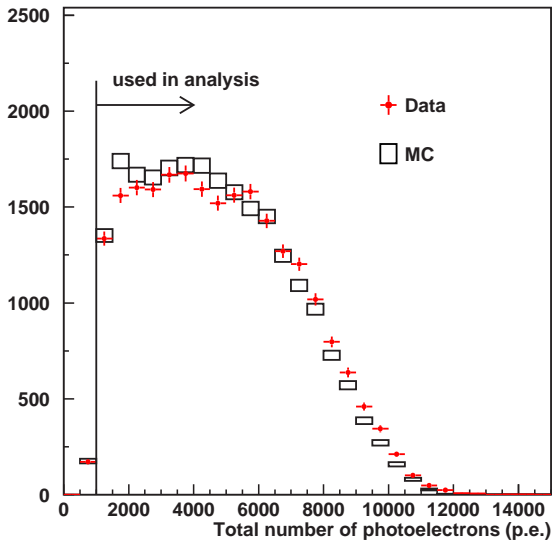


**Figure 7.21:** The distribution of the total number of photoelectron for the FC1R $\mu$  sample in 1KT. Red points show data and black boxes show a Monte Carlo simulation. The events with a total number of photoelectrons greater than 1000 p.e. are used in the spectral analysis.

**Table 7.6:** Summary of the event selections for FC1R $\mu$  sample in data and a Monte Carlo simulation. The number of events remained after each selection step is listed. The numbers inside the parentheses is the fraction of events which are remained from the previous selection step. The reduction rate in data and a Monte Carlo simulation for each step agrees well.

Selection criteria	Data	MC
Fiducial-C	62,773	74,000
Visible energy > 30 MeV	62,762 ( $\sim 100\%$ )	74,000 (100%)
Fully contained	46,950 (74.8%)	54,641 (73.8%)
1-ring	25,959 (55.3%)	30,186 (55.2%)
$\mu$ -like	23,426 (90.2%)	27,927 (92.5%)
Total # of p.e. > 1000	23,254 (99.3%)	27,717 (99.2%)
Final sample for analysis	23,254	27,717

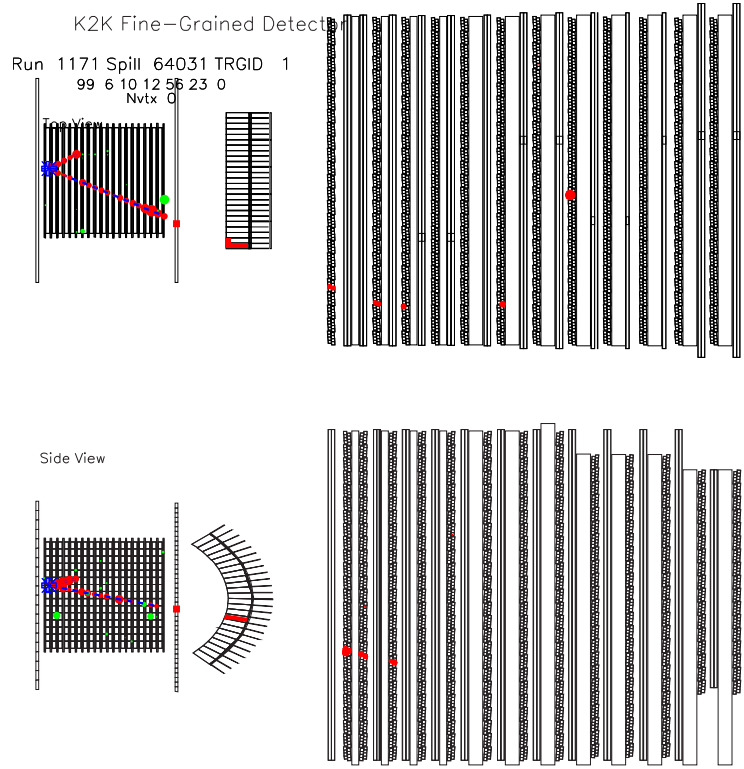


**Figure 7.22:** Event display of a typical SciFi-MRD 2-track events. Red points show hits in detectors and a blue point in SciFi represents the reconstructed vertex point for this event.

### Selection for SciFi-MRD 1-track and 2-track events

In the track reconstruction of SciFi, the most energetic track is taken as a first track of the event. Events in which the first track starts from inside SciFi, penetrates the downstream TGC and LG into MRD, and the track end is contained in MRD are selected as “SciFi-MRD events”. The first track of a SciFi-MRD event is regarded as a muon scattered via a charged current interaction, and an energy of the muon is reconstructed by using the range of the track. If protons or pions scattered from a interaction penetrate at least three SciFi layer, second or more tracks are also reconstructed. Events with no second track or only one second track are selected. Among the SciFi-MRD events, the events which have only first track are referred as “1-track events” and the events which have one first and one second tracks are referred as “2-track events”.

### Fiducial volume cut

A vertex is taken to be the middle point of the closest upstream water tank in 1-track events, and the intersection of the first and the second tracks is taken as a vertex in 2-track events. The fiducial volume of SciFi is defined as following: Among the 19 layers of water tanks in SciFi, the 1st to 17th layers are used as a fiducial region along the beam ( $z$ ) direction, and a square region of  $2.2 \text{ m} \times 2.2 \text{ m}$  centered at the beam axis is used as a fiducial region in horizontal ( $x$ ) and vertical ( $y$ ) directions. Total fiducial mass is 5.9 t including aluminum structure of a fractional weight of 15%. The events whose reconstructed vertex is inside the fiducial volume are selected.

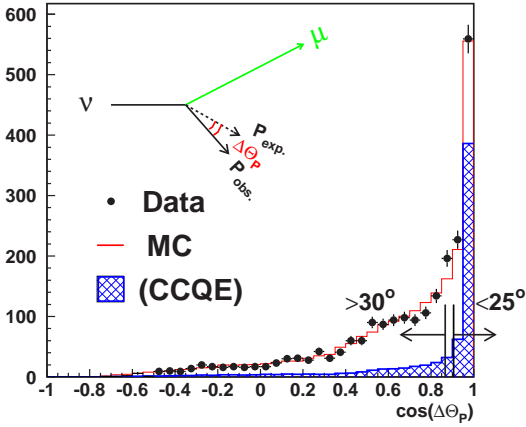


**Figure 7.23:** The distribution of cosine of the angular difference between the expected and the observed second track directions,  $\cos \Delta\theta_p$ , in SciFi-MRD 2-track events. Black points shows data and red histogram shows a Monte Carlo simulation. Blue hatched area indicate the fraction of CC-qe interaction in the Monte Carlo simulation. Events with  $\Delta\theta_p$  less than  $25^\circ$  (greater than  $30^\circ$ ) are classified as QE (non-QE) sample.

### Separation of 2-track into QE and non-QE enhanced samples

The direction of a scattered proton can be predicted by using the momentum and angle of the first track assuming the event is induced by CC-qe interaction;

$$\vec{p}_p = (-p_{\mu x}, -p_{\mu y}, p_{\nu}^{\text{rec}} - p_{\mu} \cos \theta_{\mu}) \quad , \quad (7.13)$$

where  $\vec{p}_p$  is a predicted momentum vector of scattered proton,  $p_{\mu x}$  and  $p_{\mu y}$  are, respectively,  $x$  and  $y$  component of the first track (muon) momentum vector,  $p_{\mu}$  and  $\theta_{\mu}$  are, respectively, the first track momentum and angle with respect to the beam direction, and  $p_{\nu}^{\text{rec}}$  is the reconstructed neutrino momentum calculated by assuming CC-qe interaction;

$$p_{\nu}^{\text{rec}} = \frac{1}{2} \cdot \frac{m_p^2 - m_n^2 - m_{\mu}^2 + 2m_n E_{\mu}}{m_n - E_{\mu} + p_{\mu} \cos \theta_{\mu}} \quad . \quad (7.14)$$

If the second track of a 2-track event is reconstructed in the direction of  $(\tan \theta_{xz}, \tan \theta_{yz}, 1)$ , where  $\theta_{xz}$  and  $\theta_{yz}$  are projected angle of the second track onto  $x$ - $z$  and  $y$ - $z$  planes, respectively, the angular difference ( $\Delta\theta_p$ ) between the expected ( $\vec{p}_p$ ) and the reconstructed directions can be calculated as

$$\cos \Delta\theta_p = \frac{-p_{\mu x} \cdot \tan \theta_{xz} - p_{\mu y} \cdot \tan \theta_{yz} + p_{\nu}^{\text{rec}} - p_{\mu} \cos \theta_{\mu}}{\sqrt{[(p_{\nu}^{\text{rec}})^2 + p_{\mu}^2 - 2p_{\nu}^{\text{rec}} p_{\mu} \cos \theta_{\mu}] \cdot [\tan^2 \theta_{xz} + \tan^2 \theta_{yz} + 1]}} \quad . \quad (7.15)$$

In the case of CC-qe interaction,  $\Delta\theta_p$  may become small, while the expected and the observed second track directions are not correlated so much in the case of non-qe interactions. Fig. 7.23 shows the distribution of  $\cos \Delta\theta_p$  for SciFi-MRD 2-track sample. As is expected, most of CC-qe events are in the small  $\Delta\theta_p$  region. Using this kinematic information, SciFi-MRD 2-track sample is further classified into two categories; if an event has  $\Delta\theta_p$  less than  $25^\circ$ , it is categorized into QE sample, while if an event has  $\Delta\theta_p$  greater than  $30^\circ$ , it is categorized into non-QE sample.

After the selection criteria are imposed onto the FGD events, 5,963 1-track events, 764 2-track QE events, and 1,288 2-track non-QE events are remaining. These are also used in the spectral analysis together with FC1R $\mu$  in 1KT. According to a Monte Carlo simulation, 60% of 2-track QE events come from CC-qe interactions, while 85.7% of 2-track non-QE events come from interactions other than CC-qe.

### 7.4.3 Basic distributions of FC1R $\mu$ and SciFi-MRD samples

Fig. 7.24 show basic distributions for FC1R $\mu$  sample in 1KT. The momentum and angular distributions of the muon candidates are shown in upper left and right figures, respectively, while the distributions of the reconstructed neutrino energy ( $E_\nu^{\text{rec}}$ ) and 4-momentum transfer squared ( $Q_{\text{rec}}^2 = (p_\mu - p_\nu^{\text{rec}})^2$ ) calculated by assuming CC-qe interaction are shown in lower left and right figures, respectively. In each figure in Fig. 7.24, a fraction of CC-qe interactions estimated by a Monte Carlo simulation is shown by a blue hatched histogram.

The same figures for SciFi-MRD 1-track, 2-track QE, and 2-track non-QE samples are shown in Fig. 7.25, 7.26, and 7.27, respectively. Here again, the fraction of CC-qe interaction in each distribution is indicated by the hatched histograms, which is estimated by a Monte Carlo simulation.

The model in the Monte Carlo simulation shown here is NEUT-0000 (the original Neut-MC, see Sec. 4.2.7 and Table 4.4), where data and the Monte Carlo simulation have some discrepancies in all figures. Several systematic studies had been done in 1KT detector against these discrepancies.

As shown in Fig. 7.28, the discrepancies in the momentum and neutrino energy distributions are found to be within the uncertainty of energy scale which is estimated to be  $^{+2}_{-3}\%$  in 1KT.

However the discrepancies in the angular distribution and also in the  $Q^2$  distribution cannot be explained by any detector systematics such as angular resolution, angular bias, or a bias in vertex reconstruction. Fig. 7.29 shows the results of several systematic studies on possible angular biases. In the cosmic ray data, the Monte Carlo simulation shows about  $2^\circ$  better angular resolution than data [44]. Therefore, the effect of the difference in angular resolution had been studied by smearing the reconstructed angle of muons by  $2^\circ$  in the Monte Carlo simulation, which is shown by the yellow histogram in Fig. 7.29. In the studies of cosmic ray data, it had also been found that the vertex fitter tends to reconstruct the vertex to be at a point about 5–10 cm shifted toward the particle direction only in data [44]. Therefore, this effect had been studied by changing the  $z$  position and the radius of the fiducial volume by  $\pm 10$  cm, which is shown by green and blue histograms in Fig. 7.29. Furthermore, a possible effect of angular shift due to the vertex shift is also considered by adding  $+1^\circ$  to the muon angle in the simulation, which is shown by the purple histogram.

In conclusion, the deficit in the forward region and large angle scattering in data cannot be explained in any cases of systematic biases. Therefore, we have modified the models in our Monte Carlo simulations for our spectrum and oscillation analysis within their uncertainties, which will be discussed in the next section. The descriptions on their modifications are already given in Sec. 4.2.

### 7.4.4 Choice of neutrino interaction models

As mentioned in the previous section, there exists a clear deficit in the forward region in our data compared with the model of NEUT-0000, and it is not due to the detector systematics. Furthermore, the  $\chi^2$  fitting to estimate the neutrino spectrum, which will be described in the following sections, have been performed with the use of NEUT-0000, but it is found that the  $\chi^2$  minimum does not settle at the reasonable size ( $\chi_{\text{min}}^2 = 290.8/197\text{d.o.f.}$ , which probability is 0.0015%) and the non-qe/qe ratio is found to be un-physically small value of about 0.66 relative to the initial value in MC. Therefore, we have concluded that the models employed in our MC do not reproduce our experimental data due to the lack of the knowledge of neutrino

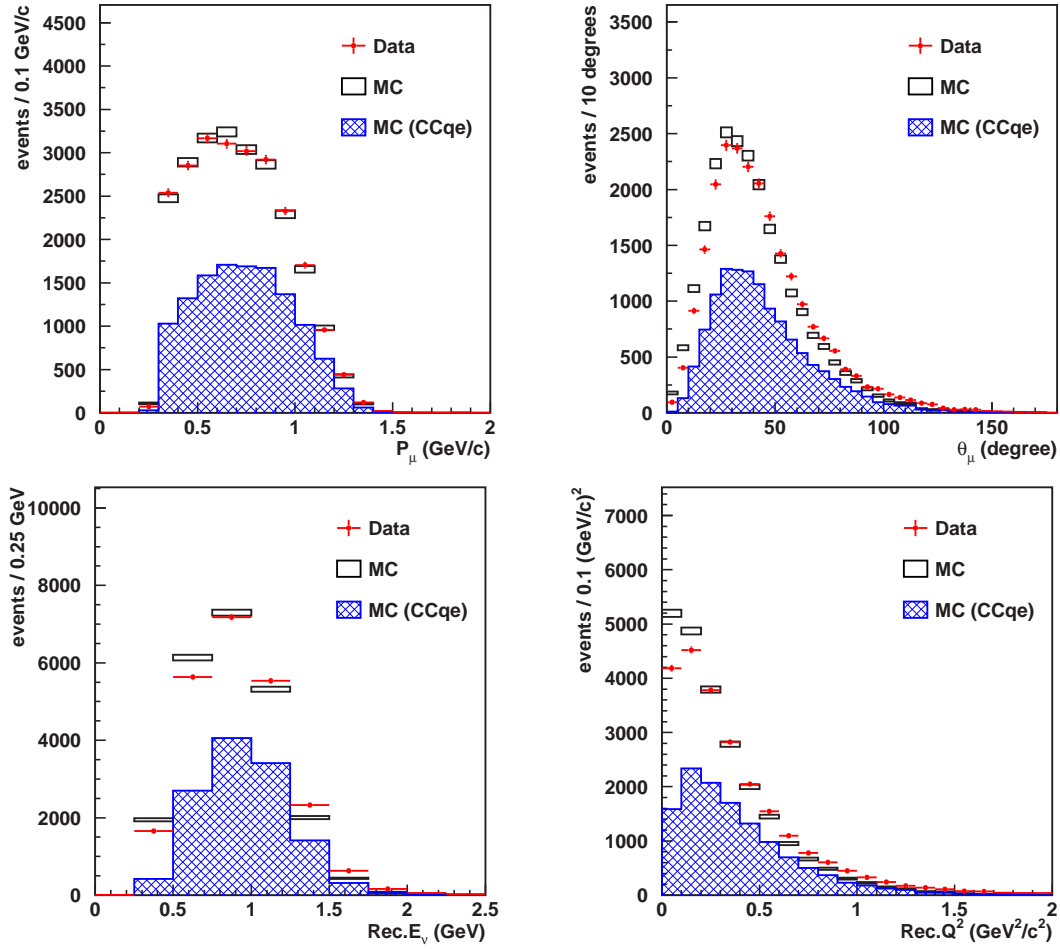


**Figure 7.24:** The momentum (upper left) and angular (upper right) distributions of scattered muons in FC1Rμ sample, and the distributions of the reconstructed neutrino energy (lower left) and the reconstructed 4-momentum transfer squared (lower right) for FC1Rμ sample. In all figures, red points show data and black boxes show a Monte Carlo simulation. The fraction of CC-qe events in FC1Rμ estimated by MC is also shown by blue hatched histogram in each figure.

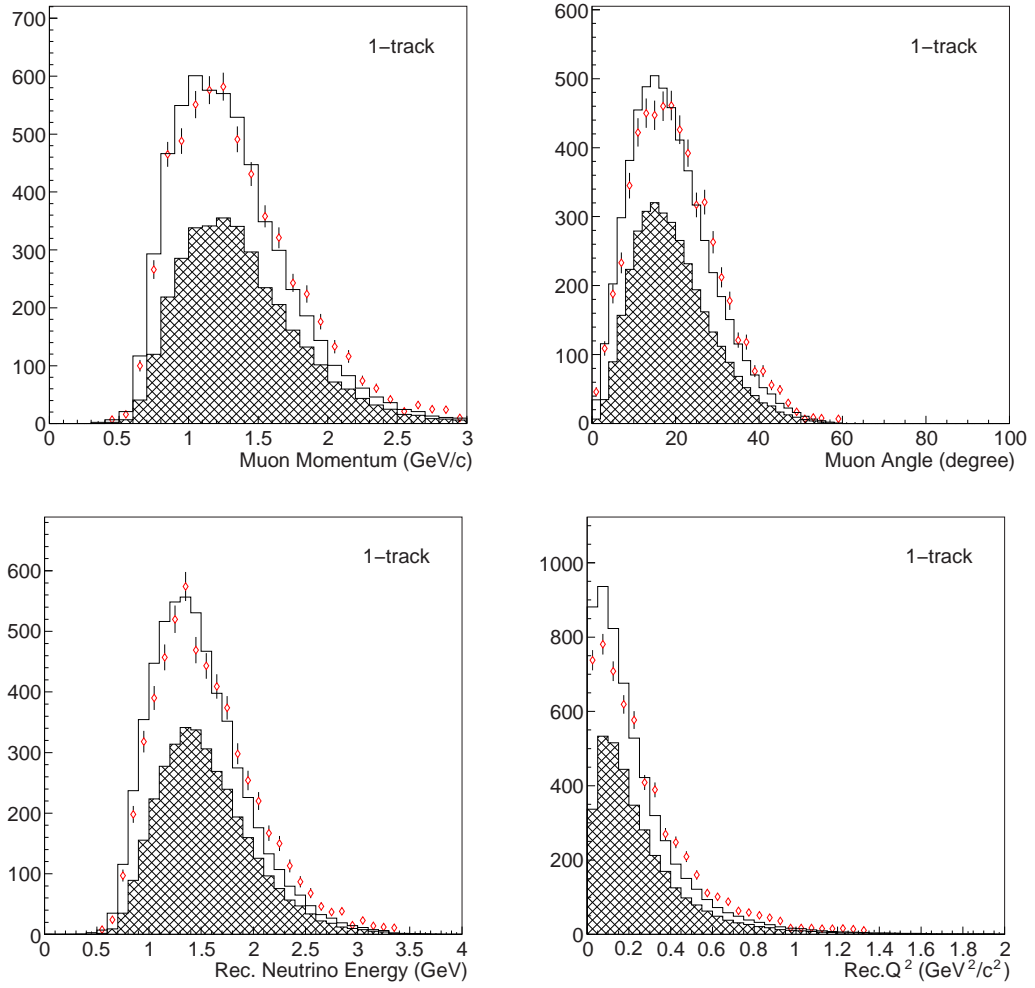


**Figure 7.25:** The momentum (upper left) and angular (upper right) distributions of scattered muons in SciFi-MRD 1-track sample, and the distributions of the reconstructed neutrino energy (lower left) and the reconstructed 4-momentum transfer squared (lower right) for SciFi-MRD 1-track sample. In all figures, red points show data and a black histogram show a Monte Carlo simulation. The fraction of CC- $q\bar{e}$  events in SciFi-MRD 1-track estimated by MC is also shown by a hatched histogram in each figure.

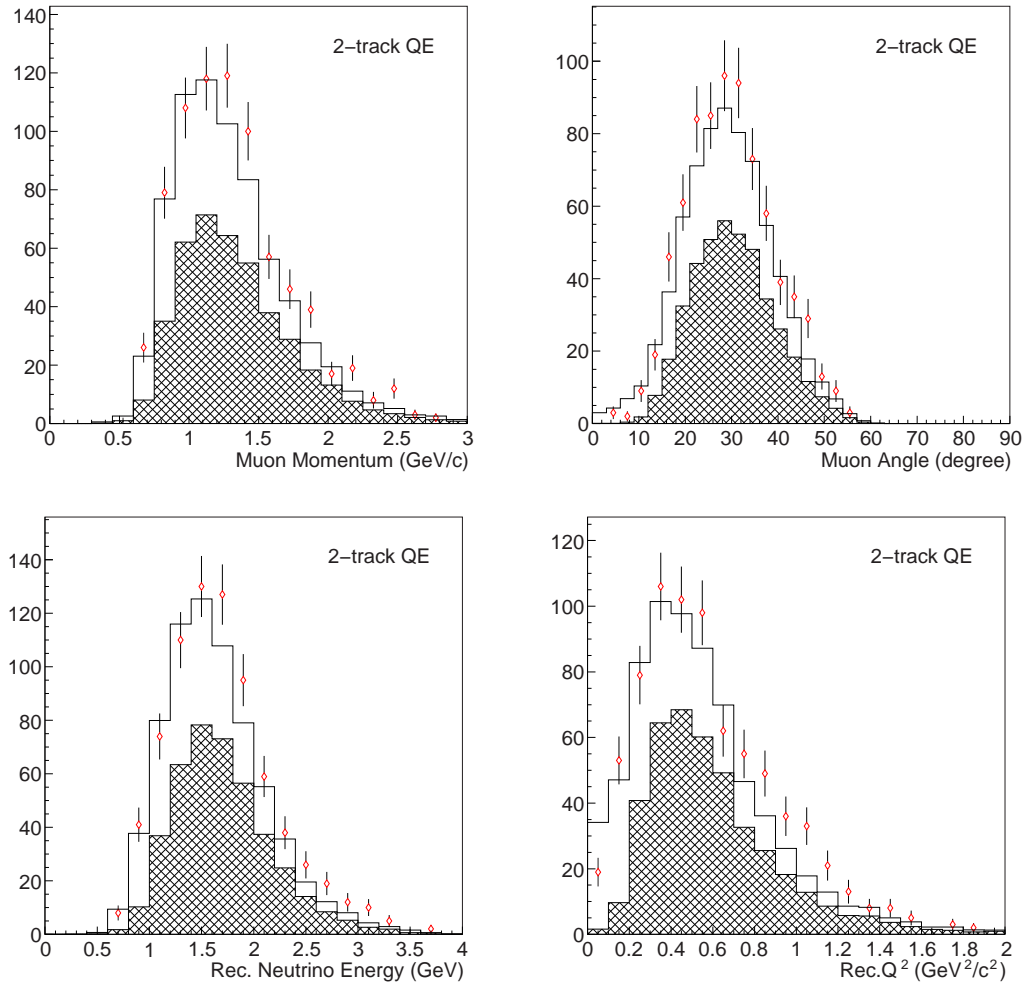


**Figure 7.26:** The momentum (upper left) and angular (upper right) distributions of scattered muons in SciFi-MRD 2-track QE sample, and the distributions of the reconstructed neutrino energy (lower left) and the reconstructed 4-momentum transfer squared (lower right) for SciFi-MRD 2-track QE sample. In all figures, red points show data and a black histogram show a Monte Carlo simulation. The fraction of CC-qe events in SciFi-MRD 2-track QE estimated by MC is also shown by a hatched histogram in each figure.



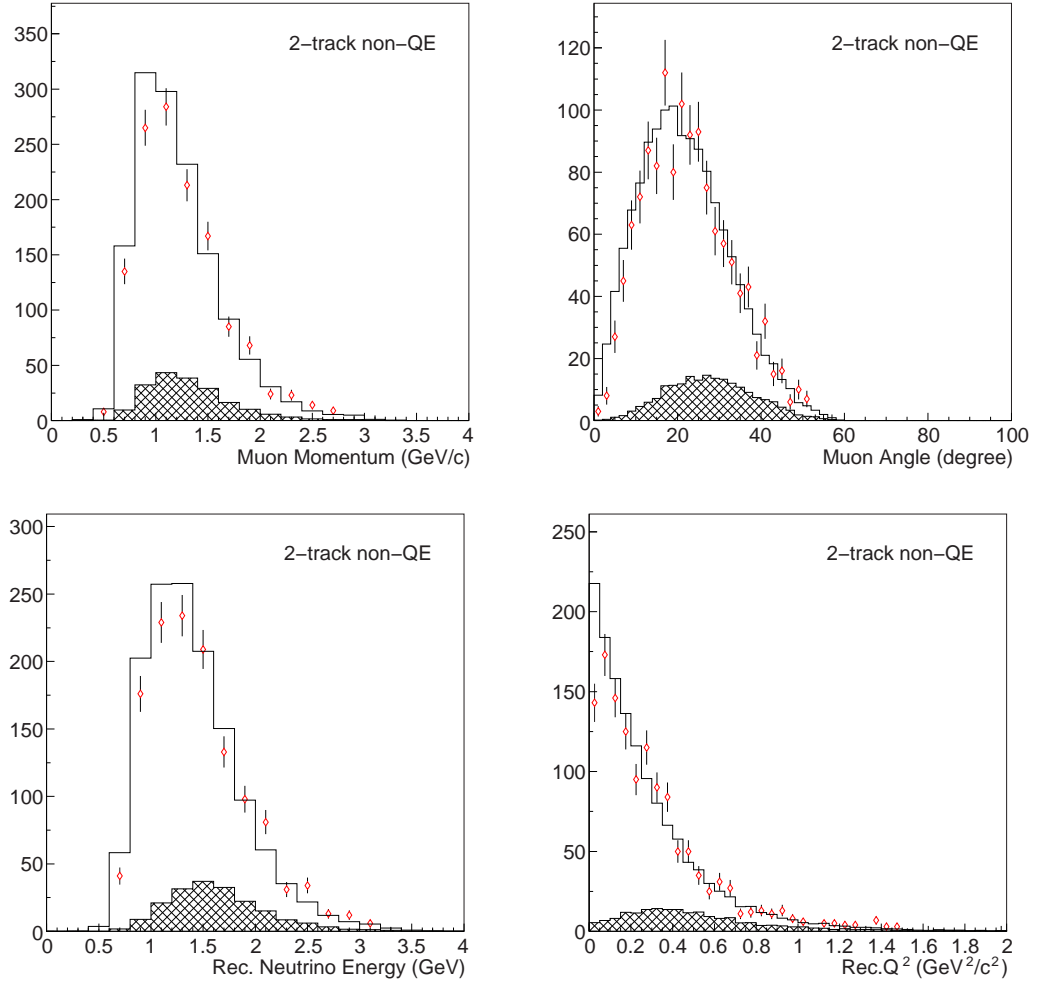


**Figure 7.27:** The momentum (upper left) and angular (upper right) distributions of scattered muons in SciFi-MRD 2-track non-QE sample, and the distributions of the reconstructed neutrino energy (lower left) and the reconstructed 4-momentum transfer squared (lower right) for SciFi-MRD 2-track non-QE sample. In all figures, red points show data and a black histogram show a Monte Carlo simulation. The fraction of CC-qe events in SciFi-MRD 2-track non-QE estimated by MC is also shown by a hatched histogram in each figure.

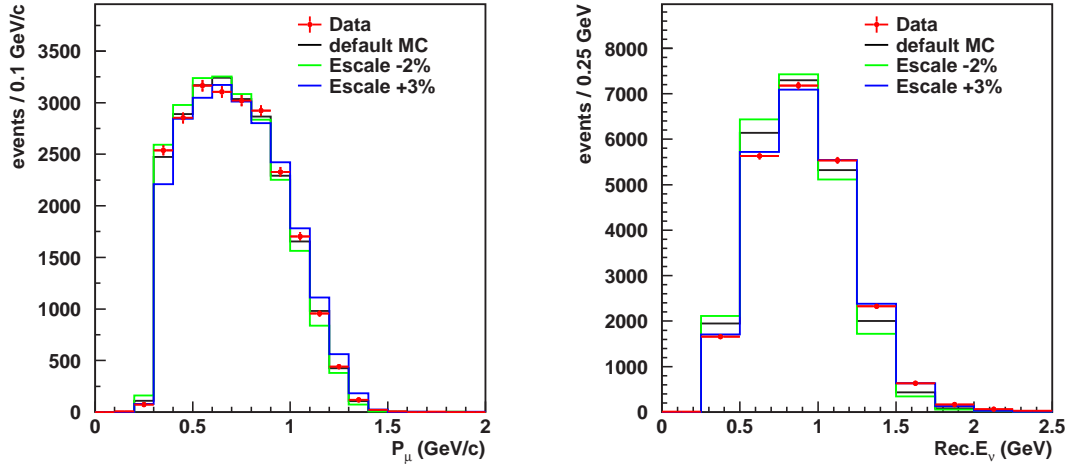


**Figure 7.28:** Systematic studies on the effect of the uncertainty in the energy scale on the momentum (left) and reconstructed neutrino energy (right) distributions in FC1R $\mu$  sample. In the Monte Carlo simulation, the momentum is scaled up and down by +3% and -2% according to the size of the uncertainty, showing that the discrepancy in the reconstructed neutrino energy distribution is within the size of the energy scale uncertainty.

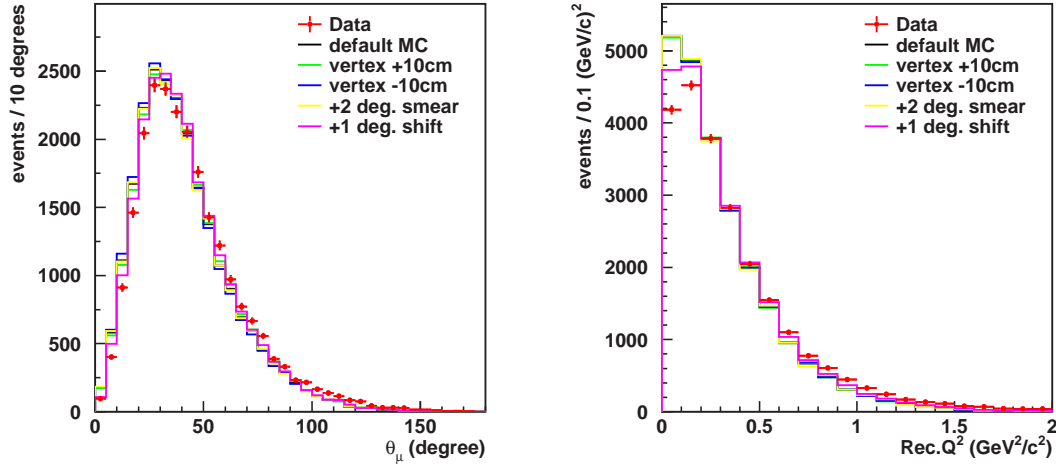


**Figure 7.29:** Systematic studies on the effect of the angular biases in the reconstruction on the angular (left) and reconstructed 4-momentum transfer squared (right) distributions in FC1R $\mu$  sample. See the text for the explanation of each histogram. Any systematic biases cannot explain the deficit in the forward region and the hard scattering in data.

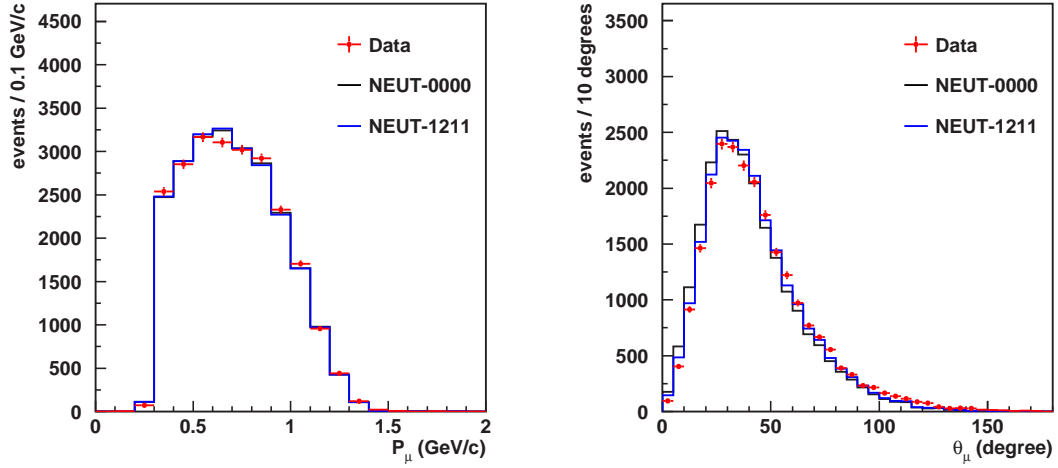


**Figure 7.30:** Comparison of the muon momentum and angular distributions between NEUT-0000 and NEUT-1211 for FC1R $\mu$  sample. Data is also superimposed in the figures.

interaction cross-section around 1 GeV region.\* We have modified the models used in our Monte Carlo simulation according to the existing models or within the size of uncertainties of existing experimental data. The detailed descriptions for the modifications are given in Sec. 4.2. The key point of the modifications is that the model for each interaction mode have been modified to have harder scattering and suppression in low  $q^2$  region.

For the interactions of (quasi-)elastic and single pion production, the existing experimental values for  $M_A$  are 1.0 GeV/ $c^2$  and have uncertainty of about 10% and 20%, respectively. In our spectral analysis, we have decided to use 1.1 GeV/ $c^2$  for (quasi-)elastic interaction and 1.2 GeV/ $c^2$  for single pion production. For the deep inelastic scattering and the coherent pion production, we employ the models by A. Bodek *et al.* [96] and J. Marteau *et al.* [105, 106], respectively, both of which suppress the interaction cross-section in the low  $q^2$  region. Fig. 7.30 show the comparison of muon momentum and angular distributions between NEUT-0000 and NEUT-1211 as well as data for FC1R $\mu$  sample, indicating that our data favors NEUT-1211 than NEUT-0000 although data still has a little deficit in the small angle region.

In summary, we have employed the model NEUT-1211 in the spectral analysis described in following sections and the oscillation analysis described in Chapter 9. It is also found that the choice of models make some biases on the measurement of the cross-section ratio of non-qe/qe, and hence the effect of choice of different models has been also studied, which is described in Sec. 7.4.6.

### 7.4.5 $\chi^2$ fitting to derive the neutrino spectrum at ND

#### An overview of the fitting method

A  $\chi^2$ -fitting is employed to derive the neutrino energy spectrum at ND from the observed muon momentum and angular distributions. The data sample used in the fitting is FC1R $\mu$ , SciFi-MRD 1-track, 2-track QE, and 2-track non-QE samples. The fitting procedure is as follows.

\*Actually, there exist no experimental data for the oxygen target in the low energy region, and hence we do not understand well the behavior of the cross-section.

1. The neutrino spectrum is divided into eight bins; 0–0.5 GeV, 0.5–0.75 GeV, 0.75–1.0 GeV, 1.0–1.5 GeV, 1.5–2.0 GeV, 2.0–2.5 GeV, 2.5–3.0 GeV, and above 3.0 GeV. The neutrino interaction modes are also separated into two categories; (quasi-)elastic (qe) and inelastic interactions (non-qe). The fitting parameters are, therefore, the weighting factors for each energy bin relative to the values estimated by Beam-MC ( $f_i^\phi$ ,  $i = 1, \dots, 8$ ) and the cross-section ratio of non-qe to qe which is also relative to the value in Neut-MC ( $R_{\text{nqe}}$ ). In order to make consistency between 1KT and FGD, the 4th bin ( $f_4^\phi$ ) is fixed to be unity during the fitting for the normalization, and another set of parameters is prepared to normalize the distributions separately in 1KT and FGD ( $P_{\text{norm}}^{\text{1KT}}$  and  $P_{\text{norm}}^{\text{FGD}}$ ).
2. The 2-dimensional distributions of the muon momentum versus scattering angle with respect to the beam direction for four categories of event sample are compared in the  $\chi^2$ -fitting. For the Monte Carlo sample, this 2-dimensional distribution is prepared separately for each of eight neutrino energy bin and each interaction mode, therefore,  $8 \times 2$  distributions are made in MC. The example distributions for data and MC are shown in Fig. 7.31.
3. The  $\chi^2$  functions for 1KT sample ( $\chi_{\text{1KT}}^2$ ) and for FGD samples ( $\chi_{\text{FGD}}^2$ ) are separately defined, and they are summed to build a combined  $\chi^2$  function ( $\chi_{\text{ND}}^2$ ). In addition to them, since the results of PIMON measurements can also restrict the neutrino energy spectrum, a  $\chi^2$  function ( $\chi_{\text{PIMON}}^2$ ) is added to  $\chi_{\text{ND}}^2$  as a constraint on the weighting factors of the spectrum. Therefore, the final form of the  $\chi^2$  function becomes

$$\chi_{\text{ND}}^2 = \chi_{\text{1KT}}^2 + \chi_{\text{FGD}}^2 + \chi_{\text{PIMON}}^2 \quad . \quad (7.16)$$

The details of each part of the  $\chi^2$  function are described in the following sections.

4. Finally, a set of fitting parameters ( $f_i^\phi$  and  $R_{\text{nqe}}$ ) are found by minimizing the  $\chi^2$  function. Same procedure is applied to the different sets of interaction models in the Monte Carlo simulation in order to estimate the dependence of fitting results on interaction models, which is discussed in Sec. 7.4.6

### Definition of $\chi^2$ function for FC1R $\mu$ sample

The momentum versus angle 2-dimensional for FC1R $\mu$  sample is binned with the interval of 0.1 GeV/c in momentum and  $10^\circ$  in angle. Bins above  $90^\circ$  are integrated into one angular bin, as shown in Fig. 7.31. The  $\chi^2$  function is defined as

$$\chi_{\text{1KT}}^2 = \sum_{m,n} \frac{(N_{m,n}^{\text{data}} - N_{m,n}^{\text{MC}})^2}{(\sigma_{m,n})^2} + \frac{(1 - P_{\text{e-scale}}^{\text{1KT}})^2}{(\sigma_{\text{e-scale}}^{\text{1KT}})^2} \quad , \quad (7.17)$$

$$N_{m,n}^{\text{MC}} = P_{\text{norm}}^{\text{1KT}} \cdot \sum_{i=1}^8 f_i^\phi \cdot (N_{m,n}^{\text{MC}[i,\text{qe}]} + R_{\text{nqe}} \cdot N_{m,n}^{\text{MC}[i,\text{nqe}]} ) \quad , \quad (7.18)$$

where  $i$  represents the bin number of neutrino energy,  $m$  and  $n$  represent the bin number of the 2-dimensional distribution of momentum versus angle,  $N_{m,n}^{\text{data}}$  is the number of contents in the  $(m,n)$ -th bin in data,  $N_{m,n}^{\text{MC}[i,\text{qe(nqe)}]}$  is the same one as data but for the  $i$ -th energy bin and qe (non-qe) interactions in the Monte Carlo simulation,  $\sigma_{m,n}$  is the error associated to the  $(m,n)$ -th bin including both statistical and systematic uncertainties, and  $P_{\text{norm}}^{\text{1KT}}$  is overall normalization factor for FC1R $\mu$  sample. In the summation over  $(m,n)$ , only the bins with contents in MC greater than 20 are used in order to avoid a possible strange bias due to small statistics. The

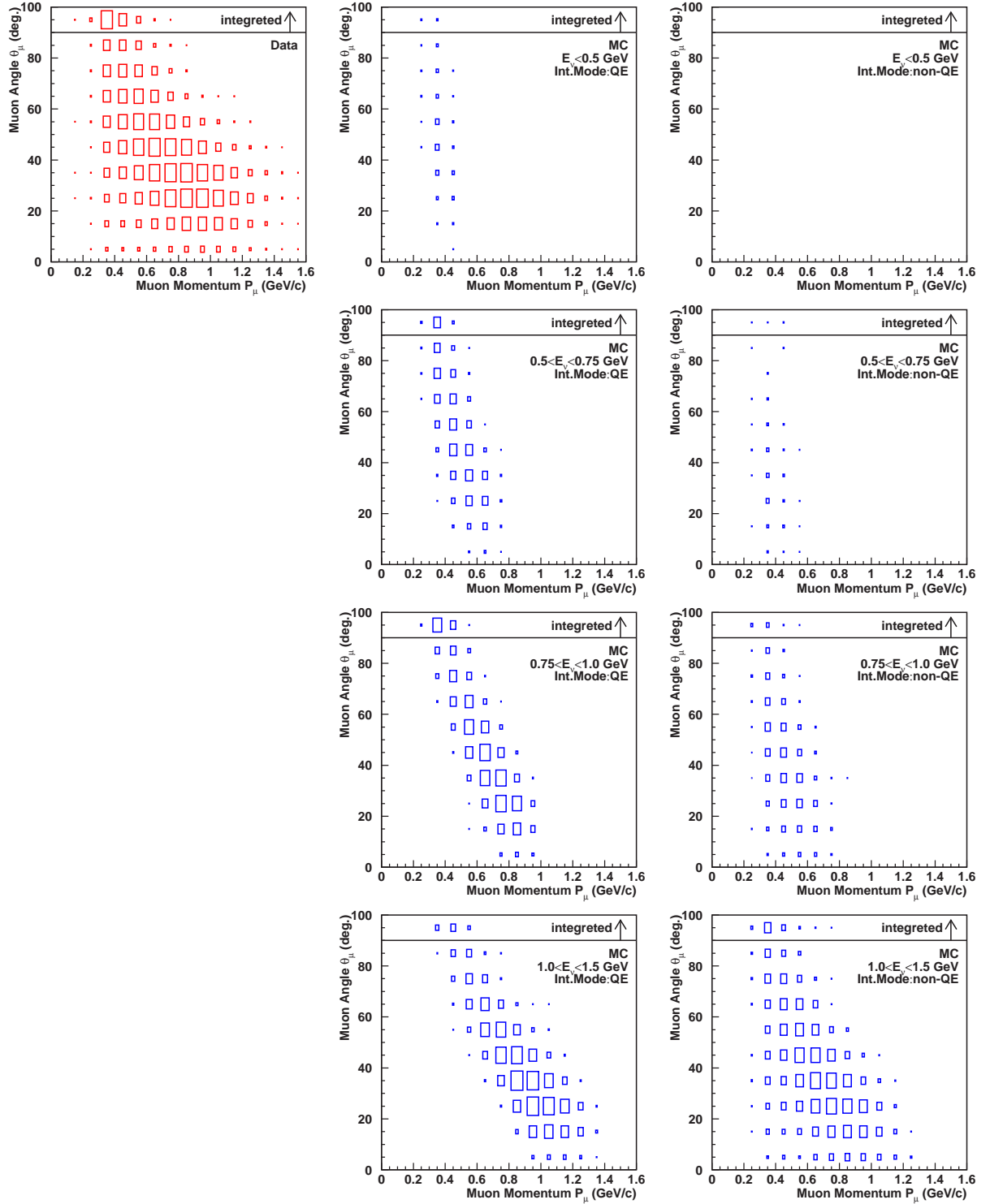


**Figure 7.31:** Two-dimensional distributions of the muon momentum versus scattering angle for data (red plot) and for the Monte Carlo simulation for each energy bin and each interaction mode (blue plots). These plots are of FC1R $\mu$  sample, and same distributions are prepared for SciFi-MRD samples. The size of each box represents the number of contents in each bin. The corresponding energy bin and interaction mode of each plot for MC is indicated in the plot. Here, only 8 distributions are shown for MC, although there are 16 distributions in total.

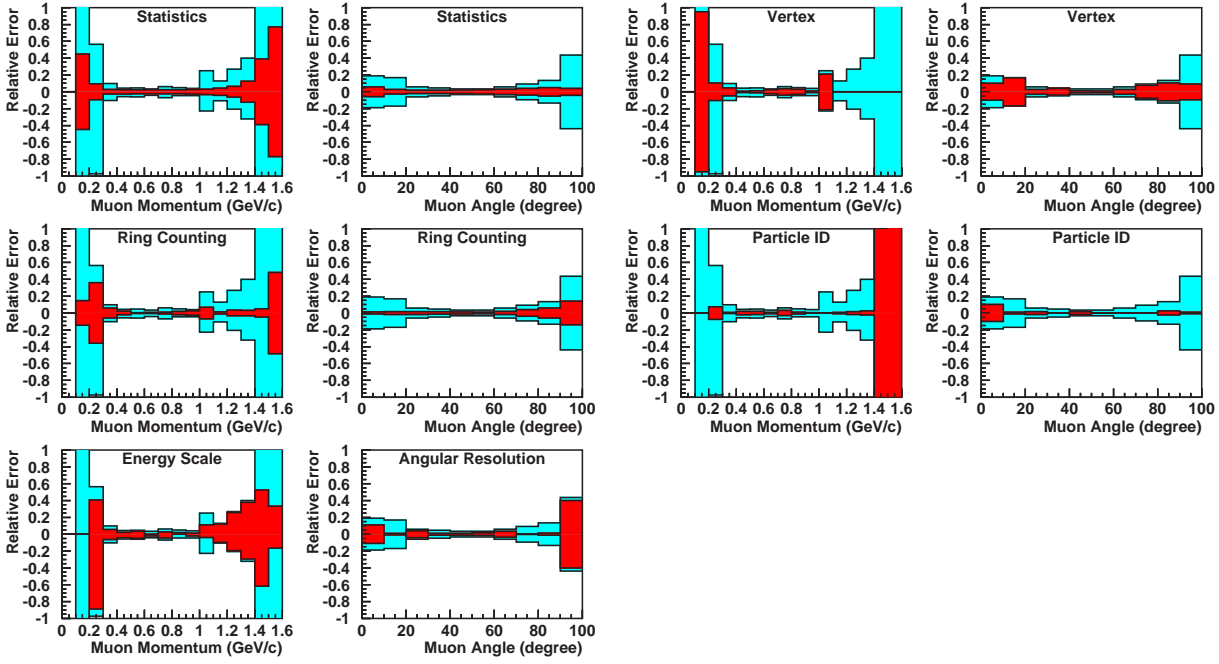


**Figure 7.32:** Contributions of various uncertainties to the momentum and angular distributions in FC1R $\mu$  sample. Relative errors are shown. In all the figures, light blue region show the size of total error and red region show the contribution of the error source specified in each figure. Statistical uncertainty is calculated to be the squared root of the number of events projected onto the momentum and angular axes.

systematic uncertainty in the energy scale is also incorporated into the  $\chi^2$  function, which is expressed by the last term in Eq. (7.17).  $P_{\text{e-scale}}^{\text{1KT}}$  is the fitting parameter for the energy scale uncertainty, which scales the  $(p, \theta)$  distribution of data up and down in the momentum direction by varying its value. As the uncertainty in the energy scale ( $\sigma_{\text{e-scale}}^{\text{1KT}}$ ),  $^{+2}_{-3}\%$  is used.

Systematic uncertainty on the  $(m, n)$ -th bin are estimated for the various sources as a function of muon momentum and angle. Each contribution to the error on each bin are illustrated in Fig. 7.32, where uncertainties on momentum and angular bins are separately shown. The method to estimate the systematic uncertainty for each source is as follows;

Vertex reconstruction: As mentioned before, there exists discrepancy of about 5–10 cm in reconstructing the vertex between data and MC. The effect of such vertex shift is studied by changing the size and the position of fiducial volume by  $\pm 10$  cm, and the difference in the distributions is quoted as the systematic error.

Ring counting: The uncertainty in the ring counting also makes effect on the momentum and angular distribution, since the goodness of the ring counting depends on the particle momentum. By changing the selection criterion for single ring events, where the ring counting likelihood  $\mathcal{F}_1$  is used, the effect of single ring event selection is studied. As seen in Fig. 7.19, there is small discrepancy around the cut position ( $\mathcal{F}_1 = 0$ ), and hence two kinds of studies have been performed. First, selection criterion is changed around  $\mathcal{F}_1 = 0$  by  $\pm 2.5$  only in data, and the difference in the momentum and angular distribution is studied. Secondly, selection criterion is

changed around  $\mathcal{F}_1 = 0$  by  $\pm 5$  in both data and MC simultaneously, and the difference of change in the distributions between data and MC is studied. The effects of these two operations are quadratically summed and quoted as the systematic errors due to the ring counting uncertainty.

Particle identification: The performance of particle identification also depends on particle momentum. The difference in the momentum and angular distribution between with and without  $\mu$ -like selection is studied, and is quoted as the systematic error.

FC/PC separation: The effect due to a variation in the criterion of FC/PC separation is studied by changing the *pomax20deg* cut by  $\pm 5\%$ , yielding a negligible effect on both momentum and angular distributions.

Angular resolution: As is also previously mentioned, the angular resolution has discrepancy of about  $2^\circ$  between data and MC. The resolution in MC is smeared by this size and the effect is studied. Furthermore, in order to make the large angle region not affect on the fitting, we quoted additional 40% error on the bins greater than  $90^\circ$ , since the consistency check between 1KT and FGD can not be done due to that FGD has no acceptance in this region and we cannot judge whether the discrepancy between data and MC in this region is really physical or not.

Energy scale: The uncertainty in the energy scale is estimated to be  $^{+2}_{-3}\%$  as mentioned before. The momentum is scaled within this size and the difference in the momentum distribution is quoted as the systematic uncertainty. In this study, the behavior of the distribution around the threshold ( $\sim 1000$  p.e.) is also investigated by changing the criteria on the total photoelectron cut.

All the systematic uncertainties above are quadratically summed on a bin by bin basis together with the statistical error, and the total error on each bin,  $\sigma_{m,n}$ , is obtained.

### Definition of $\chi^2$ function for SciFi-MRD samples

The  $\chi^2$  function for SciFi-MRD samples is built separately for 1-track, 2-track QE, and 2-track non-QE samples. In the 2-dimensional distribution of muon momentum and angle for each sample, momentum is binned into the same binning as that of neutrino energy, and angle is binned into an interval of  $10^\circ$ . In order to calculate the  $\chi^2$ , binned likelihood method is employed;

$$\begin{aligned}\chi_{\text{FGD}}^2 &= -2 \ln \lambda(\mathbf{f}) \\ &= 2 \sum_l \sum_{m,n} \left[ N_{l;m,n}^{\text{MC}}(\mathbf{f}) - N_{l;m,n}^{\text{data}} + N_{l;m,n}^{\text{data}} \cdot \ln \frac{N_{l;m,n}^{\text{data}}}{N_{l;m,n}^{\text{MC}}(\mathbf{f})} \right],\end{aligned}\quad (7.19)$$

where  $\lambda(\mathbf{f}) = \mathcal{L}(\mathbf{N}^{\text{data}}; \mathbf{N}^{\text{MC}}(\mathbf{f})) / \mathcal{L}(\mathbf{N}^{\text{data}}; \mathbf{N}^{\text{data}})$  is a ratio of a likelihood that a set of data bins,  $\mathbf{N}^{\text{data}} = \{N_{l;m,n}^{\text{data}}\}$ , is obtained when a set of MC bins,  $\mathbf{N}^{\text{MC}}(\mathbf{f}) = \{N_{l;m,n}^{\text{MC}}(\mathbf{f})\}$ , is expected, and  $\mathbf{f}$  is a set of fitting parameters such as the weighing factors for neutrino energy bins ( $f_i^\phi$ ), non-qe/qe ratio  $R_{\text{nqe}}$ , and some systematic parameters. Poisson likelihood is used for  $\mathcal{L}$ . The summation in Eq. (7.19) is performed over all the event categories ( $l = 1\text{-track}, 2\text{-track QE}, 2\text{-track non-QE}$ ) and all the  $(p_\mu, \theta_\mu)$ -bins ( $m, n$ ). For convenience,  $l = 1, 2$ , and 3 represent 1-track, 2-track QE, and 2-track non-QE samples, respectively.  $N_{l;m,n}^{\text{MC}}(\mathbf{f})$  are calculated as following steps.

First, content in each bins for each event category is calculated;

$$N_{1;m,n}^{\text{MC}} = P_{\text{norm}}^{\text{FGD}} \cdot \sum_i^8 f_i^\phi \cdot [N_{1;m,n}^{\text{MC}[i,\text{qe}]} + R_{\text{nqe}} \cdot N_{1;m,n}^{\text{MC}[i,\text{nqe}]}] , \quad (7.20)$$

$$N_{2;m,n}^{\text{MC}} = P_{\text{norm}}^{\text{FGD}} \cdot \sum_i^8 f_i^\phi \cdot [N_{2;m,n}^{\text{MC}[i,\text{qe}]} + R_{\text{rescat}} \cdot (1 - P_{\text{rescat}}) \cdot N_{2;m,n}^{\text{MC}[i,\text{qe}]} + R_{\text{nqe}} \cdot N_{2;m,n}^{\text{MC}[i,\text{nqe}]}] , \quad (7.21)$$

$$N_{3;m,n}^{\text{MC}} = P_{\text{norm}}^{\text{FGD}} \cdot \sum_i^8 f_i^\phi \cdot [N_{3;m,n}^{\text{MC}[i,\text{qe}]} - R_{\text{rescat}} \cdot (1 - P_{\text{rescat}}) \cdot N_{2;m,n}^{\text{MC}[i,\text{qe}]} + R_{\text{nqe}} \cdot N_{3;m,n}^{\text{MC}[i,\text{nqe}]}] , \quad (7.22)$$

where  $N_{l;m,n}^{\text{MC}[i,\text{qe}(\text{nqe})]}$  is the same meaning as the FC1R $\mu$  case, and  $P_{\text{norm}}^{\text{FGD}}$  is the normalization parameter for FGD samples. The second terms in Eq. (7.21) and (7.22) represent the migration between QE and non-QE samples due to the effect that a proton scattered in CC-qe interaction is re-scattered by the nucleons inside the nucleus, which makes a QE event to be identified as non-QE one.  $R_{\text{rescat}}$  is a fraction of the number of QE events migrating into non-QE sample when the proton re-scattering probability changes from 0% to 100%, and  $P_{\text{rescat}}$  is a fitting parameter which represents the uncertainty of the proton re-scattering probability.  $R_{\text{rescat}}$  is estimated to be 0.33 by a Monte Carlo study. Since the default value of the proton re-scattering probability in our Monte Carlo is set to 100%,  $P_{\text{rescat}}$  is used to rescale it. The central value of  $P_{\text{rescat}}$  is set to be 0.87 in order for our Monte Carlo simulation to reproduce the results of the measurements for the proton re-scattering in electron scattering on  $^{12}\text{C}$  target [116]. The 10% uncertainty on the probability is adopted according to its results.

Next, the detector systematics is considered as following. Migration between 1-track and 2-track samples due to the ambiguity of the efficiency for the second track finding is taken into account by following expression;

$$N'_{1;m,n}^{\text{MC}} = N_{1;m,n}^{\text{MC}} + (1 - P_{\text{2nd-eff}}) \cdot (N_{2;m,n}^{\text{MC}} + N_{3;m,n}^{\text{MC}}) , \quad (7.23)$$

$$N'_{2(3);m,n}^{\text{MC}} = N_{2(3);m,n}^{\text{MC}} + P_{\text{2nd-eff}} \cdot N_{2(3);m,n}^{\text{MC}} , \quad (7.24)$$

where  $P_{\text{2nd-eff}}$  represents the uncertainty of the second track finding efficiency, which is also incorporated in the fitting as a fitting parameter.

Finally the uncertainty of the first track finding efficiency is considered. This is taken into account in the momentum dependent form;

$$N''_{l;m,n}^{\text{MC}} = P_{\text{1st-eff}(m)} \cdot N'_{l;m,n}^{\text{MC}} , \quad (7.25)$$

where  $P_{\text{1st-eff}(m)}$  is a fitting parameter representing the uncertainty of the first track finding efficiency for the  $m$ -th momentum bin. In actual fitting, only the uncertainties in first three bins are treated as free parameters (the first momentum bin in SciFi-MRD samples is empty, and hence the second and third ones are meaningful).

Then, each content of the weighted MC,  $N''_{l;m,n}^{\text{MC}}$ , is normalized to data by total number of events in all three samples, and used in  $\chi_{\text{FGD}}^2$  as  $N_{l;m,n}^{\text{MC}}(\mathbf{f})$  in Eq. (7.19).

In order to constrain the systematic parameters within their uncertainties, constraint terms



**Table 7.7:** The central values and the uncertainties of systematic parameters incorporated in the  $\chi^2$  function of FGD.

Systematic parameters		Central values	Errors
Proton rescattering	$P_{\text{rescat}}$	0.87	0.1
Energy scale	$P_{\text{e-scale}}^{\text{FGD}}$	1.0	0.027
1st track efficiency	$P_{\text{1st-eff}(2)}$	1.0	0.5
	$P_{\text{1st-eff}(3)}$	1.0	0.5
2nd track efficiency	$P_{\text{2nd-eff}}$	1.0	0.05

are added to  $\chi_{\text{FGD}}^2$ ;

$$\chi_{\text{FGD-syst}}^2 = \frac{(P_{\text{rescat}} - P_{\text{rescat}}^0)^2}{(\sigma_{\text{rescat}})^2} + \frac{(P_{\text{2nd-eff}} - P_{\text{2nd-eff}}^0)^2}{(\sigma_{\text{2nd-eff}})^2} + \sum_m \frac{(P_{\text{1st-eff}(m)} - P_{\text{1st-eff}(m)}^0)^2}{(\sigma_{\text{1st-eff}(m)})^2} + \frac{(P_{\text{e-scale}}^{\text{FGD}} - P_{\text{e-scale}}^0)^2}{(\sigma_{\text{e-scale}})^2}, \quad (7.26)$$

where  $P^0$ 's and  $\sigma$ 's, respectively, represent the central values and the uncertainties of the systematic parameters. As is done in the FC1R $\mu$  case, the uncertainty in the energy scale in SciFi-MRD samples is also incorporated in the fitting, and the 2-dimensional distribution is scaled up and down in the momentum direction. The last term in Eq. (7.26) represents the constraint on the energy scale. The central values and the uncertainties of the systematic parameters are summarized in Table 7.7.

### Constraint of PIMON measurements on the energy spectrum

In addition to the  $\chi^2$  functions from 1KT and FGD, since PIMON measures the neutrino spectrum above 1 GeV as mentioned in Chapter 6, the results can constrain the corresponding weighting factors for the neutrino spectrum in the fitting, namely  $f_4^\phi - f_8^\phi$ . The  $\chi^2$  function for the PIMON constraint term is

$$\chi_{\text{PIMON}}^2 = \sum_{i=5}^7 \frac{(f_i^\phi - f_i^{\text{PIMON}})^2}{(\sigma_i^{\text{PIMON}})^2}, \quad (7.27)$$

where  $f_i^{\text{PIMON}}$  is the central value of the spectrum weighting factor of  $i$ -th bin derived from the PIMON measurements and  $\sigma_i^{\text{PIMON}}$  is its error. Since  $f_4^\phi$  is fixed to be unity for a normalization in the fitting and there is only one bin above 2.5 GeV in the PIMON measurements, the summation is performed from 5th to 7th bin. The central values of PIMON measurements,  $f_i^{\text{PIMON}}$ , in Eq. (7.27) is calculated as follows;

$$f_i^{\text{PIMON}} = \frac{\Phi_i^{\text{PIMON}} / \Phi_i^{\text{MC}}}{\Phi_4^{\text{PIMON}} / \Phi_4^{\text{MC}}} \quad (i = 5, 6, 7), \quad (7.28)$$

where  $\Phi_i^{\text{PIMON}}$  is the neutrino flux in  $i$ -th bin measured by PIMON and  $\Phi_i^{\text{MC}}$  is that estimated by Beam-MC. The values for  $\Phi_i^{\text{PIMON}}$ ,  $\Phi_i^{\text{MC}}$ ,  $f_i^{\text{PIMON}}$ , and  $\sigma_i^{\text{PIMON}}$  are summarized in Table 7.8.

**Table 7.8:** Summary of the numbers used in the constraint term of PIMON in the  $\chi^2$  function.

Neutrino energy (Bin number)	1.0–1.5 GeV ( $i = 4$ )	1.5–2.0 GeV ( $i = 5$ )	2.0–2.5 GeV ( $i = 6$ )	2.5 GeV– ( $i = 7$ )
$\Phi_i^{\text{PIMON}}$	$6.30 \times 10^{11}$	$3.21 \times 10^{11}$	$1.01 \times 10^{11}$	$4.27 \times 10^{10}$
$\Phi_i^{\text{MC}}$	$6.19 \times 10^{11}$	$3.35 \times 10^{11}$	$1.05 \times 10^{11}$	$3.96 \times 10^{10}$
$f_i^{\text{PIMON}}$	—	0.941	0.945	1.059
$\sigma_i^{\text{PIMON}}$	—	$+10.7\%$ $-9.9\%$	$+12.1\%$ $-17.7\%$	$+47.7\%$ $-34.0\%$

## Fitting results

By changing the weighting factors  $f_i^\phi$ , non-qe/qe ratio  $R_{\text{nqe}}$ , and systematic parameters for each detectors, the best-fit point is searched for. MINUIT [117] is used to minimize the  $\chi^2$  function. The value of  $\chi^2$  is 227.18/197 d.o.f at the best-fit point, for which the  $\chi^2$ -probability is 6.91%. The central values for the fitting parameters and their errors are summarized in Table 7.9. All the parameters including the detector systematics are found to lie within their expected errors. The error matrix for  $f_i^\phi$  and  $R_{\text{nqe}}$  is shown in Table 7.10.

The resulting distributions of the muon momentum, the muon angle, the reconstructed neutrino energy, and the reconstructed 4-momentum transfer squared for each sample are shown in Fig. 7.33 and Fig. 7.34. All the distributions show that the fitted results agree well with the data. The behavior of  $\chi^2$  value around the best-fit point as a function of each fitting parameter value is shown in Fig. 7.35, indicating that the minimization of  $\chi^2$  function have successfully done to find the global minimum point.

The fitting using only 1KT sample and only FGD samples have also been performed, and these results are summarized in Table 7.9 together with the results of the 1KT+FGD combined fitting. They are also compared in Fig. 7.36. All the parameters, except for  $R_{\text{nqe}}$ , are in agreement within their errors not depending on the data sample used in the fitting.

Several studies have been done against  $R_{\text{nqe}}$  resulting in the inconsistent values between 1KT only and FGD only fitting. In the conclusion of the studies, the reason is due to the different purity for CC-qe in each sample. It is quantitatively understood as follows: A deficit in the forward region still remain even if NEUT-1211 is chosen as a model in MC, as shown in Fig. 7.30. In the case of 1KT only fitting,  $R_{\text{nqe}}$  is decreased in order to suppress the events in the forward region since there are more non-qe events than qe ones in the forward region in FC1R $\mu$  sample. Small  $R_{\text{nqe}}$  value also decrease the events in small momentum region since there are a lot of low momentum events from non-qe interaction as shown in Fig. 7.31. In order to compensate the suppression in the low momentum region, neutrino fluxes in low energy region are increased which can be seen in Fig. 7.36. Then the fitting is settled. In fact, there is strong correlation between the weighting factors for the low energy region and  $R_{\text{nqe}}$ , which is seen in the covariance matrix of fitting parameters in Table 7.10. On the other hand, in the case of the FGD fitting, there are three samples with different purities for CC-qe, making the constraint on  $R_{\text{nqe}}$ , and  $R_{\text{nqe}}$  is settled at different value from the 1KT case.

Inferred from the behavior above, the choice of model in MC may bias the estimation of neutrino energy spectrum. Therefore we have studied the dependence of the results on models, which will discussed in the next section.

Finally, dominant contribution to the error size of the spectrum weighting factors ( $f_i^\phi$ ) is investigated by turning on and off the systematic uncertainties one by one. Fig. 7.37 shows the resulting size of errors on the fitting parameters by a fitting with systematic uncertainties on

**Table 7.9:** Summary of the  $\chi^2$  fitting results. The central values for all the fitting parameters and their errors are listed. The results with only 1KT  $\chi^2$  and only FGD  $\chi^2$  fitting are also shown as well as 1KT+FGD merged (ND) fitting results.

Fitting parameters		1KT+FGD		1KT only		FGD only	
		Values	Errors	Values	Errors	Values	Errors
0–0.5 GeV	$f_1^\phi$	1.314	0.486	1.781	0.460	1.000	(fixed)
0.5–0.75 GeV	$f_2^\phi$	1.021	0.119	1.125	0.111	0.950	1.351
0.75–1.0 GeV	$f_3^\phi$	1.007	0.092	1.012	0.086	1.487	0.433
1.0–1.5 GeV	$f_4^\phi$	1.000	(fixed)	1.000	(fixed)	1.000	(fixed)
1.5–2.0 GeV	$f_5^\phi$	0.955	0.071	0.956	0.085	1.084	0.179
2.0–2.5 GeV	$f_6^\phi$	0.962	0.084	0.966	0.120	0.927	0.133
2.5–3.0 GeV	$f_7^\phi$	1.183	0.188	1.143	0.473	1.344	0.312
3.0 GeV–	$f_8^\phi$	1.073	0.199	1.000	(fixed)	1.024	0.225
non-qe/qe	$R_{\text{nqe}}$	0.929	0.060	0.696	0.081	1.094	0.091
1KT normalization	$P_{\text{norm}}^{\text{1KT}}$	0.733	0.010	0.740	0.988	—	—
1KT energy scale	$P_{\text{e-scale}}^{\text{1KT}}$	0.971	0.004	0.975	0.005	—	—
FGD normalization	$P_{\text{norm}}^{\text{FGD}}$	0.956	0.044	—	—	0.832	0.080
FGD energy scale	$P_{\text{e-scale}}^{\text{FGD}}$	0.967	0.006	—	—	0.962	0.007
Proton rescattering	$P_{\text{rescat}}$	0.850	0.069	—	—	0.786	0.075
1st track efficiency (2nd Bin)	$P_{\text{1st-eff}(2)}$	1.536	0.093	—	—	1.485	0.102
1st track efficiency (3rd Bin)	$P_{\text{1st-eff}(3)}$	1.083	0.034	—	—	1.049	0.044
2nd track efficiency	$P_{\text{2nd-eff}}$	0.976	0.021	—	—	0.962	0.024
Minumum $\chi^2/\text{d.o.f.}$		227.18/197		83.48/74		130.83/117	
$\chi^2$ -probability		6.91%		21.12%		18.04%	

**Table 7.10:** Error matrix for  $f_i^\phi$  and  $R_{\text{nqe}}$  obtained in the  $\chi^2$  fitting. The squared root of error matrix ( $\text{sign}[\{M_{\phi,\text{nqe}}\}_{ij}] \cdot \sqrt{|\{M_{\phi,\text{nqe}}\}_{ij}|}$ ) is written here in the unit of %.

	$f_1^\phi$	$f_2^\phi$	$f_3^\phi$	$f_4^\phi$	$f_5^\phi$	$f_6^\phi$	$f_7^\phi$	$f_8^\phi$	$R_{\text{nqe}}$
$f_1^\phi$	48.9	−11.4	6.60	—	0.926	2.12	−4.16	5.12	−8.22
$f_2^\phi$	−11.4	11.9	−2.98	—	2.68	0.989	2.26	2.97	−4.10
$f_3^\phi$	6.60	−2.98	9.17	—	4.68	−0.867	4.55	2.09	−2.35
$f_4^\phi$	—	—	—	—	—	—	—	—	—
$f_5^\phi$	0.926	2.68	4.68	—	7.07	−2.12	7.64	4.93	−1.88
$f_6^\phi$	2.12	0.989	−0.867	—	−2.12	8.43	−7.58	8.17	−1.86
$f_7^\phi$	−4.16	2.26	4.55	—	7.64	−7.58	18.8	−11.2	−1.68
$f_8^\phi$	5.12	2.97	2.09	—	4.93	8.17	−11.2	19.9	−3.69
$R_{\text{nqe}}$	−8.22	−4.10	−2.35	—	−1.88	−1.86	−1.68	−3.69	6.04

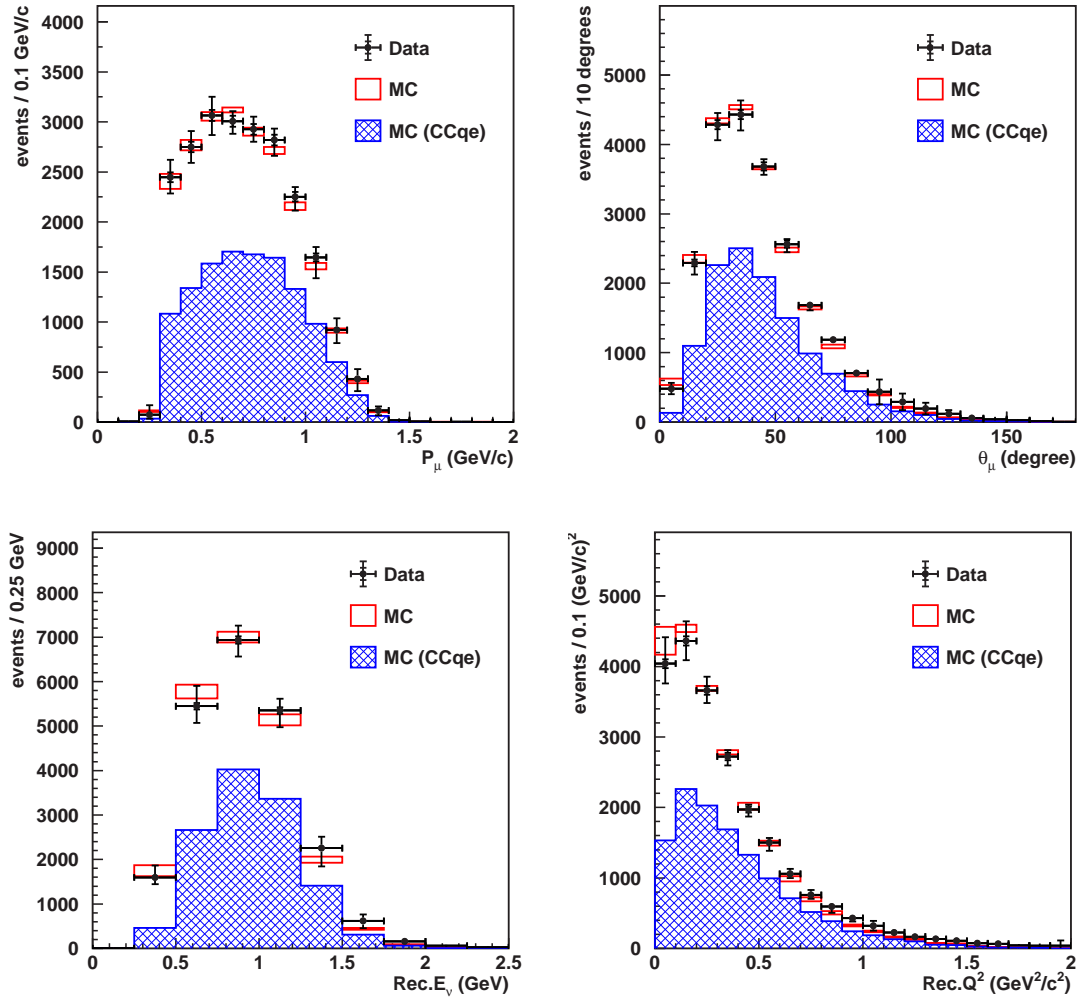


**Figure 7.33:** Distributions of the muon momentum (upper left), the muon angle (upper right), the reconstructed neutrino energy (lower left), and the reconstructed  $Q^2$  (lower right) after the fitting for FC1R $\mu$  sample. Histograms for the Monte Carlo simulations are weighted by using the fitted parameter values.

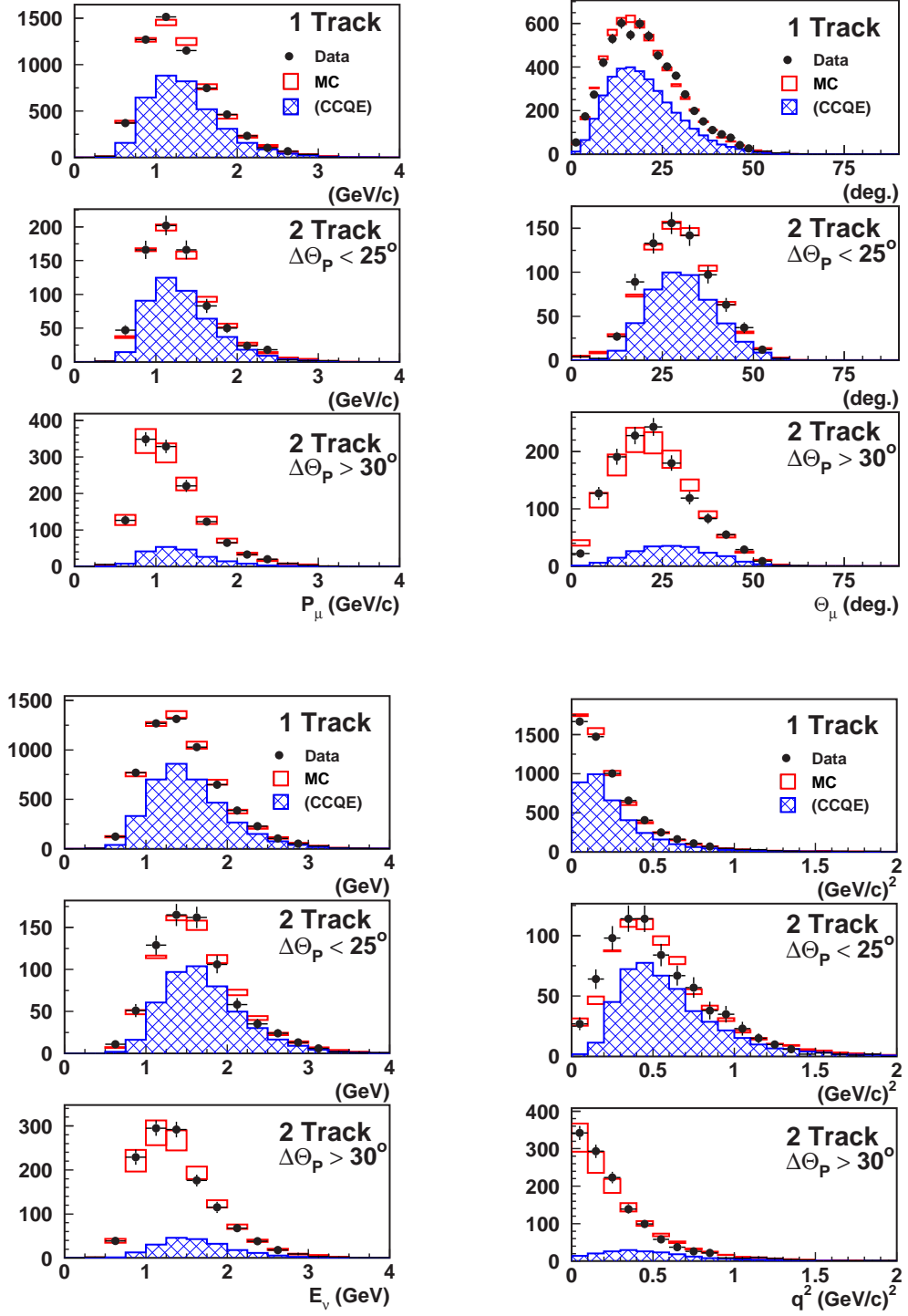


**Figure 7.34:** Distributions of the muon momentum (upper left three figures), the muon angle (upper right three figures), the reconstructed neutrino energy (lower left three figures), and the reconstructed  $Q^2$  (lower right three figures), after the fitting for SciFi-MRD samples. For each set of the distributions, top figure shows 1-track sample, middle figure shows 2-track QE sample, and bottom figure shows 2-track non-QE sample. Histograms for the Monte Carlo simulations are weighted by using the fitted parameter values.

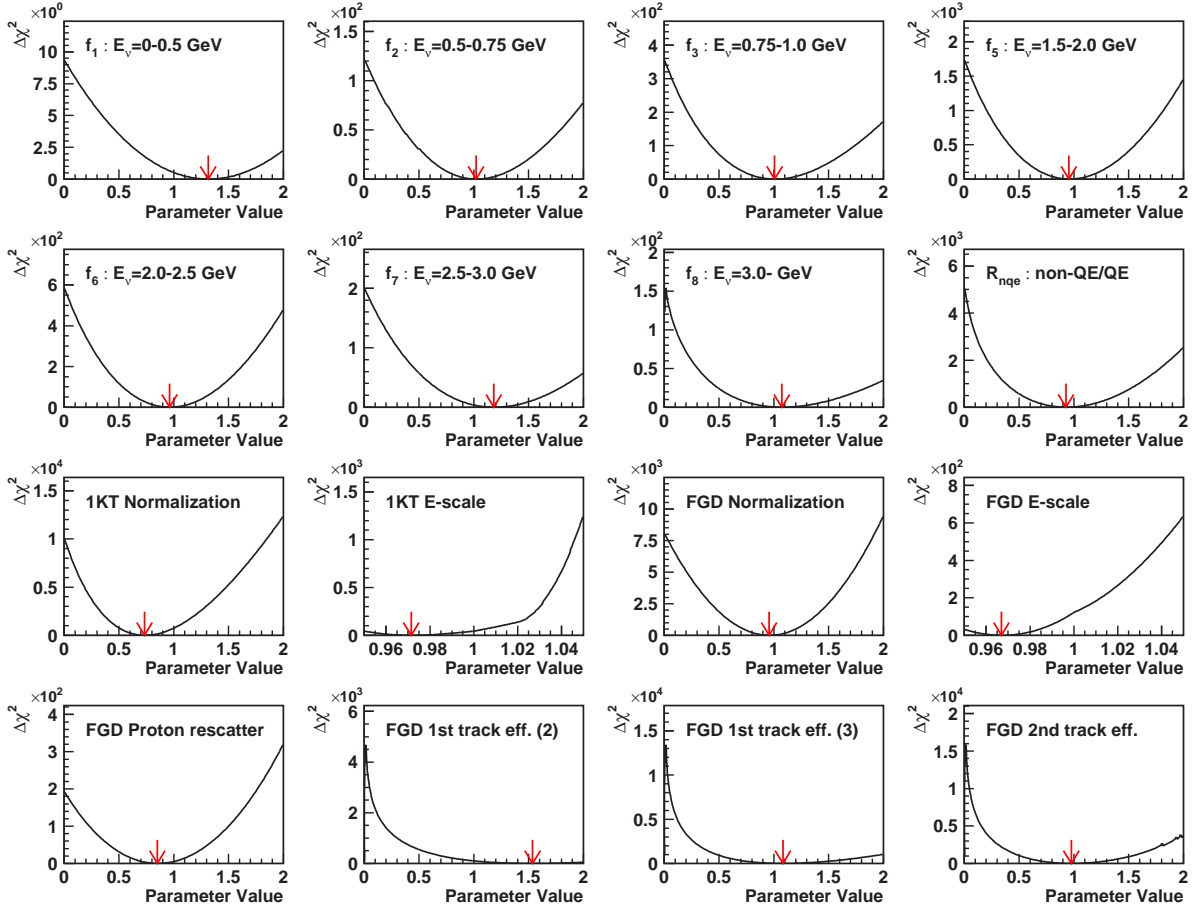


**Figure 7.35:** Behavior of  $\Delta\chi^2$  around the best fit point as a function of each fitting parameter value. In each figure, only one parameter specified in the figure is varied around the best-fit point, and  $\chi^2$  is calculated as a function of the parameter value with all other parameters fixed at the best-fit point. Horizontal axis is the value of the varied parameter and vertical axis is the  $\Delta\chi^2$ , the difference between current  $\chi^2$  and the minimum (best-fit)  $\chi^2$ . Red arrow shows the best-fit point of each fitting parameter.

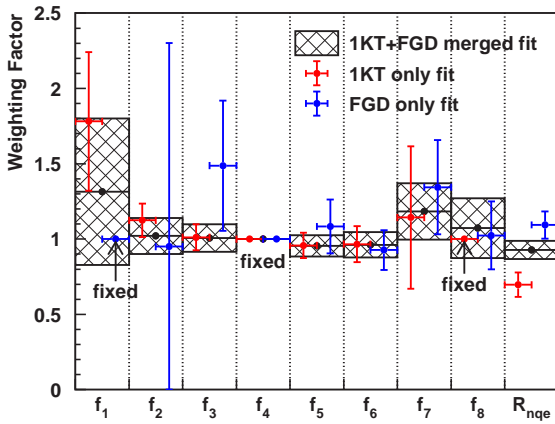


**Figure 7.36:** Comparison of the fitting results between 1KT only fitting and FGD only fitting, together with the results of the 1KT+FGD merged fitting. All the fitting parameters except for  $R_{nqe}$  agrees within their errors not depending on the data samples used in the fitting.

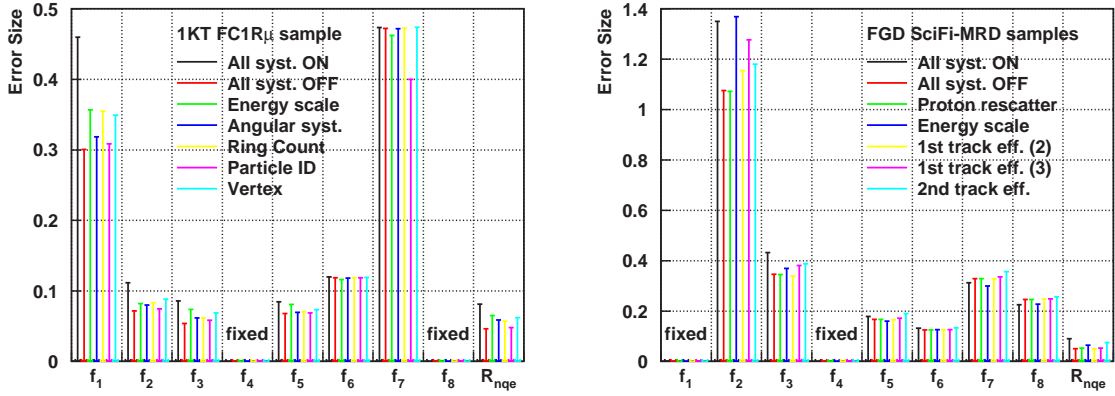


**Figure 7.37:** Error size of the fitting parameters. Left figure is of 1KT, and right figure is of FGD. Each color corresponds to the fitting with a certain systematic uncertainty specified in the figure turned on. There is only small difference in the size of error between the fitting with and without the systematic uncertainties turned on, indicating that the main contribution to the error size is statistic errors.

and off. Even when all the systematic uncertainties are turned off, the size of errors do not change so much compared to the fitting with all the systematic uncertainties on. This indicates that the dominating contribution to the errors is statistical one.

#### 7.4.6 Dependence of fitting results on interaction models

We have tried the same fitting for several sets of neutrino interaction models in order to investigate the possible bias on the results due to the choice of model. As mentioned in Sec. 4.2, we studied following changes in the neutrino interactions as their uncertainties.

In qe scattering and single pion production, the axial vector masses in the dipole formula is varied by 10% and 20%, respectively [91], while their central values are set to be  $1.1 \text{ GeV}/c^2$  and  $1.2 \text{ GeV}/c^2$ , respectively. This affects both the  $q^2$  dependence of the cross-section and the total cross-section. For the coherent pion production, two different models are compared; one is a model proposed by J. Marteau *et al.* [105, 106] which is employed in the default fitting, and the other is the Rein and Sehgal model [103]. For deep inelastic scattering, GRV94 [95] and its corrected structure function by A. Bodek and U. K. Yang [96] are studied, among which the latter is taken in the default fitting.

Several combinations of the interaction models mentioned above are studied and it is found that all the fitting parameters other than  $R_{\text{nqe}}$  do not change beyond the size of their fitting errors. The dependence of fitted  $R_{\text{nqe}}$  value on the choice of modes is shown in Fig. 7.38, as well as the  $\chi^2$  values at their best-fit points. It indicates that our experimental data favor the models with larger  $M_A$  values and more suppression in low  $q^2$  region. By varying the interaction models,  $R_{\text{nqe}}$  values is changed by  $\sim 20\%$  in all the sets of data samples used in the fitting. The systematical differences between 1KT only fitting and FGD only fitting are as discussed in the previous section. Therefore, an additional systematic error of  $\pm 20\%$  on  $R_{\text{nqe}}$  is added to the original fitting error as well as to the corresponding elements of the error matrix. The final values for the spectrum weighting factors ( $f_i^\phi$ ) and non-qe/qe ratio ( $R_{\text{nqe}}$ ) and their errors are summarized in Table 7.11, as well as their final error matrix.

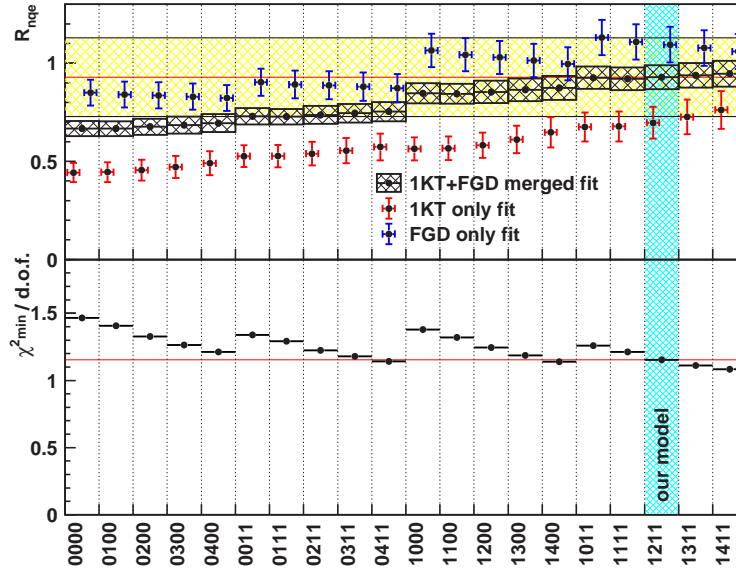


**Figure 7.38:** Dependence of fitted  $R_{\text{nqe}}$  values on neutrino interaction models (top) and  $\chi^2/\text{d.o.f.}$  values at the best-fit points (bottom). The numbers such as “0000”, “0100”, etc. are the abbreviation of the combinations of models as listed in Table 4.4. Horizontal red lines show the fitted  $R_{\text{nqe}}$  and minimum  $\chi^2$  values for the model we have adopted (model hatched with light blue color). By changing the neutrino interaction models within their uncertainties, fitted  $R_{\text{nqe}}$  value varies by about 20%. The artificially added error on  $R_{\text{nqe}}$ , as described in the text, is illustrated by the yellow band in the top figure.

## 7.5 Summary of ND analysis

The expected number of neutrino events in SK and the neutrino energy spectrum at near site have been estimated based on the measurements in the 1KT and FGD.

The number of neutrino interactions occurred in 1KT is estimated by counting the number of events with their vertex inside the 25 t fiducial volume of 1KT. Then, it is extrapolated by  $F/N$  ratio to SK. In the case of that neutrino oscillation does not exist, the number of neutrino events expected to be observed in SK is estimated to be

$$N_{\text{exp}}^{\text{SK}} = 80.6 \pm 0.3 (\text{stat.}) {}^{+7.3}_{-8.0} (\text{syst.}) \quad (7.29)$$

for the accumulated neutrino beam of  $4.79 \times 10^{19}$  POT.

The neutrino energy spectrum at near site is estimated using the  $(p_\mu, \theta_\mu)$  2-dimensional distributions in FC1R $\mu$ , SciFi-MRD 1-track, 2-track QE, and 2-track non-QE samples. The  $\chi^2$  fitting is employed to derive the spectrum weighting factors and non-qe/qe cross-section ratio relative to the values in our Monte Carlo simulation. The results of the spectrum measurements is shown in Fig. 7.39 together with the prediction of our Beam-MC, showing a good agreements with each other. The uncertainty due to neutrino interaction models is also studied. The choice of models does not bias the estimation of energy spectrum beyond its fitted error, but only affects on the value  $R_{\text{nqe}}$  by 20%, which is added to the error on it. The correlation between each energy bin and  $R_{\text{nqe}}$  is estimated in the form of an error matrix, which is shown in Table 7.11 together with their central values. It is used in the oscillation analysis described in Chapter 9.



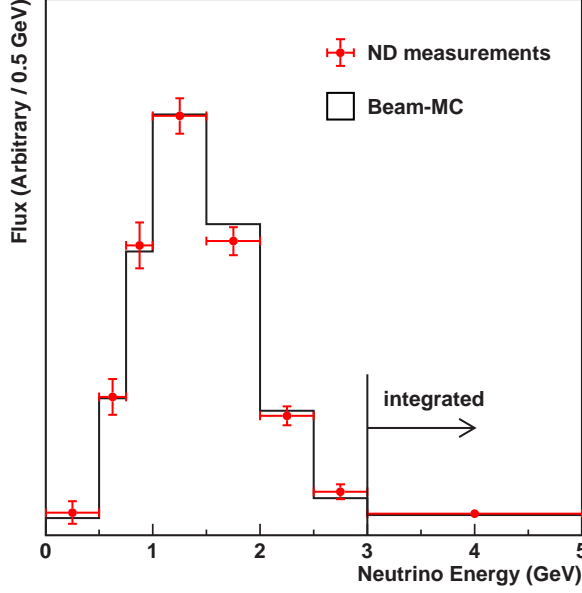


**Figure 7.39:** The neutrino energy spectrum measured at ND. The spectrum estimated by Beam-MC is overlaid by a black histogram. The results of spectrum measurements in ND are in agreement with the expectation of Beam-MC.

**Table 7.11:** The central values, errors, and error matrix for  $f_i^\phi$  and  $R_{\text{nqe}}$  used in the oscillation analysis. The square root of error matrix ( $\text{sign}[\{M_{\phi,\text{nqe}}\}_{ij}] \cdot \sqrt{|\{M_{\phi,\text{nqe}}\}_{ij}|}$ ) is written here in the unit of %. As described in the text, an additional error of 20% is added to the matrix elements corresponding to  $R_{\text{nqe}}$ .

	$f_1^\phi$	$f_2^\phi$	$f_3^\phi$	$f_4^\phi$	$f_5^\phi$	$f_6^\phi$	$f_7^\phi$	$f_8^\phi$	$R_{\text{nqe}}$
Central Values	1.314	1.021	1.007	1.000	0.955	0.962	1.183	1.073	0.929
Errors	0.487	0.119	0.092	fixed	0.071	0.084	0.188	0.199	0.203
$f_1^\phi$	48.9	-11.4	6.60	—	0.926	2.12	-4.16	5.12	-15.0
$f_2^\phi$	-11.4	11.9	-2.98	—	2.68	0.989	2.26	2.97	-7.50
$f_3^\phi$	6.60	-2.98	9.17	—	4.68	-0.867	4.55	2.09	-4.31
$f_4^\phi$ (fixed)	—	—	—	—	—	—	—	—	—
$f_5^\phi$	0.926	2.68	4.68	—	7.07	-2.12	7.64	4.93	-3.45
$f_6^\phi$	2.12	0.989	-0.867	—	-2.12	8.43	-7.58	8.17	-3.41
$f_7^\phi$	-4.16	2.26	4.55	—	7.64	-7.58	18.8	-11.2	-3.08
$f_8^\phi$	5.12	2.97	2.09	—	4.93	8.17	-11.2	19.9	-6.75
$R_{\text{nqe}}$	-15.0	-7.50	-4.31	—	-3.45	-3.41	-3.08	-6.75	20.3



# Chapter 8

## Observation in Far Detector

The observation of neutrino events in Super-Kamiokande (SK) is described in this chapter. K2K beam originated neutrino candidates in SK are selected from a large number of cosmic ray, radioactive, and atmospheric neutrino backgrounds. First, the selections for the accelerator neutrino events are given. Then, the number and some distributions of observed events are shown in following sections. The systematic uncertainties in the event selections are explained, and finally, an error matrix for the selection of  $1R\mu$  events are described in the last section of this chapter, which is used in the oscillation analysis in Chapter 9.

### 8.1 Event selection for beam originated neutrino candidates

In order to select the K2K beam originated neutrino candidates from a large number of backgrounds, GPS system is employed as is previously described. Two UTC time stamps from GPS system are compared, one is for the start time of the beam spill at KEK-PS ( $T_{\text{KEK}}$ ) and the other is for the observed time of events in SK ( $T_{\text{SK}}$ ). The time difference  $\Delta T$  is defined as follows;

$$\Delta T \equiv T_{\text{SK}} - T_{\text{KEK}} - TOF \quad , \quad (8.1)$$

where  $TOF$  is the time-of-flight of neutrinos to travel the distance from KEK to SK (249.83 km), which is estimated to be 833  $\mu\text{sec}$  assuming that neutrinos travel with the velocity of light. For the beam originated neutrino events,  $\Delta T$  should be distributed around the time window of 0–1.1  $\mu\text{sec}$  matching with the beam spills.

Events with the vertex inside 22.5 kt fiducial volume of SK and all the particles fully contained inside the inner detector (FC) are selected, for which events whole momenta of particles and their particle type can be reconstructed. The method of the event reconstruction in SK is almost the same as that in 1KT. The detailed description on the event reconstruction is given in Appendix B. Fig. 8.1 shows an event display for one of the K2K beam neutrino candidates with  $FC1R\mu$  in SK.

Following reduction steps are applied to select the FC events, which are the same as that of atmospheric neutrino analysis in SK. The selection criteria are optimized by using atmospheric neutrino data. A flow chart of the reduction steps is shown in Fig. 8.2. The number of selected events in each step is summarized in Table 8.1.

#### (1) Good beam spill selection

Among the data taken in SK, events with good beam spill condition and valid GPS status are used. The criteria for the good beam spills are described in Sec. 5.2.

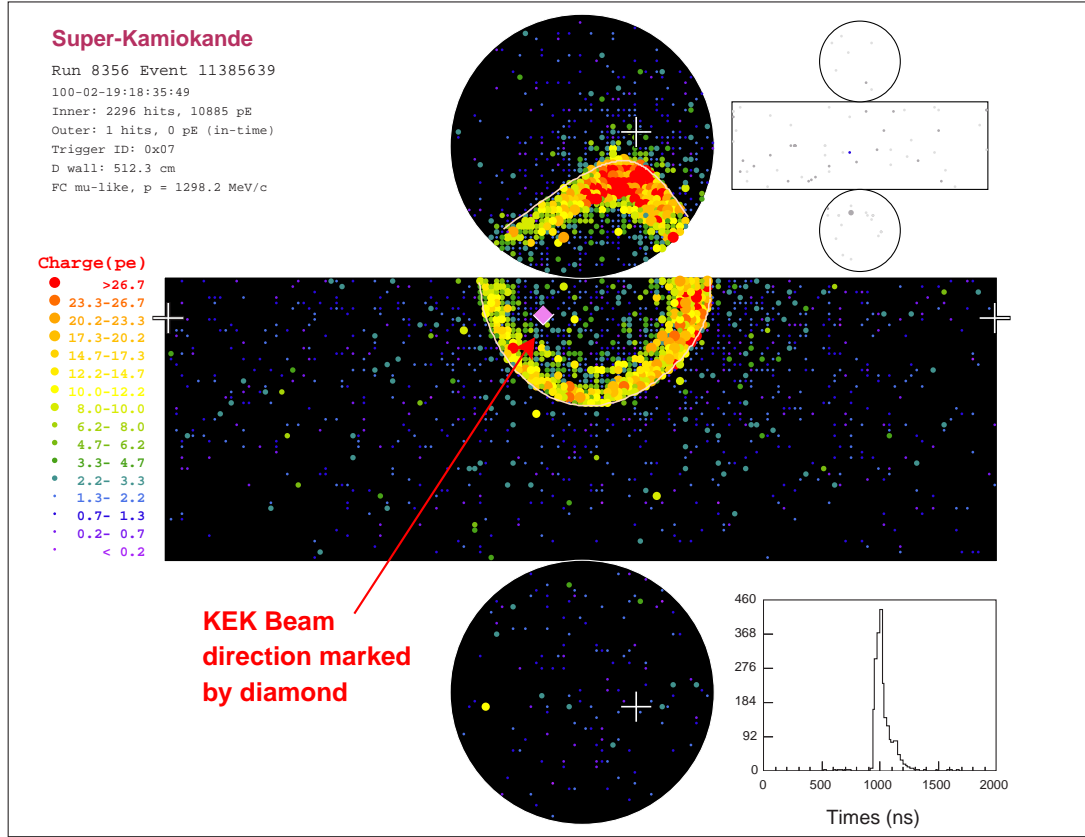


**Figure 8.1:** Event display for one of the K2K beam neutrino candidates with FC 1-ring  $\mu$ -like Cherenkov ring.

**Table 8.1:** Summary of the number of selected events in each reduction step in SK.

Selection Criteria		Data	MC
1	Analyzed number of spill	9,177,578	
	(MC) generated in the tank	—	370,607
	(MC) generated in the fiducial volume	—	167,677
2	Rough timing cut	161,763	
3	Decay electron cut	107,892	
4	HE trigger	36,560	
5	Total photoelectron cut	18,902	227,476
6	Flasher event cut	18,617	220,753
7	Outer detector cut	108	192,117
8	Fitting goodness cut	107	191,924
9	Visible energy cut	100	186,445
10	Fine timing cut	91	
11	Fiducial volume cut	56	131,530

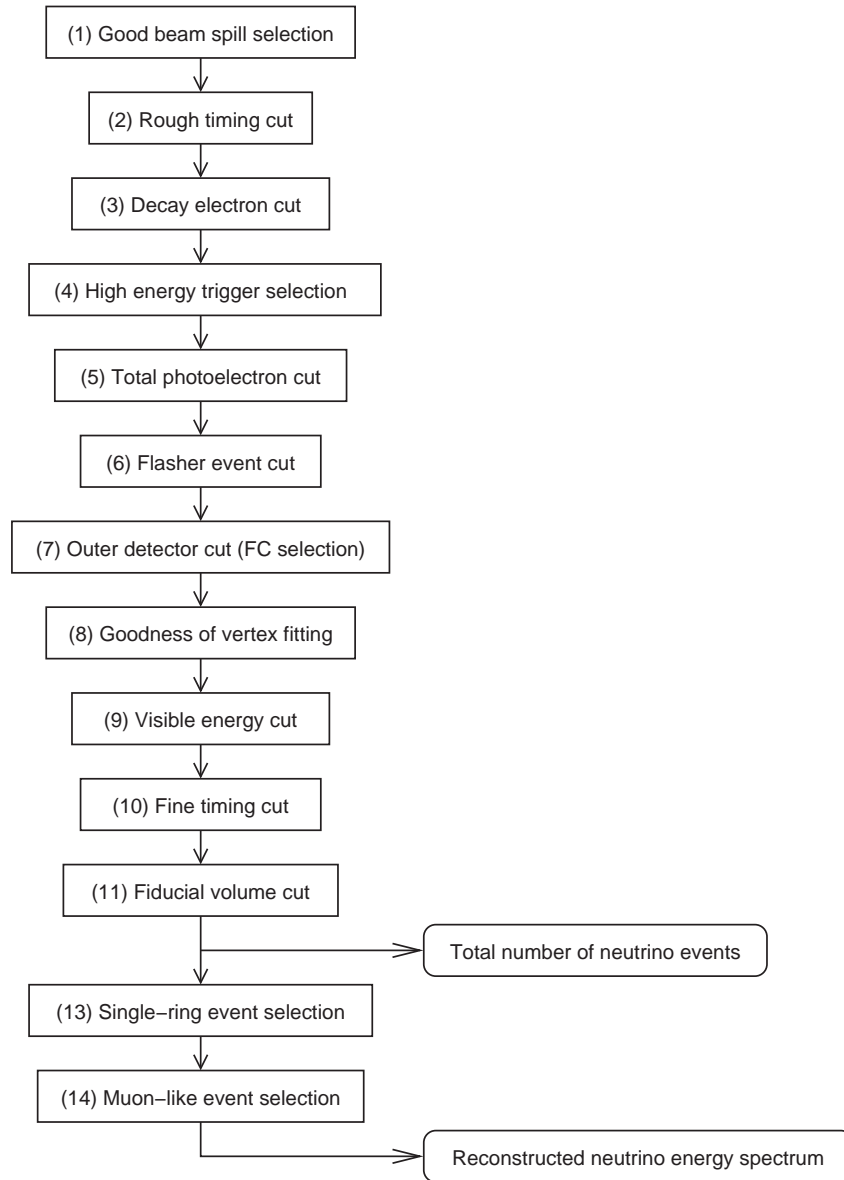


**Figure 8.2:** A flow chart of the data reduction and the event selection in the Super-Kamiokande analysis. The events remaining after the fiducial volume cut are counted in the total number of observed neutrino events in SK, while the events with only one muon-like Cherenkov ring is used to reconstruct the neutrino energy.

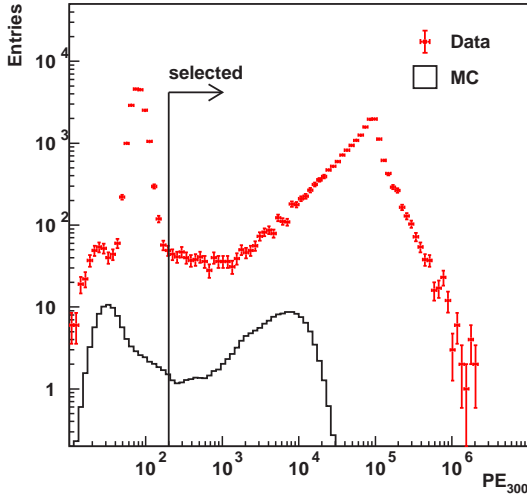


**Figure 8.3:** Distribution of the total number of photoelectrons in 300 nsec time window ( $PE_{300}$ ) for the events after high energy trigger cut. Red points are for data and black histogram is for a Monte Carlo simulation for the beam neutrinos normalized to the expected number of events for  $4.79 \times 10^{19}$  POT in the case of no oscillation.

## (2) Rough timing cut

Among all the triggered events in SK, events matching to a good beam spill inside the time window of  $|\Delta T| \leq 500 \mu\text{sec}$  are selected at this stage.

## (3) Decay electron cut

If a cosmic ray muon stops inside the tank, an electron emitted by the muon decay makes a Cherenkov ring, which may be mis-identified as a neutrino event. In order to remove such kind of possible fake events, events which have detector activity within  $20 \mu\text{sec}$  before them are rejected. A fraction of dead time caused by this selection is less than  $1/1000$  since the total trigger rate is typically  $\sim 10$  Hz.

## (4) High energy (HE) trigger

Events taken by high energy (HE) trigger are used for the K2K analysis. The trigger threshold for HE trigger is 31 hit PMTs within 200 nsec time window as described in Sec. 3.6.3, which is corresponding to 50–100 photoelectrons.

## (5) Total photoelectron cut

Events with maximum number of total photoelectrons in a sliding time window of 300 nsec ( $PE_{300}$ ) less than 200 p.e. (Fig. 8.3) are rejected in order to eliminate low energy backgrounds such as radon and gamma rays from the surrounding rock. Corresponding momentum threshold to this criteria is  $\sim 20 \text{ MeV}/c$  for electrons and  $\sim 190 \text{ MeV}/c$  for muons.

## (6) Flasher event cut

There are some flashing PMTs called “flasher” in SK, which are caused by sparks inside PMTs. They sometimes make hit pattern like Cherenkov light. In order to reject such fake events, following three cuts are applied;

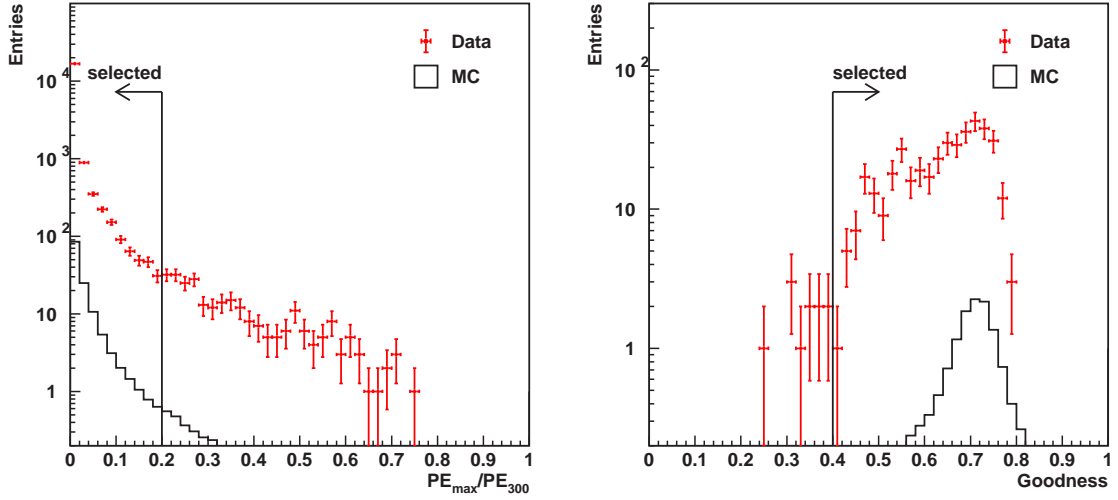


**Figure 8.4:** Distributions of  $PE_{max}/PE_{300}$  for the events after total photoelectron cut (left) and the goodness of vertex fitter for flasher cut for the events with the number of hit ID-PMTs less than 500 (right). Red points are for data and black histogram is for a Monte Carlo simulation for the beam neutrinos normalized to the expected number of events for  $4.79 \times 10^{19}$  POT in the case of no oscillation.

Maximum photoelectron cut: If a spark occurs in a PMT, this PMT produces a large charge signal in itself. In order to eliminate such events,  $PE_{max}/PE_{300} \leq 0.2$  is imposed, where  $PE_{max}$  is the number of photoelectrons of the PMT which have maximum charge among all the PMTs.

Hit timing distribution cut: Since most of the flasher events have broad hit timing distribution compared to that of neutrino events, flasher events are removed by using the width of the hit timing distribution. The minimum number of hit PMTs within 100 nsec sliding time window in the range of 300 to 800 nsec after the event trigger ( $N_{100}^{min}$ ) is searched for, and if  $N_{100}^{min}$  is greater than 14, the events are discarded. For the events with the number of hit ID-PMTs less than 800, the events are discarded if  $N_{100}^{min}$  is greater than 10.

Goodness of the fit: For the events with the number of hit ID-PMTs less than 500, the goodness of a vertex fitter is used to select the flasher events. This fitter searches for a vertex point with an assumption that all photons were produced at a point. Events with the goodness of the fitter less than 0.4 are rejected as flasher events.

### (7) Outer detector cut

In order to reject incoming cosmic ray muons, cuts using outer detector (OD) information is applied. Events which have more than 9 hit PMTs in the largest hit cluster in OD ( $N_{hitac}$ ) are rejected (left figure of Fig. 8.5). Furthermore, events which have more than 50 hit OD-PMTs within 800 nsec time window ( $N_{hita800}$ ) is removed (right figure of Fig. 8.5). These criteria effectively select the FC events.

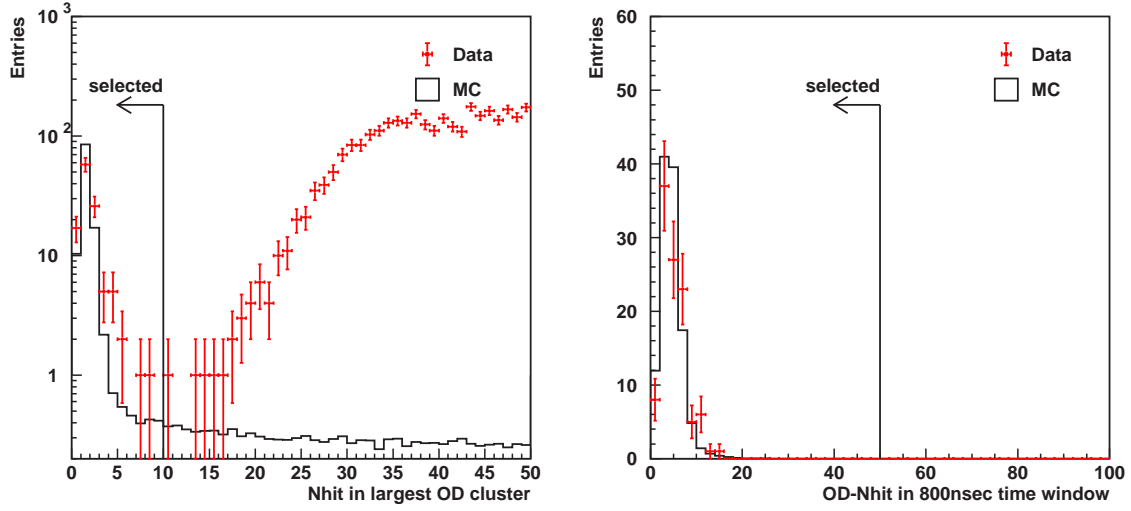


**Figure 8.5:** Distributions of the number of hit PMTs in the largest OD hit cluster ( $N_{hitac}$ ) for the events after flasher cut (left) and the number of hit OD-PMTs within 800 nsec time window ( $N_{hitac800}$ ) for the events after  $N_{hitac}$  cut (right). Red points are for data and black histogram is for a Monte Carlo simulation for the beam neutrinos normalized to the expected number of events for  $4.79 \times 10^{19}$  POT in the case of no oscillation.

### (8) Goodness of vertex fitting

A vertex fitter, TDC-fit, is applied to define the vertex point of the interaction. The algorithm of TDC-fit is described in Sec. B.1.3. Small fraction of events are removed as badly fitted ones if the goodness of the fit is less than 0 (Fig. 8.6).

### (9) Visible energy cut

In order to avoid the uncertainty of the total photoelectron cut, more well-defined energy cut is applied. Events with the visible energy ( $E_{vis}$ ) greater than 30 MeV are selected (Fig. 8.7). The visible energy is defined as a sum of energy of each ring assuming the Cherenkov light of each ring is produced by an electron. This cut corresponds to the momentum threshold of 197 MeV/ $c$  for muons.

### (10) Fine timing cut

Tighter timing cut is applied using UTC time stamps from GPS systems. Since the uncertainty of two UTC time stamps are less than  $0.2 \mu\text{sec}$  as described in Sec. 3.7.2, events inside the time window of  $-0.2 \mu\text{sec} \leq \Delta T \leq 1.3 \mu\text{sec}$  are selected as beam induced neutrino events. Fig. 8.8 shows the  $\Delta T$  distribution. Beam neutrino events are clearly identified in the time window of  $0 \mu\text{sec} \leq \Delta T \leq 1.1 \mu\text{sec}$  which matches with the width of the beam spill.

### (11) Fiducial volume cut

Finally, fiducial volume cut is imposed on the remaining events. The definition of the fiducial volume is optimized by using the atmospheric neutrino event sample observed in SK. The left figure in Fig. 8.9 shows the distribution of the distance between the reconstructed vertex point and the nearest wall of ID tank ( $D_{wall}$ ) in the atmospheric neutrino sample after the visible



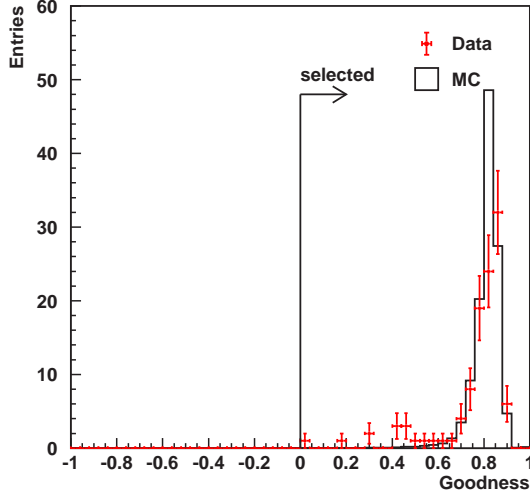


**Figure 8.6:** Distribution of the goodness of vertex fitting (TDC-fit) for the events after OD cut. Red points are for data and black histogram is for a Monte Carlo simulation for the beam neutrinos normalized to the expected number of events for  $4.79 \times 10^{19}$  POT in the case of no oscillation.

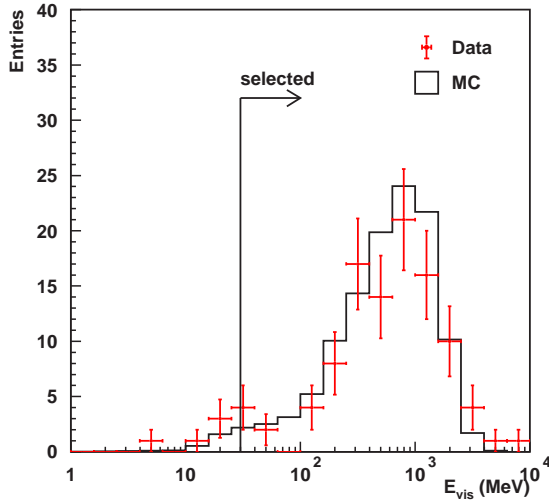


**Figure 8.7:** Distribution of the visible energy ( $E_{\text{vis}}$ ) for the events after fitting goodness cut. Red points are for data and black histogram is for a Monte Carlo simulation for the beam neutrinos normalized to the expected number of events for  $4.79 \times 10^{19}$  POT in the case of no oscillation.

energy cut ( $E_{\text{vis}} > 30$  MeV). The discrepancy around the wall ( $D_{\text{wall}} < 200$  m) is mainly due to the events which take place in the insensitive volume between the ID and OD tank, the cosmic ray muon events which remain due to the inefficiency of OD, or mis-fitted events which happened very close to the wall. In order to avoid these events, the vertex of each event is required to be farther than 200 cm from the wall of ID tank (the right figure in Fig. 8.9). This fiducial volume corresponds to water mass of 22.5 kt.

The selection efficiency for muon neutrinos of K2K beam is estimated using a Monte Carlo simulation. Fig. 8.10 shows the efficiency as a function of incident neutrino energy. The averaged efficiency for all the interactions is 77.9% for the beam configuration in K2K-Ia, and 78.4% for the configuration in K2K-Ib.

## 8.2 The number of observed neutrino events in SK

In total, 56 FC events were observed in SK during the whole run period from June 1999 to July 2001; one event was in K2K-Ia, and the other 55 events were in K2K-Ib. Timing distribution

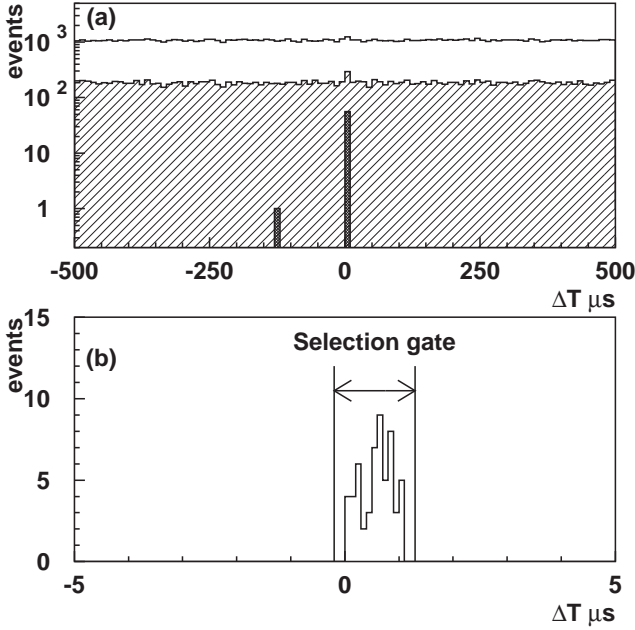


**Figure 8.8:** Distribution of the time difference ( $\Delta T$ ) between two UTC time stamps. (Top figure:) For the events within  $\pm 500 \mu\text{sec}$  time window after decay electron cut (blank histogram), after flasher event cut (hatched histogram), and after fiducial volume cut (dark hatched histogram). (Bottom figure:) For the selected events in the fiducial volume. A clear cluster of events can be seen just within  $1.1 \mu\text{sec}$  time window synchronized with the beam spill.

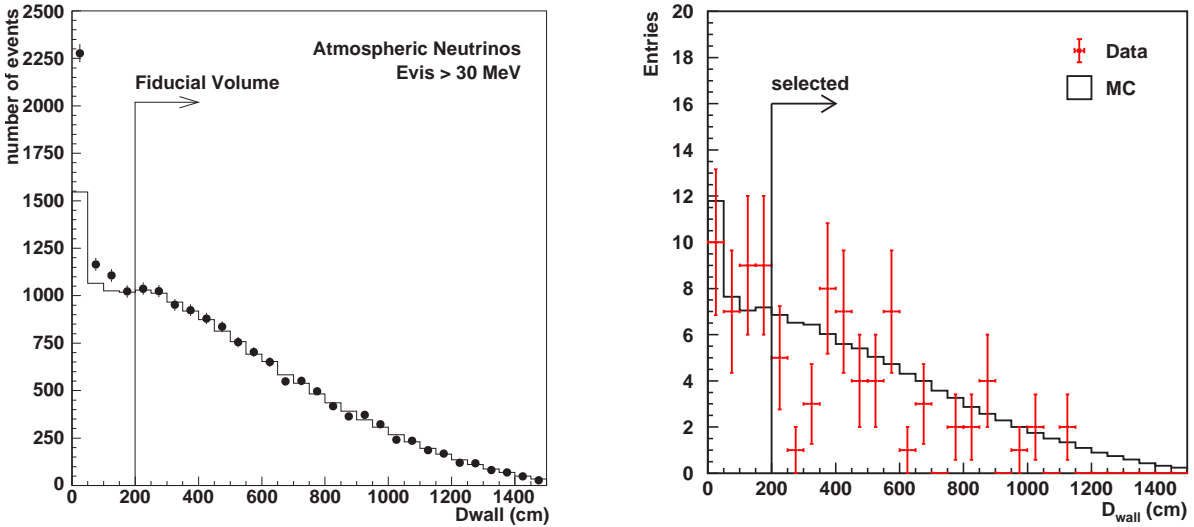


**Figure 8.9:** Distribution of the distance from the vertex point to the nearest wall of inner tank ( $D_{\text{wall}}$ ) for the events after visible energy cut for the atmospheric neutrino sample in SK (left) and for the K2K event candidates (right). In the left figure, black points are for data and the histogram is for a Monte Carlo simulation of atmospheric neutrino events. The Monte Carlo simulation is normalized to the data by the number of events in the region of  $D_{\text{wall}} > 200 \text{ cm}$ . In the right figure, red points are for data and black histogram is for a Monte Carlo simulation for the beam neutrinos normalized to the expected number of events for  $4.79 \times 10^{19}$  POT in the case of no oscillation.

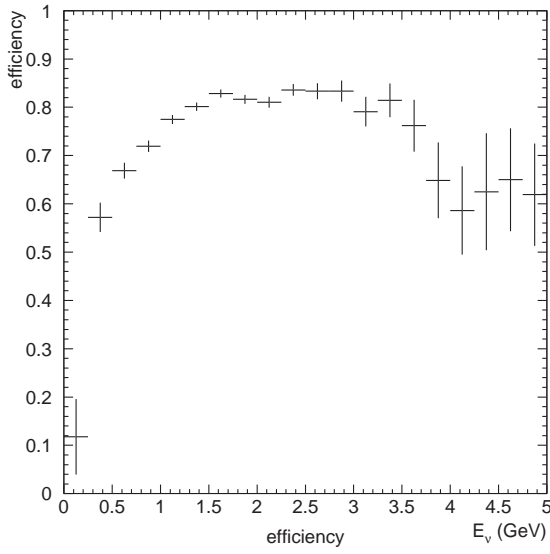


**Figure 8.10:** Selection efficiency in SK as a function of incident neutrino energy, estimated by a Monte Carlo simulation.

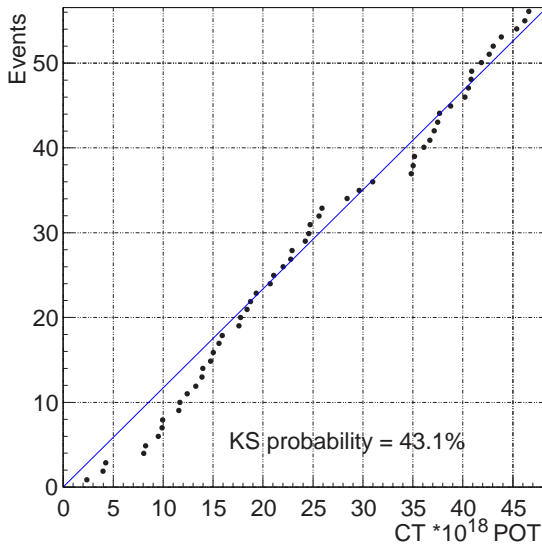


**Figure 8.11:** Relation between the accumulated number of protons on target (POT) and the number of observed events in SK. Blue line represents a linear relation between them. The probability of KS test for the hypothesis that the observation obeys the relation of blue line is 43.1%.

**Table 8.2:** Summary of observed events in SK. The observations in K2K-Ia and K2K-Ib are separately listed since the beam configurations between these two periods are different.

Event categories	Number of observed events		Expected # of events
	June 1999	rest period	
1-ring $\mu$ -like	1	29	44.0
1-ring $e$ -like	0	2	4.4
multi-ring	0	24	32.2
In total	1	55	$80.6^{+7.3}_{-8.0}$

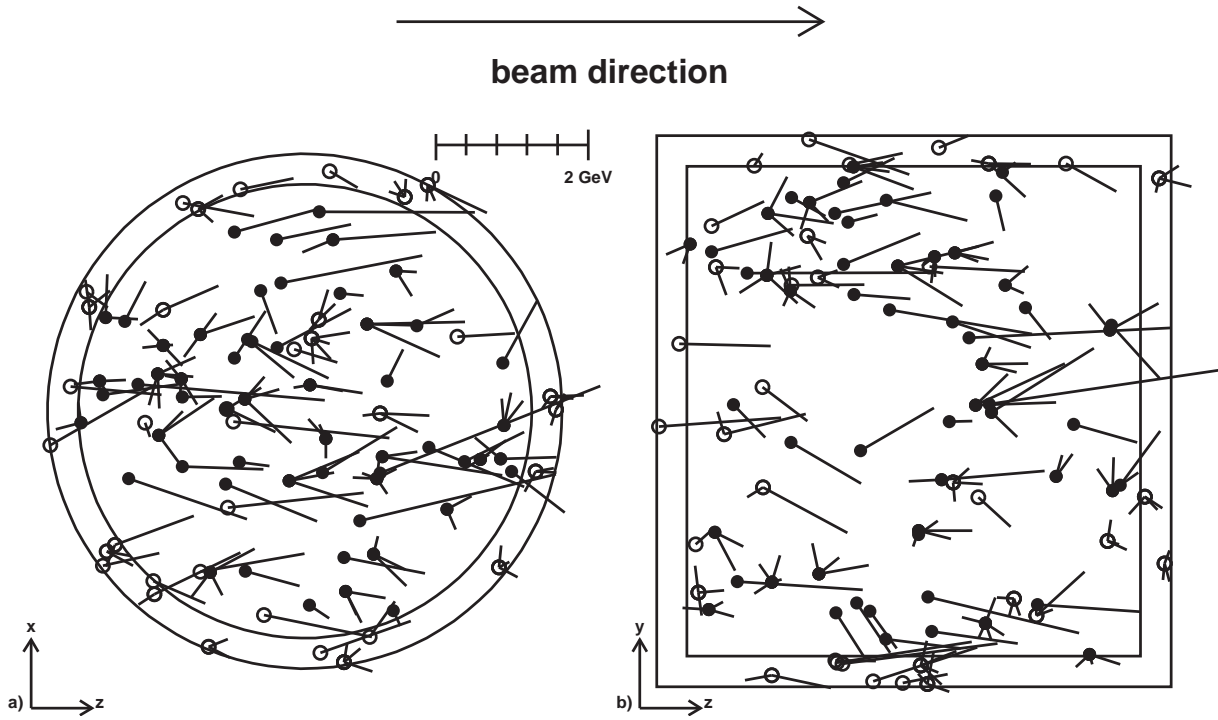


**Figure 8.12:** Distribution of the reconstructed vertex points (circles) and momentum of each ring in an event (lines) observed in SK. Left figure shows the top view and right figure shows the side view. Inner circle (left) or box (right) represent the boundary of the fiducial volume, and outer circle or box represent the wall of the inner tank. Solid (open) circles represent the events with the vertex inside (outside) the fiducial volume. Lines from the each vertex show the directions of particles in the interaction, and the length of each line represents its momentum.

for these 56 events are shown in Fig. 8.8. These events are clearly isolated from the other SK events, and they are inside the  $1.1 \mu\text{sec}$  time window synchronized with the beam spill timing, showing that these are the events induced by K2K beam neutrinos.

The relation between the accumulated number of protons on target (POT) and the number of observed events in SK is shown in Fig. 8.11. The Kolmogorov-Smirnov (KS) test has been performed for a hypothesis that our observation in SK have a linear relation between accumulated POT. The KS probability of 43.1% is obtained, indicating that the observation is consistent with the linear relation and that the events have randomly taken place.

Number of rings in each event and the momentum of each ring are also reconstructed. The event classification for observed FC events is summarized in Table 8.2. The vertex point for each event is shown in Fig. 8.12 together with the momentum and direction of each ring.

In the FC events with only one  $\mu$ -like Cherenkov ring ( $FC1R\mu$ ), the neutrino energy can be reconstructed using the muon momentum and scattering angle with respect to the beam direction as Eq. (2.2), assuming that the events are induced by CC-qe interaction. The muon momentum and angular distributions for  $FC1R\mu$  events are shown in Fig. 8.13, and the distribution of the reconstructed neutrino energy is shown in Fig. 8.14. Their expectation without neutrino oscillation is also overlaid in each figure.

A source of possible background against our signal is the atmospheric neutrino interactions. However, since its typical rate for FC events is about 8 events per day, an accidental contamination of atmospheric neutrinos into our event sample is order of  $10^{-3}$  events through the entire run period thanks to the  $1.5 \mu\text{sec}$  time window cut. One event at  $\Delta T = -122.7 \mu\text{sec}$  in the top figure of Fig. 8.8 is consistent with the event rate of atmospheric neutrino background in  $\pm 500 \mu\text{sec}$  time window.

## 8.3 Systematic uncertainty in the event selection

Systematic uncertainties in the event selection in SK are as follows.

### Event selection

The systematic uncertainties in the event selections, except for the fiducial volume cut, is estimated by changing the following thresholds; a 10% change in the  $PE_{300}$  cut, a  $\pm 3$  hits change in OD cut, and  $\pm 10$  MeV change in the  $E_{\text{vis}}$  cut. Then effect of these changes on the number of remained events is studied. In total,  $\pm 1\%$  error is quoted as the uncertainty in the event selection.

### Fiducial volume cut

The performance of the vertex fitter is checked by comparing the results of two different vertex fitters, “auto-fit” (Sec. B.1) and “MS-fit” (Sec. B.4). These two fitter were applied to atmospheric neutrino data and its Monte Carlo simulation, resulting 2% difference in data/MC ratio.

### Statistics of Monte Carlo simulation

The statistical uncertainty of the Monte Carlo simulation is 1%.

In total, 3% is quoted as the uncertainty in the selection efficiency.

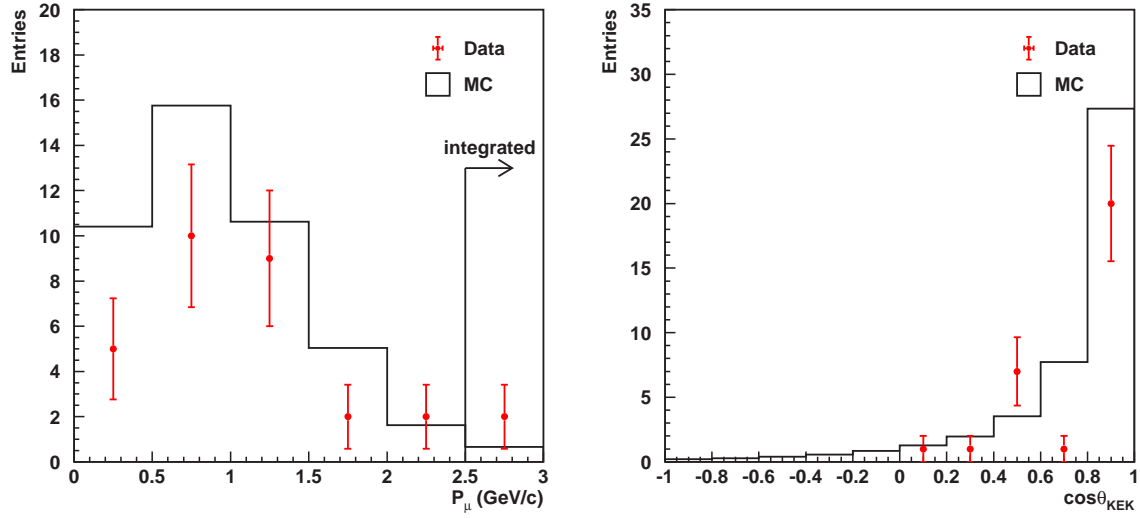


**Figure 8.13:** The Momentum (left) and angular (right) distributions for FC1R $\mu$  events in SK. The angle in the right figure is taken with respect to the neutrino beam direction. The Monte Carlo simulation is in the case of no oscillation.

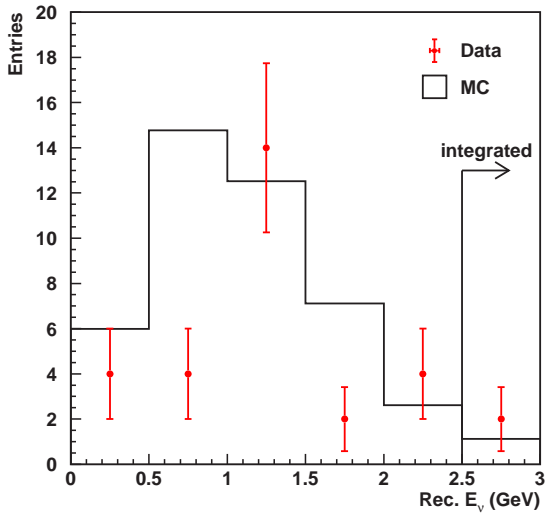


**Figure 8.14:** The distribution of the reconstructed neutrino energy for FC1R $\mu$  events in SK. The Monte Carlo simulation is in the case of no oscillation.

## 8.4 Error matrix of selection efficiency for $1R\mu$ events

The error on the selection efficiency for  $FC1R\mu$  events is estimated as a function of the incident neutrino energy in order to use it in the oscillation analysis described in Chapter 9. The neutrino energy is binned into six bins; 0–0.5 GeV, 0.5–1.0 GeV, 1.0–1.5 GeV, 1.5–2.0 GeV, 2.0–2.5 GeV, and above 2.5 GeV, which is the same binning as PIMON. Then, the error is provided in the form of  $6 \times 6$  error matrix,  $M_{\epsilon_{SK}}$ . Uncertainties due to the particle identification, the ring counting, and the energy scale are estimated.

For particle identification, a study using a Monte Carlo simulation was employed. The number of electron or gamma ray events which are mis-identified as  $\mu$ -like and that of muon events which are mis-identified as  $e$ -like are counted. The fractions of mis-identified  $\mu$ -like and  $e$ -like events are calculated as a function of energy, quadratically summed, and used as the systematic error on the selection efficiency for  $\mu$ -like events.

The atmospheric neutrino data is used in order to estimate the uncertainty due to the ring counting. Single-ring events are selected in both data and Monte Carlo simulation, and the difference in the distribution of likelihood for the separation between single-ring and multi-ring ( $\mathcal{F}_1$  described in Sec. B.2.2) are compared between data and Monte Carlo simulation. By changing the criteria to select single-ring events, its systematic uncertainty is estimated as a function of energy.

Finally, the uncertainty in energy scale is propagated to the uncertainty in the selection efficiency as a function of energy. As an error on the energy scale,  $\pm 3\%$  is used as described in Sec. 3.6.5.

All the errors above are quadratically summed, and the error matrix  $M_{\epsilon_{SK}}$  is obtained to be

$$\text{sign}(M_{\epsilon_{SK}}) \cdot \sqrt{M_{\epsilon_{SK}}} = \begin{pmatrix} 8.7 & 0 & 0 & 0 & 0 & 0 \\ 0 & 4.3 & 0 & 0 & 0 & 0 \\ 0 & 0 & 8.9 & 0 & 0 & 0 \\ 0 & 0 & 0 & 10.0 & 0 & 0 \\ 0 & 0 & 0 & 0 & 9.8 & 0 \\ 0 & 0 & 0 & 0 & 0 & 9.9 \end{pmatrix}, \quad (8.2)$$

where six columns or rows are corresponding to the six energy bins, the values are written in the unit of %, and the correlation between bins is ignored.





# Chapter 9

## Analysis for Neutrino Oscillation

Up to here, the measurements in ND, the extrapolation of ND measurements to the expectations in SK, and the observations in SK are described. During the run period from June 1999 to July 2001, corresponding to the data of  $4.79 \times 10^{19}$  accumulated protons on target, the number of observed neutrino events in SK is 56 while the expectation from the ND measurements is  $80.6^{+7.3}_{-8.0}$  in the case of that no neutrino oscillation exists; a clear deficit in the number of neutrino events can be seen. Furthermore, the neutrino energy distribution observed in SK seem to be distorted compared to that without neutrino oscillation, as shown in Fig. 8.14. These facts indicate the existence of neutrino oscillation.

In order to test the neutrino oscillation hypothesis and constrain its parameter space, an analysis for two flavor oscillation with  $\nu_\mu$  disappearance ( $\nu_\mu \rightarrow \nu_x$ ) mode have been performed by using a maximum likelihood method. This chapter describes its procedure and results in detail. First, an overview of the analysis and the definition of likelihood to be maximized are given. Next, the expected number of neutrino events and energy spectrum are re-estimated using the full information of the measurements in ND and far-to-near spectrum ratio ( $F/N$ ) with given error matrix. Then, the best-fit point of oscillation parameters, the probability for null oscillation, and constraint on oscillation parameter space from our observation are provided.

### 9.1 Overview

The signature of the neutrino oscillation with the  $\nu_\mu$  disappearance mode is a reduction in the number of neutrino events and a distortion in the neutrino energy spectrum. All the beam induced neutrino events observed in the 22.5 kt fiducial volume of SK are used to study the reduction of neutrino events. On the other hand, single-ring  $\mu$ -like events (1R $\mu$ ) are used to study the spectral distortion in order to enhance the fraction of CC-qe interactions in which the neutrino energy can be reconstructed using the momentum of muon produced in the reaction;

$$E_\nu^{\text{rec}} = \frac{1}{2} \cdot \frac{m_p^2 - m_n^2 - m_\mu^2 + 2m_n E_\mu}{m_n - E_\mu + p_\mu \cos \theta_\mu} \quad , \quad (9.1)$$

as described before.

In the estimation of expected number of events and energy spectrum in SK at each point of oscillation parameter space, the correlation between energy bins are taken into account for the errors on the neutrino spectrum and  $F/N$  ratio by quoting the errors in the form of error matrix, which are obtained in Chapter 6 and Chapter 7.

As described in the next section, the likelihood function to be maximized is defined as a product of three terms; a likelihood for the number of FC events  $\mathcal{L}_{\text{norm}}$ , a likelihood for the

spectrum shape  $\mathcal{L}_{\text{shape}}$ , and a constraint term for the systematic uncertainties  $\mathcal{L}_{\text{syst}}$ . Whole data sample taken from June 1999 to July 2001 are used in the calculation of  $\mathcal{L}_{\text{norm}}$ . However the data taken in June 1999 (K2K-Ia) is discarded in the calculation of spectrum shape part ( $\mathcal{L}_{\text{shape}}$ ) since, as is also mentioned in Sec. 3.1.2, the radius of pion production target and the current of horn magnets in K2K-Ia were different from those in the rest of the period (K2K-Ib), and hence the spectrum shape in K2K-Ia was different from that in K2K-Ib. The discarded data is corresponding to 6.5% of total POT. The number of observed FC ( $1\text{R}\mu$ ) events are 1 (1) in K2K-Ia and 55 (29) in K2K-Ib as summarized in Table 8.2. Therefore, in total, 56 FC events are used in  $\mathcal{L}_{\text{norm}}$ , while 29  $1\text{R}\mu$  events are used in  $\mathcal{L}_{\text{shape}}$ .

## 9.2 Likelihood function for the analysis

### 9.2.1 Definition of likelihood function

The definition of the likelihood function to be maximized is as following;

$$\mathcal{L}_{\text{total}}(\sin^2 2\theta, \Delta m^2, \mathbf{f}) = \mathcal{L}_{\text{norm}}(\sin^2 2\theta, \Delta m^2, \mathbf{f}) \times \mathcal{L}_{\text{shape}}(\sin^2 2\theta, \Delta m^2, \mathbf{f}) \times \mathcal{L}_{\text{syst}}(\mathbf{f}) , \quad (9.2)$$

where  $\theta$  and  $\Delta m^2$  are the mixing angle and mass squared difference in the two flavor oscillation approximation as expressed in Eq. (1.14), and  $\mathbf{f}$  is a set of parameters representing the systematic uncertainties ( $f^{\text{Ia,Ib}}$ ,  $f^{\phi, \text{nqe}}$ ,  $f^{F/N}$ ,  $f^\epsilon$ , and  $f^{\text{Escale}}$ , which are described later).

#### Normalization term

The normalization term  $\mathcal{L}_{\text{norm}}$  is just Poisson probability to observe  $N^{\text{obs}}$  ( $= 56$ ) FC events in SK when the expected number of events is  $N^{\text{exp}}$ ;

$$\mathcal{L}_{\text{norm}} = \frac{(N^{\text{exp}})^{N^{\text{obs}}}}{N^{\text{obs}}!} \cdot e^{-N^{\text{exp}}} . \quad (9.3)$$

The expected numbers of events for K2K-Ia ( $N_{\text{Ia}}^{\text{exp}}$ ) and K2K-Ib ( $N_{\text{Ib}}^{\text{exp}}$ ) are separately estimated since the spectra,  $F/N$  ratio, and their systematic errors are different between them. These two numbers are summed up to obtain the total number of events;

$$N^{\text{exp}} = N_{\text{Ia}}^{\text{exp}} + N_{\text{Ib}}^{\text{exp}} . \quad (9.4)$$

The expected number of events for each period is calculated by extrapolating the observed number of events in 1KT ( $n_{\text{Ia,Ib}}$ ) as

$$N_{\text{Ia,Ib}}^{\text{exp}} = f^{\text{Ia,Ib}} \cdot n_{\text{Ia,Ib}} \times \left[ \frac{\sum_{i,j} \left[ \Phi_i^{\text{Ia,Ib}} \cdot \sigma_{ij} \cdot \epsilon_{ij}^{\text{SK}} \cdot P(E_i; \sin^2 2\theta, \Delta m^2) \right]}{\sum_{i,j} (\phi_i^{\text{Ia,Ib}} \cdot \sigma_{ij} \cdot \epsilon_{ij}^{\text{KT}})} \cdot \frac{M_{\text{SK}}}{M_{\text{KT}}} \cdot \frac{\text{POT}_{\text{SK}}}{\text{POT}_{\text{KT}}} \right] , \quad (9.5)$$

where  $\Phi_i$  ( $\phi_i$ ) is the neutrino flux in the  $i$ -th energy bin at far (near) site,  $\sigma_{ij}$  and  $\epsilon_{ij}^{\text{SK(KT)}}$  are, respectively, the interaction cross-section of muon neutrino with water target and the detection efficiency of SK (1KT) for the FC events of the  $i$ -th energy and the  $j$ -th interaction mode,  $M_{\text{SK(KT)}}$  is the fiducial mass of SK (1KT), and  $\text{POT}_{\text{SK(KT)}}$  is the number of protons on target corresponding to the amount of data analyzed in SK (1KT).  $f^{\text{Ia,Ib}}$  is a factor relative to the central value of overall normalization for the period Ia and Ib, and it is constrained within its error. Hereafter, sub(super)scripts “Ia” and “Ib” are omitted when it is not confusing.

The oscillation probability  $P(E; \sin^2 2\theta, \Delta m^2)$  is

$$P(E; \sin^2 2\theta, \Delta m^2) = \begin{cases} 1 - \sin^2 2\theta \cdot \sin^2 \frac{1.27 \cdot \Delta m^2 \cdot L}{E} & \text{(for CC interactions)} \\ 1 & \text{(for NC interactions)} \end{cases}, \quad (9.6)$$

where  $L = 250$  km is the neutrino flight distance.

The neutrino flux at near site,  $\phi_i$ , is measured in ND detectors as described in Sec. 7.4, and they are expressed as

$$\phi_i = f_i^\phi \cdot \phi_i^{\text{MC}}, \quad (9.7)$$

where  $\phi_i^{\text{MC}}$  is the flux in the  $i$ -th energy bin predicted by Beam-MC, and  $f_i^\phi$  is the weighting factor for the  $i$ -th energy bin measured in ND.  $f_i^\phi$  make the energy spectrum vary around the results of ND measurements being constrained within its error. The flux at SK in the case of no oscillation is calculated as a product of the flux at ND and  $F/N$  flux ratio  $R_i$ ;

$$\Phi_i = R_i \times \phi_i = f_i^{F/N} \cdot R_i^{\text{MC}} \times f_i^\phi \cdot \phi_i^{\text{MC}}, \quad (9.8)$$

where  $R_i^{\text{MC}}$  is  $F/N$  ratio predicted by Beam-MC, and  $f_i^{F/N}$  is a factor relative to  $R_i^{\text{MC}}$ , which make  $F/N$  ratio vary around its central value being constrained within the error estimated by PIMON measurements.

For the neutrino interactions, the model “NEUT-1211” is employed in this analysis, which is the same one as is used in the spectrum measurements in ND. The classification of the neutrino interaction in the likelihood is also the same as that in ND analysis, i.e.  $j = \text{qe}$  (quasi-elastic interaction) or  $\text{nqe}$  (non-quasi-elastic interactions, non-qe). The total cross-section for the  $i$ -th energy bin, then, can be written as

$$\sum_{j=\text{qe}, \text{nqe}} \sigma_{ij} = f^{\text{qe}} \cdot \sigma_{i,\text{qe}}^{\text{MC}} + f^{\text{nqe}} \cdot \sigma_{i,\text{nqe}}^{\text{MC}}, \quad (9.9)$$

where  $\sigma_{i,\text{qe}(\text{nqe})}^{\text{MC}}$  is the interaction cross-section of the model used in our Monte Carlo simulation for qe (non-qe) interaction, and  $f^{\text{qe}(\text{nqe})}$  is a parameters to adjust overall cross-section ratio being constrained within the errors estimated by ND measurements. Only the relative value between  $f^{\text{qe}}$  and  $f^{\text{nqe}}$  is meaningful in our method, and hence  $f^{\text{qe}}$  is fixed to be unity and only  $f^{\text{nqe}}$  is the free parameter in the likelihood fitting. Therefore,  $f^{\text{nqe}}$  is equivalent to the non-qe/qe ratio ( $R_{\text{nqe}}$ ) in the spectrum measurements in ND.

Since  $f^\phi$  and  $f^{\text{nqe}}$  are obtained in the ND analysis in a combined form, we denote them as  $f^{\phi, \text{nqe}}$ , hereafter.

### Spectrum shape term

The spectrum shape term  $\mathcal{L}_{\text{shape}}$  is the product of the probability for each  $1\text{R}\mu$  event to be observed at the reconstructed neutrino energy of  $E^{\text{rec}}$ ;

$$\mathcal{L}_{\text{shape}} = \prod_{i=1}^{N_{1\text{R}\mu}} \text{Prob}(E_i^{\text{rec}}; \sin^2 2\theta, \Delta m^2, \mathbf{f}), \quad (9.10)$$

where  $N_{1\text{R}\mu} (= 29)$  is the number of observed  $1\text{R}\mu$  events. The probability density function, or the normalized  $E^{\text{rec}}$  distribution,  $\text{Prob}(E^{\text{rec}}; \sin^2 2\theta, \Delta m^2, \mathbf{f})$ , is expressed as

$$\begin{aligned} & \text{Prob}(E^{\text{rec}}; \sin^2 2\theta, \Delta m^2, \mathbf{f}) \\ &= \int \left[ \Phi(E^{\text{t}}) \cdot P(E^{\text{t}}; \sin^2 2\theta, \Delta m^2) \cdot \sum_j \{ \sigma_j(E^{\text{t}}) \cdot \epsilon_j^{1\text{R}\mu}(E^{\text{t}}) \cdot r_j(E^{\text{rec}}; E^{\text{t}}) \} \right] dE^{\text{t}}, \end{aligned} \quad (9.11)$$

where  $E^t$  is the true neutrino energy,  $\sigma_j(E^t)$  is the cross section ( $= \sigma_{ij}$  in Eq. (9.5)),  $\epsilon_j^{1R\mu}(E^t)$  is the detection efficiency for  $1R\mu$  events in SK, and  $r_j(E^{\text{rec}}; E^t)$  is the detector response function of SK and is the probability density function to observe the reconstructed energy of  $E^{\text{rec}}$  when the true neutrino energy is  $E^t$ .  $\epsilon_j^{1R\mu}(E^t)$  and  $r_j(E^{\text{rec}}; E^t)$  are estimated by a Monte Carlo simulation for SK detector. In actual analysis, the  $E^t$  and  $E^{\text{rec}}$  are binned with an interval of 50 MeV, and hence the integral over the true neutrino energy is replaced by a summation over true energy bins. In order to incorporate the uncertainty in the energy scale in SK, the reconstructed neutrino energies for observed events are scaled by a scaling parameter  $f^{\text{Escale}}$  constrained within the estimated uncertainty. In the similar way, the energy dependent uncertainty in the detection efficiency for  $1R\mu$  events is taken into account by replacing  $\epsilon_j^{1R\mu}$  by  $f^\epsilon \epsilon_j^{1R\mu}$ , where  $f^\epsilon$  is also a parameter adjusted within its uncertainty.

### Systematic constraint term

The distribution of the parameters describing the systematic uncertainties,  $\mathbf{f}$ , are assumed to be Gaussian and the constraint term ( $\mathcal{L}_{\text{syst}}$ ) for the parameters is expressed as

$$\begin{aligned} \mathcal{L}_{\text{syst}} = & \exp(-\Delta f^{\phi, \text{nqe}} \cdot M_{\phi, \text{nqe}}^{-1} \cdot \Delta f^{\phi, \text{nqe}}) \\ & \times \exp(-\Delta f^{F/N} \cdot M_{F/N}^{-1} \cdot \Delta f^{F/N}) \\ & \times \exp(-\Delta f^\epsilon \cdot M_\epsilon^{-1} \cdot \Delta f^\epsilon) \\ & \times \exp\left(-\frac{\Delta f^{\text{Ia}}}{2\sigma_{\text{Ia}}^2}\right) \times \exp\left(-\frac{\Delta f^{\text{Ib}}}{2\sigma_{\text{Ib}}^2}\right) \times \exp\left(-\frac{\Delta f^{\text{Escale}}}{2\sigma_{\text{Escale}}^2}\right) \end{aligned} \quad (9.12)$$

where  $\Delta f \equiv f - f_c$  is the difference of the parameter from its central value  $f_c$ ,  $M_{\phi, \text{nqe}}$ ,  $M_{F/N}$ , and  $M_\epsilon$  are the error matrices for the corresponding parameters,  $\sigma_{\text{Ia}}$  and  $\sigma_{\text{Ib}}$  are the errors on the normalization for K2K-Ia and Ib period, respectively, and  $\sigma_{\text{Escale}}$  is the error on the energy scale in SK. These systematic parameters are treated as fitting parameters in the likelihood analysis.

### 9.2.2 Input values for systematic parameters

For the neutrino energy spectrum, the values listed in Table 7.11 are used for the central values for  $f^{\phi, \text{nqe}}$  and the error matrix  $M_{\phi, \text{nqe}}$ .

For  $F/N$  ratio, since the values estimated by Beam-MC are used as the central values of  $F/N$  ratio as described in Sec. 6.3, the central values of  $f^{F/N}$  are set to be unity. On the other hand, the error matrix shown in Eq. (6.7) is used as  $M_{F/N}$ , which is estimated by PIMON above 1 GeV and by Beam-MC below 1 GeV.

The error on the selection efficiency for  $1R\mu$  events in SK is estimated in Sec. 8.4 and the matrix shown in Eq. (8.2) is used as  $M_\epsilon$ . The central values for  $f^\epsilon$  are set to be unity.

The uncertainty in the energy scale in SK is estimated to be 3% as described in Sec. 3.6.5. Therefore,  $\sigma_{\text{Escale}}$  is set to be 3%, while the central value of  $f^{\text{Escale}}$  is set to be unity.

The normalization parameters for K2K-Ia and K2K-Ib are separately treated since special treatment is needed for K2K-Ia as described before.

For the error on the normalization in K2K-Ib ( $\sigma_{\text{Ib}}$ ), the contributing systematic errors is listed in Table 7.5. Among them, uncertainties due to neutrino spectrum,  $F/N$  ratio, and interaction cross-sections are already introduced into the parameters of the likelihood function. Therefore, only uncertainties other than them are used to estimate the error on the normalization; 0.37% from 1KT statistics, 4.34% from 1KT systematics, 3% from SK systematics, and 0.6% from POT correction. In total, 5.34% is quoted as  $\sigma_{\text{Ib}}$ .

Since the amount of data taken in K2K-Ia accounts for only a small fraction of total amount of data (6.5% of total POT), the effect of uncertainty in the expected number of events in K2K-Ia is inferred to be negligible. Therefore, a simplified and conservative method is employed to estimate the error on the normalization in K2K-Ia ( $\sigma_{\text{Ia}}$ ). Unlike in the case of K2K-Ib, all the uncertainties listed in Table 7.5 are taken into account for  $\sigma_{\text{Ia}}$ . The cancellation of the errors between ND and SK due to the uncertainties in the neutrino spectrum and the cross-section ratio ( $\sigma_{\text{nonQE}}/\sigma_{\text{QE}}$ ) is already taken into account for the numbers in Table 7.5 with an assumption of no neutrino oscillation. However the cancellation is not expected in the oscillated case. Therefore, the raw errors (or errors without cancellation) are used for these two quantities. The neutrino spectrum errors above 1 GeV is quoted from the PIMON measurements, while those below 1 GeV is quoted from the ND spectrum measurements, yielding the  $\pm 9.3\%$  errors on  $N_{\text{Ia}}^{\text{exp}}$ . A  $\pm 30\%$  change in  $\sigma_{\text{nonQE}}/\sigma_{\text{QE}}$  yields  $1.6\%$  change in the detection efficiency in SK. These errors are used instead of those listed in Table 7.5. Other uncertainties are treated in the same way as K2K-Ib. In total, the expected number of neutrino events in K2K-Ia is re-estimated to be  $4.55^{+0.80}_{-0.68}$  events. This number is expected to become smaller in the oscillated case, and hence its error is also expected to become smaller accordingly. However, in this analysis, we neglect this effect and  $\sigma_{\text{Ia}} = {}^{+0.80}_{-0.68}$  event is used as constant independent from the value of oscillation parameters.

### 9.3 Re-estimation of expected number of neutrino events and spectrum at SK in the case of no oscillation

Before performing the oscillation analysis with likelihood, we re-estimate the expected number of neutrino events ( $N^{\text{exp}}$ ) and the reconstructed neutrino energy spectrum at SK without neutrino oscillation, using the results of spectrum analysis in ND. Here, Eq. (9.4), (9.5) and (9.11) are used. Many sets of parameters  $\mathbf{f}$  are randomly generated around their central values assuming Gaussian distribution with the energy correlation taken into account, and  $N^{\text{exp}}$  and  $\text{Prob}(E^{\text{rec}})$  are calculated for each set of  $\mathbf{f}$  with  $\sin^2 2\theta = 0$  (no oscillation).

Resulting distributions for  $N^{\text{exp}}$  and  $\text{Prob}(E^{\text{rec}})$  are shown in Fig. 9.1. By taking the peak position and the standard deviation of the distribution in the left figure of Fig. 9.1, the expected number of neutrino events in the case of no oscillation is estimated to be  $80.1^{+6.2}_{-5.4}$ . The error bar of each point of  $E_{\nu}^{\text{rec}}$  distribution in the right figure of Fig. 9.1 is corresponding to the standard deviation of many trial.

The contribution of each systematic uncertainty to the errors on  $N^{\text{exp}}$  and  $\text{Prob}(E^{\text{rec}})$  is estimated by turning each uncertainty on one by one. The errors on  $N^{\text{exp}}$  are summarized in Dominant contributions come from the uncertainties on the  $F/N$  ratio and the normalization. The contribution of each uncertainty to the energy spectrum is shown in Fig. 9.2 as a function of reconstructed neutrino energy. In low and high energy regions, the uncertainty in the energy scale makes a dominant contribution, while all the uncertainties except for non-qe/qe ratio make similar contribution in the medium energy region. Table 9.1.

### 9.4 Best-fit point for neutrino oscillation

The likelihood is calculated at each point in  $(\sin^2 2\theta, \Delta m^2)$  space to search for the point where the likelihood is maximized. The best-fit point in the physical region of oscillation parameter space is found to be

$$(\sin^2 2\theta, \Delta m^2) = (1.0, 2.8 \times 10^{-3} \text{ eV}^2) \quad . \quad (9.13)$$

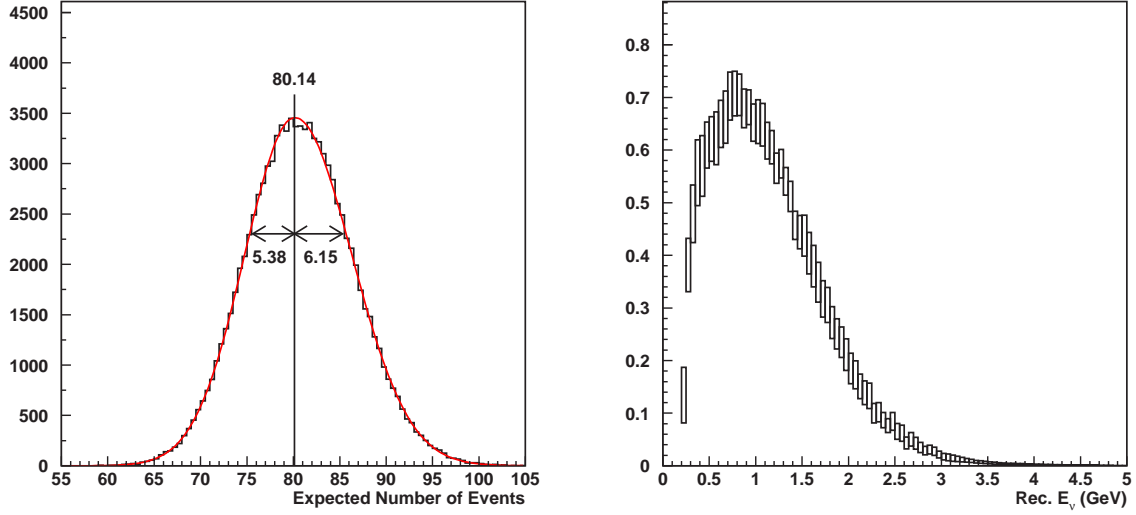


**Figure 9.1:** The distribution of expected numbers of neutrino events (left) and the reconstructed neutrino energy (right) in SK for many trial of random number generation without neutrino oscillation. In the right figure, the error bar (size of box) for each point corresponds to the standard deviation of many trial, indicating the size of error on each point.

**Table 9.1:** Summary of contribution of each systematic uncertainty to the expected number of neutrino events in SK in the case of no oscillation. The third and fourth columns are errors in the unit of events and %, respectively.

Period	Source	Errors in events	Errors in %
K2K-Ia	Total	+0.8 -0.7	+1.0 -0.9
K2K-Ib	Neutrino spectrum	+0.4 -0.5	+0.6 -0.6
	non-qe/qe	+0.4 -0.9	+0.5 -1.1
	$F/N$ ratio	+4.0 -4.1	+4.9 -5.0
	Normalization	+4.0 -4.0	+5.0 -5.0
	Subtotal in K2K-Ib	+6.1 -5.3	+7.6 -6.7
In total ( $N^{\text{exp}} = 80.1$ )		+6.2 -5.4	+7.7 -6.7

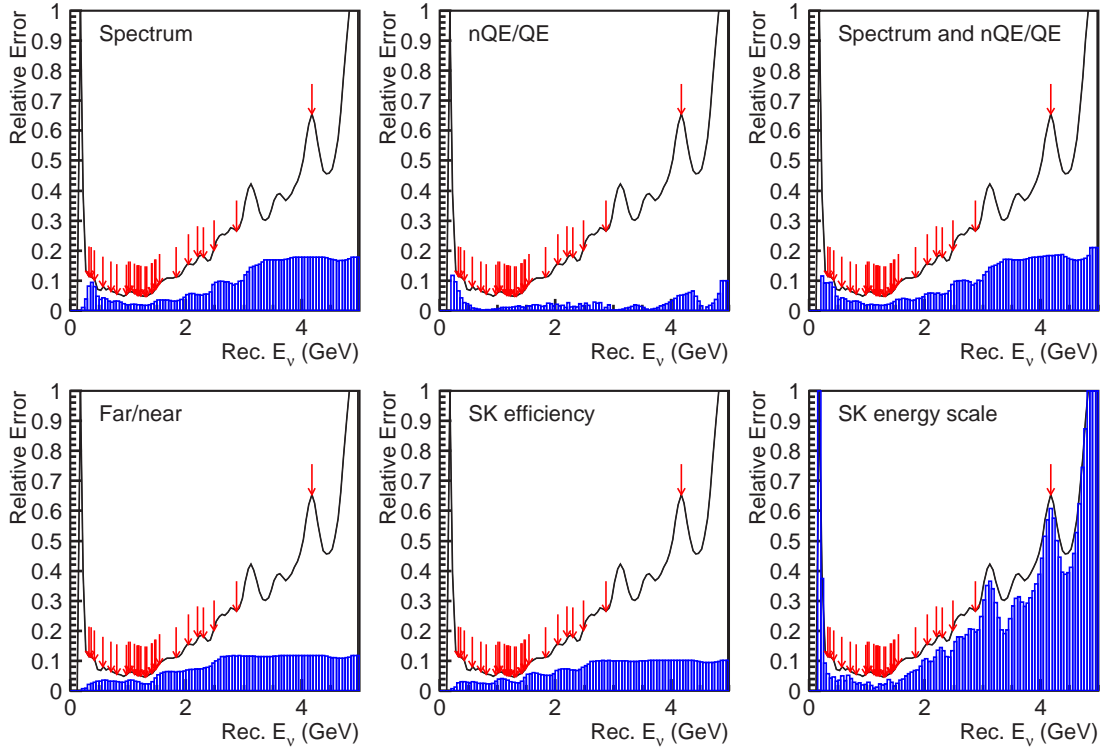


**Figure 9.2:** Contribution of various uncertainties to the reconstructed neutrino energy spectrum. Vertical axis is relative error of the spectrum. Source of uncertainty for each plot is written in the figure. Black histogram is the total error and the blue filled histogram is the contribution from each source. The red arrows in the plots indicate the reconstructed neutrino energies of 29 observed  $1R\mu$  events.

**Table 9.2:** The Best-fit points for several conditions. “Global” means the fitting with the searched region extended to unphysical region, while “Physical region” means the fitting with the searched region constrained inside the physical ration. “1R $\mu$  shape only” means the fitting with only the shape likelihood term and “Shape + Norm.” means the fitting with the total likelihood.

		$\sin^2 2\theta$	$\Delta m^2 [\text{eV}^2]$
Global	1R $\mu$ shape only	1.09	$3.0 \times 10^{-3}$
	Shape + Norm.	1.03	$2.8 \times 10^{-3}$
Physical region	1R $\mu$ shape only	1.00	$3.0 \times 10^{-3}$
	Shape + Norm.	1.00	$2.8 \times 10^{-3}$

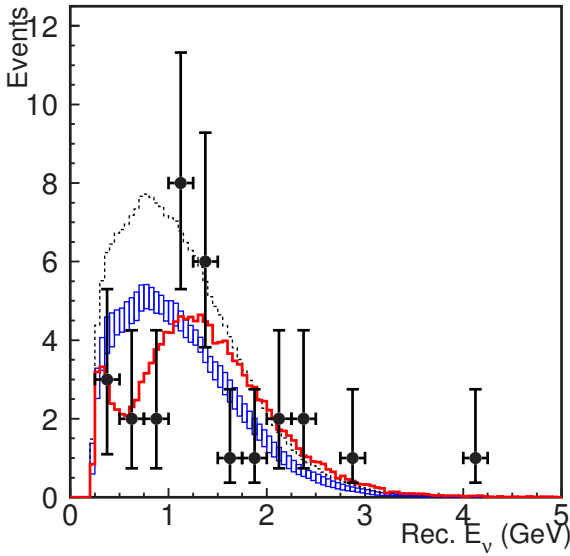


**Figure 9.3:** The reconstructed neutrino energy distribution for 1R $\mu$  sample. Points with error bars are our observation. The blue box histogram is the expected spectrum without neutrino oscillation. The solid red histogram is the best-fit spectrum. These histograms are normalized by the number of observed 1R $\mu$  events (29). In addition, the black dashed line shows the expectation with no oscillation normalized to the expected number of 1R $\mu$  events (44).

The best-fit points of fitting with the search region extended to unphysical region or with only the use of shape likelihood term are summarized in Table 9.2.

The total number of neutrino events predicted at the best-fit point in the physical region is 54.2, which is in good agreement with the observation (56) within statistical error. The observed distribution of the reconstructed neutrino energy for 1R $\mu$  events is shown in Fig. 9.3, in which the expected distribution for no oscillation case and for the best-fit oscillation parameters are overlaid. The consistency between the observed and the best-fit distributions are checked by Kolmogorov-Smirnov (KS) test. A KS probability of 79% is obtained, indicating that the best-fit spectrum shape agrees with the observation.

## 9.5 Null oscillation probability

The probability that the observations are only due to a statistical fluctuation instead of neutrino oscillation is estimated by computing the likelihood ratio of no oscillation case to the best-fit point. The probability for no oscillation is calculated to be only 0.7%. When only normalization (shape) information is used, the probability becomes 1.3% (16%).

The effect of each systematic uncertainty on the null oscillation probability is tested by turning each systematic uncertainty on one by one. The results are summarized in Table 9.3.



**Table 9.3:** Effect of each systematic uncertainty on the null oscillation probability. The numbers in the table are null oscillation probabilities when only the uncertainty in the first column is turned on, where “Statistics only” stands for all the systematic uncertainties turned off. “Norm. only” (“Shape only”) means the probability when only the normalization (spectrum shape) term is used in the likelihood, and “Norm. + Shape” means that both likelihood terms are used.

Sources of uncertainty	Norm. only	Shape only	Norm. + Shape
Statistics only	0.35%	8.2%	0.14%
Neutrino spectrum	0.36%	8.4%	0.15%
non-qe/qe ratio		8.2%	
$F/N$ ratio	0.73%	8.4%	0.24%
SK $1R\mu$ efficiency	—	8.3%	0.14%
SK energy scale	—	15.5%	0.24%
K2K-Ia norm. $\sigma_{Ia}$	0.35%	—	0.14%
K2K-Ib norm. $\sigma_{Ib}$	0.75%	—	0.28%
All uncertainties	1.27%	15.7%	0.70%

The dominant contributions to make the probability large are the uncertainties in the  $F/N$  ratio and the normalization in K2K-Ib period in the case of using only normalization term, while the uncertainty in the energy scale is the dominant contribution in the case of using only spectrum shape term. For the probability with whole likelihood, these three sources make similar contribution.

## 9.6 Constraint on the neutrino oscillation parameters

The allowed region for oscillation parameters are evaluated by calculating the likelihood ratio of at each point to at the best-fit point, which is shown in Fig. 9.4. The 90% C.L. line intersects the axis of  $\sin^2 2\theta = 1$  at  $\Delta m^2 = 1.5 \times 10^{-3}$  and  $3.9 \times 10^{-3} \text{ eV}^2$ . The behaviors of log-likelihood difference ( $-\Delta \ln \mathcal{L}$ ) as a function of  $\Delta m^2$  along the axis of  $\sin^2 2\theta = 1$  and as a function of  $\sin^2 2\theta$  along  $\Delta m^2 = 2.8 \times 10^{-3} \text{ eV}^2$  are shown in Fig. 9.5. In addition, the 68% allowed regions in the case of that only the normalization term or only the spectrum shape term is used are shown in Fig. 9.6, indicating that the flux reduction alone and the spectrum distortion alone favor the same oscillation parameter region.

## 9.7 Dependence of results on neutrino interaction models

The dependence of our results on the choice of neutrino interaction models is studied by adopting several models to the likelihood fitting. It is found that the change in the null oscillation probability is negligibly small when model is changed. As an example of change of models, Fig. 9.7 shows the difference in the reconstructed neutrino energy spectrum and the allowed region is shown, where NEUT-1211 and NEUT-0000 (see Table 4.4 in Sec. 4.2.7) are compared. As is seen in the figures, the difference is very small and within the estimated errors. The choice of the interaction models does not affect so much on the results of oscillation analysis, as is seen in Fig. 9.7.

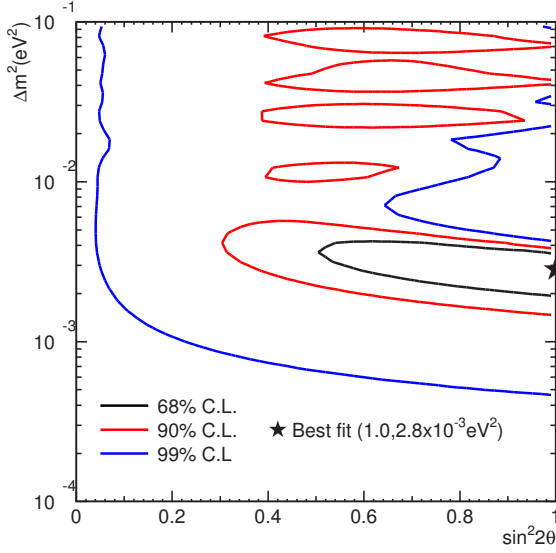


**Figure 9.4:** Allowed region of oscillation parameter constrained by K2K experiment. Black, red, and blue lines are 68%, 90%, and 99% contours, respectively. The best-fit point is indicated by a black “★” mark.

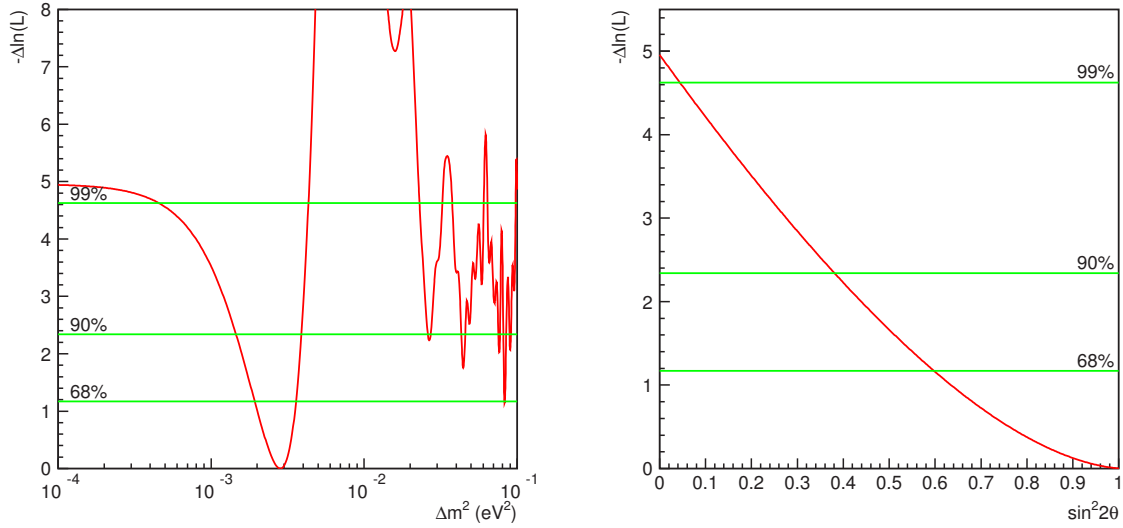


**Figure 9.5:** Behaviors of the log-likelihood difference,  $-\Delta \ln \mathcal{L}$ , as a function of  $\Delta m^2$  along the axis of  $\sin^2 2\theta = 1$  (left) and as a function of  $\sin^2 2\theta$  along  $\Delta m^2 = 2.8 \times 10^{-3} \text{ eV}^2$  (right). Green lines show the 68%, 90%, and 99% C.L. lines for  $-\Delta \ln \mathcal{L}$ .

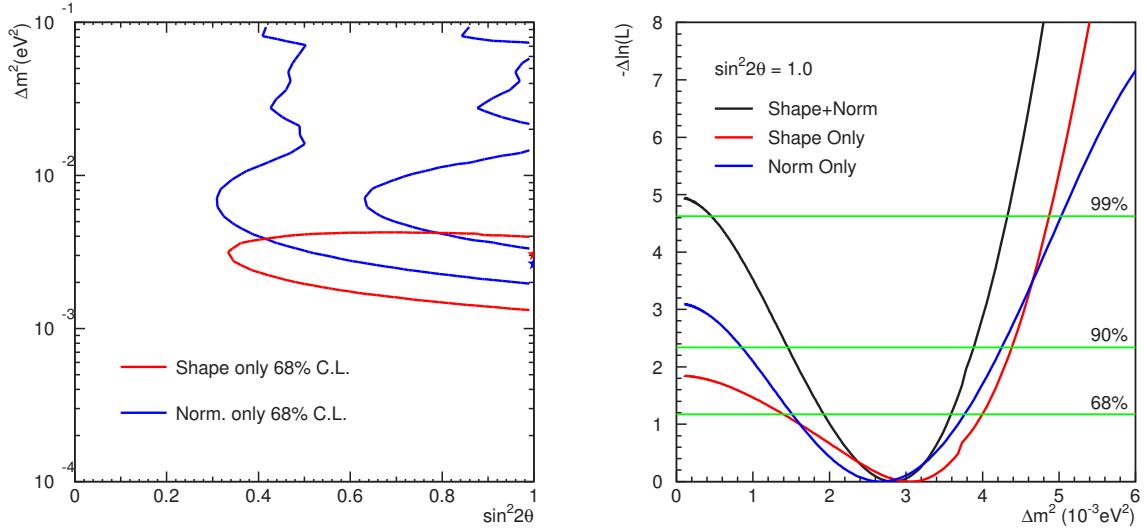


**Figure 9.6:** The 68% allowed regions of oscillation parameter space in the case of using normalization term only or spectrum shape term only (left) and their behavior of the log-likelihood difference,  $-\Delta \ln \mathcal{L}$ , as a function of  $\Delta m^2$  along the axis of  $\sin^2 2\theta = 1$  (right). In both figures, blue line shows the results of normalization term only and red line shows the results of shape term only. In left figure, the point where the normalization (shape) likelihood function is maximized along the axis of  $\sin^2 2\theta = 1$  is indicated by blue (red) “★” mark.

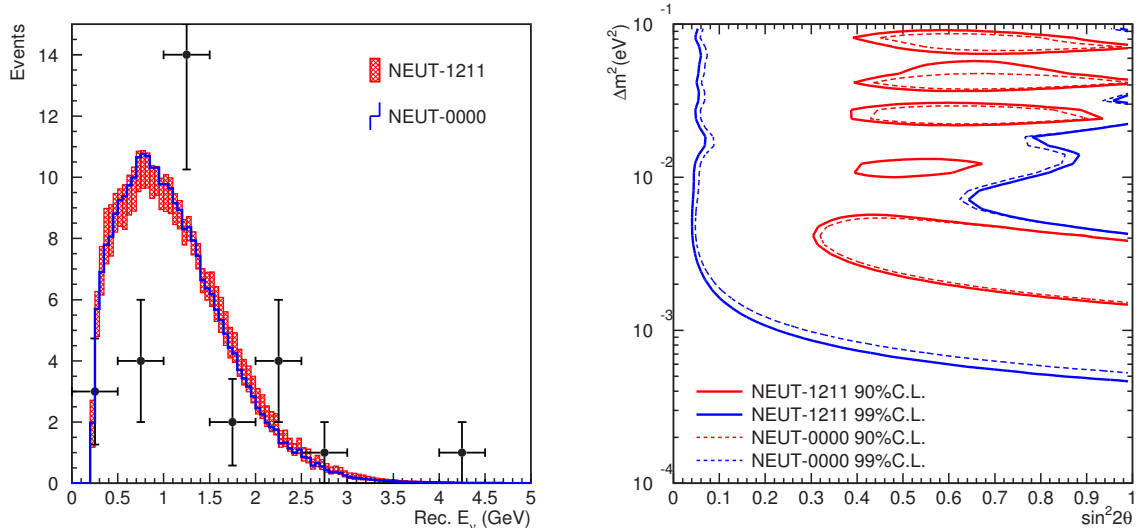


**Figure 9.7:** Comparison of different neutrino interaction models for the reconstructed neutrino energy and allowed parameter region. In the left figure, red hatched boxes are for NEUT-1211 and blue histogram is for NEUT-0000. The error bars for NEUT-1211 is the same as in Fig. 9.1. In right figure, solid lines show NEUT-1211 and dotted lines show NEUT-0000.

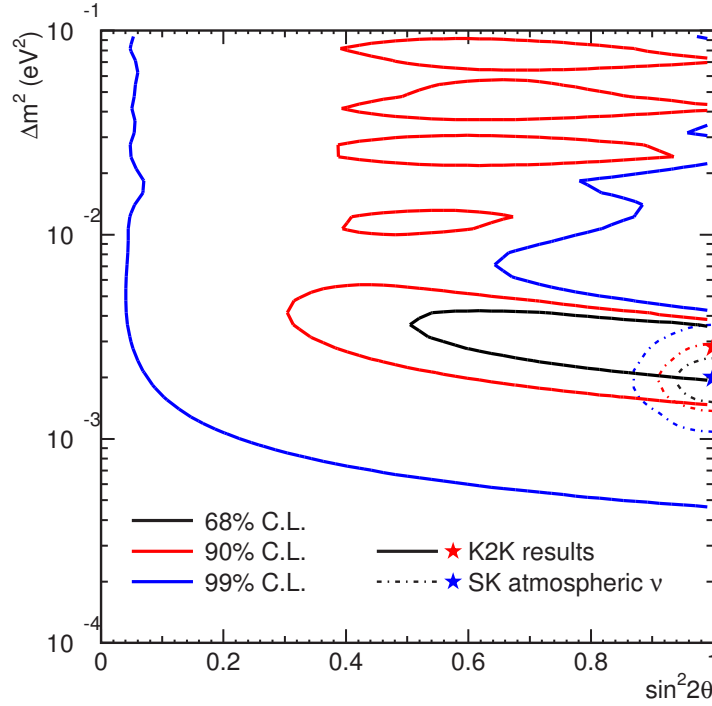


**Figure 9.8:** The allowed region of oscillation parameters constrained by K2K experiment together with that constrained by the atmospheric neutrino observation in SK [118]. The solid lines show the our results and dash-dotted lines show the results from atmospheric neutrino observation in SK. Black, red, and blue lines are for 68%, 90%, and 99% contours, respectively. The best-fit point of the K2K (SK) observation is indicated by red (blue) “★” mark.

## 9.8 Comparison with the results from atmospheric neutrino observation

Finally, Fig. 9.8 compares the allowed region estimated by our analysis with the recent results of the atmospheric neutrino observation in SK [118]. The best-fit point of the atmospheric results is at  $(\sin^2 2\theta, \Delta m^2) = (1.0, 2.0 \times 10^{-3} \text{ eV}^2)$ , and the 90% C.L. region of  $\Delta m^2$  along the  $\sin^2 2\theta = 1$  axis is  $(1.0-3.0) \times 10^{-3} \text{ eV}^2$ . Our results are also consistent with that favored by the atmospheric neutrino observation pointing the same region of the oscillation parameters.

# Chapter 10

## Discussions and Prospects

Up to the previous chapter, we have developed the analysis to obtain the information on the neutrino oscillation and its results. We have successfully probed the neutrino oscillation with strong indications: The probability to obtain our observation only due to the statistical fluctuation with no neutrino oscillation is only 0.7%, and the squared mass difference  $\Delta m^2$  has been constrained in the region of  $1.5\text{--}3.9 \times 10^{-3} \text{ eV}^2$  at the mixing angle of  $\sin^2 2\theta = 1$ , and  $\sin^2 2\theta$  has been constrained to be greater than 0.3 with the confidence level of 90%. However, there are still several issues to be improved to make our sensitivity to the neutrino oscillation better. In this chapter, some prospects to make our measurements of the oscillation parameters better are discussed.

First of all, our sensitivity is statistically limited in the current situation, and hence much more statistics is needed. For this point, our data will be doubled at the end of K2K experiment. At the same time, enlarging the fiducial volume for the analysis in SK can also increase available statistics. In the current analysis, we impose a cut on the distance between the reconstructed vertex point and the nearest wall ( $D_{\text{wall}}$ ) to be greater than 2 m, which makes the fiducial volume 22.5 kt while the whole ID volume has 32.5 kt. Therefore there is another 45% volume which potentially increases the statistics for analysis. In order to enlarge the fiducial volume, understanding of the behavior of detection efficiency for the events which occur near the ID wall, the rejection efficiency for the incoming cosmic ray muons, and behavior of the events which happen in the insensitive region between the ID and OD tanks is needed. After these studies, it is expected to enlarge the fiducial volume for K2K analysis.

In the case of our statistics for the analysis is doubled, the systematic uncertainty in the current analysis will become comparable with the statistical uncertainty. According to Table 9.3, main contributions of the uncertainties to make the sensitivity to the neutrino oscillation worse are as followings: The error on the  $F/N$  ratio and the normalization are dominant in the normalization term in the likelihood function, while the error on energy scale in SK is dominant in the spectrum shape term.

The  $F/N$  ratio in our analysis is estimated by Beam-MC, while its error is estimated based on the uncertainties in the PIMON measurements for the neutrino energy of above 1 GeV and based on ambiguities in the hadron production models for the neutrino energy of below 1 GeV. They yield about 5–10% errors on the  $F/N$  ratio. In order to reduce these errors, HARP experiment [119] was performed at CERN, which was the experiment to measure the hadron production cross-sections on various target materials with various incident beam momenta. In this experiment, we had took data with the same condition as K2K experiment; the same production target (aluminum) with the same dimensions (65 cm in length and 3 cm in diameter), and the same beam momentum (12.9 GeV/c). The data is under analysis and close to obtain the results [120, 121]. Using this measured cross section, we expect to reduce the error on  $F/N$

ratio down to about 3% level.

The uncertainty in the normalization, the dominating errors are comes from the definition of the fiducial volume both in 1KT (4%) and SK (2%). Currently, several calibration works are being done to understand the behavior of the vertex reconstruction. Hopefully, it will be expected to become a half size of the errors.

For the energy scale uncertainty, SK has 3% uncertainty. It also should be reduced to be around 1% level in order not to affect the sensitivity of K2K experiment.

Furthermore, the energy information of the multi-ring events in SK is also available to make our analysis more sensitive to the neutrino oscillation although we do not use them in the analysis described in this thesis. These events mainly come from the non-qe interactions, and hence the detailed understanding of the neutrino interaction is indispensable. For this purpose, a full active tracking detector, SciBar [122], was installed in the near detector system in the summer of 2003. With this detector, we can study the neutrino interactions precisely down to the low energy region of about a few 100 MeV. These studies also help us to reduce the uncertainties in spectrum measurements at ND, which is secondly dominating error on the spectrum shape in SK as seen in Fig. 9.2. By feeding these studies back into the analysis in SK, we may be able to introduce the multi-ring events into the spectral shape analysis with a reasonably small error.

For the spectral studies in ND, the error on the energy spectrum around 0.5–1.0 GeV should be reduced, where maximum effect of the neutrino oscillation is expected according to our results. In this thesis, the size of the error is about 10%. Here again, SciBar will be helpful since its detection threshold is as low as about 100 MeV/ $c$  in muon momentum, and hence it can measure the low energy neutrinos. Furthermore, as mentioned above, the understanding of the neutrino interactions will also reduce the error on spectrum in the low energy region since non-qe/qe ratio has strong correlation with the low energy neutrinos. At the same time as these studies being done, the uncertainty in the energy scale of the detectors should also be understood at the level of about 1%, since the current size of the energy scale uncertainty ( $\sim 3\%$ ) yields the largest errors among the detector systematics as shown in Fig. 7.32.

With the studies mentioned above, the sensitivity of K2K experiment will still become better even in the case of that the statistics will be doubled.

# Chapter 11

## Conclusion

In order to investigate the neutrino oscillation discovered in the atmospheric neutrino observation, the first long baseline neutrino experiment, the K2K experiment, have been performed with the use of accelerator produced neutrinos and their flight length of 250 km. Data taking was started in June 1999, and up to now, the experiment have been successfully operated. Based on the data taken from the beginning of the experiment to July 2001, the first oscillation analysis for the  $\nu_\mu$  disappearance is performed with the use of both the number of observed events and the observed energy spectrum. The corresponding number of protons on target is  $4.79 \times 10^{19}$  POT, which is about a half data of our goal.

First, the flux and the energy spectrum of the neutrino beam are measured in the near detector system. The flux is measured by counting the number of neutrino interactions occurred in 25 t fiducial volume of 1KT, while the energy spectrum is derived from the muon momentum distributions measured in both 1KT and FGD. The neutrino interaction itself is also studied in ND and a parameter which describes the cross-section ratio of non-quasi-elastic to quasi-elastic interactions is obtained at the same time. The measurements of neutrino energy spectrum described in this thesis is done for the first time in the K2K experiment.

Then, these measurements are extrapolated to the expected observables in Super-Kamiokande using Beam-MC which is validated by PIMON measurements. The expected number of events fully contained in the 22.5 kt fiducial volume of SK is estimated to be  $80.1^{+6.2}_{-5.4}$ , while 56 events are observed; a clear deficit in the number is found. The energy spectrum for 29 observed single-ring  $\mu$ -like events also shows a distortion in its spectral shape.

In order to estimate the significance of the reduction in number of events and the distortion in the spectrum shape, and in order to constrain the oscillation parameters, an oscillation analysis have been performed by using a maximum likelihood method. Both information from the number of events and the spectrum shape are included in the likelihood function. The best-fit values for the neutrino oscillation is found to be  $(\sin^2 2\theta, \Delta m^2) = (1.0, 2.8 \times 10^{-3} \text{ eV}^2)$ . The probability that the deficit in the number of events and the distortion in the spectrum shape are only due to a statistical fluctuation is estimated to be 0.7%, strongly disfavoring the absence of neutrino oscillation. Allowed region for the oscillation parameters are also evaluated. At maximum mixing,  $\sin^2 2\theta = 1$ , the mass squared difference is constrained to be within  $\Delta m^2 = (1.5 - 3.9) \times 10^{-3} \text{ eV}^2$  with the confidence level of 90%. The deficit in the number of events and the distortion in the spectrum shape both favor the same oscillation parameter region. Our results are consistent with the results from atmospheric neutrino observations.

In conclusion, we have obtained strong indications for the neutrino oscillation with the disappearance of muon neutrinos.





# Appendix A

## Neutrino oscillation measurements before K2K experiment

Up to now, a number of experiments and observations to search for neutrino oscillation have been performed around the world. They are categorized into four types according to their source of neutrinos; atmospheric neutrino observations, solar neutrino observations, reactor neutrino experiments, and accelerator neutrino experiments. This classification is also roughly corresponding to the one based on the sensitive region to  $\Delta m^2$ , except for the case of long baseline experiments. The accessible regions of  $L/E$  for those experiments are

$$\begin{array}{ll} \text{Atmospheric neutrino:} & 10 - 10^4 \text{ km/GeV} \\ \text{Solar neutrino:} & 10^{10} - 10^{11} \text{ km/GeV} \\ \text{Reactor neutrino:} & 1 - 10^{2.5} \text{ km/GeV} \\ \text{Accelerator neutrino:} & 10^{-2} - 10 \text{ km/GeV} \end{array}$$

in the case of vacuum oscillation. In this section, the status of the measurements on neutrino oscillation are briefly summarized. The results described here are basically what had been published at the point when the results of the K2K experiment which is the main subject of this thesis became public in the middle of 2002.

### A.1 Atmospheric neutrino observations

Protons and  $\alpha$  particles flying about in the universe always pour onto the Earth as primary cosmic rays. Atmospheric neutrinos are produced in the atmosphere of the Earth in such way that these high energy protons and  $\alpha$  particles collide and interact with the atmospheric components such as oxygen and nitrogen and create a number of secondary mesons, mainly pions and kaons, then subsequently these mesons emit neutrinos in their decay processes, as shown in the following diagram;

$$\begin{array}{llll} p, \alpha_{\text{cosmic}} + N_{\text{atmosphere}} & \rightarrow & \begin{array}{l} \pi^+(K^+) \\ \pi^-(K^-) \end{array} & + N' \\ & & \downarrow & \\ \begin{array}{l} \pi^+(K^+) \\ \pi^-(K^-) \end{array} & \rightarrow & \begin{array}{l} \mu^+ + \nu_\mu \\ \mu^- + \bar{\nu}_\mu \end{array} & \\ & & \downarrow & \\ & & \begin{array}{l} \mu^+ \rightarrow e^+ + \bar{\nu}_\mu + \nu_e \\ \mu^- \rightarrow e^- + \nu_\mu + \bar{\nu}_e \end{array} & \end{array} \quad (\text{A.1})$$

**Table A.1:** Summary of the observed  $R$  values in atmospheric neutrino experiments. In Super-Kamiokande, Kamiokande, and IMB experiments,  $R$  is evaluated in the low energy and high energy samples separately. The  $R$  values in some experiments differ from that defined in the title column. See notes given below the table for details.

Experiment	Energy Range	Exposure Time [ kton·year ]	$R \left( \frac{(N_\mu/N_e)_{\text{obs}}}{(N_\mu/N_e)_{\text{M.C.}}} \right)$
Super-Kamiokande	sub-GeV	33	$0.61 \pm 0.03 \pm 0.05$ [123]
	multi-GeV	33	$0.66 \pm 0.06 \pm 0.06$ [124]
Kamiokande	sub-GeV	8.2	$0.60^{+0.06}_{-0.05} \pm 0.05$ [128]
	multi-GeV	8.2 (FC) 6.0 (PC)	$0.57^{+0.08}_{-0.07} \pm 0.07$ [128]
IMB	$E_{\text{vis}} < 0.95$ GeV	7.7	$0.54 \pm 0.05 \pm 0.12$ [129]
	$E_{\text{vis}} > 0.95$ GeV	7.7	$1.1^{+0.07}_{-0.12} \pm 0.11^{\text{a}}$ [130]
Soudan-2	—	3.9	$0.64 \pm 0.11 \pm 0.06$ [132]
MACRO	—	4.68 years	$0.74 \pm 0.036 \pm 0.046 \pm 0.13^{\text{b}}$ [136]
Fréjus	—	2.0	$1.00 \pm 0.15 \pm 0.08$ [138]
NUSEX	—	0.740	$0.96^{+0.32^{\text{b}}}_{-0.28}$ [139]

<sup>a</sup> This value is the double-ratio of muon to total neutrino flux between the observation and the expectation;  $\frac{(N_\mu/N_{\text{total}})_{\text{obs}}}{(N_\mu/N_{\text{total}})_{\text{MC}}}$ .

<sup>b</sup> These values are only the ratio of the observed to expected muon neutrino flux;  $N_\mu^{\text{obs}}/N_\mu^{\text{MC}}$ .

The energy spectrum of these neutrino has a peak about 1 GeV, and extends to the order of 100 GeV. The main production process of neutrinos with the energy of about GeV region is the subsequence of pion decays, which results in the flux ratio of  $(\nu_\mu + \bar{\nu}_\mu)/(\nu_e + \bar{\nu}_e)$  to be ideally 2. In the simulation, this ratio is predicted with the uncertainty of 5%, whereas the absolute flux have the uncertainty of 20%.

The ratio  $(\nu_\mu + \bar{\nu}_\mu)/(\nu_e + \bar{\nu}_e)$  has been measured in several experiments: Super-Kamiokande [54, 123, 124], Kamiokande [125, 126, 127, 128], and IMB [129, 130], which use water-Cherenkov type detectors, and Soudan-2 [131, 132], MACRO [133, 134, 135, 136], Fréjus [137, 138], and NUSEX [139] which use iron-calorimeter type detectors. Both types of detector have the capabilities to identify a event as neutrino induced event by the containment of the vertex, and to identify the particle type as  $\mu$ -type or  $e$ -type by the Cherenkov ring pattern in the water-Cherenkov type detectors or by the hit distribution in the iron-calorimeter type detectors. In each experiment, the number of  $\mu$ -like neutrino events  $N_\mu$  and the number of  $e$ -like neutrino events  $N_e$  are counted, and the ratio  $(N_\mu/N_e)_{\text{obs}}$  is taken and compared to that estimated by Monte Carlo simulation;

$$R \equiv \frac{(N_\mu/N_e)_{\text{obs}}}{(N_\mu/N_e)_{\text{MC}}} . \quad (\text{A.2})$$

Instead of  $R$ , only the ratio of observed to expected muon neutrino flux,  $(N_\mu)_{\text{obs}}/(N_\mu)_{\text{MC}}$ , is evaluated in MACRO and NUSEX experiment, and the double-ratio of muon to total neutrino flux between observation and expectation,  $(N_\mu/N_{\text{total}})_{\text{obs}}/(N_\mu/N_{\text{total}})_{\text{MC}}$ , is calculated in the multi-GeV analysis of IMB experiment. The value  $R$  observed in each experiment is summarized in Table A.1.

Historically, Kamiokande and IMB experiments observed the significantly small  $R$  values away from unity [126, 127, 128, 129, 130], which was called “atmospheric neutrino anomaly”. On the other hand, Fréjus and NUSEX experiments observed  $R$  to be consistent with unity [138,

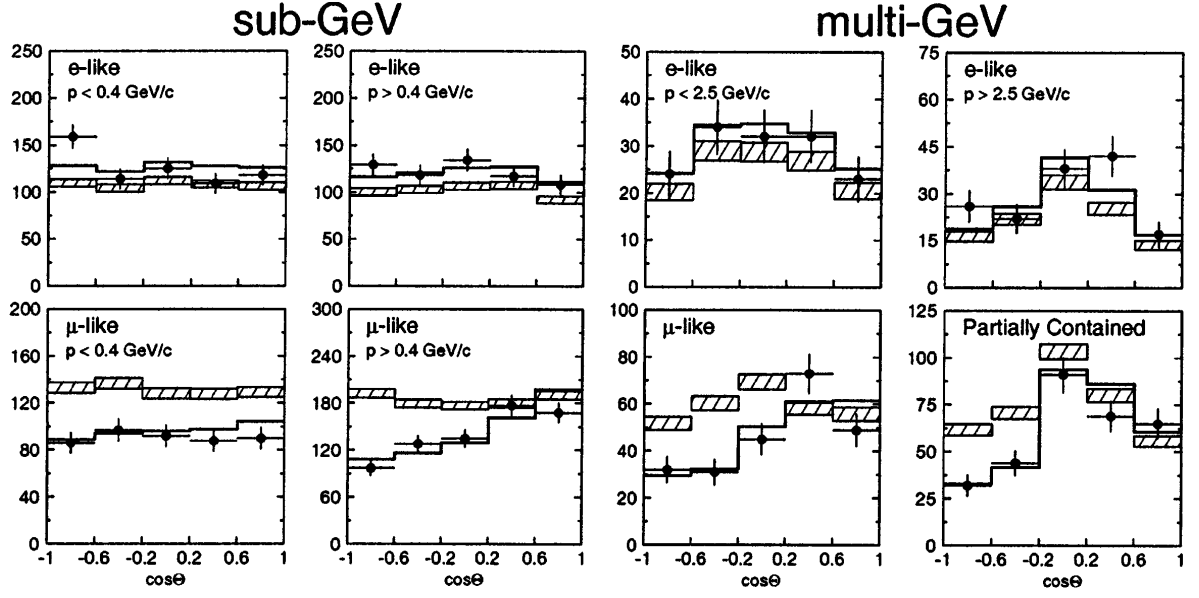


**Figure A.1:** The zenith angle distribution of the  $\mu$ -like and  $e$ -like events in Super-Kamiokande [140]. The upward-going particles have  $\cos \Theta < 0$  and the downward-going particles have  $\cos \Theta > 0$ . The sub-GeV samples are the events with visible energy  $E_{\text{vis}}$  of less than 1.33 GeV, while the multi-GeV samples are the events with  $E_{\text{vis}}$  of greater than 1.33 GeV. In sub-GeV samples, the events with the reconstructed momentum of less than and greater than 0.4 GeV/ $c$  are separately shown. The multi-GeV  $e$ -like samples are also shown for the events with the reconstructed momentum less than and greater than 2.5 GeV/ $c$ , separately. The multi-GeV  $\mu$ -like samples are shown for the FC and PC events. The expectations of the Monte Carlo simulation without oscillation and with  $\nu_\mu \rightarrow \nu_\tau$  oscillation for the best fit are also drawn in each figure by hatched boxes and solid histograms, respectively.

139], though with poor statistics. Later, Super-Kamiokande and Soudan-2 experiments have been carried out with higher statistics, and they provided the consistent results with Kamiokande experiment.

The evidence of neutrino oscillation was clearly shown by the dependence of  $R$  on the zenith angle in Super-Kamiokande experiment [140]. The upward-going neutrinos are originally produced in the atmosphere of the opposite side of the globe and travel more than 10,000 km distance through the Earth, whereas the downward-going neutrinos are created in the upper air and travel the distance of only several 10 km to the detector. Therefore, the zenith angle in which neutrino is coming have a good correspondence to the distance neutrino travels after its production, which is the oscillation baseline  $L$  in Eq. (1.11). The direction of incoming neutrino have correlation with the that of lepton produced by its charged-current interaction such that the lepton has a trend to be scattered in the same direction as the incoming neutrino travels. Therefore, the zenith angle of the scattered lepton observed by the direction of Cherenkov ring in the water-Cherenkov type detector is also corresponding to the oscillation baseline  $L$ . If neutrino oscillation actually exists with the oscillation parameters being in a certain region, the value  $R$  should have some dependence on the zenith angle of scattered lepton in the manner of characteristic of neutrino oscillation.

Fig. A.1 shows the zenith distributions of scattered lepton for  $\mu$ -like and  $e$ -like events observed in Super-Kamiokande [140]. The event samples of four energy regions are separately figured for both  $\mu$ -like and  $e$ -like events. “Sub-GeV (multi-GeV)” is the event sample with the visible

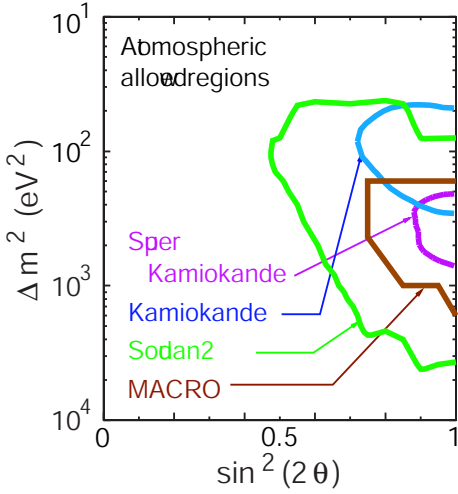


**Figure A.2:** Allowed regions of the oscillation parameters for  $\nu_\mu \rightarrow \nu_\tau$  mode. The results obtained in Kamiokande, Super-Kamiokande, MACRO, and Soudan-2 are shown. In each experiment, the region inside the contour line is allowed by the results of atmospheric neutrino observations with the confidence level of 90%.

energy  $E_{\text{vis}}$  less (greater) than 1.33 GeV. Sub-GeV events with the reconstructed momentum of less than and greater than 0.4 GeV/c are separately shown. In the multi-GeV samples,  $e$ -like events are shown for the reconstructed momentum less than and greater than 2.5 GeV/c, separately, and  $\mu$ -like events are also shown for the events fully contained (FC) and partially contained (PC) in the detector, separately. The results of Monte Carlo simulations without neutrino oscillation and with  $\nu_\mu \rightarrow \nu_\tau$  oscillation are also shown in Fig. A.1 by hatched boxes and solid histograms, respectively. Since the zenith angle distributions in  $\mu$ -like sample show clear deficit in upward-going events whereas those in  $e$ -like sample are almost consistent with the case of no oscillation, these results indicate that the scenario of  $\nu_\mu \rightarrow \nu_\tau$  oscillation is strongly favored rather than either  $\nu_\mu \rightarrow \nu_e$  or no oscillation. Analyzed with the assumption of neutrino oscillation, the observation gave the allowed region of the mixing angle and the mass squared difference to be

$$\sin^2 2\theta_{\mu\tau} > 0.88, \quad 1.5 \times 10^{-3} \text{ eV}^2 < \Delta m^2 < 5 \times 10^{-3} \text{ eV}^2 \quad (\text{A.3})$$

in the two flavor oscillation case, and

$$0.4 < \sin^2 \theta_{23} < 0.7, \quad \sin^2 \theta_{13} < 0.35, \quad 1.5 \times 10^{-3} \text{ eV}^2 < \Delta m_{23}^2 < 5 \times 10^{-3} \text{ eV}^2 \quad (\text{A.4})$$

in the three flavor oscillation case with the confidence level of 90%.

In addition to the Super-Kamiokande observation, the flux of upward-going muons was analyzed in the Kamiokande and MACRO experiments. They also showed the deficit in the vertical direction compared to the horizontal direction, giving the parameter regions for  $\nu_\mu \rightarrow \nu_\tau$  oscillation to be consistent with Super-Kamiokande results. The allowed regions obtained in several experiments are shown in Fig. A.2. Furthermore, it is another possible scenario to explain the deficit of the muon neutrino flux that  $\nu_\mu$  oscillates into a sterile neutrino,  $\nu_s$ , which does not interact with matter at all. However, according to the analyses of the upward-going muon sample with the matter effect, or so-called the MSW effect [141, 142] in the Earth taken into account, this mode is disfavored with 99% C.L. with respect to  $\nu_\mu \rightarrow \nu_\tau$  oscillation in Super-Kamiokande and MACRO experiments [143, 144]. Therefore, again, the results from the atmospheric neutrino observations strongly favor the oscillation mode  $\nu_\mu \rightarrow \nu_\tau$  to explain the deficit and the zenith angle distribution of muon neutrino flux.

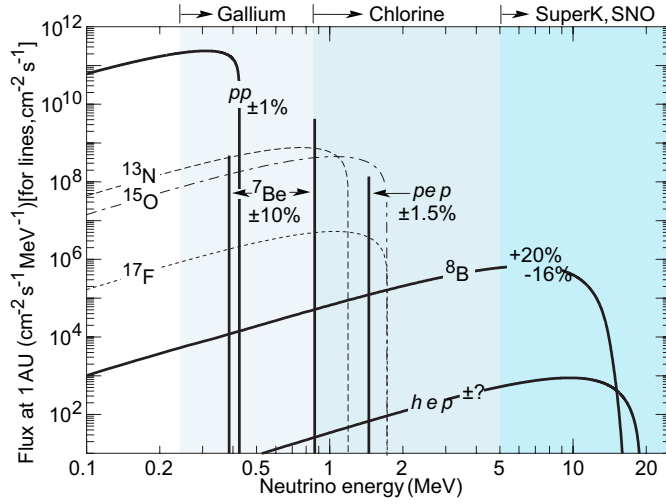


**Figure A.3:** The solar neutrino spectrum predicted by the standard solar model. The spectra for the  $pp$  chain are shown by solid curves, while the spectra for the CNO chain are shown by dotted curves. The neutrino fluxes from continuum sources are given in units of number  $\text{cm}^{-2}\text{s}^{-1}\text{MeV}^{-1}$  at one astronomical unit (1 AU). The spectra is calculated by J. N. Bahcall *et al.*, which is often referred to as BP2000 [145].

## A.2 Solar neutrino observations

The Sun is a main-sequence star at a stage of stable hydrogen burning. It produces an intense flux of electron neutrinos as a consequence of nuclear fusion reactions in the Sun. The energy of the neutrinos distributes from about 100 keV up to 15 MeV, as shown in Fig. A.3. The distance between the Sun and the Earth is 1 AU, i.e.  $1.5 \times 10^8$  km. Therefore, the sensitive region to the  $\Delta m^2$  of the oscillation  $\nu_e \rightarrow \nu_x$  reaches down to the order of  $10^{-11} \text{ eV}^2$ .

There are two detection methods to observe solar neutrinos; the radiochemical technique and the water-Cherenkov technique.

The radiochemical experiments exploit electron neutrino absorption on nuclei, and the amount of the produced isotopes are counted after a certain period of exposure. The Homestake chlorine experiment [146] uses the reaction

$$\nu_e {}^{37}\text{Cl} \rightarrow e^- {}^{37}\text{Ar} \quad (\text{threshold } 814 \text{ keV}) \quad , \quad (\text{A.5})$$

while CALLEX [147], GNO [148], and SAGE [149] experiments uses the reaction

$$\nu_e {}^{71}\text{Ga} \rightarrow e^- {}^{71}\text{Ge} \quad (\text{threshold } 233 \text{ keV}) \quad . \quad (\text{A.6})$$

According to the standard solar model (SSM), the dominant contribution in the chlorine experiment comes from  ${}^8\text{B}$  neutrinos, but  ${}^7\text{Be}$ ,  $pep$ ,  ${}^{13}\text{N}$ , and  ${}^{15}\text{O}$  neutrinos also contribute. In addition to them, the most abundant  $pp$  neutrinos can be detected in gallium experiments. The results from these experiments are summarized in Table A.2. All the experiments observed significantly less capture rate than the SSM predictions; it is only about 1/3 of the SSM prediction in Homestake experiment, and is about 60% in GALLEX, GNO, and SAGE experiments. This was historically called “solar neutrino deficit problem”.

Kamiokande and Super-Kamiokande experiments use the detectors of water-Cherenkov type. They can detect solar neutrinos via  $\nu e$  elastic scattering;

$$\nu_x e^- \rightarrow \nu_x e^- \quad , \quad (\text{A.7})$$

where  $\nu_x$  is  $\nu_e$ ,  $\nu_\mu$  or  $\nu_\tau$ , i.e. all active neutrinos. The energy threshold of Kamiokande and Super-Kamiokande experiments are 7 MeV and 5 MeV, respectively. Therefore, they detect pure  ${}^8\text{B}$  neutrinos because the contribution of  $hep$  neutrinos is negligibly small according to SSM. Both

**Table A.2:** Summary of the results from solar neutrino experiments and a comparison with the SSM predictions. The first four experiments use the radiochemical technique, and the others use the water-Cherenkov technique to observe solar neutrinos. The first and the second errors in the experimental results are statistical and systematic errors, respectively.

Experiment	$^{37}\text{Cl} \rightarrow ^{37}\text{Ar}$ (SNU) <sup>a</sup>	$^{71}\text{Ga} \rightarrow ^{71}\text{Ge}$ (SNU) <sup>a</sup>	$^8\text{B}$ $\nu$ flux ( $10^6 \text{cm}^{-2}\text{s}^{-1}$ )
Homestake [146]	$2.56 \pm 0.16 \pm 0.16$	—	—
GALLEX [147]	—	$77.5 \pm 6.2^{+4.3}_{-4.7}$	—
GNO [148]	—	$65.8^{+10.2+3.4}_{-9.6-3.6}$	—
SAGE [149]	—	$67.2^{+7.2+3.5}_{-7.0-3.0}$	—
Kamiokande [150]	—	—	$2.80 \pm 0.19 \pm 0.33^b$
Super-Kamiokande [151]	—	—	$2.32 \pm 0.03^{+0.08b}_{-0.07}$
SNO [152]	—	—	$1.76^{+0.06}_{-0.05} \pm 0.09^c$
	—	—	$2.39^{+0.24}_{-0.23} \pm 0.12^b$
	—	—	$5.09^{+0.44+0.46d}_{-0.43-0.43}$
BP2000 prediction	$7.6^{+1.3}_{-1.1}$	$128^{+9}_{-7}$	$5.05^{+1.01}_{-0.81}$

<sup>a</sup> SNU (Solar Neutrino Unit) =  $10^{-36}$  captures per atom per second.

<sup>b</sup> Flux measured via the neutral-current reaction.

<sup>c</sup> Flux measured via  $\nu e$  elastic scattering.

<sup>d</sup> Flux measured via the charged-current reaction.

experiments observed significantly less neutrino fluxes than what SSM predicts [150, 151], as well as the radiochemical experiments above. It was about a half flux of the prediction as shown in Table A.2.

SNO [153] is another experiment using water-Cherenkov type detector, started in 1999. The energy threshold in SNO is 5 MeV, as same as that in Super-Kamiokande. Therefore, SNO also measures the fluxes of  $^8\text{B}$  solar neutrinos. However, since SNO uses heavy water ( $\text{D}_2\text{O}$ ) instead of normal one ( $\text{H}_2\text{O}$ ), it can take advantage of measuring charged-current and neutral-current events as well as  $\nu e$  elastic scattering events, separately. The detectable reactions in SNO are

$$\nu_e d \rightarrow e^- p p \quad (\text{charged-current}) \quad (\text{A.8})$$

$$\nu_e d \rightarrow e^- p n \quad (\text{neutral-current}) \quad (\text{A.9})$$

in addition to the reaction of Eq. (A.7). The charged-current reaction is sensitive only to electron neutrinos, while the neutral-current reaction and elastic scattering are sensitive to all active neutrinos. The fluxes of charged-current ( $\phi^{\text{CC}}$ ), neutral-current ( $\phi^{\text{NC}}$ ), and elastic scattering ( $\phi^{\text{ES}}$ ) are separately measured using the differences of  $\cos \theta_\odot$  distributions among them, where  $\theta_\odot$  is the angle of events with respect to the direction from the Sun to the Earth. The results of SNO are as follows [152];

$$\phi_{\text{SNO}}^{\text{CC}} = \phi(\nu_e) = (1.76^{+0.06}_{-0.05} \pm 0.09) \times 10^6 \text{ cm}^{-2}\text{s}^{-1} \quad , \quad (\text{A.10})$$

$$\phi_{\text{SNO}}^{\text{ES}} = \phi(\nu_e) + 0.154\phi(\nu_{\mu,\tau}) = (2.39^{+0.24}_{-0.23} \pm 0.12) \times 10^6 \text{ cm}^{-2}\text{s}^{-1} \quad , \quad (\text{A.11})$$

$$\phi_{\text{SNO}}^{\text{NC}} = \phi(\nu_e) + \phi(\nu_{\mu,\tau}) = (5.09^{+0.44+0.46}_{-0.43-0.43}) \times 10^6 \text{ cm}^{-2}\text{s}^{-1} \quad . \quad (\text{A.12})$$

The fluxes  $\phi(\nu_e)$  and  $\phi(\nu_{\mu,\tau})$  deduced from these results are shown in Fig. A.4, as well as the SSM prediction. Here, if only each of  $\phi_{\text{SNO}}^{\text{CC}}$  and  $\phi_{\text{SNO}}^{\text{ES}}$  is considered, these fluxes are significantly less than the SSM prediction, as observed in other experiments. However, when  $\phi_{\text{SNO}}^{\text{NC}}$

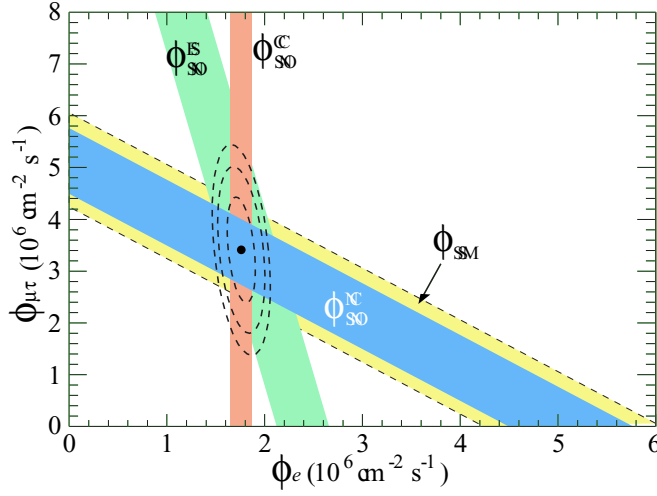


**Figure A.4:** The fluxes of  $^8\text{B}$  solar neutrino,  $\phi(\nu_e)$  and  $\phi(\nu_{\mu,\tau})$ , deduced from SNO measurements. The bands show the results of flux measurements for charged-current (CC), elastic scattering (ES), and neutral-current (NC) with  $1\sigma$  error. The band of SSM prediction is also presented. The contours show the 68%, 95%, and 99% joint probability for  $\phi(\nu_e)$  and  $\phi(\nu_{\mu,\tau})$ .

is considered, this flux represents the total flux of active neutrinos, and is remarkably consistent with the SSM prediction. These three fluxes together taken into account, the resultant  $\phi(\nu_{\mu,\tau}) = (3.41^{+0.45+0.48}_{-0.45-0.45}) \times 10^6 \text{ cm}^{-2}\text{s}^{-1}$ , providing the direct evidence for solar  $\nu_e$  flavor transition.

In addition to these flux measurements, the energy spectrum of recoil electrons and the fluxes were measured in the daytime and nighttime, separately. They are affected by the matter effect in the Earth, although no evidence of its effect has been found, so far [151, 154]. The global analysis combining the all results from the solar neutrino observations together strongly favors the  $\nu_e \rightarrow \nu_x$  oscillation with the MSW effect in the Sun. The allowed region of the  $\nu_e \rightarrow \nu_x$  oscillation parameters lies in  $(\sin^2 2\theta, \Delta m^2) = (0.64 - 0.97, (3 - 19) \times 10^{-5} \text{ eV}^2)$  in the Large Mixing Angle (LMA) region with 95% C.L. [155], as shown in Fig. A.5.

### A.3 Reactor neutrino experiments

Nuclear reactors are abundant sources of electron anti-neutrinos, which are created in nuclear  $\beta$ -decay of neutron rich fission products. The energy spectrum of reactor neutrinos is well-calculated. The average energy of the neutrinos is about 3 MeV, and the distribution extends up to about 8 MeV. The detectors are located at the distance of a few 10 m to 1 km from the reactor core, depending on experiments. Therefore, the sensitive region to  $\Delta m^2$  differs from  $10^{-3}$  to  $1 \text{ eV}^2$ , depending on its distance.

Up to now, several experiments such as CHOOZ [156], Palo Verde [157], Bugey [158], and so on, were performed using reactor neutrinos. These experiments used detectors filled with liquid scintillator\*. They measured reactor electron anti-neutrino via the inverse  $\beta$ -decay reaction;

$$\bar{\nu}_e p \rightarrow e^+ n \quad . \quad (\text{A.13})$$

The neutrino events were identified by the prompt signal of two 511 keV  $\gamma$ -rays from the positron ( $e^+$ ) annihilation followed by a delayed coincident signal of  $\gamma$ -ray from neutron ( $n$ ) capture onto a nuclear. The signal-to-background ratio was estimated by comparing the data with reactor-on and with reactor-off.

\*Krasnoyarsk experiment [159] used a detector of hexagonal prism filled with granulated polyethylene.



**Table A.3:** Summary of the results from reactor neutrino experiments. The limits on  $\Delta m^2$  and  $\sin^2 2\theta$  in the table are obtained by the analysis of the  $\bar{\nu}_e \rightarrow \bar{\nu}_x$  oscillation. The values of  $\Delta m^2$  and  $\sin^2 2\theta$  are respectively corresponding to those at  $\sin^2 2\theta = 1$  and at large  $\Delta m^2$  region with 90% C.L. In the Bugey experiment, the ratio of observed to expected  $\bar{\nu}_e$  events  $((\bar{\nu}_e)_{\text{obs}}/(\bar{\nu}_e)_{\text{exp}})$  are evaluated for each distance, while the limits on  $\Delta m^2$  and  $\sin^2 2\theta$  are derived from the data of all distance combined.

Experiment	Distance from Reactor	$(\bar{\nu}_e)_{\text{obs}}/(\bar{\nu}_e)_{\text{exp}}$	$\Delta m^2$ [eV <sup>2</sup> ]	$\sin^2 2\theta$
CHOOZ [156]	1.1 km	$1.01 \pm 0.028 \pm 0.027$	$< 0.0007$	$< 0.10$
Palo Verde [157]	0.75, 0.89 km	$1.01 \pm 0.024 \pm 0.053$	$< 0.0011$	$< 0.17$
Bugey [158]	15, 40, 95 m	—	$< 0.01$	$< 0.02$
	15 m	$0.988 \pm 0.004 \pm 0.05$	—	—
	40 m	$0.994 \pm 0.010 \pm 0.05$	—	—
	95 m	$0.915 \pm 0.132 \pm 0.05$	—	—
Gösgen [160, 161]	37.9, 45.9, 64.7 m	$1.05 \pm 0.02 \pm 0.05$	$< 0.019$	$< 0.21$
Rovno [162, 163]	18.3, 25.3 m	$0.985 \pm 0.018 \pm 0.034$	$< 0.04$	$< 0.2$
Krasnoyarsk [159]	57.0, 57.6, 231.4 m	—	$< 0.0075$	$< 0.15$
Savannah River [164]	18, 24 m	$0.987 \pm 0.006 \pm 0.037$	—	$< 0.24$

No experiment have found the evidence of  $\bar{\nu}_e$  disappearance, so far<sup>†</sup>. The excluded regions of  $\Delta m^2$  and  $\sin^2 2\theta$  provided by these experiments are shown in Fig. A.5 and also summarized in Table A.3. The most sensitive results around  $\Delta m^2 \sim 10^{-3} - 10^{-2}$  eV<sup>2</sup> are obtained by CHOOZ experiment. Assuming Eq. (1.16), CHOOZ provided the upper limit on  $\bar{\nu}_e \rightarrow \bar{\nu}_x$  oscillation to be  $\Delta m_{13}^2 < 7 \times 10^{-4}$  eV<sup>2</sup> at  $\sin^2 2\theta_{13} = 1$ , and  $\sin^2 2\theta_{13} < 0.10$  in large  $\Delta m_{13}^2$  region.

## A.4 Accelerator neutrino experiments

Accelerator-produced neutrinos are also available to explore neutrino oscillation. The advantage of the use of accelerator neutrinos is that the energy of neutrino is controllable. Several experiments were performed using neutrino beams with various energies. The experiments which give the most stringent results at present are briefly summarized below, as well as in Table A.4. The resulting excluded/allowed regions are also shown in Fig. A.5.

CHORUS [165] and NOMAD [166] experiments at CERN-SPS have searched for  $\nu_\tau$  events which is oscillated from  $\nu_\mu$ . The baseline of both experiments is about 800 m. Almost pure  $\nu_\mu$  beam with the average energy of about 25 GeV is used. Corresponding sensitive region to  $\Delta m^2$  is above about 1 eV<sup>2</sup>. CHORUS experiment used the emulsion target to identify the  $\tau$  decay by event topology, while NOMAD experiment used drift chambers and calorimeters to analyze  $\tau$  events by kinematic distributions. Both experiments found no evidence for the oscillation signal. The NOMAD experiment provided a constraint on  $\nu_\mu \rightarrow \nu_\tau$  oscillation to be  $\Delta m^2 < 0.7$  eV<sup>2</sup> at  $\sin^2 2\theta = 1$  and  $\sin^2 2\theta < 3.3 \times 10^{-4}$  for large  $\Delta m^2$ . The CHORUS experiment also gave similar constraint to what NOMAD gave.

The region of  $\Delta m^2$  between 0.3 and 100 eV<sup>2</sup> was explored by two old experiments, CDHSW [171] and CHARM [172], using  $\nu_\mu$  beam at CERN-PS. The average neutrino energy was 1 to 1.5 GeV. Each of them used two similar detectors. One was placed at 130 m downstream the production target, and other was placed at 770 m further downstream. The observed fluxes at near and

<sup>†</sup>Recently, at the end of 2002, KamLAND experiment, a reactor neutrino experiment with a baseline of about 180 km, provided the first evidence for the reactor electron anti-neutrino disappearance with the oscillation parameter of around  $\Delta m^2 \approx 6.9 \times 10^{-5}$  eV<sup>2</sup> [25]. This result is consistent with the solar LMA solution.



**Table A.4:** Summary of the results from accelerator neutrino experiments. The table is roughly sorted by sensitive regions of experiments to  $\Delta m^2$  in the upper, middle, and lower columns. The values for  $\sin^2 2\theta$  is expressed in the unit of  $10^{-3}$ . All the limits are with the confidence level of 90%. The CDHSW and CHARM experiments have two detectors at different distance, which corresponds to the two numbers of distance in the table.

Neutrino Energy	Distance from Neutrino Source	Oscillation Mode	$\Delta m^2$ [eV <sup>2</sup> ]	$\sin^2 2\theta$ [ $\times 10^{-3}$ ]
CHORUS (CERN) [165]				
$\langle E_\nu \rangle = 27$ GeV	$L = 0.82$ km	$\nu_\mu \rightarrow \nu_\tau$	$< 0.6$	$< 0.68$
		$\nu_e \rightarrow \nu_\tau$	$< 7.5$	$< 52$
NOMAD (CERN) [166]				
$\langle E_\nu \rangle = 24$ GeV	$L = 0.836$ km	$\nu_\mu \rightarrow \nu_\tau$	$< 0.7$	$< 0.33$
		$\nu_e \rightarrow \nu_\tau$	$< 5.9$	$< 15$
CCFR (FNAL) [167, 168, 169]				
$\langle E_\nu \rangle = 140$ GeV	$L = 1.4$ km	$\nu_\mu(\bar{\nu}_\mu) \rightarrow \nu_e(\bar{\nu}_e)$	$< 1.6$	$< 1.8$
		$\nu_\mu(\bar{\nu}_\mu) \rightarrow \nu_\tau(\bar{\nu}_\tau)$	$< 1.4$	$< 8.1$
		$\nu_e(\bar{\nu}_e) \rightarrow \nu_\tau(\bar{\nu}_\tau)$	$< 17$	$< 210$
NuTeV (FNAL) [170]				
$\langle E_\nu \rangle = 140$ GeV	$L = 1.4$ km	$\nu_\mu(\bar{\nu}_\mu) \rightarrow \nu_e(\bar{\nu}_e)$	$< 2.6$	$< 1.1$
CDHSW (CERN) [171]				
$\langle E_\nu \rangle = 1.5$ GeV	$L = 0.13, 0.9$ km	$\nu_\mu \rightarrow \nu_\mu$	$< 0.23$ or $> 100^a$	$< 100$
CHARM (CERN) [172]				
$\langle E_\nu \rangle = 1.5$ GeV	$L = 0.13, 0.9$ km	$\nu_\mu \rightarrow \nu_\mu$	$< 0.29$ or $> 22^a$	$< 170$
		$\nu_\mu \rightarrow \nu_e$	$< 0.19$	$< 80$
BNL-E776 (BNL) [173]				
$E_\nu^{\text{peak}} = 1$ GeV <sup>b</sup>	$L = 1$ km	$\nu_\mu(\bar{\nu}_\mu) \rightarrow \nu_e(\bar{\nu}_e)$	$< 0.075$	$< 30$
KARMEN (Rutherford) [174, 175]				
$E_\nu < 52.8$ MeV <sup>c</sup>	$L = 0.018$ km	$\bar{\nu}_\mu \rightarrow \bar{\nu}_e$	$< 0.055$	$< 1.7$
		$\nu_e \rightarrow \nu_\tau$	$< 0.77$	$< 338$
LSND (LAMPF) [176, 177]				
$E_\nu < 52.8$ MeV <sup>c</sup>	$L = 0.030$ km	$\bar{\nu}_\mu \rightarrow \bar{\nu}_e$	$0.03 - 0.05$	$3.8 - 14$
		$\nu_\mu \rightarrow \nu_e$	$0.03 - 0.3$	$0.5 - 30$

<sup>a</sup> Since the near detector, as well as far detector, sees the effect of neutrino oscillation for large  $\Delta m^2$ , and the difference of the flux between near and far detectors becomes smaller, such analysis that compares observations in near and far detectors usually lose the sensitivity in large  $\Delta m^2$  region.

<sup>b</sup> The energy spectrum of neutrino in BNL-E776 is wide band and it extends up to about 10 GeV, having a peak around 1 GeV.

<sup>c</sup> Neutrinos are created in the decay of pions and muons at rest. Therefore, neutrinos from the pion decay have a monochromatic energy of 29.8 MeV, and neutrinos from the muon decay have energy described by Michel spectrum which have a endpoint at 52.8 MeV.

far sites were compared to each other, and no evidence for  $\nu_\mu$  disappearance was found. The region excluded by CDHSW is  $0.23 < \Delta m^2 < 100 \text{ eV}^2$  at  $\sin^2 2\theta = 1$  and  $\sin^2 2\theta > 0.05$  at  $\Delta m^2 = 0.3 \text{ eV}^2$  with the confidence level of 90%, as shown in the lower left figure of Fig. A.5.

KARMEN [174, 175], and LSND [176, 177] experiments explored rather lower  $\Delta m^2$  region, down to around  $0.1 \text{ eV}^2$ , in  $\bar{\nu}_\mu \rightarrow \bar{\nu}_e$  mode. They used neutrinos produced in the decay of muons at rest. Therefore, neutrino energy distributes in the region less than 52.8 MeV, which is described by well-known Michel spectrum. The baseline of KARMEN and LSND was 18 m and 30 m, respectively. They both had the capability to identify  $\bar{\nu}_e$  events by looking at the signals of  $e^+$  from  $\bar{\nu}_e p \rightarrow e^+ n$  and subsequent  $\gamma$ -ray from neutron capture. The LSND reported the positive evidence for  $\bar{\nu}_e$  appearance with an oscillation probability of  $(0.264 \pm 0.067 \pm 0.045)\%$  [177]. This result provided the allowed region of oscillation parameters for  $\bar{\nu}_\mu \rightarrow \bar{\nu}_e$  mode to be  $0.03 < \Delta m^2 < 0.05 \text{ eV}^2$  at  $\sin^2 2\theta = 1$  and  $0.0038 < \sin^2 2\theta < 0.14$  for large  $\Delta m^2$  region with 90% C.L., as shown in Fig. A.5. On the contrary, KARMEN found no indication of oscillation signal, and excluded large part of allowed region given by LSND. CCFR [167] and NuTeV [170] also performed the oscillation analysis in  $\nu_\mu(\bar{\nu}_\mu) \rightarrow \nu_e(\bar{\nu}_e)$  mode for little bit larger  $\Delta m^2$  region. However they could not find any evidence for oscillation to result in excluding almost all part of LSND allowed band above  $\Delta m^2 = 60 \text{ eV}^{2\dagger}$ . All the experimental results above combined, the remaining allowed  $(\sin^2 2\theta, \Delta m^2)$  space of LSND for  $\nu_\mu \rightarrow \nu_e$  is a slanting narrow band region which lying between about  $(4 \times 10^{-2}, 0.2 \text{ eV}^2)$  and  $(3 \times 10^{-3}, 1 \text{ eV}^2)$  with the confidence level of 90% [179].

---

<sup>†</sup>Recently, NOMAD experiment also performed  $\nu_\mu \rightarrow \nu_e$  analysis. No evidence for oscillation was found, and a part of the LSND allowed band above  $\Delta m^2 = 10 \text{ eV}^2$  has been excluded [178].

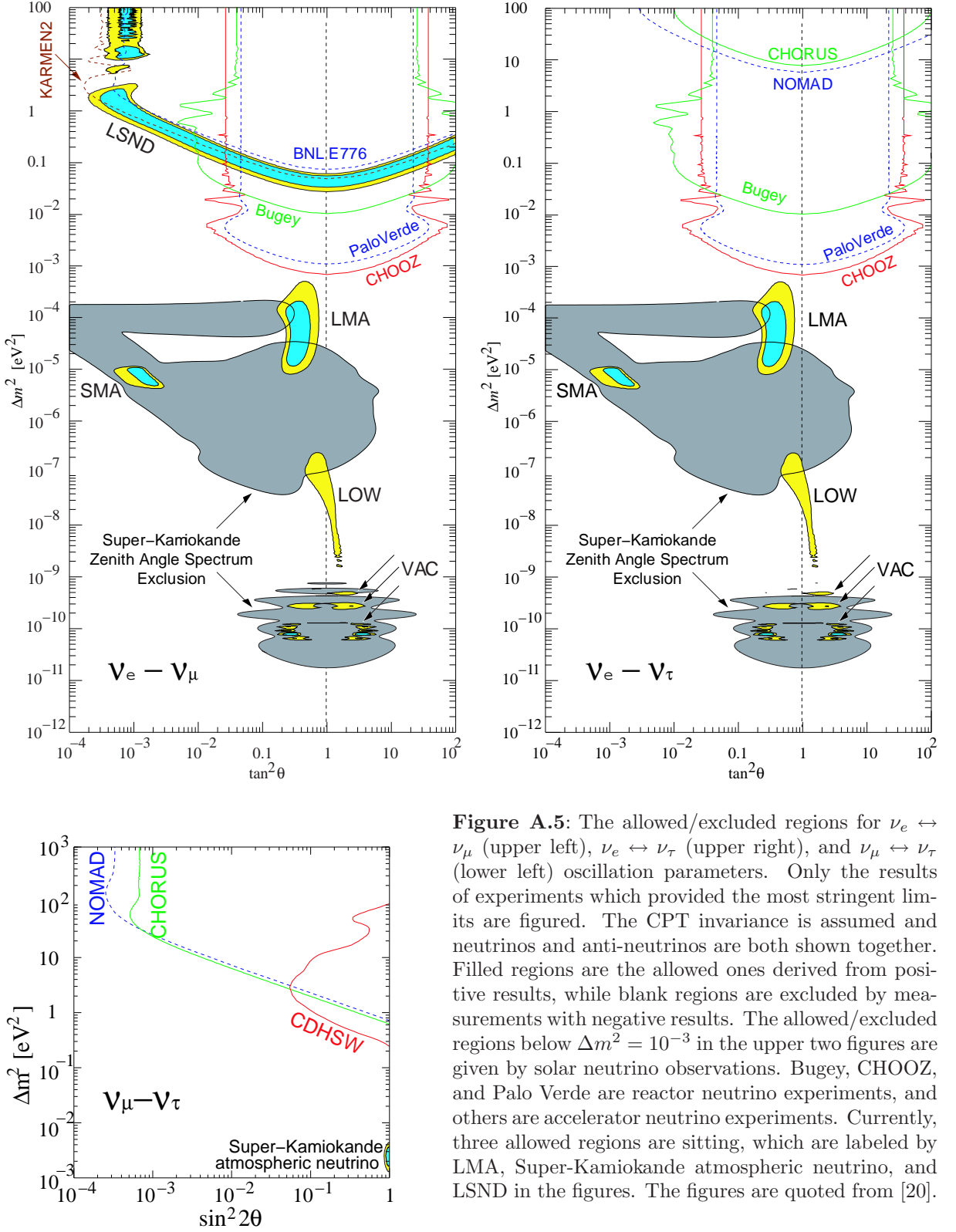


**Figure A.5:** The allowed/excluded regions for  $\nu_e \leftrightarrow \nu_\mu$  (upper left),  $\nu_e \leftrightarrow \nu_\tau$  (upper right), and  $\nu_\mu \leftrightarrow \nu_\tau$  (lower left) oscillation parameters. Only the results of experiments which provided the most stringent limits are figured. The CPT invariance is assumed and neutrinos and anti-neutrinos are both shown together. Filled regions are the allowed ones derived from positive results, while blank regions are excluded by measurements with negative results. The allowed/excluded regions below  $\Delta m^2 = 10^{-3}$  in the upper two figures are given by solar neutrino observations. Bugey, CHOOZ, and Palo Verde are reactor neutrino experiments, and others are accelerator neutrino experiments. Currently, three allowed regions are sitting, which are labeled by LMA, Super-Kamiokande atmospheric neutrino, and LSND in the figures. The figures are quoted from [20].



# Appendix B

## Event Reconstruction in Water Cherenkov Detectors

In the analysis of 1KT and SK, selected events are reconstructed by following procedures in order, which are almost the same in 1KT and SK.

- (1) Vertex finding (auto-fit)
- (2) Ring counting
- (3) Particle identification (PID)
- (4) Precise vertex finding (MS-fit)
- (5) Momentum determination
- (6) Correction to the number of rings (ring correction)
- (7) Correction to the number of rings for the events in 1KT (ring correction II)

The procedures above are applied to all the event remaining after the event reduction, and the number of Cherenkov rings, and the direction, the particle type, and the momentum of each ring in each event are obtained.

### B.1 Vertex finding (auto-fit)

First, the vertex position is reconstructed using the timing information of hit PMTs. The vertex finding of this step is called “auto-fit”. The vertex finding algorithm of auto-fit consists of three steps.

#### B.1.1 Point-fit

Vertex position of each event is roughly estimated in the first step assuming all the photons are emitted from a point source at the same time. The time of flight of photon is subtracted from the hit timing of each PMT. The residual time of each PMT  $t_i$  is calculated by

$$t_i = t_i^0 - \frac{n}{c} \times |\vec{P}_i - \vec{O}| \quad , \quad (\text{B.1})$$

where  $t_i^0$  and  $\vec{P}_i$  is the hit timing and the position of  $i$ -th PMT,  $n$  is the refractive index of water,  $c$  is the velocity of light, and the vertex point is assumed to be  $\vec{O}$ . The position  $\vec{O}$  is searched

so that the distribution of  $t_i$  becomes sharp peak since all the hit PMTs should have similar  $t_i$  values when  $\vec{O}$  is at the true vertex. This vertex reconstruction algorithm is called “point-fit”. The estimator for the goodness of the fit is defined as

$$G_p = \frac{1}{N} \sum_i^N \exp \left( -\frac{(t_i - t_0)^2}{2(1.5 \times \sigma)^2} \right) \quad , \quad (\text{B.2})$$

where  $N$  is the number of hit PMTs,  $t_0$  is the mean value of  $t_i$ , and  $\sigma$  is the time resolution of PMT taken to be 2.5 nsec. The numerical factor 1.5 is chosen to optimize the fitter performance. The vertex point  $\vec{O}$  is determined so that it gives the maximum value of  $G_p$ .

The particle direction is also roughly estimated by summing up the charge weighted vector over all hit PMTs:

$$\vec{d}_0 = \sum_i^N q_i \times \frac{\vec{P}_i - \vec{O}_0}{|\vec{P}_i - \vec{O}_0|} \quad , \quad (\text{B.3})$$

where  $\vec{d}_0$  is the estimated particle direction,  $\vec{O}_0$  is the vertex point obtained by the point-fit, and  $q_i$  is the detected charge by  $i$ -th PMT.

The vertex point and the particle direction obtained here are used in the next step.

### B.1.2 Ring edge search

The direction of particle and the outer edge of the dominant Cherenkov ring is estimated in this step. In order to determine them, an estimator  $Q(\theta_{\text{edge}})$  is defined as follows:

$$Q(\theta_{\text{edge}}) = \frac{\int_0^{\theta_{\text{edge}}} \text{PE}(\theta) d\theta}{\sin \theta_{\text{edge}}} \times \left( \frac{d \text{PE}(\theta)}{d\theta} \bigg|_{\theta=\theta_{\text{edge}}} \right)^2 \times \exp \left( -\frac{(\theta_{\text{edge}} - \theta_{\text{exp}})^2}{2\sigma_\theta^2} \right) \quad , \quad (\text{B.4})$$

where  $\theta_{\text{exp}}$  and  $\sigma_\theta$  are the opening angle of Cherenkov ring expected from the charge within the cone and its resolution, respectively, and  $\text{PE}(\theta)$  is the distribution of the observed charge as a function of the opening angle  $\theta$  with respect to the particle direction. The effect of the water transparency and the PMT acceptance on the observed charge are corrected in this expression. The direction of particle is changed around  $\vec{d}_0$  so that the  $Q(\theta_{\text{edge}})$  is maximized. The angle of ring edge  $\theta_{\text{edge}}$  is determined to satisfy the following two conditions:

- (1)  $\theta_{\text{edge}} > \theta_{\text{peak}}$ , where  $\theta_{\text{peak}}$  is the angle at which the  $\text{PE}(\theta)$  takes its maximum.
- (2)  $\frac{d^2 \text{PE}(\theta)}{d\theta^2} \bigg|_{\theta=\theta_{\text{edge}}} = 0$ .

Fig. B.1 shows a typical distribution of  $\text{PE}(\theta)$  and its second derivative. The edge of the dominant Cherenkov ring in a event is found as pointed in the figure.

### B.1.3 TDC-fit

The vertex point and the particle direction are determined more precisely in this step by TDC-fit. Here the track length of the charged particle and the scattered Cherenkov photons are taken into account in the TDC-fit, while a point-like light source is assumed in the point-fit.

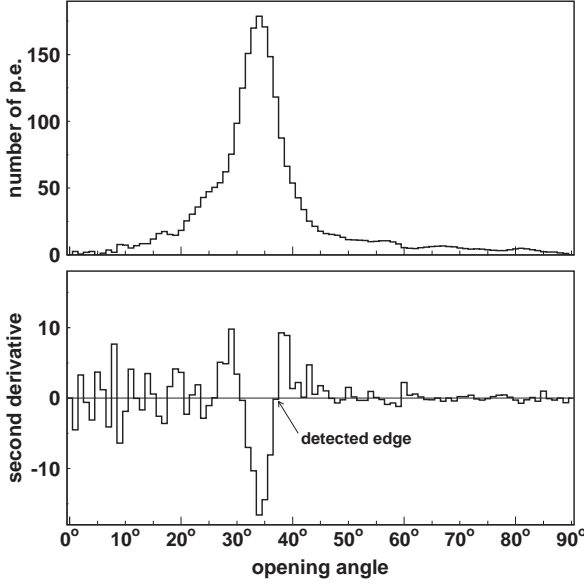


**Figure B.1:** A typical distribution of  $PE(\theta)$  (upper figure) and its second derivative (lower figure). The edge of dominant Cherenkov ring is found as pointed in the lower figure.

The time residual of the  $i$ -th PMT,  $t_i$ , is defined by

$$t_i = \begin{cases} t_i^0 - \frac{1}{c} \times |\vec{X}_i - \vec{O}| - \frac{n}{c} \times |\vec{P}_i - \vec{X}_i| & \text{for PMTs inside the Cherenkov ring} \\ t_i^0 - \frac{n}{c} \times |\vec{P}_i - \vec{O}| & \text{for PMTs outside the Cherenkov ring} \end{cases} \quad (\text{B.5})$$

where  $\vec{O}$  is assumed vertex point which is fitted in this step,  $\vec{X}_i$  is the position at which Cherenkov photons are emitted toward the  $i$ -th PMT. The definition of other symbols are the same as before.

The estimator of the TDC-fit is consist of three different estimators. Depending on the location of hit PMTs and their hit timing, one estimator is chosen to be used for each PMT.

For the hit PMTs located inside the Cherenkov ring, the estimator  $G_I$  is defined by

$$G_I = \sum_i \frac{1}{\sigma_i^2} \exp \left( -\frac{(t_i - t_0)^2}{2(1.5 \times \sigma)^2} \right) \quad , \quad (\text{B.6})$$

where  $\sigma_i$  is the time resolution of the  $i$ -th PMT depending on the detected number of photoelectrons,  $\sigma$  is the time resolution for the average number of photoelectrons of all hit PMTs, and  $t_0$  is the mean time residual.

For the hit PMTs outside the Cherenkov ring, the definition of the estimator changes depending on the time residual of each PMT. In the case of the hit timing is later than  $t_0$ , the contribution of scattered photons are also considered in addition to the direct Cherenkov light. The definition of estimators is as follows:

$$\begin{aligned} G_{O1} &= \sum_i \frac{1}{\sigma_i^2} \left[ \exp \left( -\frac{(t_i - t_0)^2}{2(1.5 \times \sigma)^2} \right) \times 2 - 1 \right] && \text{for } t_i \leq t_0 \\ G_{O2} &= \sum_i \frac{1}{\sigma_i^2} \left[ \max \left( \exp \left( -\frac{(t_i - t_0)^2}{2(1.5 \times \sigma)^2} \right), G_{\text{scat}}(t_i, t_0) \right) \times 2 - 1 \right] && \text{for } t_i > t_0 \end{aligned} \quad (\text{B.7})$$

where the estimator for the scattered photons,  $G_{\text{scat}}(t_i, t_0)$ , is

$$G_{\text{scat}}(t_i, t_0) = \frac{R_q}{1.5^2} \cdot \exp \left( -\frac{(t_i - t_0)^2}{2(1.5 \times \sigma)^2} \right) + \left( 1 - \frac{R_q}{1.5^2} \right) \cdot \exp \left( -\frac{t_i - t_0}{60 \text{ nsec}} \right) \quad . \quad (\text{B.8})$$

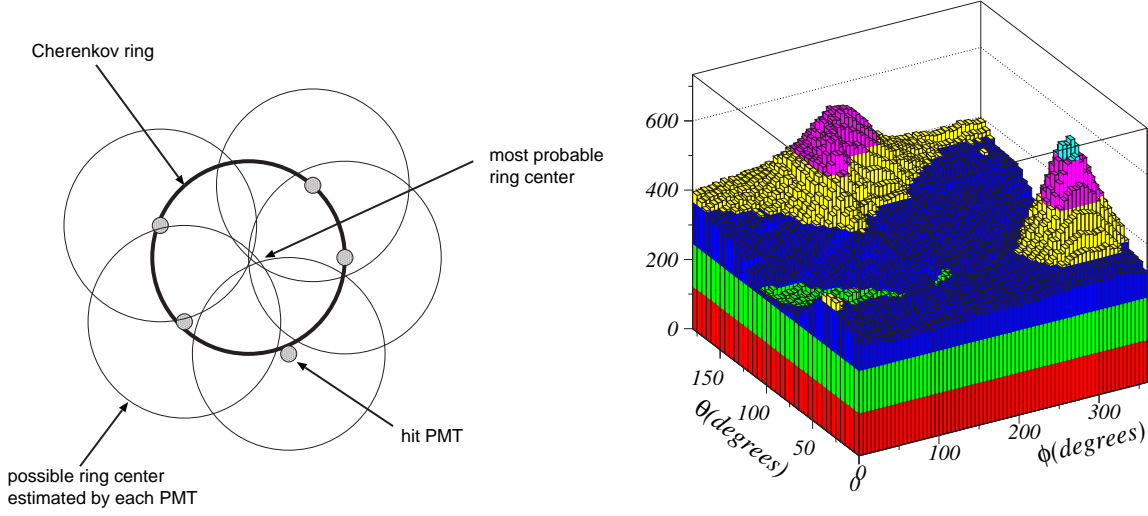


**Figure B.2:** The basic idea of the ring candidate search (left) and a typical charge of Cherenkov rings derived by Hough transformation. Left figure: The point where the most of the circles for possible center are intersecting is recognized as the direction of a Cherenkov ring. Right figure: Peaks in the charge map is corresponding to the possible Cherenkov ring direction with respect to the vertex point.

In this expression,  $R_q$  is the fraction of the charge detected inside the Cherenkov ring, and the numerical factors are chosen to optimize the performance of the fitter.

Then the whole estimator of the TDC-fit is defined as

$$G_{\text{TDC}} = \frac{G_I + G_{O1} + G_{O2}}{\sum_i \frac{1}{\sigma_i^2}} . \quad (\text{B.9})$$

The vertex point and the direction of particle are determined to maximize this estimator.

## B.2 Ring counting

With the knowledge of the vertex point found in the auto-fit, the ring counting algorithm determines the number of Cherenkov rings and the direction of each ring.

### B.2.1 Ring candidate search

The algorithm starts the ring candidate search. First, the expected charge from the Cherenkov ring found in the vertex fitting is subtracted from the charge of each PMT. Then we use a pattern recognition method called ‘‘Hough transformation’’ [180]. Left figure in Fig. B.2 illustrates the basic idea of the ring candidate search. A spherical coordinate centered on the vertex point is considered so that the direction of each Cherenkov ring or PMT is considered to be a point on the sphere. Assuming the opening angle of Cherenkov ring to be  $42^\circ$ , possible ring direction is estimated using a certain hit PMT by drawing the virtual circle with its center being at the PMT and its radius corresponding to  $42^\circ$  opening angle (thin circles in Fig. B.2). The point



where the most of the circles estimated by all hit PMTs are intersecting is recognized as the direction of a Cherenkov ring.

In the practical case, a Hough space is defined using the polar angle  $\Theta$  and the azimuthal angle  $\Phi$  with respect to the reconstructed vertex. Instead of drawing the virtual circles, the expected charge distribution  $f(\theta)$  weighted with the observed charge of each hit PMT is mapped onto the  $(\Theta, \Phi)$  space, where  $\theta$  is the angle between the direction to the PMT under consideration and to each  $(\Theta, \Phi)$  point seen from the vertex. This operation is applied to all the hit PMTs. As a result of this Hough transformation, a possible ring center becomes visible as a peak of charge on the map. Right figure in Fig. B.2 shows a typical charge map derived by this operation, where two peaks can be seen as candidates of ring direction.

### B.2.2 Ring candidate test

Next, the ring candidates are tested using a likelihood method. Supposing  $N$  rings are already found in an event, the test for the  $(N+1)$ -th ring candidate is carried out by comparing two likelihoods; the likelihood  $\mathcal{L}_{N+1}$  for the assumption that the event has  $N+1$  rings including this candidate and the likelihood  $\mathcal{L}_N$  for the assumption that the event has only  $N$  rings which are already found. The likelihood function for the assumption of  $N+1$  rings is defined as

$$\mathcal{L}_{N+1} = \sum_i \log \left( \text{prob} \left( q_i^{\text{obs}}, q_i^{\text{exp}} = \sum_{n=1}^{N+1} \alpha_n \cdot q_{i,n}^{\text{exp}} \right) \right) , \quad (\text{B.10})$$

where  $q_i^{\text{obs}}$  is the observed number of photoelectron in  $i$ -th PMT,  $\alpha_n \cdot q_{i,n}^{\text{exp}}$  is the expected number of photoelectron in  $i$ -th PMT which photon originates from the  $n$ -th Cherenkov ring, and the summation for  $i$  is performed over the PMTs inside the  $(N+1)$ -th Cherenkov ring. The scale factors  $\alpha_n$  ( $n=1, \dots, N+1$ ) are selected to maximize the  $\mathcal{L}_{N+1}$ . The probability function,  $\text{prob}(q_i^{\text{obs}}, q_i^{\text{exp}})$ , is defined as

$$\text{prob}(q_i^{\text{obs}}, q_i^{\text{exp}}) = \begin{cases} \frac{1}{\sqrt{2\pi}\sigma} \exp \left( -\frac{(q_i^{\text{obs}} - q_i^{\text{exp}})^2}{2\sigma^2} \right) & (\text{for } q_i^{\text{exp}} > 20 \text{ p.e.}) \\ \text{convolution of single p.e. distribution} & \\ \text{and a Poisson distribution} & (\text{for } q_i^{\text{exp}} < 20 \text{ p.e.}) \end{cases} \quad (\text{B.11})$$

where  $\sigma$  is the resolution for  $q_i^{\text{exp}}$ .

In the case of that there is no candidate which satisfies  $\mathcal{L}_{N+1} \geq \mathcal{L}_N$ , the number of rings in this event is determined to be  $N$ . For the ring candidate with  $\mathcal{L}_{N+1} \geq \mathcal{L}_N$ , the following four estimators for the goodness of the ring are calculated:

- $\mathcal{F}_1$  : The difference  $\mathcal{L}(N+1) - \mathcal{L}(N)$  corrected for the total photoelectrons.
- $\mathcal{F}_2$  : The average of the expected photoelectrons in PMTs located around the edge of  $(N+1)$ -th ring,  $Q_{\text{edge}}$ , where the PMTs overlapped with other  $N$  rings are not taken into account to make  $Q_{\text{edge}}$ .
- $\mathcal{F}_3$  : The average of the expected from  $(N+1)$ -th ring,  $Q_{\text{out}}$ , calculated over the PMTs located outside the  $(N+1)$ -th ring and off the others  $N$  rings. The difference  $Q_{\text{edge}} - Q_{\text{out}}$  is used in the estimator.
- $\mathcal{F}_4$  : The residual photoelectrons from the expected photoelectrons with the  $N$  rings assumption are used. The total amount of the residual p.e.s is calculated as

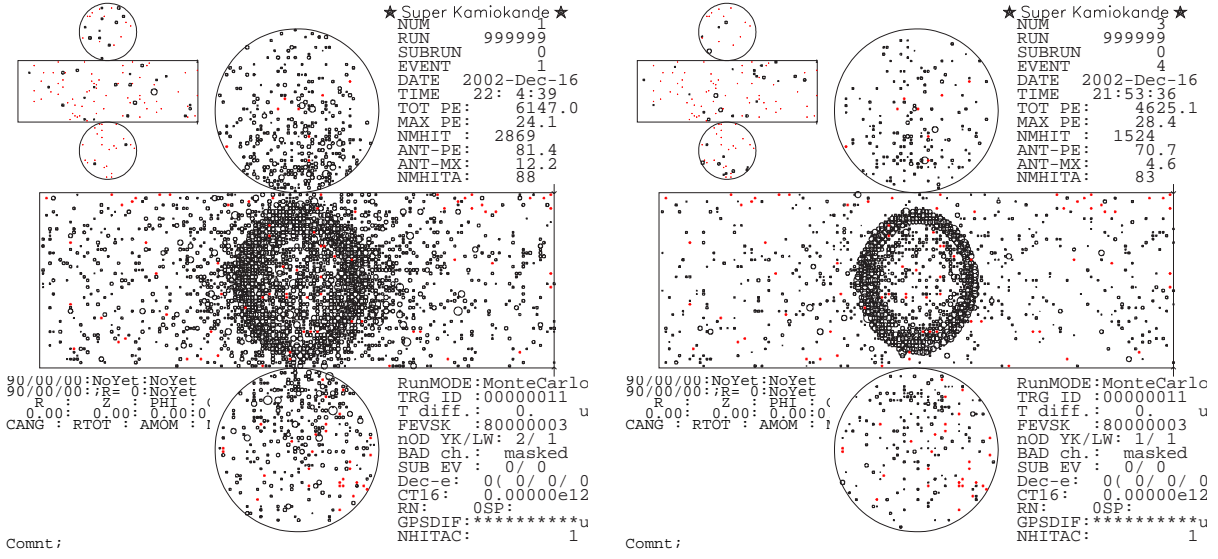


**Figure B.3:** Typical Cherenkov ring images for an electron event (left) and a muon event (right). The ring produced by an electron have diffuse edge while that produced by an muon have sharp edge. These events are generated by the Super-Kamiokande detector simulation, in which an electron and an muon with their momentum of 700 MeV/c is injected horizontally from the center of the detector.

$|\sum q_i^{\text{res}} \cdot \vec{e}_i|$ , where  $\vec{e}_i$  is a unit vector from the reconstructed vertex to the  $i$ -th PMT.

These estimators have large values if the candidate is probable. The final estimator to test the ring candidate is made as the linear sum of  $\mathcal{F}_1$ ,  $\mathcal{F}_2$ ,  $\mathcal{F}_3$ , and  $\mathcal{F}_4$  with some weight:

$$\mathcal{F} = w_1 \cdot \mathcal{F}_1 + w_2 \cdot \mathcal{F}_2 + w_3 \cdot \mathcal{F}_3 + w_4 \cdot \mathcal{F}_4 \quad (\text{B.12})$$

where the weights  $w_i$  ( $i=1, 2, 3, 4$ ) are optimized to have the good performance. If there are no candidate which satisfies  $\mathcal{F} \geq 0$ , the number of rings in this event is finally determined to be  $N$ . If there exists the candidate satisfying  $\mathcal{F} \geq 0$ , it is regarded to be the  $(N+1)$ -th ring, and the candidate search for the  $(N+2)$ -th ring starts.

### B.3 Particle identification (PID)

The particle identification (PID) algorithm classifies Cherenkov rings into two types, a showering type ( $e$ -like) and non-showering type ( $\mu$ -like). Fig. B.3 shows typical Cherenkov images for an electron event and for a muon event. As shown in the figure, the Cherenkov ring from an electron or a gamma-ray has a diffuse edge since such a ring is made of Cherenkov photons from multiple particle produced in an electro-magnetic showering process. On the other hand, a muon or a pion produces a sharper ring caused by single charged particle. The PID algorithm uses this feature of Cherenkov ring patterns. In addition, since a muon or a pion with a lower momentum has its velocity ( $\beta$ ) smaller apart from unity, the opening angle of its Cherenkov ring gets smaller, whereas it does not occur down to very low energy in the case of an electron or a gamma-ray. The PID algorithm also uses this difference in the opening angles. The observed pattern of the photoelectron distribution is compared with the expected ones for an electron and a muon, and then one of two types which matches better is selected for the PID of the ring.

### B.3.1 Expected charge distribution

#### Expected charge distribution for an electron

The expected charge distribution for an electron is made by the Monte Carlo simulation. In practical case, we create the angular distribution of the expected photoelectrons reaching the circular area of 50 cm diameter on the virtual surface of a sphere of 16.9 m radius centered on the vertex point, which distribution is given as a function of the opening angle and the electron momentum,  $Q_e^{\text{exp}}(p, \theta)$ . Using  $Q_e^{\text{exp}}(p, \theta)$ , expected photoelectrons for the  $i$ -th PMT from the  $n$ -th ring is calculated as

$$q_{i,n}^{\text{exp}}(e) = \alpha_n(e) \times Q_e^{\text{exp}}(p_n, \theta_{i,n}) \times \left(\frac{R}{r_i}\right)^{1.5} \times \frac{1}{\exp(r_i/L)} \times f(\Theta_i) \quad , \quad (\text{B.13})$$

where

- $q_{i,n}^{\text{exp}}(e)$  : expected p.e.s for the  $i$ -th PMT from the  $n$ -th ring with assumption that the particle producing the  $n$ -th ring is an electron.
- $\alpha_n(e)$  : normalization factor.
- $\theta_{i,n}$  : opening angle between the  $i$ -th PMT direction and the  $n$ -th ring direction.
- $r_i$  : distance from the vertex to the  $i$ -th PMT.
- $R$  : radius of the virtual sphere, 16.9 m.
- $L$  : light attenuation length in water.
- $f(\Theta_i)$  : correction function for the PMT acceptance as a function of the photon incident angle  $\Theta_i$ .

The factor  $(R/r_i)^{1.5}$  comes from the distance dependence of the light intensity.

#### Expected charge distribution for a muon

The expected distribution of photoelectrons for a muon is analytically calculated as

$$q_{i,n}^{\text{exp}}(\mu) = \left( \alpha_n(\mu) \times \frac{\sin^2 \theta_{i,n}}{r_i \left( \sin \theta_{i,n} + r_i \cdot \frac{d\theta}{dx} \Big|_{x=x_i} \right)} + q_{i,n}^{\text{knock}} \right) \times \frac{1}{\exp(r_i/L)} \times f(\Theta_i) \quad , \quad (\text{B.14})$$

where

- $q_{i,n}^{\text{exp}}(\mu)$  : expected photoelectrons for the  $i$ -th PMT from the  $n$ -th ring with assumption that the particle producing the  $n$ -th ring is a muon.
- $\alpha_n(\mu)$  : normalization factor.
- $q_{i,n}^{\text{knock}}$  : expected photoelectrons for the  $i$ -th PMT from knock-on electrons.
- $x$  : distance from the initial vertex position along the muon trajectory.
- $x_{i,n}$  : distance from the initial vertex position to the muon position where Cherenkov photons are emitted toward the  $i$ -th PMT

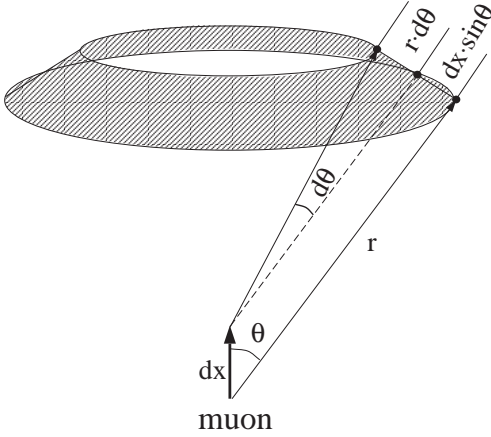


**Figure B.4:** A schematic view of the Cherenkov radiation from a muon. Cherenkov photons are emitted to the area of  $2\pi r \sin \theta (dx \sin \theta + r d\theta)$  while a muon travels the distance of  $dx$ .

$\theta$  : Cherenkov opening angle of the muon traversing at  $x$ .

$\theta_{x_{i,n}}$  : Cherenkov opening angle of the muon traversing at  $x = x_{i,n}$ .

In this expression, the term  $\sin^2 \theta$  comes from the angular dependence of the Cherenkov light intensity, and the term  $r(\sin \theta + r(d\theta/dx))$  comes from the area to which the Cherenkov photons are emitted. As shown in Fig. B.4, a muon emits Cherenkov photons toward the area of  $2\pi r \sin \theta (dx \sin \theta + r d\theta)$  while it travels the distance of  $dx$  with decreasing the Cherenkov angle due to the ionization energy loss of muon in the water.

### B.3.2 Estimation of the particle type

The estimation of the particle type for each ring by the Cherenkov ring pattern information is performed using likelihood functions defined as

$$\mathcal{L}_n(e \text{ or } \mu) = \prod_i \text{prob} \left( q_i^{\text{obs}}, q_{i,n}^{\text{exp}}(e \text{ or } \mu) + \sum_{n' \neq n} q_{i,n'}^{\text{exp}} \right), \quad (\text{B.15})$$

where  $q_i^{\text{obs}}$  is the observed photoelectrons in  $i$ -th PMT,  $q_{i,n}^{\text{exp}}(e \text{ or } \mu)$  is the expected photoelectrons of  $i$ -th PMT from the  $n$ -th ring with an assumption that the particle producing the ring is an electron (Eq. (B.13)) or a muon (Eq. (B.14)),  $q_{i,n'}^{\text{exp}}$  is the expected photoelectron of  $i$ -th PMT from the  $n'$ -th ring without particle type assumption, and the probability function  $\text{prob}(q^{\text{obs}}, q^{\text{exp}})$  is the same one as is used in Eq. (B.11) in the ring counting algorithm. The product in Eq. (B.15) is done over the PMTs inside the  $n$ -th ring. The expected photoelectrons  $q_{i,n}^{\text{exp}}(e)$  and  $q_{i,n}^{\text{exp}}(\mu)$  are selected to maximize  $\mathcal{L}_n(e)$  and  $\mathcal{L}_n(\mu)$ , respectively, by changing the direction and the opening angle of the  $n$ -th Cherenkov ring. Then the likelihood using the ring pattern information is translated into a  $\chi^2$  parameters as

$$\chi_n^2(e \text{ or } \mu) = -2 \log \mathcal{L}_n(e \text{ or } \mu) - \text{constant}, \quad (\text{B.16})$$

and the probability to detect  $q_i^{\text{obs}}$  in each PMT is calculated by

$$\mathcal{P}_n^{\text{pattern}}(e \text{ or } \mu) = \exp \left( - \frac{(\chi_n^2(e \text{ or } \mu) - \min[\chi_n^2(e), \chi_n^2(\mu)])^2}{2\sigma_{\chi_n^2}^2} \right), \quad (\text{B.17})$$

where the resolution of the  $\chi_n^2$  distribution is approximated to be  $\sigma_{\chi_n^2} = \sqrt{2N}$  using the number of PMTs ( $N$ ) used in the likelihood calculation in Eq. (B.15).

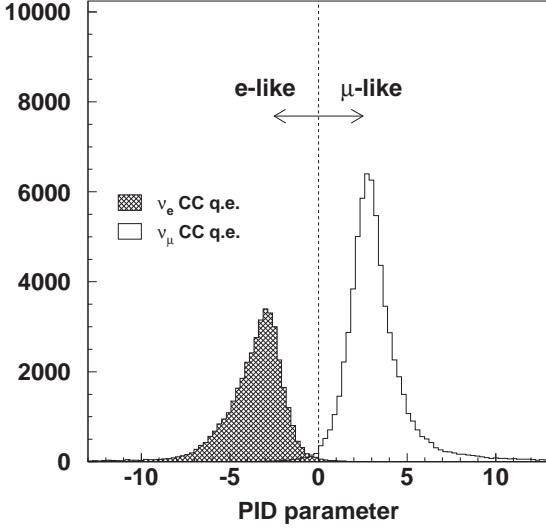


**Figure B.5:** The distribution of the PID estimator for fully-contained (FC) single-ring events. The hatched (blank) histogram is for the CC-qe events of electron (muon) neutrinos in which event only an electron (a muon) is expected to be visible. Clear separation between the electron events and the muon events can be seen. These histograms are estimated by a Monte Carlo simulation used in Super-Kamionande.

The probability using the information of the opening angle of the Cherenkov ring is calculated by

$$\mathcal{P}_n^{\text{angle}}(e \text{ or } \mu) = \exp\left(-\frac{(\theta_n^c - \theta_n^{\text{exp}}(e \text{ or } \mu))^2}{2(\delta\theta_n)^2}\right) \quad , \quad (\text{B.18})$$

where  $\theta_n^c \pm \delta\theta_n$  is the reconstructed opening angle of the  $n$ -th ring, and  $\theta_n^{\text{exp}}(e \text{ or } \mu)$  is the expected Cherenkov angle of the  $n$ -th ring calculated from the estimated momentum with an assumption that the particle producing the ring is an electron or a muon.

Finally, the total probability is defined as

$$\begin{aligned} \mathcal{P}_1(e \text{ or } \mu) &= \mathcal{P}_1^{\text{pattern}}(e \text{ or } \mu) \times \mathcal{P}_1^{\text{angle}}(e \text{ or } \mu) && \text{for single-ring events} \\ \mathcal{P}_n(e \text{ or } \mu) &= \mathcal{P}_n^{\text{pattern}}(e \text{ or } \mu) && \text{for multi-ring events} \end{aligned} \quad (\text{B.19})$$

where the probability estimated by only the pattern information ( $\mathcal{P}_n^{\text{pattern}}$ ) is used for multi-ring events since the estimation of the opening angle works relatively worse in the case of multi-ring events.

We usually use the estimator of the particle identification in the following form;

$$\mathcal{P}_n = \sqrt{-\log \mathcal{P}_n(\mu)} - \sqrt{-\log \mathcal{P}_n(e)} \quad , \quad (\text{B.20})$$

where  $\mathcal{P}_n < 0$  ( $\mathcal{P}_n > 0$ ) stands for  $e$ -like ( $\mu$ -like) ring. Fig. B.5 shows the PID likelihood distribution for single ring events ( $\mathcal{P}_1$ ) estimated by a Monte Carlo simulation, where muon events and electron events are clearly separated at  $\mathcal{P}_1 = 0$ .

## B.4 Precise vertex finding (MS-fit)

The auto-fit algorithm gives a relatively worse vertex resolution in the longitudinal direction for single-ring events since a vertex shift along the ring direction changes the time of flight of photons evenly for all PMTs and hence the estimator of the fitting does not change so much. In order to obtain more precise vertex point, the fitting using the ring pattern information, so-called “MS-fit”, is applied to single-ring events. The result of auto-fit is left to be used for multi-ring events.

In the algorithm of the MS-fit, the observed photoelectron distribution is compared with the expected one by a likelihood method in which an estimator is maximized by changing the vertex point and the direction of the Cherenkov ring. The definition of the likelihood is the same as that used in the PID algorithm, in which the particle type and the Cherenkov opening angle are determined. After the modification of the vertex point and the ring direction, the vertex position is further adusted perpendicularly to the ring direction to maximize the goodness  $G_{\text{TDC}}$  defined in TDC-fit (Eq. (B.9)). These processes are iterated until the changes in the vertex position and the ring direction become less than 5 cm and  $0.5^\circ$ , respectively.

## B.5 Momentum determination

The momentum of each particle is estimated by the observed number of photoelectrons inside the cone with a half opening angle of  $70^\circ$  with respect to the direction of the corresponding Cherenkov ring. In order to determine the momentum for individual rings, the observed photoelectrons in hits PMTs are separated into the contribution from each ring. The separation of the observed photoelectrons is done based on the expected photoelectron distribution of each ring as a function of the opening angle  $\theta$  and uniform in azimuthal angle  $\phi$ . The observed number of photoelectrons in the  $i$ -th PMT contributed from the  $n$ -th ring is estimated as

$$q_{i,n}^{\text{obs}} = q_i^{\text{obs}} \times \frac{q_{i,n}^{\text{exp}}}{\sum_{n'} q_{i,n'}^{\text{exp}}} , \quad (\text{B.21})$$

where  $q_i^{\text{obs}}$  is the observed number of photoelectrons in the  $i$ -th PMT,  $q_{i,n}^{\text{obs}}$  is the fractional number of photoelectrons from the  $n$ -th ring in the  $i$ -th PMT,  $q_{i,n}^{\text{exp}}$  is the expected number of photoelectrons from the  $n$ -th ring in the  $i$ -th PMT, and the summation in the expression is done over all the rings.

To calculate the total number of photoelectrons inside the  $70^\circ$  cone, the number of photoelectrons in each PMT is corrected for the light attenuation in water and the acceptance of the PMT as follows;

$$RTOT_n = \frac{G_{\text{MC}}}{G_{\text{data}}} \left[ \sum_{\substack{\theta_{i,n} < 70^\circ \\ t_i \in [-50, 250] \text{ nsec}}} \alpha \times \left( q_{i,n}^{\text{obs}} \times \exp\left(\frac{r_i}{L} \times \frac{\cos \Theta_i}{f(\Theta_i)}\right) \right) - \sum_{\theta_{i,n} < 70^\circ} S_i \right] , \quad (\text{B.22})$$

where

- $\alpha$  : normalization factor.
- $G_{\text{data}}, G_{\text{MC}}$  : relative PMT gain parameter for data and MC.
- $q_{i,n}^{\text{obs}}$  : observed number of photoelectrons in the  $i$ -th PMT contributed from the  $n$ -th ring.
- $\theta_{i,n}$  : opening angle between the  $i$ -th PMT direction and the  $n$ -th ring direction.
- $t_i$  : time of flight subtracted hit time of the  $i$ -th PMT.
- $L$  : light attenuation length in water.
- $r_i$  : distance from the vertex position to the  $i$ -th PMT.

- $f(\Theta_i)$  : correction function for the PMT acceptance as a function of the photon incident angle into PMT ( $\Theta_i$ ).
- $S_i$  : expected number of photoelectrons in the  $i$ -the PMT contributed from scattered light.

The summation is restricted inside the time window of from  $-50$  nsec to  $+250$  nsec around the peak of the time of flight subtracted hit timing distribution in order to reject the effect of the electron from muon decay. The relations between  $RTOT$  and the momentum of an electron and a muon are estimated by the Monte Carlo simulation, and using these relationship, the value of  $RTOT$  is translated into the momentum of an electron for a  $e$ -like ring and that of a muon for a  $\mu$ -like ring.

## B.6 Correction to the number of rings (ring correction)

Finally, the number of rings is corrected in this stage. Mis-fitted rings tend to have low momentum and overlapped with other energetic rings. There are two cuts to reject the mis-fitted rings. The first rejection criteria are

- (1-a)  $E_A < E_B$  :  $E_A$  and  $E_B$  are the visible energy of ring-A and ring-B, respectively,  
and
- (1-b)  $|\theta_A - \theta_B| < 30^\circ$  : the angle between the direction of the ring-A  $\theta_A$  and that of ring-B  $\theta_B$ ,  
and
- (1-c)  $E_A \cos(\theta_A - \theta_B) < 60$  MeV.

The second rejection criteria are

- (2-a)  $E_A / \sum_i E_i < 0.05$   
and
- (2-b)  $E_A < 40$  MeV.

If one of two criteria is satisfied, the ring-A is discarded as a fitting mistake.

## B.7 Correction to the number of rings for the events in 1KT (ring correction II)

In addition to the ring correction above, further ring correction is done only in the 1KT reconstruction algorithm, called “ring correction II”. Some events in 1KT contain a few noise hit PMTs with large charges, in which the ring counting algorithm makes mis-fitting resulting in finding the additional fake ring. A typical event for this kind of mis-fitting is shown in Fig. B.6. There are two hit PMTs with large charges around the center of the figure, which clearly seem to be noise hits, and the fake ring illustrated by an ellipse of blue thin line had been found due to the existence of these hits. In order to eliminate such fake rings, the following procedures are applied to the events with 2 rings in 1KT.



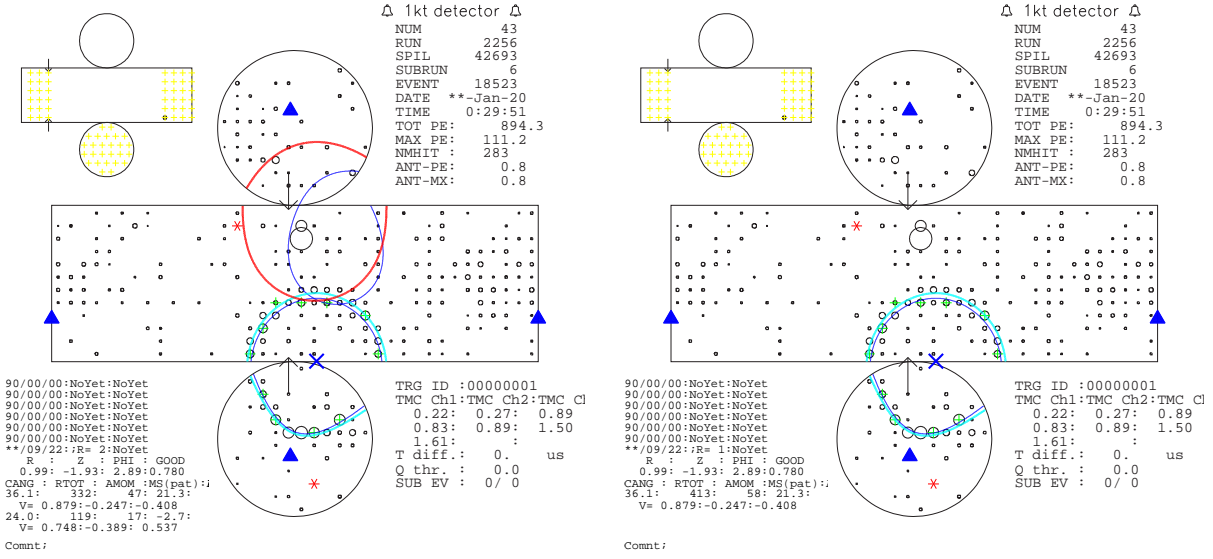


**Figure B.6:** A typical event in which the ring correction II is applied to and the fake ring is removed in 1KT. The left figure shows the results of the ring counting before the ring correction II is applied, in which the large isolated charge around the center of the display makes a fake ring. However, it is removed after ring correction II is applied as shown in the right figure.

First, the number of the isolated hit PMTs with large charge,  $N_{ILQ}$ , is counted. The definition of “isolated hit PMT with large number of photoelectrons” is

- (1) the PMTs with the charge of larger than 60 photoelectrons,
- (2) the PMT which satisfies the condition (1) is located outside the  $60^\circ$  cone with respect to the 1st ring direction,
- (3) the PMT which satisfies the condition (1) is located inside the  $60^\circ$  cone with respect to the 2nd ring direction,
- (4) within two neighboring PMT layers, there is only one or two PMTs which satisfies above three conditions.

Then following cuts are imposed to reject the fake ring.

- (3-a)  $N_{ILQ} > 0$  in the event.

and

- (3-b)  $p_2(e) < 50 \text{ MeV}/c$ , where  $p_2(e)$  is the reconstructed momentum of 2nd ring with the assumption that the 2nd ring is  $e$ -like.

The 2nd ring of the event which satisfies both of these condition is eliminated as a fake ring due to isolated hit PMTs with large charge.



# Appendix C

## Systematic Uncertainties in PIMON Analysis

Systematic errors on the neutrino spectra at ND and SK and  $F/N$  ratio due to various sources are estimated in the PIMON analysis. Here, they are briefly explained. The errors on the spectra at ND and SK in June 1999 and in Nov. 1999 are separately summarized in Table C.1, and Table C.2, and the errors on  $F/N$  ratio are summarized in Table C.3.

### Fitting error

Three errors are quoted on the each data point of the Cherenkov light distributions: The error due to spill-by-spill fluctuation is estimated by  $\frac{(\text{R.M.S. of ADC distribution})}{\sqrt{\text{number of spills}}}$ . The uncertainty of the PMT gain adjustment is estimated to be 10% and 5% for June 1999 and Nov. 1999 runs, respectively, as described in Sec. 3.3.1. The uncertainty of lower gain operation in Nov. 1999 run is estimated by the difference between data with gain of 20 and 50 at the same refractive index  $n = 1.00129$ . These errors are fed to the fitting, and hence they are included in the fitting error.

### Mirror reflectivity

The calibration using laser system have confirmed that the mirror reflectivity have no radiation damage within 6% during the PIMON runs. A few percent of deterioration of the reflectivity around the beam center considered, the difference of the results are quoted as the systematic error of the mirror reflectivity.

### Refractive index uncertainty

The major contribution to the uncertainty of the refractive index of freon gas is from its wavelength dependence. Two situations are compared: One is that the refractive index calibrated by primary proton beam is used in the MC, and the other is that the wavelength dependence of the refractive index is included in MC. In both case, the fitting has been performed to reconstruct the pion kinematics, and the difference between these results are quoted as the systematic error.

### Difference between the low and high beam intensity

As mentioned before, the PIMON data had been taken with the lower beam intensity than in the normal run. A main difference between the low and high beam intensity is the profile and divergence of the proton beam. During PIMON runs, the beam profile was about 30% narrower

than that in the normal runs. Using Beam-MC, the difference between the normal and the narrower beam profile is quoted as the systematic error.

### **Injection point of the proton beam onto the target**

The injection point of the proton beam onto the target during the PIMON runs was the same as that in the normal runs within 1 mm. The Beam-MC study had been performed in order to estimate the effect of the difference of the beam injection point.

### **Beam stability during the PIMON run**

Proton beam was monitored using V39out- and TGT-SPICs. The fluctuation of the center of the proton beam during the PIMON runs was about 0.1–0.2 mm. The yield of secondary muons was monitored by MUMON. It was also stable within 4.6% and 1.4% in June 1999 run and Nov. 1999 run, respectively. In order to estimate the systematic errors from them, the proton injection point was fluctuated at several points and their relusting differences are quoted as the errors.

### **Beam stability during the normal run**

The uncertainty from the instability of the injection point and the profile of proton beam during the normal runs is also estimated by employing the MC simulation.

### **Azimuthal symmetry of the magnetic field inside the horn magnets**

In the analysis of PIMON measurements, the azimuthal symmetry of the magnetic field inside the horn magnets is assumed. As mentioned in Sec. 3.1.2, we had observed asymmetry of the magnetic field of about 15%, although the measurement of the magnetic field have large uncertainty. The fitting results with no asymmetry and 15% asymmetry are compared and the difference is quoted as the systematic errors.

### **Alignment of the PIMON**

PIMON is well aligned with respect to the center of the beam line. The results of an optical survey ensures that the height of the mirror is aligned with the precision of within 1 mm, and the horizontal position is adjusted to the designed beam axis within a few hundred  $\mu\text{m}$ . The systematic errors from the incorrect alignment is negligibly small.

### **Background subtraction using the mirror-off data**

The data with the mirror rotated up to  $14.5^\circ$  off from the nominal direction were taken, which proved that the background components are uniform. The systematic errors from the background subtraction using the mirror-off data is negligible.

### **Subtraction of the electro-magnetic components**

The shape of the Cherenkov light distribution contributed from the electro-magnetic components is well reproduced by Beam-MC. Therefore, the error on absolute normalization of the electro-magnetic components in the  $\chi^2$ -fitting is used to estimate the systematic errors on the neutrino spectrum. It makes only negligibly small effect.

### **Fitting method**

Different MC are used to make the template histograms of Cherenkov light distribution to study the effect of fitting method: Cho-CERN and GCALOR hadron packages and different horn currents. This difference makes the secondary pion profile and divergence. It had been studied whether the fitting settled down at the same results even in the case of that the different MC's were used. The difference of results is quoted as the systematic errors from the fitting method.

### **Contribution of pions decaying before PIMON**

The uncertainty of the contribution of the pion decay before PIMON is estimated by comparing two different hadron models, Cho-CERN and GCALOR.

### **Radial distribution of pions**

Difference of radial distribution of pions affects to the decay probability of pion since some part of pions is absorbed in the wall of the decay volume. This makes the change in the energy spectrum of the neutrino beam. Using two different hadron models, Cho-CERN and GCALOR, the effect of the different radial distribution of pions is studied.

### **Bin size of pion kinematics ( $p_\pi, \theta_\pi$ )**

Flat population inside each  $(p_\pi, \theta_\pi)$  bin is assumed in the PIMON analysis, whereas there is the structure inside the bin in the actual case. The systematic bias from this assumption is estimated by comparing the full Beam-MC and the Beam-MC with flat bins of  $(p_\pi, \theta_\pi)$ .

### **Uncertainty of neutrino flux below 1 GeV**

PIMON cannot predict the neutrino flux below 1 GeV. As mentioned in the previous section, the errors on the neutrino flux in the region below 1 GeV are estimated using the Beam-MC by varying the value of parameters in Eq. (4.4) within 90% C.L.

**Table C.1:** Summary of systematic errors of the PIMON measurements on the spectra at ND and SK in June 1999. Upper table shows the errors at ND and lower table shows those at SK. In the table, “—” means negligibly small error.

Errors on neutrino spectrum at near detector in June 1999							
Energy bins [GeV]		0.0–0.5	0.5–1.0	1.0–1.5	1.5–2.0	2.0–2.5	2.5–
1.	Fitting error			±11.7%	±9.2%	±17.2%	+25.1%
2.	Mirror reflectivity			−1.4%	+4.2%	−3.5	−8.7%
3.	Refractive index			—	—	—	—
4.	PMT saturation correction			±0.5%	±1.2%	±1.4%	+30.0%
5.	Low/high beam intensity			−5.5%	±1.0%	+10.0%	+7.0%
6.	Beam injection point			−1.5%	+6.8%	−10.0%	+8.9%
7.	Beam stability (PIMON run)			±1.9%	±4.3%	±5.0%	±12.7%
8.	Beam stability (normal run)			—	—	+0.8%	+3.8%
9.	$\phi$ asymmetry of horn field			−2.9%	−0.9%	+32.6%	−3.2%
10.	PIMON alignment			—	—	—	−19.0%
11.	Subtraction of background			—	—	—	—
12.	Subtraction of EM component			—	—	—	−74.0%
13.	Fitting method			+6.8%	−7.7%	−15.3%	+12.0%
14.	Pion decay before PIMON			±0.9%	±1.9%	±2.8%	−21.0%
15.	Radial distribution of pions			±0.2%	±0.4%	±2.3%	±1.3%
16.	Binning of pion kinematics			±2.0%	−2.7%	−7.2%	±20.0%
Total				+13.9%	+13.2%	+39.0%	+49.0%
				−13.6%	−13.3%	−27.0%	−88.0%

Errors on neutrino spectrum at Super-Kamiokande in June 1999							
Energy bins [GeV]		0.0–0.5	0.5–1.0	1.0–1.5	1.5–2.0	2.0–2.5	2.5–
1.	Fitting error			±14.7%	±9.6%	±19.3%	+26.7%
2.	Mirror reflectivity			−1.6%	+3.1%	−0.7	−9.0%
3.	Refractive index			—	—	—	—
4.	PMT saturation correction			±0.8%	±1.2%	±2.0%	+20.0%
5.	Low/high beam intensity			−7.0%	±6.5%	+4.5%	+6.5%
6.	Beam injection point			−2.5%	+9.1%	−10.0%	+3.6%
7.	Beam stability (PIMON run)			±3.2%	±3.7%	±5.0%	±12.8%
8.	Beam stability (normal run)			+1.2%	−1.9%	+1.8% −1.0%	+4.2% −4.3%
9.	$\phi$ asymmetry of horn field			−2.4%	−7.5%	+38.8%	−10.7%
10.	PIMON alignment			—	—	—	—
11.	Subtraction of background			—	—	—	—
12.	Subtraction of EM component			—	—	—	−60.0%
13.	Fitting method			+11.0%	−10.2%	−12.3%	+1.6% 32.0%
14.	Pion decay before PIMON			±2.3%	±5.7%	±6.3%	±0.4%
15.	Radial distribution of pions			—	±0.2%	±1.4%	±21.0%
16.	Binning of pion kinematics			−1.4%	−2.7%	−7.4%	−13.0%
Total				+18.8% −17.2%	+15.2% −18.8%	+44.4% −27.1%	+42.3% −77.5%

**Table C.2:** Summary of systematic errors of the PIMON measurements on the spectra at ND and SK in Nov. 1999. Upper table shows the errors at ND and lower table shows those at SK. In the table, “—” means negligibly small error.

Errors on neutrino spectrum at near detector in Nov. 1999							
Energy bins [GeV]		0.0–0.5	0.5–1.0	1.0–1.5	1.5–2.0	2.0–2.5	2.5–
1.	Fitting error			±6.2%	±4.8%	±7.7%	±12.0%
2.	Mirror reflectivity			−2.0%	+2.9%	+3.4	+0.6%
3.	Refractive index			−5.1%	+7.3%	+4.6%	+37.0%
4.	PMT saturation correction			—	—	—	—
5.	Low/high beam intensity			−1.2%	+0.6%	+4.0%	+5.0%
6.	Beam injection point			—	−2.0%	—	−4.8%
7.	Beam stability (PIMON run)			—	—	—	±5.5%
8.	Beam stability (normal run)			±1.0%	+1.0% −1.9%	+4.4% −1.1%	+6.3% −3.4%
9.	$\phi$ asymmetry of horn field			−3.6%	+5.2%	+0.7%	−10.6%
10.	PIMON alignment			—	—	—	—
11.	Subtraction of background			—	—	—	—
12.	Subtraction of EM component			—	—	—	—
13.	Fitting method			+6.8%	−7.7%	−15.3%	+12.0% −21.0%
14.	Pion decay before PIMON			±0.2%	±0.8%	±0.5%	±0.4%
15.	Radial distribution of pions			±0.5%	±1.0%	±4.3%	±20.0%
16.	Binning of pion kinematics			+2.7%	−2.4%	−7.0%	−10.0%
Total				+9.2% −9.6%	+10.7% −9.9%	+12.1% −17.7%	+47.7% −34.0%

Errors on neutrino spectrum at Super-Kamiokande in Nov. 1999							
Energy bins [GeV]		0.0–0.5	0.5–1.0	1.0–1.5	1.5–2.0	2.0–2.5	2.5–
1.	Fitting error			±8.1%	±4.9%	±7.6%	+12.0%
2.	Mirror reflectivity			−3.1%	+1.8%	+4.0	+0.3%
3.	Refractive index			−8.6%	+5.4%	+1.1%	33.0%
4.	PMT saturation correction			—	—	—	—
5.	Low/high beam intensity			−2.1%	−1.5%	+3.1%	+7.8%
6.	Beam injection point			—	—	—	4.9%
7.	Beam stability (PIMON run)			—	—	—	4.8%
8.	Beam stability (normal run)			+1.6% −2.1%	+0.3% −1.5%	+4.1% −1.6%	+16.0% −0.2%
9.	ϕ asymmetry of horn field			−5.7%	+2.5%	+0.7%	+9.8%
10.	PIMON alignment			—	—	—	—
11.	Subtraction of background			—	—	—	—
12.	Subtraction of EM component			—	—	—	—
13.	Fitting method			+11.0%	−10.2%	−12.3%	+1.6% 32.0%
14.	Pion decay before PIMON			±0.5%	±1.5%	±1.1%	—
15.	Radial distribution of pions			±0.5%	±0.5%	±3.1%	±10.0%
16.	Binning of pion kinematics			+0.5%	−2.4%	−5.4%	−15.4%
Total				±13.8% −11.9%	+8.1% −15.8%	+10.6% −15.8%	+42.1% −39.5%

**Table C.3:** Summary of systematic errors of the PIMON measurements on the far-to-near spectrum ratio in June 1999 and Nov. 1999. Upper table shows the errors in June 1999 and lower table shows those in Nov. 1999. In the table, “—” means negligibly small error.

Errors on far-to-near spectrum ratio in June 1999							
Energy bins [GeV]		0.0–0.5	0.5–1.0	1.0–1.5	1.5–2.0	2.0–2.5	2.5–
1.	Fitting error			+3.2% –4.5%	+6.2% –4.9%	+2.0% –5.7%	+8.5% –5.8%
2.	Mirror reflectivity			–0.1%	+0.4%	+3.5	–0.3%
3.	Refractive index			—	—	—	—
4.	PMT saturation correction			±0.6%	±0.5%	±1.3%	±4.2%
5.	Low/high beam intensity			–6.0%	–5.3%	–6.6%	±0.5%
6.	Beam injection point			–1.0%	+2.1%	–0.6%	–4.8%
7.	Beam stability (PIMON run)			±1.0%	±1.5%	±3.4%	±1.1%
8.	Beam stability (normal run)			+0.7% –0.3%	–2.3%	+0.9% –1.5%	–3.4%
9.	$\phi$ asymmetry of horn field			+0.5%	–6.7%	+4.7%	+4.9%
10.	PIMON alignment			—	—	—	—
11.	Subtraction of background			—	—	—	—
12.	Subtraction of EM component			—	—	—	+72.0%
13.	Fitting method			+4.0%	+1.4% –3.0%	+3.2% –4.6%	–14.5%
14.	Pion decay before PIMON			±1.4%	±3.8%	±3.4%	±1.6%
15.	Radial distribution of pions			—	—	±1.0%	±7.2%
16.	Binning of pion kinematics			–0.6%	—	—	–13.0%
17.	Hadron production model (MC)	+5.1% –9.5%	+7.3% –2.5%	+5.5% –7.8%	+7.8% –11.3%	+8.7% –11.2%	+73.6% –22.8%
Total		+5.1% –9.5%	+7.3% –2.5%	+5.5% –7.8%	+7.8% –11.3%	+8.7% –11.2%	+73.6% –22.8%

Errors on far-to-near spectrum ratio in Nov. 1999							
Energy bins [GeV]		0.0–0.5	0.5–1.0	1.0–1.5	1.5–2.0	2.0–2.5	2.5–
1.	Fitting error			+2.2% –2.9%	+2.2% –2.1%	+3.2% –2.9%	+1.0% –0.9%
2.	Mirror reflectivity			–1.2%	–1.1%	+0.5	–0.3%
3.	Refractive index			–3.7%	–1.8%	–3.3%	–2.6%
4.	PMT saturation correction			—	—	—	—
5.	Low/high beam intensity			–1.9%	–3.7%	–1.9%	+2.9%
6.	Beam injection point			—	+1.2%	—	—
7.	Beam stability (PIMON run)			—	—	—	±0.5%
8.	Beam stability (normal run)			+1.6% –1.8%	+1.5% –2.1%	+1.2% –1.4%	+9.0%
9.	$\phi$ asymmetry of horn field			–2.6%	–2.4%	–2.4%	–1.0%
10.	PIMON alignment			—	—	—	—
11.	Subtraction of background			—	—	—	—
12.	Subtraction of EM component			—	—	—	—
13.	Fitting method			+4.0%	+1.4% –3.0%	+3.2% –4.6%	–14.5%
14.	Pion decay before PIMON			±0.7%	±0.7%	±1.7%	±0.5%
15.	Radial distribution of pions			—	±0.5%	±1.3%	±8.5%
16.	Binning of pion kinematics			–2.1%	—	+1.7%	–7.1%
17.	Hadron production model (MC)	+5.1% –9.5%	+7.3% –2.5%	+4.9% –6.5%	+3.3% –6.5%	+5.4% –7.5%	+12.8% –18.5%
Total		+5.1% –9.5%	+7.3% –2.5%	+4.9% –6.5%	+3.3% –6.5%	+5.4% –7.5%	+12.8% –18.5%

# References

- [1] W. Pauli, *Letter to the Physical Society of Tübingen* (1930), unpublished, the letter is reproduced in Brown, L.M. (1978), *Physics Today*, **31**, No. 9, 23.
- [2] E. Fermi, *Z. Phys.* **88**, 161 (1934).
- [3] F. Reines and C. L. Cowan, Jr., *Phys. Rev.* **92**, 830 (1953).
- [4] G. Danby *et al.*, *Phys. Rev. Lett.* **9**, 36 (1962).
- [5] M. L. Perl *et al.*, *Phys. Rev. Lett.* **35**, 1489 (1975).
- [6] K. Kodama *et al.* (DONUT Collaboration), *Phys. Lett.* **B504**, 218 (2001), hep-ex/0012035.
- [7] S. L. Glashow, *Nucl. Phys.* **22**, 579 (1961).
- [8] S. Weinberg, *Phys. Rev. Lett.* **19**, 1267 (1967).
- [9] A. Salam, In *Novel Symposium*, **No. 8** (1968).
- [10] J. Drees (LEP Collaborations and LEP Electroweak Working Group), *the XX International Symposium on Lepton and Photon Interactions at High Energy*, Rome, Italy (2001).
- [11] V. M. Lobashev *et al.*, *Phys. Lett.* **B460**, 227 (1999).
- [12] C. Weinheimer *et al.*, *Phys. Lett.* **B460**, 219 (1999).
- [13] K. Assamagan *et al.*, *Phys. Rev.* **D53**, 6065 (1996).
- [14] R. Barate *et al.* (ALEPH Collaboration), *Eur. Phys. J.* **C2**, 395 (1998).
- [15] D. N. Spergel and J. N. Bahcall, *Phys. Lett.* **B200**, 366 (1988).
- [16] T. J. Loredo and D. Q. Lamb, *Annal. NY Acad. Sci.* **571**, 601 (1989).
- [17] F. T. Avignone and J. I. Collar, *Phys. Rev.* **D41**, 682 (1990).
- [18] P. J. Kernan and L. M. Krauss, *Nucl. Phys.* **B437**, 243 (1995), astro-ph/9410010.
- [19] D. N. Spergel *et al.*, *Astrophys. J. Suppl.* **148**, 175 (2003), astro-ph/0302209.
- [20] K. Hagiwara *et al.* (Particle Data Group), *Phys. Rev.* **D66**, 010001 (2002).
- [21] Z. Maki, M. Nakagawa, and S. Sakata, *Prog. Theor. Phys.* **28**, 870 (1962).
- [22] M. Kobayashi and T. Maskawa, *Prog. Theor. Phys.* **49**, 652 (1973).
- [23] Y. Itow *et al.*, *The JHF-Kamioka neutrino project* (2001), as Letter of Intent, hep-ex/0106019.

- [24] A. Piepke (KamLAND Collaboration), Nucl. Phys. Proc. Suppl. **91**, 99 (2001).
- [25] K. Eguchi *et al.* (KamLAND Collaboration), Phys. Rev. Lett. **90**, 021802 (2003), hep-ex/0212021.
- [26] A. O. Bazarko (BooNE Collaboration) (2002), hep-ex/0210020.
- [27] K. Nishikawa *et al.*, *Proposal for a Long Baseline Neutrino Oscillation experiment using KEK-PS and Super-Kamiokande* (1995), as KEK-PS proposal (E362).
- [28] H. Murayama, <http://hitoshi.berkeley.edu/neutrino/>.
- [29] Y. Yamanoi *et al.*, IEEE Trans. on Applied Superconductivity **10**, 252 (2000).
- [30] M. Kohama, Master's thesis, Kobe University (1997), in Japanese.
- [31] H. Noumi *et al.*, Nucl. Instrum. Meth. **A398**, 399 (1997).
- [32] Y. Yamanoi *et al.*, KEK-preprint 97-225 (1997).
- [33] Y. Yamanoi *et al.*, KEK-preprint 99-178 (1999).
- [34] K. H. Tanaka *et al.*, KEK-preprint 91-27 (1991).
- [35] T. Maruyama, Ph.D. thesis, Tohoku University (2000).
- [36] T. Inagaki, Master's thesis, University of Tokyo (1998), in Japanese.
- [37] H. Kume *et al.*, Nucl. Instrum. Meth. **205**, 443 (1983).
- [38] A. Suzuki *et al.*, Nucl. Instrum. Meth. **A329**, 299 (1993).
- [39] S. Nakayama, Master's thesis, University of Tokyo (1999), in Japanese.
- [40] T. Tanimori *et al.*, IEEE Trans. Nucl. Sci. **36**, 497 (1989).
- [41] H. Ikeda *et al.*, Nucl. Instrum. Meth. **A320**, 310 (1992).
- [42] H. Ishino, Master's thesis, Tokyo Institute of Technology (1996), in Japanese.
- [43] Y. Kobayashi, Master's thesis, University of Tokyo (1999), in Japanese.
- [44] A. Shima, Master's thesis, Kyoto University (2001), in Japanese.
- [45] A. Suzuki *et al.* (K2K Collaboration), Nucl. Instrum. Meth. **A453**, 165 (2000), hep-ex/0004024.
- [46] B. J. Kim *et al.*, Nucl. Instrum. Meth. **A497**, 450 (2003), hep-ex/0206041.
- [47] T. Iwashita, Ph.D. thesis, Kobe University (2003).
- [48] S. Kawabata *et al.*, Nucl. Instrum. Meth. **A270**, 11 (1988).
- [49] M. Yoshida, Ph.D. thesis, Osaka University (2001).
- [50] T. Ishii *et al.* (K2K MRD Group), Nucl. Instrum. Meth. **A482**, 244 (2002), hep-ex/0107041.



- [51] Y. Asano *et al.*, Nucl. Instrum. Meth. **A259**, 430 (1987).
- [52] Y. Ikegami *et al.*, IEEE Trans. Nucl. Sci. **36**, 665 (1989).
- [53] T. Inagaki, Ph.D. thesis, Kyoto University (2001).
- [54] S. Fukuda *et al.*, Nucl. Instrum. Meth. **A501**, 418 (2003).
- [55] K. Okumura, Ph.D. thesis, University of Tokyo (1999).
- [56] M. Shiozawa, Ph.D. thesis, University of Tokyo (1999).
- [57] K. Ishihara, Ph.D. thesis, University of Tokyo (1999).
- [58] S. Yamada, Ph.D. thesis, University of Tokyo (2003).
- [59] H. G. Berns and R. J. Wilkes, IEEE Trans. Nucl. Sci. **47**, 340 (2000), hep-ex/9909021.
- [60] T. A. Gabriel, J. D. Amburgey, and B. L. Bishop (1977), ORNL/TM-5619.
- [61] C. Zeitnitz and T. A. Gabriel, Nucl. Instrum. Meth. **A349**, 106 (1994).
- [62] A. Fasso, A. Ferrari, J. Ranft, and P. R. Sala, *FLUKA: Present status and future developments* (1993), given at 4th International Conference on Calorimetry in High-energy Physics, La Biodola, Italy, 19-25 Sep 1993.
- [63] *GEANT – Detector Description and Simulation Tool*, Application Software Group, Computing and Networks Division, CERN (1993), CERN Program Library Long Writeup W5013.
- [64] R. A. Lundy *et al.*, Phys. Rev. Lett. **14**, 504 (1965).
- [65] D. Dekkers *et al.*, Phys. Rev. **137**, B962 (1965).
- [66] W. F. Baker *et al.*, Phys. Rev. Lett. **7**, 101 (1961).
- [67] J. R. Sanford and C. L. Wang, AGS internal report BNL-11299 and BNL-11479, Brookhaven National Laboratory (1967), unpublished.
- [68] C. L. Wang, Phys. Rev. Lett. **25**, 1068 (1970).
- [69] A. Yamamoto, KEK Report 81-13 (1981).
- [70] G. J. Marmer *et al.*, Phys. Rev. **179**, 1294 (1969).
- [71] G. J. Marmer and D. E. Lundquist, Phys. Rev. **D3**, 1089 (1971).
- [72] Y. Cho *et al.*, Phys. Rev. **D4**, 1967 (1971).
- [73] J. G. Asbury *et al.*, Phys. Rev. **178**, 2086 (1969).
- [74] J. V. Allaby *et al.*, CERN Report No. CERN-TH-70-12 (1970), unpublished.
- [75] Private communication with W. Gajewski, a K2K collaborator. I heard that there is a document in CERN reports which gives the information on Cho-CERN, but I could not find it. See also K2K internal note BEAM/BMMC/00-001.

- [76] E. D. Commins and P. H. Bucksbaum, *Weak interactions of leptons and quarks* (Cambridge University Press, 1983).
- [77] Y. Hayato, Nucl. Phys. Proc. Suppl. **112**, 171 (2002).
- [78] J. Kameda, Ph.D. thesis, University of Tokyo (2002).
- [79] S. J. Barish *et al.*, Phys. Rev. **D16**, 3103 (1977).
- [80] N. J. Baker *et al.*, Phys. Rev. **D23**, 2499 (1981).
- [81] S. Bonetti *et al.*, Nuovo Cim. **A38**, 260 (1977).
- [82] S. V. Belikov *et al.*, Z. Phys. **A320**, 625 (1985).
- [83] C. H. Llewellyn Smith, Phys. Rept. **3**, 261 (1972).
- [84] K. L. Miller *et al.*, Phys. Rev. **D26**, 537 (1982).
- [85] L. A. Ahrens *et al.*, Phys. Rev. Lett. **56**, 1107 (1986).
- [86] C. H. Albright, C. Quigg, R. E. Shrock, and J. Smith, Phys. Rev. **D14**, 1780 (1976).
- [87] F. A. Brieva and A. Dellafiore, Nucl. Phys. **A292**, 445 (1977).
- [88] D. Rein and L. M. Sehgal, Ann. Phys. **133**, 79 (1981).
- [89] D. Rein, Z. Phys. **C35**, 43 (1987).
- [90] R. P. Feynman, M. Kislinger, and F. Ravndal, Phys. Rev. **D3**, 2706 (1971).
- [91] V. Bernard, L. Elouadrhiri, and U. G. Meissner, J. Phys. **G28**, R1 (2002), hep-ph/0107088.
- [92] G. M. Radecky *et al.*, Phys. Rev. **D25**, 1161 (1982).
- [93] T. Kitagaki *et al.*, Phys. Rev. **D34**, 2554 (1986).
- [94] M. Pohl *et al.*, Lett. Nuovo Cim. **24**, 540 (1979).
- [95] M. Glück, E. Reya, and A. Vogt, Z. Phys. **C67**, 433 (1995).
- [96] A. Bodek and U. K. Yang, Nucl. Phys. Proc. Suppl. **112**, 70 (2002), hep-ex/0203009.
- [97] P. Musset and J. P. Vialle, Phys. Rept. **39**, 1 (1978).
- [98] J. E. Kim, P. Langacker, M. Levine, and H. H. Williams, Rev. Mod. Phys. **53**, 211 (1981).
- [99] M. Derrick *et al.*, Phys. Rev. **D17**, 1 (1978).
- [100] H. Sarikko, Proc. of the NEUTRINO'79 p. 507 (1979).
- [101] S. Barlag *et al.* (Amsterdam-Bologna-Padua-Pisa-Saclay-Turin), Zeit. Phys. **C11**, 283 (1982).
- [102] T. Sjostrand, CERN Report No. CERN-TH-7112-93 (1994), hep-ph/9508391.
- [103] D. Rein and L. M. Sehgal, Nucl. Phys. **B223**, 29 (1983).

- [104] P. Marage *et al.* (BEBC WA59 Collaboration), Z. Phys. **C31**, 191 (1986).
- [105] J. Marteau, Eur. Phys. J. **A5**, 183 (1999), hep-ph/9902210.
- [106] J. Marteau, J. Delorme, and M. Ericson, Nucl. Instrum. Meth. **A451**, 76 (2000).
- [107] L. L. Salcedo, E. Oset, M. J. Vicente-Vacas, and C. Garcia-Recio, Nucl. Phys. **A484**, 557 (1988).
- [108] C. H. Q. Ingram *et al.*, Phys. Rev. **C27**, 1578 (1983).
- [109] G. Rowe, M. Salomon, and R. H. Landau, Phys. Rev. **C18**, 584 (1978).
- [110] M. Nakahata *et al.* (Kamiokande Collaboration), J. Phys. Soc. Jap. **55**, 3786 (1986).
- [111] E. Bracci *et al.*, CERN Report No. CERN-HERA-72-1 (1972).
- [112] A. S. Carroll *et al.*, Phys. Rev. **C14**, 635 (1976).
- [113] Private communication with T. Maruyama, a K2K collaborator, on 23 and 25 March 2003 by e-mail.
- [114] J. Hill, K2K internal report BEAM/BMMC/01-002, High Energy Accelerator Research Organization (KEK) (2001), unpublished.
- [115] H. Park, K2K internal report *SciFi Analysis Manual*, High Energy Accelerator Research Organization (KEK) (1999), unpublished.
- [116] K. V. Alanakian *et al.*, Phys. Atom. Nucl. **61**, 207 (1998).
- [117] F. James, *MINUIT — Function Minimization and Error Analysis — Reference Manual*, Computing and Networks Division, CERN (1994), CERN Program Library Long Writup D506.
- [118] K. Nishikawa, *Results and Status of Current Accelerator Neutrino Experiments* (2003), given at 21th International Symposium on Lepton and Photon interactions at High Energies, Fermi National Accelerator Laboratory, Batavia, Illinois U.S.A., 11-16 Aug. 2003.
- [119] The HARP Collaboration, CERN Report No. CERN-SPSC-99-35 SPSC-P-315 (1999).
- [120] The HARP Collaboration, CERN Report No. CERN-SPSC-2004-018 SPSC-M-717 (2004).
- [121] J. J. Gomez-Cadenas, *HARP measurement of pions yields in a replica target of the K2K experiment* (2004), given at 21th International Conference on Neutrino Physics and Astrophysics (NEUTRINO 2004), Collège de France, Paris, France, 14-19 June 2004.
- [122] K. Nitta *et al.* (The K2K SciBar Group) (2004), contributed to 10th Vienna Conference on Instrumentation, Vienna, Austria, 16-21 Feb 2004, to appear in Nucl. Instrum. Meth., hep-ex/0406023.
- [123] Y. Fukuda *et al.* (Super-Kamiokande Collaboration), Phys. Lett. **B433**, 9 (1998a), hep-ex/9803006.
- [124] Y. Fukuda *et al.* (Super-Kamiokande Collaboration), Phys. Lett. **B436**, 33 (1998b), hep-ex/9805006.

- [125] M. Koshiba (Kamiokande Collaboration), *Nuovo Cim.* **C9**, 141 (1986).
- [126] K. S. Hirata *et al.* (Kamiokande-II Collaboration), *Phys. Lett.* **B205**, 416 (1988).
- [127] K. S. Hirata *et al.* (Kamiokande-II Collaboration), *Phys. Lett.* **B280**, 146 (1992).
- [128] Y. Fukuda *et al.* (Kamiokande Collaboration), *Phys. Lett.* **B335**, 237 (1994).
- [129] R. Becker-Szendy *et al.*, *Phys. Rev.* **D46**, 3720 (1992).
- [130] R. Clark *et al.*, *Phys. Rev. Lett.* **79**, 345 (1997).
- [131] W. W. M. Allison *et al.* (Soudan-2 Collaboration), *Nucl. Instrum. Meth.* **A376**, 36 (1996).
- [132] W. W. M. Allison *et al.* (Soudan-2 Collaboration), *Phys. Lett.* **B449**, 137 (1999), hep-ex/9901024.
- [133] C. De Marzo *et al.* (MACRO Collaboration), *Nuovo Cim.* **C9**, 281 (1986).
- [134] S. P. Ahlen *et al.* (MACRO Collaboration), *Nucl. Instrum. Meth.* **A324**, 337 (1993).
- [135] M. Ambrosio *et al.* (MACRO Collaboration), *Nucl. Instrum. Meth.* **A486**, 663 (2002).
- [136] M. Ambrosio *et al.* (MACRO Collaboration), *Phys. Lett.* **B434**, 451 (1998), hep-ex/9807005.
- [137] C. Berger *et al.* (Fréjus Collaboration), *Nucl. Instr. Meth.* **A262**, 463 (1987).
- [138] K. Daum (Fréjus Collaboration), *Z. Phys.* **C66**, 417 (1995).
- [139] M. Aglietta *et al.* (NUSEX Collaboration), *Europhys. Lett.* **8**, 611 (1989).
- [140] Y. Fukuda *et al.* (Super-Kamiokande Collaboration), *Phys. Rev. Lett.* **81**, 1562 (1998c), hep-ex/9807003.
- [141] S. P. Mikheev and A. Y. Smirnov, *Sov. J. Nucl. Phys.* **42**, 913 (1985).
- [142] L. Wolfenstein, *Phys. Rev.* **D17**, 2369 (1978).
- [143] S. Fukuda *et al.* (Super-Kamiokande Collaboration), *Phys. Rev. Lett.* **85**, 3999 (2000), hep-ex/0009001.
- [144] M. Ambrosio *et al.* (MACRO Collaboration), *Phys. Lett.* **B517**, 59 (2001), hep-ex/0106049.
- [145] J. N. Bahcall, M. H. Pinsonneault, and S. Basu, *Astrophys. J.* **555**, 990 (2001), astro-ph/0010346.
- [146] B. T. Cleveland *et al.*, *Astrophys. J.* **496**, 505 (1998).
- [147] W. Hampel *et al.* (GALLEX Collaboration), *Phys. Lett.* **B447**, 127 (1999).
- [148] M. Altmann *et al.* (GNO Collaboration), *Phys. Lett.* **B490**, 16 (2000), hep-ex/0006034.
- [149] J. N. Abdurashitov *et al.* (SAGE Collaboration), *Phys. Rev.* **C60**, 055801 (1999), astro-ph/9907113.

- [150] Y. Fukuda *et al.* (Kamiokande Collaboration), Phys. Rev. Lett. **77**, 1683 (1996).
- [151] S. Fukuda *et al.* (Super-Kamiokande Collaboration), Phys. Rev. Lett. **86**, 5651 (2001), hep-ex/0103032.
- [152] Q. R. Ahmad *et al.* (SNO Collaboration), Phys. Rev. Lett. **89**, 011301 (2002a), nucl-ex/0204008.
- [153] J. Boger *et al.* (SNO Collaboration), Nucl. Instrum. Meth. **A449**, 172 (2000), nucl-ex/9910016.
- [154] Q. R. Ahmad *et al.* (SNO Collaboration), Phys. Rev. Lett. **89**, 011302 (2002b), nucl-ex/0204009.
- [155] S. Fukuda *et al.* (Super-Kamiokande Collaboration), Phys. Lett. **B539**, 179 (2002), hep-ex/0205075.
- [156] M. Apollonio *et al.* (CHOOZ Collaboration), Phys. Lett. **B466**, 415 (1999), hep-ex/9907037.
- [157] F. Boehm *et al.*, Phys. Rev. **D64**, 112001 (2001), hep-ex/0107009.
- [158] Y. Declais *et al.*, Nucl. Phys. **B434**, 503 (1995).
- [159] G. S. Vidyakin *et al.*, JETP Lett. **59**, 390 (1994).
- [160] J. L. Vuilleumier *et al.* (CalTech-SIN-TUM Collaboration), Phys. Lett. **B114**, 298 (1982).
- [161] G. Zacek *et al.* (CalTech-SIN-TUM Collaboration), Phys. Rev. **D34**, 2621 (1986).
- [162] A. A. Kuvshinnikov, L. A. Mikaelyan, S. V. Nikolaev, M. D. Skorokhvatov, and A. V. Etenko, JETP Lett. **54**, 253 (1991).
- [163] A. I. Afonin *et al.*, Sov. Phys. JETP **67**, 213 (1988).
- [164] Z. D. Greenwood *et al.*, Phys. Rev. **D53**, 6054 (1996).
- [165] E. Eskut *et al.* (CHORUS Collaboration), Phys. Lett. **B497**, 8 (2001).
- [166] P. Astier *et al.* (NOMAD Collaboration), Nucl. Phys. **B611**, 3 (2001), hep-ex/0106102.
- [167] A. Romosan *et al.* (CCFR/NuTeV Collaboration), Phys. Rev. Lett. **78**, 2912 (1997), hep-ex/9611013.
- [168] K. S. McFarland *et al.*, Phys. Rev. Lett. **75**, 3993 (1995), hep-ex/9506007.
- [169] D. Naples *et al.* (CCFR/NuTeV Collaboration), Phys. Rev. **D59**, 031101 (1999), hep-ex/9809023.
- [170] S. Avvakumov *et al.* (NuTeV Collaboration), Phys. Rev. Lett. **89**, 011804 (2002), hep-ex/0203018.
- [171] F. Dydak *et al.*, Phys. Lett. **B134**, 281 (1984).
- [172] F. Bergsma *et al.* (CHARM Collaboration), Z. Phys. **C40**, 171 (1988).
- [173] L. Borodovsky *et al.*, Phys. Rev. Lett. **68**, 274 (1992).

- 
- [174] B. Armbruster *et al.* (KARMEN Collaboration), Phys. Rev. **D65**, 112001 (2002), hep-ex/0203021.
  - [175] B. Armbruster *et al.*, Phys. Rev. **C57**, 3414 (1998), hep-ex/9801007.
  - [176] C. Athanassopoulos *et al.* (LSND Collaboration), Phys. Rev. Lett. **81**, 1774 (1998), nucl-ex/9709006.
  - [177] A. Aguilar *et al.* (LSND Collaboration), Phys. Rev. **D64**, 112007 (2001), hep-ex/0104049.
  - [178] P. Astier *et al.* (NOMAD Collaboration), Phys. Lett. **B570**, 19 (2003), hep-ex/0306037.
  - [179] E. D. Church, K. Eitel, G. B. Mills, and M. Steidl, Phys. Rev. **D66**, 013001 (2002), hep-ex/0203023.
  - [180] E. R. Davies, *Machine Vision: Theory, Algorithms, Practicalities* (Academic Press, San Diego, 1997).